Mechanistic Modelling of *in vitro* Transporter Processes to Improve Drug-Drug Interaction Predictions

by

Simon John Carter

Thesis

Submitted to the University of Warwick

for the degree of

Doctor of Philosophy

School of Engineering

July 2019

Contents

List of Tables

List of Figures

"A scientist must also be absolutely like a child. If he sees a thing, he must say that he sees it, whether it was what he thought he was going to see or not. See first, think later, then test"
D. N. Adams. So Long, and Thanks for All the Fish. 1984.

Acknowledgments

Declarations

This thesis is submitted to the University of Warwick in support of my application for the degree of Doctor of Philosophy. It has been composed by myself and has not been submitted in any previous application for any degree. The experimental in Chapter 4 was obtained whilst I was employed by UCB Pharma Ltd. (Slough, UK) and has been used with the kind permission of UCB Pharma Ltd.. The experimental work in Chapters 3 and 5 were obtained as part of my studentship at AstraZeneca Cambridge (U.K.) and Mölndal (Sweden) respectively. This thesis has not been submitted for a degree at any other university.

Parts of this thesis have been published or submitted for publication by the author:

Journal Articles:

S.J. Carter, M.J. Chappell and P. Sharma. Use of a Mechanistic Modelling Approach for the Determination of the Amount of OATP1B1 in HEK293-OATP1B1 Cells. *The Journal of Pharmaceutical Sciences (Short Communication) Draft*, 2019.

S.J. Carter, A.S. Ferecskó, L. King, K. Ménochet, T. Parton, and M.J. Chappell. A Mechanistic Model to Determine the Uptake and Metabolism of Atorvastatin and Inhibition by Cyclosporine in Rat Hepatocytes Using a High Throughput Method. *Xenobiotica*. Submitted June 2019.

S.J. Carter, B. Chouhan, P. Sharma and M.J. Chappell. Measurement of Pitavastatin and Eltrombopag in Human Hepatocytes to Improve the PBPK Prediction of Transporter-Mediated Drug-Drug Interactions. *CPT: Pharmacometrics & Systems Pharmacology Draft*. 2019.

Presentations and Posters:

PKUK Poster (2018): S.J. Carter, B. Chouhan, M.J. Chappell and P. Sharma: Measurement of substrate and inhibitor to improve inhibition modelling.

DMDG Open Meeting Student Presentation and Poster (2018): S.J. Carter, B. Chouhan, M.J. Chappell and P. Sharma: Use of micro-rate constants to improve transporter mediated drug-drug interaction (TrDDI) modelling.

Postgraduate Symposium - Presentation. School of Engineering (2017): Mechanistic modelling of in vitro transporter data to improve translational modelling of the transporter-mediated human pharmacokinetics and DDI predictions. Lessons learned so far.

PKUK Poster (2016): S.J. Carter, M.J. Chappell and P. Sharma: Updated - Use of Mechanistic Models to Determine Kinetic Parameters of a Fluorescent Probe in the Presence and Absence of a Prototypical Inhibitor in HEK293-OATP1B1 cells.

QSPUK Poster (2016): S.J. Carter, M.J. Chappell and P. Sharma: Use of mechanistic models to determine kinetic Parameters of a fluorescent probe in the presence and absence of a Prototypical Inhibitor in HEK293-OATP1B1 cells.

DMDG Open Meeting Student Presentation and Poster (2015): S.J. Carter, P. Sharma and M.J. Chappell: Modelling approaches to transporter kinetics.

Abstract

There is currently a need to evaluate the interaction of drugs in the liver and at the liver membrane, to determine whether the potential for a drug-drug interaction in the clinic could adversely affect a patients prognosis. The interactions of drugs or probe substrates with liver membrane transporters are currently poorly understood at a molecular level, and there is strong interest in terms of the pharmacology of the transporters and how we can examine and understand these interactions through mathematical models. Currently the dynamics of interactions through the use of micro-rate constants, where steady-state assumptions are not implied in data analysis are less favoured. Whilst modelling and data analysis conducted using Michaelis-Menten type kinetics (defined as macro-rate constant mechanistic models), under the assumption of rapid equilibration of substrate with the transporter (association with the transporter is almost instantaneous) are more common. The aim of this thesis is to improve the determination of transporter mediated drug-drug interactions (TrDDIs) in *in vitro* liver specific cellular systems through the use of structurally identifiable mechanistic models describing the dynamics of the interaction between substrates and inhibitors. This was done by the design of experiments to optimise the data collected for substrate and inhibitors for use within the mechanistic models across different cellular systems (human cell lines, rat and human hepatocytes) under different inhibition conditions. Mechanistic models were developed to obtain robust model fits that adequately described the interaction between substrates and inhibitors, whilst gaining an insight in terms of model selectivity, given the data available. The structural identifiability of the mechanistic models was assessed to ensure that the unknown parameters in the model could be estimated from the experimental data. The mode of inhibition was determined through the use of mechanistic models for each experimental chapter and compared with conclusions drawn in the in literature. The potential for a clinical TrDDI was evaluated for the experimental work in cryopreserved human hepatocytes (Chapter 5), through a worst case scenario static

drug interaction model at the entrance to the liver using an "*R value*", and through the use of a semi-quantitative physiologically based pharmacokinetic (PBPK) model. All the micro-rate constant mechanistic models were at least structurally locally identifiable with no parameters unknown. Conversely, the macro-rate constant mechanistic were only structurally locally identifiable if both substrate and inhibitor were measured (see Chapter 5). Otherwise one to two parameters had to be known for the macro-rate constant mechanistic models to be structurally locally identifiable. Concurrent with the structural identifiability analysis results, in each of the experimental chapters, the use of micro-rate constant mechanistic models were always the best fitting model to the experimental data based on goodness of fit statistics compared to the use of Michaelis-Menten macro-rate constant mechanistic models. Both the micro-rate constant and macro-rate constant mechanistic models were in agreement with regards to the mechanism of inhibition in all experimental cases, whilst the steady-state assumptions required for the use of the Michaelis-Menten equation were only valid for the micro-rate constants derived in Chapter 5. This supported the use of scaled micro-rate constant parameters in Chapter 5 to Michaelis-Menten parameters in the semi-quantitative mechanistic PBPK model in Chapter 6, where there was a potential for a clinical TrDDI given the *in vitro* data, which was at odds with the determined *R value*. In conclusion, this work strongly supports the use of micro-rate constants in mechanistic modelling of *in vitro* TrDDIs to formally test steady-state assumptions through more robust, structurally identifiable parameter estimates.

Abbreviations

AIC	Akaike information criterion
ATP	Adenosine triphosphate
AUC	Area under the curve
BCRP	Breast cancer resistance protein
BCS	Biopharmaceutics classification system
BDDCS	Biopharmaceutics drug disposition classification system
BIC	Bayesian information criterion
BSEP	Bile salt export protein
CsA	Cyclosporine A
CYP	Cytochrome P450
DCF	2',7'-dichlorofluorescein
DDI	Drug-drug interaction
DILI	Drug induced liver injury
DMEM	Dulbeccos modified essential medium
DMSO	Dimethyl sulphoxide
EMA	European medicines agency
FBS	Fetal bovine serum
FDA	Federal drugs agency
FIM	Fisher information matrix
FO	First order linearisation
FOCE	First order conditional expectation linearisation

GST	Glutathione-s-transferase
HBSS	Hanks buffered salt solution
HEK293	Human embryonic kidney cell line 293
HPLC	High performance liquid chromatography
HRMS	High resolution mass spectrometry
IWRES	Individual weighted residuals
KHB	Krebs-Henseleit buffer
LC	Liquid chromatography
MATE	Multidrug and toxin extrusion transporter
MCMC	Markov chain Monte-Carlo
MDR	Multidrug resistance transporter
MRP	Multidrug resistance associated proteins
MSMS	Tandem mass spectrometry
NSAID	Non-steroidal anti-inflammatory drug
NTCP	Na^+ taurocholate co-transporting polypeptide
OATP	Organic anion transporting polypeptide
OCT	Organic cation transporter
ODE	Ordinary differential equation
PBPK	Physiologically based pharmacokinetic model
PD	Pharmacodynamics
PK	Pharmacokinetics
RSE	Relative standard error
RMSRE	Relative mean square root error
SAEM	Stochastic approximation expectation maximisation
SD	Standard deviation of the mean
SE	Standard error of the mean

SGI	Structurally globally identifiable
SI	Structurally (locally) identifiable
SLC	Solute carrier
SULT	Sulphotransferase
UPLC	Ultra-performance liquid chromatography
TrDDI	Transporter mediated drug-drug interaction
YLD	Years living with a disability
wBIC	Weighted BIC

Chapter 1

Introduction

Life expectancy has steadily increased from the latter half of the 20th century for men and women by approximately eight and six years respectively [12]. As life expectancy has increased, so the number of patients who have sought treatment for multiple age-related diseases has also increased. A global collaborative effort evaluating the prevalence of infectious and non-infectious diseases and determination of a "years living with a disability" (YLD) value, found that diseases associated with increasing age; stroke and heart disease, hearing loss, diabetes, and chronic obstructive pulmonary disease, showed a greater than 10 % increase over the period of 2010-2016 compared to all other YLD values when normalised by age group [13]. The increase in YLD values for more age related diseases shows that there is a requirement to fill the current unmet need in terms of the treatment of an ageing population which will increase based on current trends and which also spans socio-economic barriers. Treatment of the increasingly ageing population is likely to be across multiple diseases. It is therefore rare that a patient will be taking just one drug, and is likely to receive multiple drugs to treat the multi-faceted symptoms of non-communicable diseases on a long term basis or life. Understanding how multiple drugs interact at a cellular level has the potential to improve a patient's quality of life and helps to decrease the attrition of drugs in the clinic. It is here that mathematical modelling can play a key holistic role in understanding the relationships between what can easily or routinely measured, e.g. drug in blood, and what is happening away from where it is measured e.g. in the liver or some pharmacological target, is vital in order to make sure that what is dosed to a patient has the highest chance of being efficacious (sufficient exposure at the site of action), whilst minimising the chance of adverse effects that can potentially be life threatening.

The study of drug disposition processes, namely; absorption from the dose site into the circulation, distribution of the drug into tissues, metabolism of the drug and excretion into urine or faeces of the parent and/or metabolites of an administered drug in the body is termed *pharmacokinetics* (PK). The study of the pharmacological action of a drug at the site of action or via a downstream biomarker that can be measured is termed *pharmacodynamics* (PD). These processes do not occur in isolation, and thus the analysis of PK-PD relationships is known as *pharmacometrics* [14]. PK and/or PD are studied by developing mathematically derived models of the underlying processes

involved in the data that are observed, along with error in the measurements themselves [14, 15].

Models are simplifications of processes in the body, and their development is based on both an understanding of the underlying physiology or mechanism from the literature and personal experience, and as such approximate what we think is happening. Obtaining meaningful parameters from the modelling process - the so-called "inverse problem" and often the most difficult [15], will depend on the experimental design, the ensuing errors and the complexity of the model considered. For example a simple one compartment PK model following an intravenous injection with two parameters (clearance from the compartment through metabolism and/or excretion, and the apparent volume of the compartment), up to vast biochemical models (e.g. the JAK-STAT model investigated by Anguelova et al. [16] with 31 compartments and 51 parameters). These are two extreme examples of mechanistic models, and whilst a highly complex mechanistic model can be written, unless there are sufficient data across time and states (measurements of the compartmental concentrations), accurate estimation of the parameters will not be possible. Therefore before the costly exercise of data generation from experiments is run, it is advisable to look at the structure of the model itself, and evaluate whether we can actually obtain the desired measurement output from the model, assuming limitless noise free data - known as structural identifiability [17] will be described in the next Chapter 2, and then applied across the experimental and modelling chapters (Chapters 3, 4 and 5).

There is currently an unmet need to evaluate the interaction of drugs in the liver and at the liver membrane as this is the first point of call for all orally absorbed drugs and food. As such the liver "sees" much higher concentrations than the rest of the body. Such is the importance of the liver, that prior to submission of a new drug to the regulatory agencies, assessments have to be made both in terms of enzyme interactions, but also at the liver plasma membrane transporters at the sinusoid and bile canaliculus [18, 19]. The interactions of drugs with liver membrane transporters are currently poorly understood at a molecular level [20]. There is strong interest in terms of the pharmacology of the transporters and how we can examine and understand these interactions through mathematical models [20–22], and it is this that this thesis will study in an attempt to further the knowledge base and understanding in this field.

1.1 Aims and Objectives

The aim of this thesis is to improve the determination of transporter mediated drug-drug interactions (TrDDIs) in *in vitro* liver specific cellular systems through the use of structurally identifiable mechanistic models describing the dynamics of the interaction between substrates and inhibitors.

Currently the mechanistic modelling and data analysis of transporter mediated uptake are conducted using Michaelis-Menten kinetics, which have been expanded upon for transporters from the original development for enzyme kinetics. The use of the

Michaelis-Menten equation (see Chapter 2, Eq.) is valid under the following assumptions [15, 23, 24]:

1. The initial substrate concentration is much larger than the transporter concentration.

2. It then follows that the association to the transporter (k_a, is very rapid) is thus in rapid equilibrium with the transporter.

3. The free transporter (T_f) is therefore affected by the dissociation rate constant from the transporter (k_d).

4. The rate limiting step in the transport of substrate into the cell is the translocation rate constant (k_t).

Models that use the Michaelis-Menten derivation are referred to in this thesis as *macro-rate constant models*. If for these models, the steady-state rate transport constants (V_{max} and K_m) are split back into their constituent micro-rate constants (defined as *micro-rate constant models* in this thesis), then these assumptions can be formally tested.

Therefore this thesis will try to answer the main aim and that above relating to steady-state assumptions via a series of objectives for a selection of substrates where transporter mediated movement into the cell dominates over passive movement into the cell:

1. Develop mechanistic models that characterise the data, and are possible given the available observations from *in vitro* cellular drug uptake experiments, extending the work of Grandjean [25] to include inhibition of transport.

2. Evaluate the effectiveness of both macro-rate constant models and micro-rate constant models with the inclusion of substrate and inhibitor and determine their structural identifiability for a given model and observations available.

3. Design experiments to optimise the data collected for substrate and inhibitors for use within the mechanistic models across different cellular systems (human cell lines, rat and human hepatocytes) under different inhibition conditions.

4. Using the micro-rate constant and macro-rate constant mechanistic models, obtain robust model fits that adequately describe interaction between substrates and inhibitors, whilst gaining an insight in terms of model selectivity.

5. Compare if from obtained *in vitro* TrDDI whether: The use of a static clinical interaction model based on the ratio of the AUCs calculated in absence and presence of inhibitor at the entrance to the liver (R *value*). Or through the use a more dynamic PBPK modelling approach, which takes into account the liver physiology offers a more realistic description of the potential for transporter mediated drug-drug interactions (TrDDIs) in the clinic.

1.2 Thesis Outline

This thesis follows a logical path through the literature, and mechanistic modelling techniques employed and their relevance to cellular drug uptake experiments. This is followed by three experimental chapters that look at the uptake of substrate and its subsequent inhibition through different scenarios, before the development of a semi-mechanistic PBPK model based on the final experimental chapter. The chapters are summarised below:

Chapter 2: Provides an in depth review of transporter physiology and mechanisms of action obtained from the literature. The transporters will be split into two distinct sections; Non-energy (ATP) dependent transporters and ATP dependent transporters, with the former of more experimental relevance here. An introduction to structural identifiability analysis and practical identifiability through parameter estimation software is also provided.

Chapter 3: The uptake of a fluorescent substrate (2,7-dichlorofluorescein, DCF) into human embryonic kidney cells (HEK293) that overexpress human OATP1B1 (hOATP1B1) is considered as an alternative to the more costly radiolabelled substrates or the analysis of substrates using mass spectrometry. The mode of inhibition of gemfibrozil, which has been shown to have a mixture of enzymatic and transporter mediated DDIs, on liver specific hOATP1B1 was determined experimentally and through the use of mechanistic modelling.

Chapter 4: Provides a more complex cellular structure of isolated rat hepatocytes, which possess a full compliment of transporters and enzymes. A high throughput centrifugal oil layer method is described (that was partially developed during my MSc. dissertation) and applied to the uptake of an HMG-CoA reductase inhibitor (atorvastatin) and its inhibition by the immunosuppressant cyclosporine (CsA), which has been shown to be a potent inhibitor of transporters in the clinic using mechanistic modelling.

Chapter 5: Builds on the outcomes of Chapters 3 and 4 and provides a simultaneous analysis of both substrate (pitavastatin, another HMG-CoA reductase inhibitor) and an inhibitor (eltrombopag) in the same sample of cryopreserved human hepatocytes. A mechanistic modelling approach is again undertaken to understand the mode of inhibition of eltrombopag. Eltrombopag is used to stimulate platelet formation, and the dose is carefully monitored to prevent over/under production of platelets and thus consideration of pitavastatin and eltrombopag is important in TrDDI consideration

Chapter 6: Provides the development of a qualitative semi-mechanistic PBPK model using the data obtained from Chapter 5 to simulate clinical PK profiles in the absence and presence of inhibitor through Monte-Carlo simulations in R. This model includes passive movement of drug into and out of the cell, as well as transporter mediated interactions obtained from Chapter 5 and other selected information from the literature regarding the elimination of both pitavastatin and eltrombopag.

Chapter 7: Provides summaries and conclusions from the experimental and modelling chapters and suggestions for further work.

Chapter 2

Background and Data Analysis

The liver is the major organ responsible for elimination of most drugs from the systemic circulation, but first of all they need to cross the cell membrane (both in the gut and the liver), either via passive diffusion or via an uptake transporter protein. Drug transporters in the liver are key components in the elimination of many drugs; both for uptake into the hepatocytes (where they can be metabolised) from the blood, as well as excretion back into the blood to be circulated to the rest of the body or into the bile [26]. For more lipophilic drugs such as gemfibrozil or cyclosporine A, passive diffusion dominates over transporter mediated uptake [9, 27]. For amphiphillic drugs that are weak acids (e.g. pitavastatin or atorvastatin), which are less lipophilic and also have a small charge at physiological pH, uptake of drugs into the liver via a saturable carrier protein dominates and is the rate limiting step in clearance from the blood [28].

There is a large body of literature dedicated to clinical DDIs at an enzymatic level, with much less work dedicated to a transporter level or combined transporter / metabolism level. Indeed, a PubMed search of "Drug-Drug Interaction" with "metabolism" or "transporter" or both and then filter the search to "Clinical Trials" and "Journal Articles", 66 % of the references were "metabolism", whilst "transporter" or both were 14 % and 13 %, respectively (Table 2.1). It is interesting to note that in 2018, the number of "transporter" DDI publications has remained steady since 2013, and coincides with when the EMA [18] and the previous FDA (2012) guidance documents first included transporter mediated drug drug interactions (TrDDIs). Articles for "metabolism" only have decreased by 16 %, whilst studies where both "metabolism" and "transporters" were included have remained unchanged (see Table 2.1). It is encouraging to see that journal issues are also now dedicated to progressing the knowledge of transporters and their importance in pharmacokinetic and pharmacodynamic interactions (e.g. *Clinical Pharmacology and Therapeutics*, 2018, volume 105, issue 5).
The rest of this chapter is sectioned into three parts: The first section will cover the current knowledge and biology of drug transporters, how we can study them and their importance with regard to the potential for TrDDIs. A small section on drug metabolism will also be included as a major route of elimination of most drugs, but also because of the effect that some of the metabolites have on transporters both as substrates themselves and inhibitors. The second section is concerned with the development and use of

Table 2.1: Number of journal articles in PubMed regarding DDIs between 1969-2018

Search terms	Total References (% of total)	2018* (% of total)
"Drug-Drug Interaction"	3173	382
"Drug-Drug Interaction" AND metabolism	2104 (66 %)	164 (42 %)
"Drug-Drug Interaction" AND transporter	458 (14 %)	52 (14 %)
All Three	414 (13 %)	32 (8 %)

up to date of search: 01/11/2018

mechanistic models, their power in furthering our knowledge of cellular kinetics, but also the limitations in terms of the information we can obtain. An important pre-requisite for the use of mechanistic models is an identifiability analysis with respect to the structure of the mathematical model to be used, and whether we can obtain meaningful parameter estimates from the model in its postulated form, or whether it needs to be modified, or simplified. Such analysis of mechanistic models can also be used to guide experimental design as to what information would improve the chance of estimating the unknown parameters. The final section underlines efforts made to link *in vitro* data and *in vivo*/clinical data either by extrapolating from a cellular level up to a whole body level through the use of physiologically based models, or by correlating physicochemical properties to clinical data.

2.1 Transporters

Transporters are promiscuous in nature across prokaryotes and eukaryotes both for the uptake of nutrients and exclusion of toxins [29]. Functioning transporter genes in humans (excluding regulatory subunits) account for nearly 5 % of the total number of genes in the human body [30]. The promiscuous nature of transporters has spawned two opposing views on how molecules cross membranes passively: the more mainstream belief of passive diffusion across phospholipid bilayers; and the belief that passive movement across membranes is via a host of low capacity uptake transporters, most of which are currently unidentified [31]. The view of how molecules passively cross membranes, whether it be through diffusion or a host of not yet discovered transporters, is of little relevance, it is more the manner for which it occurs, i.e. "passive" movement of molecules is a very rapid process relative to transporter kinetics and is practically unsaturable in laboratory experiments (linear uptake across concentrations).

Hallifax and Houston [32] found that the time to reach a plateau for a lipophilic amine, imipramine, was 30 s in rat hepatocytes and most of the uptake was seen at the first timepoint of 10 s. The cell concentration:medium concentration ratio (commonly known as K_p) obtained in either inactivated cells (no viable transporter) or at high concentrations of imipramine were similar ($K_p = 120$ and 150 respectively), indicative

of passive permeability and high intracellular binding of these drugs [32].

In comparison the time to reach a maximum for a transporter substrate, rosuvastatin in plated rat hepatocytes was around 15 min [33], and although a K_p value was not stated, it can be estimated from figure 4 in the article, assuming that the concentration in the medium is the same as the dose at the 15 min timepoint. The K_p decreased around 13-fold from an estimated K_p of 90 at 0.1 μM to 7 at 300 μM ([33], 15 min timepoint). Whilst a very rough calculation, it helps to illustrate the point that the uptake process drives the cellular concentration for acidic drugs where passive permeability is less, as seen in the n-fold decrease in K_p for rosuvastatin, in comparison to fold decrease for imipramine where passive diffusion outweighed the transporter element [32, 33].

The rest of this section will be split into two distinct parts; those transporters that do not require cellular energy (ATP) directly - the Solute Carrier (SLC) family of transporters, also known as *secondary active transporters* [29]; and those that are ATP dependent and are part of the ATP Binding Cassette family of transporters (ABC). To simplify the notation for transporters across species below, genes will be described in *italics*, whilst proteins are not. Human genes, proteins or enzymes will given in capital letters, or when general features are discussed, whilst for animal specific genes, proteins or enzymes only the first letter is capitalised [34]. The species will be marked accordingly or left blank when discussing general features: human (h), rat or rodent (r, depending on the context), mouse (mu), dog (d) and monkey (mo).

2.1.1 Non-ATP Dependent Transporters

The solute carriers span a broad range of transporters with around 52 different families and around 400 genes in humans and are mainly membrane bound [29]. They cover transport across a broad range of substrates: amino acids, organic anions and bile acids, organic cations, metals, neurotransmitters, sugars and DNA base sugars [30]. SLCs are ubiquitous in their distribution in the human body from muscle and intestine to the brain [35] and are therefore important in disease and as attractive drug targets [30, 36, 37]. With so many SLCs across such a broad range of substrates and distribution, it can be easily seen why some authors state that passive movement of molecules may be as a result of numerous low capacity transporters [22]. This section will concentrate on four families in more depth (genes in brackets): the OATP superfamily (*SLCO*), NTCP (*SLC10A1*), OCT (*SLC22*) and MATE (*SLC47*) as they are the main SLCs of interest in the liver, the first two deal with the sodium independent and dependent transport of large bulky (> 350 Da) amphipathic (mainly) anions which have a small negative charge at physiological pH (7.4), whilst the second two deal with smaller molecular weight (<500 Da) (mainly) cations which have a small positive charge at physiological pH [38, 39].

2.1.1.1 OATP (*SLCO*)

A major transporter protein family involved in the uptake of weakly acidic molecules with a molecular weight of > 350 Da (both endogenous substrates and drugs) [38]

across membranes, the organic anion transporting polypeptides (OATP) are ubiquitous in their tissue distribution in the human body. They are the most abundant of all transporters in the liver [40], and have a large range of endogenous substrates from bile acids to prostaglandins [35]. They function using intracellular HCO_3^- or glutathione as a counter ion [38] with substrate transported through a positively charged central pore via a rocker-switch mechanism [3], with two distinct inward and outward facing sides [41] (see Fig. 2.1). This mechanism is distinct for counter transporting proteins in that the faces "switch" over, whilst for the other transporters in this chapter, whether they are non-ATP dependent or ATP dependent seem to act through a "hinge switch" mechanism, where the substrate binds in an open state and then moves through the pore as the protein closes and then opens on the other side of the pore, releasing the substrate (see Fig. 2.2) [4, 5].
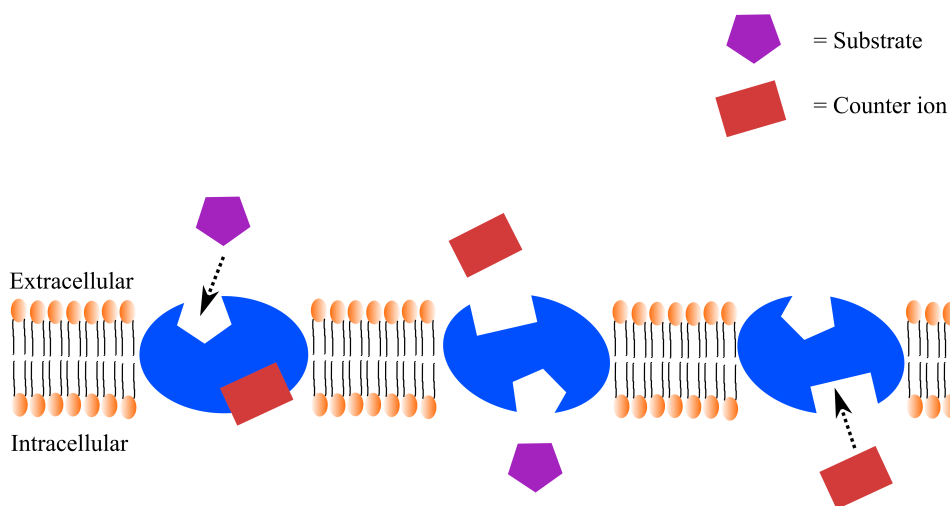
Figure 2.1: Schematic of transporter function via a rocker-switch mechanism. A counter ion is already bound in first step before the substrate binds. The transporter then switches outward and inward facing sides and releases the substrate and counter ion. The transporter then returns to its original state. This is a simplification of the process presented by Huang et al. [3] of the Glycerol-triphosphate mechanism in *E. coli*.

There are currently six different sub-families of the OATP family [42], and they have been extensively reviewed in the past literature in detail [30, 35, 38, 43, 44], therefore they will be briefly summarised below and updated where new information has arisen. The main families involved in uptake of xenobiotics into the liver, as well as those that have been deemed important for study by regulatory bodies (hOATP1B1 and 1B3) and the International Transporter Consortium (hOATP1A2, hOATP1B1, hOATP1B3 and hOATP2B1) [45] are discussed below.

OATP1A (*SLCO1A2*)
OATP1A exists as a single form in humans (hOATP1A2), whilst in rodents there are multiple subtypes (rOatp1a1, 1a3-6), which potentially can make exact correlations difficult between species. As a family, OATP1A protein is found in; cholangiocytes in

humans (liver cells which line the bile duct), hepatocytes in rats [40], with high abundance in brain capillaries, proximal tubules in the kidneys [38] and duodenum [46] in humans, and is upregulated in certain cancers [37]. The presence of hOATP1A2 in human intestine was refuted by Drozdzik et al. [47] who found no mRNA or protein in the small intestine or colon in six organ donors, which was backed up by a proteomics study in pooled human liver microsomes from 13 donors [48]. However the limit of quantification (LOQ) was around 1-2 fmol/μg protein for all transporters, whilst most proteins were measured at a tenth of the LOQ [47]. Glaeser et al. [46] used mRNA detection, as well as immunohistochemistry and immunofluorescence from biopsies in 10 healthy volunteers to show hOATP1A2 and hMDR1 both present in enterocytes. Whilst immunofluorescence and immunohistochemistry clearly showed the presence of hOATP1A2 in enterocytes, the amount of hOATP1A2 protein was not measured [46]. This suggests that whilst hOATP1A2 is present in the duodenum at least, it was below the LOQ for the hOATP1A2 peptides used in LC-MS Glaeser et al. [46], Drozdzik et al. [47]. In rats, 26-32 % of the total hepatic rOatp was rOatp1a1 and 1a4 making them important transporters, whilst in human liver samples hOATP1A2 was not observed [40]. Endogenous substrates in humans and rats include a preference for unconjugated bile acids (e.g. cholic acid) over conjugated bile acids (e.g. taurocholic acid and glycholic acid), as well as hormones (e.g. dehydroepiandosterone, estradiol-17β-glucuronide) [35].

OATP1B (*SLCO1B1, SLCO1B3*)

There are two subtypes of OATP1B in humans (hOATP1B1 and 1B3), whilst in rodents there is only rOatp1b2 [35]. They are a liver specific family with hOATP1B1, hOATP1B3 and hOCT1 having the highest abundance of all SLCs associated with the uptake of drugs in human hepatocytes [40, 49]. hOATP1B1 and hOATP1B3 contribute 12 % and 7 % respectively to the total OATP in human hepatocytes, whilst rOatp1b2 is similar to the total OATP1B in humans of 16-17 % [40]. hOATP1B3 has been observed in oncogenic tissues outside of the liver (breast, lung and prostate) [37, 38] and down-regulation of hOATP1B3 in prostate cancer cells is associated with docetaxel resistance [37]. Endogenous substrates which overlap with OATP1A vary across rat and human, with rOatp1b2 transporting less bile acids compared with human hOATP1B1 and 1B3, and rOatp1a transporting the other bile acids [35]. A slight preference for unconjugated bile acids over conjugated bile acids was seen in in hOATP1B1 and 1B3 cell lines [50].

The reason that hOATP1B1 and 1B3 are of interest enough to the drug regulatory bodies to warrant inhibition or substrate studies (if > 25 % of the uptake is due to hOATP1B1 and hOATP1B3) [51] is due to certain hOATP1B1 polymorphisms leading to reduced activity, putting a greater burden on hOATP1B3 to transport substrates in the liver. An example of an hOATP1B1 polymorphism is hOATP1B1*15*15, which is the result of a single nucleotide substitution of T521>C, and leads to a 104 % increase in the area under the curve (AUC) of repaglinide in the homozygous 521CC compared to the wild type 521TT carrier and a tendency for lower blood glucose concentrations [52]. It has also been reported that patients with the hOATP1B1*15*15 phenotype have

a much greater chance of pravastatin-induced myopathy, due to increased concentration in the plasma [53]. Bosgra et al. [54] found that the activity of HEK293-hOATP1*15 was similar to mock transfected cells for rosuvastatin, and that in a PBPK model for humans this decreased the total uptake clearance into the liver by 23% [54].

The hOATP1B1*14*14 polymorphism is present in 0.74-0.77 of African-Americans, and 0.3-0.51 of Caucasians [55] who all have increased hOATP1B1 protein expression in hepatocytes and therefore an increase in the maximum uptake velocity (V_{max}), leading to a decrease in the predicted plasma exposure of statins, due to an increased liver uptake [56]. hOATP1B1 and 1B3 are significantly reduced by 3-fold and 8-fold respectively in caucasian fatty liver [57], making cholesterol lowering drug choice in patients with fatty liver more important. As well as polymorphisms in hOATP1B1 or hOATP1B3 individually, in patients where both hOATP1B1 and hOATP1B3 are absent, due to deletions in the *SLCO1B1* and *SLCO1B3* genes manifest as Rotor syndrome in around 1 *per* million people [58]. Patients with Rotor syndrome have higher bilirubin glucuronide plasma levels (conjugated hyperbilirubinaemia) and increased urinary excretion of bilirubin glucuronides as well mild jaundice. Interestingly in *Slco1a/1b*$^{-/-}$ mice, oral administration of methotrexate gave similar plasma concentrations to wild-type mice, but following intravenous administration, methotrexate plasma concentrations were higher in knockouts and this could be partially attributed to the liver:plasma ratio of 43 in wild type versus 4 in knockouts due to the decreased uptake through muOATP1a/1b [58].

OATP2B1 (*SLCO2B1*)

OATP2B1 is seen across species, and is separate to OATP2A1 which is ubiquitous in its distribution [35]. OATP2B1 is found in human intestine, liver, brain capillaries, eye and placenta, and transports taurocholic acid in both rats and humans, but only steroid precursors in humans [35, 59]. In human liver, the expression of hOATP2B1 was found to be approximately equal to hOATP1B3, however in sandwich-cultured human hepatocytes, the expression of hOATP2B1 was found to be upregulated 7-fold [60]. It is upregulated in fatty livers, but not enough to counter the reduction in hOATP1B1 and 1B3 [57]. Polymorphisms in hOATP2B1 are associated with rates of minimal residual disease after treatment [61], as well as survival in prostate cancer [62] and are therefore important in considerations during treatment of prostate cancer.

2.1.1.2 NTCP (*SLC10A1*)

Na$^+$ Taurocholate Co-transporting Polypeptide (NTCP) is an important transporter that mediates the sodium dependent uptake of anions, and was first noted by Schwarz et al. [63] due to its saturable uptake of taurocholic acid in rats. It is separate from OATP in that it co-transports two sodium ions with the substrate into the hepatocyte [64]. It is liver specific to the basolateral membrane of hepatocytes, and within the liver of Caucasians it constitutes 6 % of the total abundance of transporters [57]. It plays an important role in the enterohepatic recycling of conjugated and unconjugated bile acids in humans helping to maintain bile acid homeostasis [65]. Liu et al. [66]
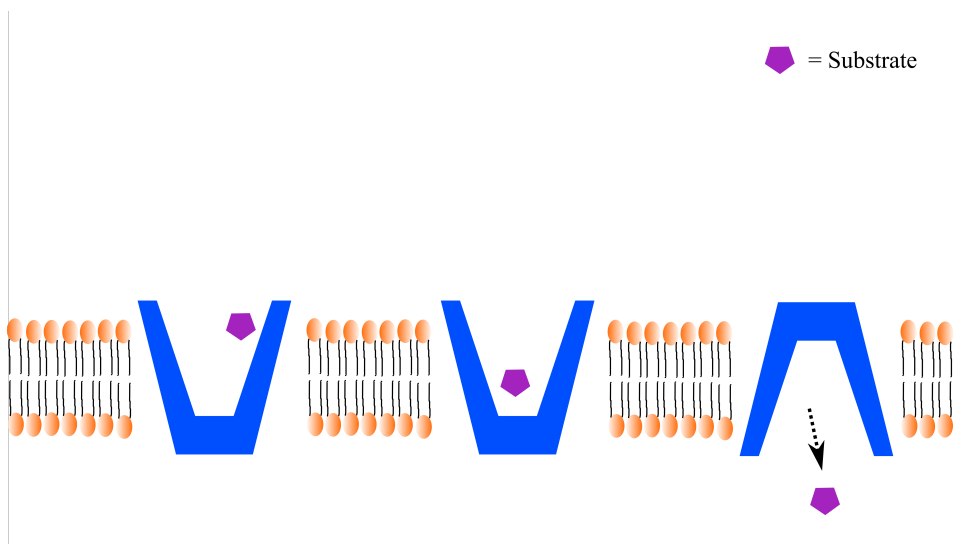
Figure 2.2: Schematic of transporter function for co-transport. Substrate binds in the first step, then moves towards the other side of the membrane. The transporter then switches the "open" side releasing substrate, adapted from [4, 5].

reported an increase in both conjugated and unconjugated bile acids in individuals who are homozygous for the S267F mutation in Chinese individuals, as well as decreased vitamin D levels. NTCP has been reported to correlate with the entry of hepatitis virus into the liver, and is important in the innate immune response to the virus [67].

2.1.1.3 OCT (*SLC22*)

There are three members of the organic cation transporter (OCT) family in humans with a broad ranging distribution throughout the body and they have been covered in more depth by [38, 68]. hOCT1 is highly expressed in liver [68] and has 12 % of the total abundance of transporters in human Caucasian males [57]. OCT2 is highly expressed in human kidney only, but is highly expressed in rodent liver and kidney [68]. OCT3 is highly expressed in the basolateral membrane of liver in human and rodents, and is important in the homeostasis of the central nervous system [69]. They are polymorphic, with 20 different alleles for hOCT1 and the allelic frequencies are ethnicity dependent [70].

The OCT family has a large overlap in endogenous substrates, and is responsible for the transport of catecholamines, monoamines and neurotransmitters down their respective electrochemical gradient into the cell, but can also move substrates out of the cell depending on the direction of gradient [38]. The mechanism by which uptake occurs changes depending on the concentration in the blood, either as a uniporter, or as a more efficient exchanger with an intracellular organic cation [68]. The change between uptake mechanisms from a high affinity to a low affinity state, means that the Michaelis-Menten constant (K_m) or point at which 50 % of transporter sites are occupied, is in the millimolar range (compared to low micromolar for OATP and NTCP), which combined with a higher passive permeability makes identification of substrates more difficult [68]. Due to

the large expression of OCT2 in the kidney, observed polymorphisms and clinical DDIs with the glucose lowering drug metformin, it is listed as a likely target for DDIs [18, 19]. The international transporter consortium recommended conducting studies with both hOCT1 and hOCT2 in human cell lines because of observed clinical DDIs [45].

2.1.1.4 MATE (*SLC47A*)

The Multidrug And Toxin Extrusion (MATE) transporter has three members in humans: MATE1, MATE2 and MATE2K, whilst in rodents there are no analogues that correspond to hMATE2 and 2K, with rMate2 more similar to hMATE1 [71]. hMATE1 is expressed throughout the body with high expression in adrenal gland, kidney, canalicular membrane in the liver and skeletal muscle, while hMATE2 and hMATE2K only express in the kidney, but transcripts have been observed for hMATE2K in various tissues [71]. Within the liver, hMATE accounts for 1 % of the total protein abundance [57], and in the renal cortex hMATE1 expression was ten-fold higher than in the liver [72]. hMATE1 expression was similar to hOCT2 expression in the renal cortex (18 % and 26 % of the relative expression respectively) [72]. There are numerous single nucleotide polymorphsims (SNPs) in MATE1 and MATE2 amongst different ethnic populations, all leading to decreased activity [5, 73, 74]. The SNPs in MATE transporters do not significantly alter the plasma pharmacokinetics of the generally used probe substrate metformin or endogneous substrate thiamine, but decrease the renal clearance [5, 73, 74], and depending on which MATE is affected, may increase or decrease the blood glucose lowering effect of metformin in healthy volunteers or patients with type 2 diabetes [73].

MATE functions as an electroneutral transporter, with an organic cation counter transported with either H^+ or Na^+ depending on the proton gradient, as well as the sodium gradient respectively [5, 71]. As such it can transport in either direction, but this is normally out of the cell. When hMATE1 was co-transfected with hOCT2 in HeLa cells, it decreased the uptake of metformin to 24 % of OCT2 only, in the kidney at least, and with a similar K_m for metformin [5]. This shows that MATE and OCT act in unison to increase the elimination of organic cations either into the bile, urine or in the case of the placenta, from the foetal circulation to the maternal [75].

2.1.2 ATP Dependent Transporters

The ATP Binding Cassette (ABC) family of transporters is able to move molecules out of cells against a concentration gradient, which is an essential way of excreting molecules that may be seen as toxic to cells. This is at the cost of a cellular energy source in the form adenosine triphosphate (ATP) and the enzyme ATPase to cleave a phosphate group, to generate the energy to drive these transporters [7] (see Fig. 2.3 for schematic). However, it is thought that for MRP1 at least, only one of the ATPases is active, whilst the fate of the other ATP is not clear [76]. Like the SLC transporters they are seen across prokaryotes and eukaryotes alike, indeed the first example of a multi-drug resistance (MDR) transporter was published in 1974 in bacteria that showed resistance to tetracycline [77]. The isolation of the MDR1 gene in tumours followed in

1987 [78], and since then numerous examples have been observed in tissues and organs in the human body as well as oncogenic and infected tissues. There are currently 51 different members of the ABC family from A-G [79]. Four members will be discussed here due to their importance in drug disposition and DDIs: MDR1 (*ABCB1*), MRP1-4 (*ABCC1-4*), BCRP (*ABCG2*) and BSEP (*ABCB11*).
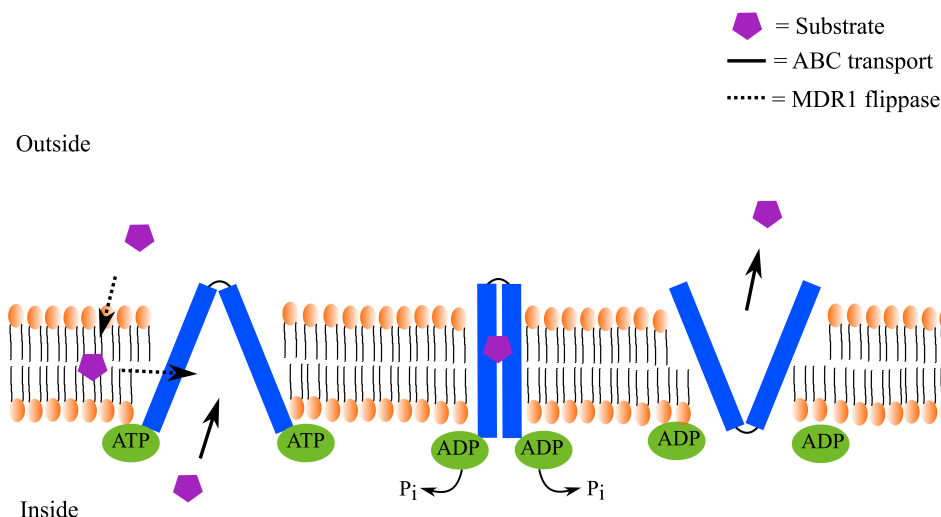
Figure 2.3: Schematic of transporter function for ATP dependent transport. Substrate binds to the transporter active site in the first step from inside the cell (solid lines) or from the lipid bilayer. Binding activates ATPase which cleaves off inorganic phosphate (P_i) and instigates movement of substrate towards the other side of the membrane as the transporter switches the open side, releasing substrate. Modified from Sharom [6] and Chang [7].

2.1.2.1   MDR1 (*ABCB1*)

Multidrug resistance transporter 1 (MDR1), or P-glycoprotein (P-gp) as it is also known, is the second most abundant ATP transporter in the small intestine and third most abundant in the colon [47]. hMDR1 accounts for 2 % of the total transporter abundance in the liver of caucasians [57], where it is present at the canicular side of the hepatocyte membrane. It is also found in the endothelial cells of the brain, in the brush border membrane in the kidney, as well as maternal-foetal barriers and blood-testis barrier [80]. MDR1 is essential for the removal of toxins away from these organs of importance as well as protecting the foetus from maternal toxins, so much so, that in dogs deficient in dMdr1, foetal toxicity and neural toxicity were observed after dosing with ivermectin (an MDR1 substrate) [80].

The three main polymorphisms that are studied in the literature; 1236C>T, 2677G>T/A and 3435C>T [81, 82], were reviewed across diseases in depth by Wolking et al. [81]. What is apparent is the discrepancy between the amounts of hMDR1 protein produced in patients with the polymorphisms, partially due to the low patient numbers in many studies [81]. hMDR1 upregulation is associated with resistance to drugs used in: oncology, epilepsy, and bacterial and viral infections amongst others [80, 81]. hMDR1

is upregulated in oncogenic tissues, with a lower relapse rate of high risk children with acute lymphoblastic leukemia who possess the 3435CT or TT polymorphism compared to 3435CC (61 % and 40 % respectively, $p = 0.02$), and an increase in bone marrow toxicity during therapy with doxorubicin for 3435TT patients compared to 3435CC patients ($p < 0.0001$) [82]. β-amyloid is an endogenous substrate of MDR1 in the brain [81], and the three polymorphisms above were found to be associated with Alzheimers disease susceptibility in a meta-analysis of the literature by Zhong et al. [83], with 2677G>T/A offering some protection, whilst the others increased susceptibility to Alzheimers disease.

MDR1 has been reported to act as a "flippase" or "hydrophobic vacuum cleaner" for drugs within the plasma membrane, expelling substrates before they enter the cell [76, 84], but it is also able to move substrates from inside to outside the cell, as the substrate binding site opens into the cytoplasm as well as the plasma membrane (Fig. 2.3, [6, 7, 76]). hMDR1 is able to bind multiple separate drugs with at least four binding sites [85], some of which can modulate the transport of other drugs at low concentrations by binding to MDR1 and activating ATP hydrolysis, but are not substrates themselves, whilst at higher concentrations, the same drug may inhibit MDR1 [86]. MDR1 transports a large variety of endogenous substrates from small molecular weight lipophilic substances, e.g. ethinyl estradiol (MW 296 Da, [87]), to large molecular weight peptides, e.g. β-amyloid (MW 4514 Da, [81]). The extensive number of substrates and distribution in important organs for restriction of drug entry, along with its role in multi-drug resistance, is why hMDR1 investigations are included in all drug submissions to regulatory authorities [18, 19].

2.1.2.2 MRP1-4 (*ABCC1-4*)

Multidrug resistance associated proteins (MRPs) were, like MDR1 above, found due to their role in multidrug resistance in tumours, with hMRP1 the first to be discovered in lung tumours and hMRP2-4 following later [88]. There are currently 12 members of the *ABCC* family in humans [89] including hMRP1-4 which will be covered here in more detail as they are important in efflux of xenobiotics.

MRP1 (*ABCC1*)

hMRP1 is ubiquitous in its distribution, in the plasma membrane of blood-tissue barriers of importance such as the brain, liver, heart, kidney and intestine as well as within mitochondria, and is extensively covered in the literature [88, 90]. In a meta-analysis of the literature, the expression of hMRP1 protein in liver was similar to hMRP2 (~ 0.4 pmoles/10^6 cells) [57]. In the intestine, hMRP1 protein was undetectable, but mRNA was present, suggesting its presence at low levels [47]. Whilst the distribution is ubiquitous, high expression is limited to certain specialist cells in tissues with a high turnover rate or protective role, e.g. crypt cells in the intestine, bronchial and bronchiolar epithelial cells and foetal blood vessels [90]. It is highly polymorphic with at 17 SNPs that are seen across ethnicities, with four frequent polymorphisms (4002G>A, 2168G>A, 825T>C and 2012G>T) that were seen to increase adverts events in oncology treatment

[91]. The presence of high intracellular reactive oxygen species (ROS) increases MRP1 expression, and is another reason it is likely upregulated in cancer cells, whilst high intracellular glutathione (a ROS scavenger) downregulates MRP1 expression [90]. MRP1 uses intracellular glutathione to stimulate transport of some endogenous substrates, whilst others are not stimulated by GSH, e.g. bilirubin and estradiol-17β-glucuronide respectively [90, 92]. MRP1 is also important in the immune response as the physiological efflux pump for leukotriene C_4 in mast cells [90]. MRP1 differs from other ABC transporters in that only the second ATPase is functional (the right hand side of schematic in Fig. 2.3), whilst the first ABC region is required for function of the transporter [90].

In cancer cell lines hMRP1 is found in the plasma membrane of origin tissues where it would not normally be present, partly due to inhibition of tumour suppressor genes [90]. In resistant cell lines, it is also found in intracellular vesicles and mitochondria preventing oncology drugs such as doxorubicin from reaching their target in the nucleus [93]. Intracellular vesicles of MRP1 follow a physiological function, whereby MRP1 translocates to the plasma membrane when unconjugated bilirubin is present, acting as a cellular reservoir for excretion as required [90]. hMRP1 has a clinically recognised role in various diseases due to its presence in sanctuary organs and tissues, where the overlap with other transporters is small, e.g. cancer, cystic fibrosis, chronic obstructive pulmonary disease and depression [88, 94].

MRP2 (*ABCC2*)

hMRP2 is exclusively localised to the apical membrane [95], and is the apical equivalent of hMRP1 [96]. It is highly expressed in the small intestine (10 % of total membrane protein), colon (25 % of total membrane protein) [47], and liver (31 % of relative protein abundance in Caucasians [57]), but less so in the kidneys (5 % of relative transporter protein expression, [72]), and not seen in the blood-brain barrier under normal circumstances [95]. The importance of MRP2 in the liver can be seen in humans with Dubin-Johnson syndrome and Esai Hyperbilirubinaemic rats which are both deficient in MRP2. Both show increased plasma bilirubin glucuronide levels (both monoglucuronide and diglucuronide), jaundice (stress induced only in humans) and enlarged dark pigmented livers, as well a large increase in MRP3 to try and compensate for the lack of MRP2 [95, 97]. From the studies in Dubin-Johnson syndrome patients and Esai Hyperbilirubinaemic rats, it can be seen that MRP2 is the major transporter responsible for conjugated bilirubins in the liver. Wen et al. [98] expressed seven common hMRP2 SNPs in HEK293 cells and evaluated the accumulation of 2 different substrates in cell-lines or inside-out vesicles. The SNP S789F had a 1.5-fold increase in calcein AM accumulation which was due to a 50 % decrease in protein expression, and this SNP was also noted as "probably damaging" with reference to Dubin-Johnson syndrome and was close to the SNP R768W seen in Dubin-Johnson syndrome patients [95]. V417I showed reduced activity of 30-50 % even after normalising for protein and was observed to show a decrease in hMRP2 mRNA in the placenta in early gestation [98], but was labelled

as benign in its effects in Dubin-Johnson syndrome [95]. Estradiol-17-β-glucuronide, a substrate for multiple transporters including MRP2 was implicated in cholestasis during pregnancy, likely due to prolonged internalisation of rMrp2 and bile salt export protein (rBsep), in female rat hepatocytes at least [99], underlying the importance of MRP2 in the physiological processing of bile salts under normal conditions.

MRP3 (*ABCC3*)

hMRP3 is the most abundant transport protein in the colon (36 % of total transporter protein), has a similar abundance to hMDR1 in the small intestine (10 % [47]) and 12 % of the relative protein abundance in the liver [57]. It is also the most abundant transporter in the skin, contributing 20 % of total mRNA in the skin [100]. MRP3 is a high capacity transporter, with a key role in the excretion of bilirubin glucuronides out of the hepatocytes in the periportal region of the liver into the blood stream. This allows the uptake of bilirubin glucuronides further towards the central veins by hOATP1B1 and 1B3 to prevent saturation of ABC mediated transporter excretion into the bile under normal physiological conditions [58, 101]. The function of MRP3 in bilirubin glucuronide cycling and its upregulation in cholestasis and disease helps to explain the increase in conjugated bilirubin in the plasma and urine of Dubin-Johnson syndrome patients and Esai Hyperbilirubinaemic rats, whilst in Rotor syndrome patients or Oatp1a/b knockout mice, total bilirubins (both conjugated and uncojugated) are excreted almost entirely by the kidneys [101]. MRP3 seems to also act as a reserve transporter that is upregulated during cholestasis [97]. Like other ABC transporters, hMRP3 is correlated with drug resistance and survival in cancer, and like hMRP1 seems to be present in cytoplasmic vesicles (in primary urinary bladder cancer at least, [102]). However in comparison to hMRP1, knockdown of hMRP3 genes *in vitro* in breast cancer derived cell lines, improved the effectiveness of doxorubicin, more so than an equivalent knockdown of hMRP1, potentially making it more attractive as a target for drug-resistant chemotherapy [102].

MRP4 (*ABCC4*)

MRP4 is broadly expressed in sanctuary organs (brain, liver and kidneys) as well as platelets [103–105]. Expression is high in renal proximal tubule cells facing the urine collecting ducts, and high on the luminal side of the brain capillary. In the liver, expression is variable and like MRP3 is upregulated during cholestasis to increase urinary excretion of conjugated bile acids [104]. hMRP4 is present almost exclusively on the plasma membrane of platelets, with a similar expression level to Na$^+$/K$^+$ ATPase [105]. MRP4 is the physiological transporter for urate, and can transport other cyclic nucleotides, e.g. cGMP and cAMP, as well other endogenous messengers (e.g. DHEA) [104]. Evidence for cAMP transport is supported by studies in muMrp4 knockouts, whereby platelets had a 60 % increase in intracellular cAMP due to defective export, leading to increased clotting times [105, 106]. hMRP4 is highly expressed (mRNA and protein) in lung cell carcinoma cells, with mRNA expression up to 1000 greater than healthy surrounding

tissue [107]. An SNP in *hABCC4* (3463A>G) has also been implicated in increased kidney damage in HIV positive patients taking anti-retrovirals [108].

2.1.2.3   BCRP (*ABCG2*)

Breast cancer resistance protein (BCRP) is a half ABC transporter and may form homodimers or heterodimers with other BCRP proteins. It is highly expressed in the placenta at the maternal side [109]. BCRP represents > 80 % of the total ABC mRNA in the blood vessels at the blood-brain barrier (8 times greater than P-gp mRNA), and 20 times greater than in the cortex [110]. Expression is low in liver (0.34 % of relative abundance [57]), small intestine and colon (lowest expression of ABC transporters [47, 49]) and kidney proximal tubules [111]. Like MRP4, BCRP is important in urate transport and detection of polymorphisms in BCRP in erythrocytes are positively correlated with gout, a disease due to insufficient excretion of urate, that leads to painful uric acid crystal deposition in joints and kidneys [112]. Like other ABC transporters it is upregulated in tumours, having originally been isolated from the resistant MCF7 human breast cancer cell line [111]. Increased hBCRP was seen to be associated with more aggressive head and neck tumours, as well as right-sided colon cancer with shorter survival [113, 114]. However, the presence of higher BCRP mRNA (and also MDR1) in clear cell renal cell carcinoma samples from patients was associated with increased survival and decreased metastasis, that was more limited to the carcinoma compared to surrounding healthy tissue [115]. This "protective" role for an ABC transporter is counter intuitive to what one would expect given the ABC transporter examples above, and warrants extra research. As these studies were all across different tumours and ethinicities (Caucasian, Hispanic and Chinese), it may well depend on where the tumour is as to whether an up or down regulation affects survival. Like hMDR1, hBCRP was also included in the FDA guidance document with *in vitro* studies to examine whether a molecule is a substrate or inhibitor as part of the submission process [19].

2.1.2.4   BSEP (*ABCB11*)

Bile salt export protein (BSEP) is a phylogenetically ancient transporter that is found in plants, fish and mammals [116]. It is highly expressed in the liver at the bile canaliculus, representing 7 % of relative transporter abundance in Caucasian liver [57], and no role outside the liver has been found [117]. BSEP is vitally important in the transport gradient of bile salts and the rank order of transport is conserved between rodents and humans [116]. The importance of this can be seen in progressive familial intrahepatic cholestasis type 2 (PFIC-2), where in patients, no BSEP can be detected and where the concentration of bile salts in the bile is only 1 % of normal [116]. Without the efficient shuttling of the bile salts linked with a deficiency in BSEP, severe cholestasis occurs and this is positively correlated with the development of hepatocarcinoma in children [118]. Inhibition of BSEP therefore maybe an important factor in the development of drug induced liver injury (DILI), but not enough to lead to cholestatis itself [119, 120].

2.2 Metabolism

One cannot really consider transporters in isolation in the body without consideration of metabolism of endogenous and xenobiotic molecules as well, and this summary is based in part on the book of Gibson and Skett [121] who describe the complex interplay between transport and metabolism. The role of drug metabolism in the body is to make the drug molecule more water soluble, ideally decreasing cell permeability, potency and toxicity, so that the metabolite has to be transported into the urine or faeces, and from there it can be safely eliminated from the body. This section will briefly go through the two "phases" of drug metabolism within the human body and their relevance and importance to the work presented here, including DDIs, and relevant guidelines from the drug regulators that are now being applied to transporters.

2.2.0.1 Phase I - Functionalisation reactions

There are two main families involved in the hydroxylation, or functionalisation of a drug molecule (prior to conjugation) in the body: Cytochrome P450 (CYP, included here) and the flavin containing mono-oxygenases (FMOs) found within the endoplasmic reticulum of cells. The latter will hydroxylate only soft nucleophiles on a nitrogen or sulphur atom, but not on a carbon atom [121].

There are 18 different hCYPs [122], with hCYP1-3 responsible for metabolism of 78 % of drugs on the market in 2008 (CYP3A4/5, 2C9, 2D6 and 2C19 comprising 80 % of the total) [123], with protein expression that are up to 100-fold greater than hOATP1B1 in hepatocytes [49, 124]. The main CYP responsible for the metabolism of xenobiotics; hCYP3A4, is also highly expressed in the intestine (as well as hCYP2C9), brain and kidneys and is therefore important in the amount of drug entering the systemic circulation from the gut. Whilst hCYP3A4 in enterocytes in the small intestine are only expressed at 1 % of the level in the liver, the large surface area of the small intestine makes hCYP3A4 important in limiting systemic exposure of substrates. The importance of intestinal hCYP3A4 is illustrated where the local inhibition of intestinal hCYP3A4 by grapefruit juice led to a large increase in systemic exposure [125], has led to it being included in the drug packaging inserts of hCYP3A4 substrates. An elegant in-depth meta-analysis on the world-wide population genotypes in 12 CYPs (56945 subjects) published by Zhou et al. [126] clearly shows the level of polymorphisms in CYPs across populations, with, for example, CYP3A5*3 as the largest polymorphism across all ethnicities comprising 41-100 % alleles, whilst CYP2D6 and CYP2A6 show the largest number of alleles across ethnicities with around 13 different alleles.

With the broad range of drugs that are metabolised by the CYPs, the potential for DDIs is vast and may, if not left unchecked, lead to death. Therefore a whole field of journals are dedicated to this and is a major part of any new drug registration submission to the regulatory authorities [18, 19]. Briefly, if a single enzyme is responsible for > 20-25 % for metabolism of a drug, then clinical studies with inhibitors must be undertaken (same for non-CYP enzymes). The drug and its major metabolites need to

be ascertained *in vitro* as to whether they are competitive and time-dependent inhibitors and then, using either static or physiologically based pharmacokinetic (PBPK) modelling techniques, predict the clinical risk [18, 19].

2.2.0.2 Phase II - Conjugation reactions

There are multiple types of conjugation reactions that occur in the body: glucuronidation, sulphation, glutathione conjugation (all discussed here), amino acid conjugation, N-acetylation and methylation, with the last reaction seemingly increasing the lipophilicity of a molecule. With the exception of glucuronidation, which exists in the endoplasmic reticulum, close to CYP3A, the enzymes for conjugation reactions are in the cytoplasm of numerous cell types common to those described above and for transporters: liver, kidney, intestine (glucuronidation), brain, and male and female gonads (glutathione conjugation to "scavenge" reactive oxygen species which may damage the sperm and ovum). The role of conjugation, will in general, further increase the polarity of molecules by addition of a bulky molecule which is then transported out of the cell. This is primarily to polar hydroxyl and primary amides following Phase I functionalisation reactions. However, glucuronidation, sulphation and N-acetylation can lead to reactive metabolites which bind to protein or DNA adducts leading to liver toxicity.

The addition of a large bulky glucuronide sugar moiety via the UDP- glucuronosyl transferases (UGTs) is important in the clearance of at least 20 % of clinical drugs on the market mainly via UGT1 and as such are important in their elimination [127]. Carboxylic acid containing molecules (such as statins and NSAIDs) have the potential to be metabolised by UGT1 into an acyl-glucuronide. Under most circumstances the acyl-glucuronide is transported harmlessly into the bile and faeces, where the glucoronide may come off due to intestinal pH or a bacterial glucuronidase leading to re-absorption and entero-hepatic recycling. Under certain conditions the acyl-glucuronide can migrate around the aromatic group it is situated on to become a Schiff base, which can then covalently bind to protein in the intestine and liver, leading to DILI (see Van Vleet et al. [128] for further details).

The addition of a SO_3 group to a molecule is via the sulphotransferases (SULTs) with SULT1A1 and 1B1 as the most important in sulphation of molecules in humans, and comprise 70 % of the SULTs in the liver (with SULT1B also the main in the intestine) [129]. SULTs are important in the detoxification process of molecules in the liver and intestine, but are also important in the activation of the carcinogenic polyaromatic hydrocarbons (in particular SULT1A1) [130].

Glutathione is a bulky tripeptide that is transferred to an electrophilic moiety on a substrate via the enzyme glutathione-S-transferase (GST) family or if the electrophile is particularly strong, non-enzymatically. There are 7 sub-families of cytosolic GSTs, and polymorphisms are most common in μ, θ and π sub-families. These polymorphisms are important in various diseases from oncology to neurodegenerative diseases and are reviewed in depth by Allocati et al. [131].

2.3 Transporter Substrates and Inhibitors

Examples of typical endogenous substrates have been included in the above sections where possible for each transporter. It can be observed from the above, that it is rare for any substrate to be purely specific for one transporter, with the exceptions of leukotriene C_4 (MRP1, [90]) and urate (MRP4, [104]). Subtype specific substrates and inhibitors for clinical and *in vivo* studies are hard to find due to overlapping specificities across both rodent and human OATPs, and it is this that makes clear conclusions from DDI studies in humans less clear cut. In rodents, knockout animals can be used to investigate the overall transporters that may lead to human DDIs, e.g. mice lacking mouse Oatp1a/1b, which had 40-fold higher concentrations of bilirubin, 4-fold higher unconjugated bile acid levels and increased HDL cholesterol concentrations in blood compared to wild type animals [101]. The human equivalent looks at specific genotypes and phenotypes to help explain clinically observed DDIs.

In this section xenobiotic substrates and some inhibitors have been included, but are far from a comprehensive list of interactions and drugs. Table 2.2 illustrates the complexity of examining transporter mediated DDIs both from a substrate and inhibitor point of view. Simple static models have been proposed which calculate the estimated AUC ratios in the absence and presence of inhibitor (The "R Value" see Eq. 2.1, [19, 132]), or clinically observed changes, where the R value is given by:

$$\text{R Value} = 1 + \frac{f_{u.plasma}I_{in.max}}{K_I}, R \geq 1.1 \qquad (2.1)$$

where $f_{u.plasma}$ is the fraction unbound of the inhibitor in the plasma (the minimum value proposed in the FDA draft guidance [19] is 0.01, due to error in measurements below this value), K_I is the inhibition constant (μM, or K_{inact} for non-competitive inhibition), and the maximum concentration of inhibitor at the inlet to the liver ($I_{in.max}$) is calculated according to:

$$I_{in.max} \; (\mu\text{M}) = \frac{C_{max} + \frac{F_aF_gK_aDose}{Q_h}}{R_b} \qquad (2.2)$$

where C_{max} is the maximum plasma concentration of the inhibitor (μM), F_aF_g is the fraction absorbed multiplied by the intestinal availability, K_a is the absorption rate constant (/min), $Dose$ is the dose of inhibitor (nmol), Q_h is human hepatic blood flow (70 kg male) = 1112(16 % CV)-1450 ml/min [2, 133]), and R_b is the blood:plasma ratio. A R value of greater than 1.1 indicates that there is a possibility of a TrDDI.

As the *R Value* is used in this situation to determine the maximal inhibitory effect at the entrance to the liver i.e. the sinusoid, the concentration needs to be estimated at a site distant from the blood from where it was taken. $I_{in.max}$ therefore takes this into account through the use drug specific factors: F_aF_g which often given as 1 as a worst case scenario as estimation is difficult [19]. K_a which can be estimated through the determination of the mean residence time following intravenous and oral administration (see Chapter 6, Table), or set at as 0.1 /min, the minimum gastric emptying time [132] and R_b which is normally determined *in vitro* through addition of drug to naive blood

which is then separated and analysed.

For example, in the case of atorvastatin, the calculated R value with cyclosporine A (CsA) was 3.1 (Table 2.2), which is greater than the FDA cut-off of 1.1 [19], and makes further investigations important if this was a new drug filing. In this case the R value, calculated at a single dose of 380 mg of CsA gave a conservative increase compared to a clinical study. Healthy volunteers who took atorvastatin for four days and then two doses of CsA (175 mg) showed a 15-fold higher plasma exposure of atorvastatin and its metabolites compared to those on tacrolimus, with an increased risk of rhabdomyolysis in chronic patients [134]. Pitavastatin has been suggested as a sensitive clinical substrate for OATP1B1 inhibition [9], and based on the calculated R values of 65 and 13 for the potent hOATP1B1 and 1B3 inhibitors rifamycin or rifampicin respectively (see Table 2.2 [132, 135]) back this up. Indeed a 7-fold increase in pitavastatin exposure was observed when an IV infusion of rifampicin was given [9], confirming the R value calculated by Hirano et al. [132]. Pei et al. [136] evaluated the effect of irbesartan as well as the hOATP1B1 521T>C polymorphism (heterozygotes TC versus wild type TT) on the pharmacokinetics and pharmacodynamics of repaglinide in Chinese volunteers. A significant increase in repaglinide exposure and glucose lowering effect in the presence of irbersartan was observed in wild type OATP1B1, 521TT, subjects (see Table 2.2), but not in heterozygote OATP1B1, 521TC, subjects. This was consistent with lower OATP1B1 activity in the liver and therefore lower concentration at the site of action of repaglinide in subjects (see 2.1.1 - hOATP1B1) [136]. Irbesartan is also a substrate of hOATP1B1 and 1B3 [137]. Unfortunately, the plasma concentration was not measured in the clinical study [136]. Evaluation of clinical metformin inhibition, like that for repaglinide, also involves measuring the pharmacokinetic and pharmacodynamic effect and has recently been reviewed in depth [138]. Two drugs used in oncology (docetaxel and paclitaxel) have also been included, as drug resistance has been attributed partly to upregulation of OATP1B3 [37] and MDR1 in tumours [139]. Therefore as well as potential DDIs in the host, DDIs in the tumour also need to be evaluated to counter drug resistance.

Table 2.2: Examples of transporter substrates and their inhibitors as well as potential DDI risk

Substrate	Transporter (pmol/min/mg prot)	Inhibitor (K_I/IC_{50}, μM)	R Value (FDA)	Comments	Ref
Statins					
Atorvastatin	OATP1B1				
	V_{max}=3.8±0.3, K_m=0.9±0.2	CsA 0.02±0.004^{PC}	3.1	Calculated	[140]
	V_{max}=120, K_m=0.62(0.45)	Gem 32±4	1.5	Article R value	[135]
	V_{max}=120, K_m=0.62(0.45)	RifSV 0.3±0.08	51	Article R value	[135]
	V_{max}=6.6±1.2, K_m=0.8±0.2	Ataz 1.3	1	Calculated	[141]
	OATP1B3				
	V_{max}=2.3±1.4,	Ataz 0.37	1	Calculated	[141]

Table 2.2 continued...

Substrate	Transporter (pmol/min/mg prot)	Inhibitor (K_I/IC_{50}, μM)	R Value (FDA)	Comments	Ref
	K_m=0.7±1.5				
	OATP2B1				
	(V_{max}=24±8,	Ataz 5.1	1	Calculated	[141]
	K_m=2.8±1.6)*				
	NTCP				
	(V_{max}=2260±1184,				[142]
	K_m=185±108)*				
	MRP2				
	K_m=7.2 ± 1.6			ATPase activity	[143]
	MDR1				[144]
Pitavastatin	OATP1B1				
	V_{max}=340,	Gem 32(4)	1.08	Article R value	[135]
	K_m=1.3±0.3				
	V_{max}=340,	RifSV	101	Article R value	[135]
	K_m=1.3±0.3	0.3±0.08			
		Rifp 0.47±0.03	13	Article R value	[132]
	OATP1B3*				[132]
	OATP2B1				
	(V_{max}=7.4±1.4,				[132]
	K_m=1.2±0.3)*				
	MDR1			OATP1B1/MDR	[132]
	MRP2			OATP1B1/MRP2	[132]
	K_m=8.9±1.4			ATPase activity	[143]
	BCRP			OATP1B1/BCRP	[132]
Diabetes					
Repaglinide	OATP1B1	CsA 0.02[PC]	3.2	PBPK model	[145]
		CsA	2	PBPK model	[146]
			(1.4-2.3)		
		Gem	1.6	PBPK model	[146]
			(1.4-2.8)		
		Ibstn*2		Clinical	[136]
				Inc AUC 34 %	
	OATP1B3	CsA 0.06[PC]	3.2	PBPK model	[145]
Metformin	OCT1			Clinical	[147]
		Imip (↓87 %)			[148]
	OCT2			Clinical	[73]
	MATE1			Clinical	[73]
	MATE2			Clinical	[73]
Sartans					
Valsartan	OATP1B1				
	V_{max}=3.9±0.5,				[149]
	K_m=1.4±0.2				
	V_{max}=33(33-34),	Ltnb (2.6)*2	1.06	Article R value	[150]
	K_m=21(20-22)				
		Ctnb		↑ V_{max} & K_m	[150]
		Gem (39)	1.2	Calculated	[151]
		Gem-G (20)	2.3	Calculated	[151]
	OATP1B3				
	V_{max}=135±40,				[149]

Table 2.2 continued...

Substrate	Transporter (pmol/min/mg prot)	Inhibitor (K_I/IC_{50}, μM)	R Value (FDA)	Comments	Ref
	$K_m=18\pm6$				
		Gem-G (100)	1.06	Calculated	[151]
	MRP2				
	$V_{max}=895\pm578$,			OATP1B1/MRP2	[149]
	$K_m=30\pm18$				
Irbesartan	OATP1B1				
	($V_{max}=17$ (9 %),				[137]
	$K_m=0.7$ (29 %))^{*3}				
	OATP1B3				
	($V_{max}=27$ (56 %),				[137]
	$K_m=11.9$ (77 %))^{*3}				
Oncological					
Docetaxel	OATP1B1				
	$V_{max}=38\pm47$,				[152]
	$K_m=0.4\pm1.3$				
		Sfnb $0.07^{*2,PC}$			[153]
	OATP1B3				
	$K_m=0.32\pm0.06$				[154]
	$V_{max}=480\pm90$,				[152]
	$K_m=14\pm7$				
	MRP2				[154]
	MDR1			OATP1B1/MDR1	[152]
				OATP1B3/MDR1	
Paclitaxel	OATP1B1				
	$V_{max}=22\pm3$,				[139]
	$K_m=0.4\pm0.2$				
	OATP1B3				
	$V_{max}=14\pm5$,				[139]
	$K_m=2.4\pm1.4$				
	MDR1				[155]
	MRP2				[155]

PC = pre-co-incubation, CsA = cyclosporine, Gem = gemfibrozil, Gem-G = gemfibrozil glucuronide, RifSV = rifamycin SV, Rifp = rifampicin, Ataz = atazanavir, Ibstn = irbesartan, Imip = imipramine, Ltnb = lenvatinib, Ctnb = ceritinib, Sfnb = sorafenib, *= minor contribution,^{*2}= also a substrate,^{*3} = per 1×10^6 cells. R values calculated according to Eq. 2.1

2.4   Mechanistic Modelling

To gain information regarding the specific uptake of endogenous and xenobiotic substrates via the solute carriers (see 2.1.1) as well as their subsequent inhibition (see Table 2.2), one needs to develop models which allow the determination of their kinetic parameters. This can be done in two ways: through the determination of the initial uptake velocity and multiple concentrations (often through a single early timepoint), or via the use of a mechanistic modelling approach, normally through the use of ordinary differential equations (ODEs). The former of these two approaches can be used to obtain good initial estimates in the latter models, which generally include more model parameters. Structural identifiability of the models used is an essential pre-requisite for ODE based models for the estimation of unknown parameters, both in terms of what combinations

(if any) of the parameters and states are estimatable from the available observations, and this will be described in a separate section below.

2.4.1 Structural Identifiability

Approaches for structural identifiability assume a model structure of the form:

$$\dot{x}(t, \theta) = f(x(t, \theta), u(t), \theta) \tag{2.3}$$

$$x(t_0) = x_0(\theta) \tag{2.4}$$

$$y(t, \theta) = h(x(t, \theta), u(t), \theta) \tag{2.5}$$

where $x(t, \theta) \in \mathbb{R}^n$ is the state vector, $u(t) \in \mathbb{R}^q$ is the input vector, $y(t, \theta) \in \mathbb{R}^m$ is the observations vector and $\theta \in \mathbb{R}^p$ is the vector of unknown parameters which belong to the feasible parameter space $\theta \in \Theta$ and f and h are smooth functions. If there is a second parameter vector $\bar{\theta}$ and state vector $\bar{x}$ which is then compared simultaneously with the original model output using successive iterations, such that:

$$h(x(t, \bar{\theta}), u(t), \bar{\theta}) \equiv h(\bar{x}(t, \theta), u(t), \theta)$$

if in a neighbourhood $\mathbb{N} \in \Theta$, implies that $\theta = \bar{\theta}$, then the model is at least structurally locally identifiable (SI). If $\mathbb{N} = \Theta$, then the individual parameters $\theta_i \in \theta$ are unique and the model is SGI. If under any circumstances:

$$h(x(t, \bar{\theta}), u(t), \bar{\theta}) \neq h(\bar{x}(t, \theta), u(t), \theta)$$

except when $\theta = \bar{\theta} = 0$, then the model and all the parameters therein are unidentifiable [24].

Prior to parameter estimation, or indeed the generation of experimental data, it is important to evaluate, assuming perfect (noise-free) data, whether the proposed mathematical model is at least structurally locally identifiable. In other words, there exists a subset of parameters or parameter combinations that are unique or locally identifiable, with no model parameters unidentifiable, within the premise of the model structure and observation(s) [17]. Assuming a known input/output relationship, if all the parameters within a given model are uniquely identifiable, then the model and all the parameters within the model are structurally globally identifiable (SGI). Without a formal structural identifiability analysis, it would not be known if the parameters and the structure of model itself are unidentifiable, and would not affect the output making any parameter or state values estimated experimentally meaningless as they could be replaced with any number without affecting the measurement.

Determination of identifiability with micro-rate constant models (see Fig. 2.4) and macro-rate constant models (those based on the Michalis-Menten equation for transporters) were evaluated using different mathematical approaches by Grandjean et al. [24], Grandjean [25]:

- The similarity transformation approach - symbolic, proposed for non-linear sys-
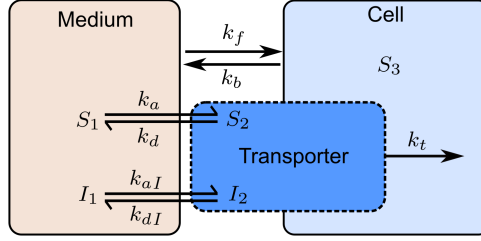
Figure 2.4: Schematic of a micro-rate constant model of ordinary differential equations (ODEs) derived for initial parameter estimates for substrate (S) uptake into cells and competitive inhibition by inhibitor (I). X_1 and X_2 are the amount of X (S or I) in the medium and bound to transporter respectively, S_3 is the intracellular amount of S. k_f and k_b are the passive rate constants into and out of the cell respectively, k_a and k_{aI} are the transporter association rate constants for S and I respectively, assuming free transporters are available, k_d and k_{dI} are the dissociation rate constants for S and I respectively and k_t is the substrate translocation rate constant into the cell from S_2

tems by Vajda et al. [156]

- The differential algebra approach - numeric, via large number integers

- The algebraic input/output approach - numeric, via large number integers [157, 158]

- The observable normal form - symbolic [24]

- Taylor series expansion - symbolic, becomes intractable due to complexity of expansions [24]

As a micro-rate constant model for substrate only has previously been shown to be SGI (see [24, 25]), the model was extended to include the binding of inhibitor to transporter under the assumption of competitive inhibition only (see Fig. 2.4) using the algebraic input/output analysis method in Maple 2018 32bit (Maplesoft, Waterloo, Ontario, Canada) using the code provided in Evans et al. [158].

If the transporter components of Fig. 2.4 for substrate and inhibitor are written in chemical reaction form:

$$S_1 + T_f \underset{k_d}{\overset{k_a}{\rightleftharpoons}} S_2 \overset{k_t}{\rightarrow} S_3 \tag{2.6}$$

$$I_1 + T_f \underset{k_{dI}}{\overset{k_{aI}}{\rightleftharpoons}} I_2 \tag{2.7}$$

where X = the amount of substrate (S) or inhibitor (I), X_1 and X_2 are the amount in the medium and bound to transporter respectively, and S_3 is the amount of intracellular substrate. k_a and k_{aI} are the transporter association rate constants for S and I respectively, assuming free transporters (T_f) are available, k_d and k_{dI} are the dissociation rate constants for S and I respectively and k_t is the substrate translocation rate constant into the cell from S_2. Then the law of mass action for both the substrate and inhibitor

gives:

$$\frac{dS_1}{dt} = -k_f S_1 - k_a S_1 T_f + k_d S_2 + k_b S_3 \tag{2.8}$$

$$\frac{dS_2}{dt} = k_a S_1 T_f - (k_d + k_t) S_2 \tag{2.9}$$

$$\frac{dS_3}{dt} = k_f S_1 + k_t S_2 - k_b S_3 \tag{2.10}$$

$$\frac{dI_1}{dt} = -k_{fI} I_1 - k_{aI} I_1 T_f + k_{dI} I_2 + k_{bI} I_3 \tag{2.11}$$

$$\frac{dI_2}{dt} = k_{aI} I_1 T_f - k_{dI} I_2 \tag{2.12}$$

$$\frac{dT_f}{dt} = -T_f(k_a S_1 + k_{aI} I_1) + (k_d + k_t) S_2 + k_d S_3. \tag{2.13}$$

where k_f and k_{fI} are the passive rate constants for the movement of drug into the cell for substrate and inhibitor respectively, and k_b and k_{bI} are the passive rate constants for the movement of drug out of the cell for substrate and inhibitor respectively. As it is rare that T_f is known, but assuming that T_o is conserved, T_f can then be eliminated in Eqs. 2.8-2.12 [15, 25] to give:

$$T_f = T_o - S_2 - I_2 \tag{2.14}$$

giving modified equations for substrate and inhibitor:

$$\frac{dS_1}{dt} = -k_a S_1(T_o - S_2 - I_2) + k_d S_2 \tag{2.15}$$

$$\frac{dS_2}{dt} = k_a S_1(T_o - S_2 - I_2) - (k_d + k_t) S_2 \tag{2.16}$$

$$\frac{dS_3}{dt} = k_t S_2 \tag{2.17}$$

$$\frac{dI_1}{dt} = -k_{aI} I_1(T_o - S_2 - I_2) + k_{dI} I_2. \tag{2.18}$$

$$\frac{dI_2}{dt} = k_{aI} I_1(T_o - S_2 - I_2) - k_{dI} I_2. \tag{2.19}$$

To reduce the set of 5 ODEs (3 for substrate (medium, transporter and intracellular) and 2 for inhibitor (medium and transporter)), the transporter compartment for substrate (S_2) and inhibitor (I_2) can be factored out based on the conservation of substrate (S) or inhibitor (I), where at $t = 0$, all states in the model sum to the doses (D_S and D_I

respectively) (Eq. 2.20 and 2.21):

$$D_S = S_1 + S_2 + S_3,$$

$$\therefore S_2 = D_S - S_1 - S_3 \quad (2.20)$$

$$D_I = I_1 + I_2,$$

$$\therefore I_2 = D_I - I_1. \quad (2.21)$$

This simplifies the mechanistic model from five to three compartments, but retains the overall same number of model parameters. The model equations are then given by:

$$\frac{dS_1}{dt} = -k_f S_1 - k_a S_1 \left(T_o - (D_S - S_1 - S_3) - (D_I - I_1)\right)$$
$$+ k_d \left(D_S - S_1 - S_3\right) + k_b S_3 \quad (2.22)$$

$$\frac{dS_3}{dt} = k_f S_1 + k_t \left(D_S - S_1 - S_3\right) - k_b S_3 \quad (2.23)$$

$$\frac{dI_1}{dt} = -k_{aI} I_1 \left(T_o - (D_S - S_1 - S_3) - (I - I_1)\right) + k_{dI} \left(I - I_1\right) \quad (2.24)$$

where k_f and k_b represent the passive rate constants into and out of the cell respectively. Initial conditions for the model are given by: $[D_S, 0, D_I]$, and the unknown parameter vector consists of: $\{k_f, k_a, T_o, k_d, k_t, k_b, k_{aI}, k_{dI}\}$. The experimental observation assuming only substrate is measured is given by:

$$y = kS_3 \quad (2.25)$$

where k is a scalar (1/Cell volume in experimental chapters presented here) transferring from amount (S_3) to the measured concentration y. This model (Eqs. 2.22 - 2.24) was found to be SGI using the algebraic input/ouput analysis method [158] in Maple on a Lenovo Laptop (2.9 GHz, 4 Gb RAM, Intel Core i5-5200U processor), see Appendix A for output. A downside of this method of analysis is that the three compartment model for substrate only (including S_2) has an observation that is a combination of two states, i.e. $y = k(S_2 + S_3)$, which is not currently supported in the code presented by Evans et al. [158] (Evans, personal communication), or in the online tool COMBOS [159]. It is also not possible to include multiple different doses in the ODEs used in the software for parameter estimation if they are to be analysed simultaneously (Monolix 2018R2 (Lixoft, Antony, France)).

It was deemed important to evaluate the model form used during parameter estimation, but also in Chapter 4, a mixture of rate constants presented above (termed micro rate constant in future chapters) and a Michaelis-Menten equation for metabolism led to the models and the resulting expression in the structural identifiability analysis becoming too complex and intractable for determination of structural global indentifiability. Therefore, determination as to whether a mechanistic model was at least structurally identifiable was deemed sufficient. One method to determine structural local identifia-

bility uses the `Identifiability Analysis` package, developed by Jirstrands group at the Fraunhofer-Chalmers Institute in Sweden [16, 160] and implemented here using Wolfram Mathematica 11.3 (Wolfram Research Inc, Illinois, USA). Given a set of ordinary differential equations (ODEs) with an unknown parameter vector, known input and a set of measurable observations, this method gives a Boolean answer to the structural identifiability problem, including a list of any unidentifiable parameters and the number required to be known (degrees of freedom, d.o.f.) for the model to become at least structurally locally identifiable. The package uses large value random prime numbers as replacements for the parameters, states and inputs in the calculations performed to obtain a modified Jacobian matrix of the partial derivatives up to a limit of $n + p$ as any iterations beyond this will be derivatives of those already present and are therefore already included [16, 160]. Any symmetries within the matrix (indicating unidentifiability) are then destroyed to efficiently determine the local identifiability (or combinations) of parameters and state variables [16, 160] (see Appendix B and C for examples of a micro-rate constant model and macro-rate constant model respectively). Another option for the determination of structural local identifiability is the `STRIKE-GOLDD` package [161] in Matlab (Mathworks, Massachusetts, USA), which re-casts identifiability analysis as an extension of observability through the use of extended Lie derivatives to include the parameters and initial conditions (in a similar way to that described above). Initial testing of STRIKE-GOLDD (version 1.0.4.Beta) within Matlab R2017a gave the same answers as the `Identifiability Analysis` package, but was often intractable on a Viglen desktop PC (3.6 GHz, 16 Gb RAM, Intel Core i7-4790 processor) during the Lie derivative expansion compared to the `Identifiability Analysis` package and was therefore not used further.

2.4.2 Initial Velocity Models

An early use of the determination of isolated hepatocyte uptake by taurocholic acid was described in 1975 [63]. The authors used a centrifugal oil spin technique to separate hepatocytes from the medium in which they were present into a dense bottom layer (3M KOH in this case). Determination of kinetics was derived from the initial uptake velocity, where uptake was deemed to be linear across four timepoints (15, 30, 45 and 60 s). Initial adsorption to the plasma membrane was described through extrapolation of an early timepoint, which ended before the first timepoint was actually taken and was therefore determined graphically through the use of a Scatchard plot (bound/free taurocholic acid against bound). The initial velocity was plotted on a double reciprocal plot (a Lineweaver-Burke plot, see Fig. 2.5b for example) to obtain the maximum uptake velocity (V_{max}, pmol/min) and Michaelis-Menten constant (K_m, nmol/ml). Competitive inhibition of taurocholic acid by a conjugated bile acid (taurochenodeoxycholic acid) was also determined through the double reciprocal plot and via a Dixon plot (1/(initial velocity) versus incubation concentration) to determine an inhibition constant (K_I) that is approximately half of K_m and indicative of higher affinity for the transporter than taurocholic acid [63].
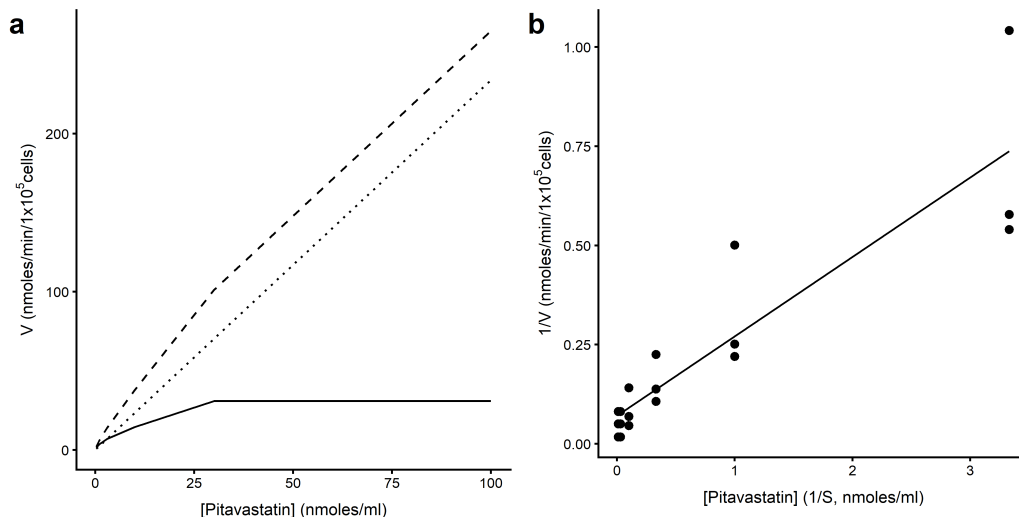
Figure 2.5: **a** Yamazaki plot of initial velocity at 15 sec against pitavastatin incubation concentration, dashed line = total, dotted line = passive, solid line = saturable uptake. Approximate parameters V_{max} = 300 pmol/min/10^6 cells, K_m = 10 nmol/ml **b** Lineweaver-Burke (double reciprocal) plot using "Active" from **a**. Parameter estimates V_{max} =1/y intercept= 141 pmol/min/10^6 cells (RSE = 36 %), K_m = gradient $\times V_{max}$= 28 nmol/ml (RSE = 21 %)

To generate these plots, a detailed experimental design was required, consisting of: 4 timepoints $\times$ 5 concentrations of taurocholic acid $\times$ 3 taurochenodeoxycholic acid $\sim$ 60 datapoints. The disadvantage of this method is that use of Eq. 2.26 to obtain the uptake clearance (CL_{up}, μL/min) from the V_{max} and K_m according to:

$$CL_{up} = \frac{V_{max}x}{K_m + x} \qquad (2.26)$$

where x is the concentration of substrate in the medium at t = 0 i.e. the dose, is that the equation does not allow for passive movement of drug. This can lead to a deviation of the double-reciprocal plot from linearity at higher concentrations, which could be seen in a follow up paper which examined the uptake of an anionic substrate bromosulphophtalein [162].

There are three different techniques (one using curve stripping, and two using experimental techniques) with the same outcome used to allow for passive movement of substrate (P_{dif}) depending on the experimental system used (Eq. 2.27). The first technique was used by Yamazaki et al. [163] who calculated initial velocities over the assumed linear uptake phase using an oil spin method. The gradient obtained at high concentrations of substrate (indicative of passive movement of substrate) is subtracted to obtain the saturable only part of the uptake (known as a "Yamazaki plot"). The saturable uptake is then fitted to Eq. 2.26 using a non-linear least squares approach. Examples of a Yamazaki plot and the subsequent double reciprocal plot using data from Chapter 5 are given in Figs. 2.5a and b respectively. As the Lineweaver-Burke plot is a double reciprocal plot, as the incubation concentration increases to saturate the uptake

process, so the points become clustered around the origin and the curve fitting becomes insensitive (see Fig. 2.5b). The converse is also true, at low incubation concentrations the velocity can be more variable, for which the curve fitting becomes more sensitive to (see Fig. 2.5b). However, the obtained parameters from the either the Yamazaki plot or the Lineweaver-Burke plot can then be used as initial estimates in macro-rate constant models.

The second technique for the separation of passive and active components, involves using hepatocytes that are kept at 4 °C to stop any "active" processes and uptake experiments undertaken, this can then be subtracted from the total to again obtain the transporter-mediated uptake. This technique has many failings, with the main one being that it is assumed that membrane fluidity does not change at low temperatures [164] and has been shown to under-predict passive movement of drug in the literature, compared to estimation of passive movement at 37 °C in a mechanistic model [8, 164–166].

The final method for the separation of passive and active components is frequently used in experiments where plated cell lines (devoid of transporter proteins) have particular transporter proteins inserted as an expression vector, and the uptake of substrate compared to the same cell lines where a mock expression vector is used [164, 167, 168]. The mock expression vector cells will only, in theory, possess passive permeability characteristics and can therefore be subtracted from the transporter expressing cell lines. This and the first approach given above are used for calculating values for passive movement of substrate in cell-lines (see Chapter 3).

2.4.3 Mechanistic Models of Uptake

A mechanistic modelling approach is routinely applied in the transporter literature in the study of uptake into hepatocytes using Eq. 2.27, and assumes that the difference between passive movement in and out of the cell is only related to the volume and fraction unbound in the cell, and that no efflux via a transporter occurs [33, 164, 165, 169, 170] namely:

$$CL_{up} = \frac{V_{max}x}{K_m + x} + P_{dif}x. \tag{2.27}$$

where P_{dif} is the passive uptake clearance (ml/min). For Eq. 2.27 to be used in a mechanistic model it has to be decided where the observations are taken experimentally; either from the medium [171], from the cells [8, 170, 172] or both cells and medium [171, 173]. Determining factors as to whether cellular and/or medium concentrations are measured are: structural identifiability analysis outcomes, time/cost of analysis (LC-MSMS, or radioactivity) and sensitivity of the method to observe changes between concentrations as well as the lower limit of detection. It is expected that there will be an initial small decrease in medium concentration corresponding to the uptake of drug into cells (see Baker and Parton [170], Soars et al. [171]), whilst at higher doses of substrate, one will only see a straight line as uptake is saturated. If extraction is complete from the medium at lower doses, no information can be gleaned from medium concentrations only (See Chapter 4), therefore the measure of uptake into the cells will be the main

focus as this can give a broader understanding of drug disposition into cells (including metabolism, which may be subtly missed in the medium concentration). An extension to Eq. 2.27 to include the amount in the medium as well as the cellular amount (in the absence of metabolism) would give ODEs which are the opposite in sign to each other, i.e. substrate lost from the medium = substrate gained in the cell. If Eq. 2.27 was extended to include metabolism via additional clearance terms per metabolite (e.g. as in Menochet et al. [33]), then substrate lost from the medium would not equal substrate gained in the cell, unless the metabolite formed is also measured.

There are also certain assumptions with regard to the use of the Michaelis-Menten equation above (Eq. 2.27) from its original development for enzyme kinetics and that have been expanded upon for transporters [15, 23, 24]:

1. The initial substrate concentration is much larger than the transporter concentration.

2. It then follows that the association to the transporter (k_a is very rapid) is thus in rapid equilibrium with the transporter.

3. The free transporter (T_f) is therefore affected by the dissociation rate constant from the transporter (k_d).

4. The rate limiting step in the transport of substrate into the cell is the translocation rate constant (k_t).

As mechanistic models use multiple time courses across concentrations and experiments (up to 150 datapoints) [8, 33, 164, 170], there should be sufficient information with which to use the Michaelis-Menten equation in its initial polynomial form using micro-rate constants, as the maximum number of unknown parameters and states is for a substrate only model is at most 13 (passive with membrane binding, transporter mediated uptake and single metabolism rate constant). The combined model output of the amount bound to the transporter (X_2) and the amount within the cell (X_3), mulitplied by the inverse of the cell volume (V_{cell}) to give a concentration to match the experimental observation is given by:

$$y = \frac{1}{V_{cell}} (X_2 + X_3).$$

(2.28)

This poses a problem, as one needs to know the number of cells in a sample and also which cellular volume to use. Within the literature, there are multiple methods used to measure cell volume (see Table 2.3): Using radiolabelled markers to determine intracellular volume and the adherent water layer [32, 174, 175]; packed cell volume combined with microscopy [170, 176]; and the use of proteomics [49]. Which cellular volume should then be used? Does it depend on the species and also the format (i.e. hepatocytes vs. cell-lines) that is being looked at? Most importantly, does the cell volume used actually affect the parameters to be estimated? It is also important to note that the cell volume will also change depending on the number of nuclei within the cell (proportional to the amount of histones/DNA [49], which for hepatocytes can routinely be $\geq 1 < 16$ [177].

31

To decrease the uncertainty in this volume, one could estimate the cell volume as an unknown parameter for each experiment based on an initial estimate from Table 2.3. This can give spurious results if the data are sparse for a particular experiment (e.g. see Chapter 3, pre-co-incubation scenario). Therefore literature values and the mean or median are used in each following experimental chapter, and then whichever volume gave the smallest BIC was then used a fixed constant and the data was also normalised to this value.

Table 2.3: Literature values for cellular volume

Sample Type	Method	Volume (μl/10^6)	Ref.
CHO	Mean of literature	1.4	[164]
CHO	Using fluorescent dye and holographic microscopy	1.6 ± 0.7 ($n = 56$)	[176]
HEK293	Using fluorescent dye and holographic microscopy	2 ± 0.5 ($n = 14$)	[176]
HEK293	[^{14}C]-urea	4 ± 0.2^a	[178]
Median (HEK293)		3	
Rat H	Packed cell volume and confocal microscopy	6.5	[170]
Rat H	[^{3}H]-water, [^{1}4C]-sucrose	3.9 ± 0.3 ($n = 42$)	[175]
Rat H	[^{3}H]-water, [^{1}4C]-sucrose	2.2 ± 0.46^b	[32]
Geometric mean (Rat H)		3.8	
Human H	sphere of $r = 6.76$ μm	1.2	[179]
Human H	sphere of $r = 8.1$ μm	2	[180]
Human H	[^{3}H]-water, [^{1}4C]-dextran	2.3 ± 0.3	[174]
Human H	'Proteomic Ruler'	3 ($n = 7$)	[49]
Median (Human H)^c		2.7	
HepG2	'Proteomic Ruler'	0.8 ($n = 7$)	[49]

CHO = Chinese Hamster ovary cell line, HEK293 = Human Embryonic kidney cell line 293, H = Hepatocyte, HepG2 = hepatocarinoma cell line, ^{a} = adjusted from /mg to /10^6 using HEK-MOCK cellularity (See Chapter 3, ^{b}= adjusted from /mg to /10^6 using hepatocellularity [181], ^{c} = measured estimates only used)

2.4.4 Micro-rate Constant Scaling

To allow comparison to certain literature values from micro-rate constants up to macro-rate constants, the equation used to describe saturable uptake needs to be re-arranged to yield the classic Michaelis-Menten form from the parameter estimates obtained. This is based on the assumptions listed above (see points 2.4.3 to give the maximum velocity (V_{max} Eq 2.29) and the concentration at which 50 % of the maximum velocity (K_m, Eq. 2.30). The corresponding macro parameters are given by:

$$V_{max} \text{ (pmol/min/}10^6 \text{ cells)} = k_t T_o \times 1000 \tag{2.29}$$

where k_t is the translocation from the transporter into the cell, and T_o is the total amount of transporters responsible for uptake, and 1000 is the scalar from nmol/min/10^6 cells to pmol/min/10^6.

To enable the concentration at which 50 % either uptake transporters ($K_{m.up}$) are occupied to be calculated in nmol/ml, the association rate constant (k_a) must first be converted into /μM/min/10^6 cells by multiplying by the medium volume V_{medium} in

which 1×10^6 cells are present.

$$K_m \text{ (nmol/ml)} = \frac{(k_d + k_t)}{V_{medium} k_a}. \tag{2.30}$$

To enable the equilibrium dissociation rate constant for substrate (K_D) or inhibition (K_I) to be calculated in nmol/ml, k_a or k_{aI} must be converted into $/\mu M/min/10^6$ cells as *per* Eq. 2.30.

$$K_D \text{ or } K_I \text{ (nmol/ml)} = \frac{k_{dI}}{V1 \times (k_a or k_{aI})}. \tag{2.31}$$

For non-competitive inhibition, an inactivation constant (K_{inact} (nmol/ml)) is calculated by multiplying the K_I by the dimensionless term α using:

$$K_{inact}(\text{nmol/ml}) = K_{I.up}\alpha. \tag{2.32}$$

These macro parameters can be further scaled to yield uptake clearance ($\mu l/min/10^6$ cells) in the absence (CL_{up}) and presence of inhibitor ($CL_{up.app}$) using:

$$CL_{up} \text{ } (\mu l/min/10^6 \text{cells}) = \frac{V_{max}}{K_m}. \tag{2.33}$$

For competitive inhibition, within the $CL_{up.app}$ (Eq. 2.35), K_m becomes an apparent $K_{m.app}$:

$$K_{m.app}(\text{nmol/ml}) = K_{m.up}\left(1 + \frac{I}{K_{I.up}}\right) \tag{2.34}$$

where I is the incubation concentration of the inhibitor.

$$CL_{up.app} = \frac{V_{max}}{K_m\left(1 + \frac{I}{K_I}\right)} = \frac{V_{max}}{K_{m.D.app}} \tag{2.35}$$

For non-competitive inhibition within the $CL_{up.app}$, V_{max} becomes an apparent $V_{max.app}$ using:

$$V_{max.app} = \frac{V_{max}}{1 + \frac{I}{K_{inact}}} \tag{2.36}$$

and

$$CL_{up.app} = \frac{\frac{V_{max}}{\left(1 + \frac{I}{K_{inact}}\right)}}{K_m} = \frac{V_{max}}{(1 + \frac{I}{K_{inact}})K_{m.D}} = \frac{V_{max.app}}{K_m}. \tag{2.37}$$

2.4.5 Parameter Estimation and Practical Identifiability

The estimation of parameters within a mechanistic modelling framework for both fixed effects (one set of parameter estimates for the population) and random effects (where parameter estimates vary with the individual) and the estimates of errors on the parameters therein is termed non-linear mixed effects modelling [182, 183]. Practical identifiability is concerned not just with the experimental design, but also the model structure. It is concerned with whether given the experimental data (i.e. discrete data or observations taken at selected intervals in time), the parameters and their variance can be estimated

[184]. This is intrinsically linked to structural identifiability described above (see Section 2.4.1). If a model is structurally unidentifiable, no matter how much data one can obtain for the model states presented, then any parameters obtained from the experiment may be effectively meaningless. If a model is at least structurally locally identifiable, then the parameter estimates and the variances of the parameters are obtained from the data and experimental design [185]. By models, we mean state space models of the form given by Eqs. 2.3- 2.4. The state space models considered, need to be extended here to include the fixed effects, random effects and their variances [182, 185] so that:

$$\dot{x}_i(t, \phi_i) = f(x_i(t, \phi_i),\ u_i(t),\ \phi_i), \qquad x_i(t_0) = x_0(\phi_i) \tag{2.38}$$

$$y_{ij}(t, \phi_i) = g(\phi_i, \theta, x_{ij}) + h(\phi_i, \theta, x_{ij})\varepsilon ij, \qquad 1 \le i \le n,\ 1 \le j \le m_i \tag{2.39}$$

where y_{ij} is the jth observation (total observations for individual i, m_i) of the ith individual (total individuals, n), ϕ_i is the unknown parameter vector for the ith individual. The within-group errors ε_i and residual unexplained variance η_i (with a corresponding covariance matrix, Ω) are assumed to be random variables that are mutually independent with mean 0 and variance σ^2, $(\eta_{i\sim i.i.d.} N(0, \Gamma))$. g and h are non-linear smooth functions of ϕ_i.

There are multiple software platforms upon which parameters and their variances can be estimated. Some are free packages allied to R [186], reviewed by [187], or Matlab (The Mathworks Inc., Massachusetts USA) [188], whilst others are commercial packages that require licenses (NONMEM (Icon Plc, Dublin, Ireland), Monolix (Lixoft, Antony, France) and WinNonLin (Pharsight, Missouri, USA)). All of these packages have the same objective; to obtain maximum likelihood estimates of the parameters that minimise the variance between the observed and the predicted data [189]. The profile-likelihood algorithm is an attractive offering, as it combines structural identifiability with parameter estimation to generate profiles for parameter estimates [188]. If both upper and lower confidence limits are obtained, then the parameter is deemed to be practically identifiable (and thus at least structurally locally identifiable), if a single bound is obtained, as well as an estimate, then the parameter is practically locally identifiable, whilst a flat profile indicates practical non-identifiability [188]. This method was not however implemented here as both fixed and random effects models were not instigated, and also due to the fact that all compartments are defined in terms of concentrations [188]. For the micro-rate constant models in the experimental chapters, the transporter compartment volume is not known. The cell volume is in the region of 3×10^{-3} ml, of which the total plasma membrane has been estimated to be 1 % of this volume [49], which may introduce instabilities in the data analysis.

The package used for parameter estimation was the Monolix suite (Lixoft, Antony France). In the Monolix algorithm, a mixed effects model is seen as a missing data problem, comprising the observed data y_{ij} and the non-observed data obtained from the random effects model (ϕ_i), giving the complete data $(y,\ \phi) = (y_{ij}, \phi_i)_{1 \le i \le n,\ 1 \le j \le m}$ [182].

Monolix uses the stochastic approximation of the expectation maximisation (SAEM) method, where a stochastic procedure simulates the random effect data (ϕ_i) at each iteration step ϕ^{k+1} from the conditional distribution $p(.|y; \theta_k)$ and then updates the maximisation of the likelihood ($\arg\max_\theta L$) according to the following [182, 190]:

$$s_{k+1} = s_k + \gamma_k \left(\tilde{S} \left(y, \phi^{(k+1)} \right) - s_k \right) \tag{2.40}$$

and

$$\theta_{k+1} = \arg\max_\theta L \left(s_{k+1}, \theta \right) \tag{2.41}$$

where s_k is the stochastic approximation, γ is a sequence of positive step sizes decreasing to 0, k is the iteration step, $\tilde{S}$ is the minimum sufficient statistics of the complete model, with a value in a subset of real numbers $\mathbb{R}^m$ and θ is the unknown parameter vector. If the simulation step is not successful, then the algorithm employs a Markov chain Monte-Carlo (MCMC) method to obtain ϕ which is then passed to the simulation step above [182]. Initial step sizes of 1 allows flexibility in the iterations to converge to a local neighbourhood around the maximum likelihood estimate of the parameters ($\hat{\phi}$), then with smaller step the estimations are refined to ensure convergence [182]. This does not guarantee that the maximum likelihood estimate of the parameters will be the global maximum, and therefore every 50 iterations a simulated annealing step is included to help move the estimates away from a local minimum [190].

Once the algorithm has converged to $\hat{\theta}$, and assuming that the log likelihood is sufficiently smooth, then it is possible to estimate the Fisher information matrix (FIM), and the observed Fisher information of the likelihood is obtained directly from the simulated missing data [182]. The inverse of the FIM is then the variance-covariance matrix Ω and the parameter variances can be calculated.

The MlxTran model files for use in Monolix 2018R2 for each experimental chapter (Chapter 3, 4 and 5), can be found in Appendix F, whilst the data (in .csv) format can be found in the online version of the thesis.

2.4.5.1 Optimal Design of Experiments

For each of the experimental chapters (Chapters 3-5), the timepoints taken, as well as the number of concentrations were based on the assumption that each is a hydrophilic anion at physiological pH and thus substrate for transporter into the cell. As discussed above (see Section 2.1), the uptake into the cells is slower than more lipopilic substrates [32, 33] and therefore timepoints tend to be weighted towards the beginning of the experiment to capture the initial uptake into the cell, whilst metabolism dominates at later timepoints. The choice of experimental timepoints are therefore based on prior literature and personal experience, which may offer a sub-optimal experimental design to reduce the residual error on the estimation of parameters and thus the practical identifiability of the parameters.

To prospectively design experiments to maximise the information obtained through the choice of timepoints, assuming that the mechanistic model used is correct, is known

as *Optimal Design* [191]. Optimal design of experiments are becoming more common in pharmacometrics modelling, where, based on literature or past experience, prospective timepoints can be selected for new clinical trials, for example when timepoints are limited due to invasiveness e.g. in neonates or young infants or for practicality e.g. in Phase III trials [191, 192]. There are multiple optimality algorithms that take advantage of the inverse of FIM which gives the covariance matrix [193], with the maximisation of the derivative of the FIM, termed *D-optimality* as the most relevant to this work. There are multiple software packages and stand alone functions that can be used for D-optimal design experiments, based in R (PFIM [194]), Matlab (PopDes [191]) or both (PopED [195]). Stromberg et al. [193] evaluated these approaches through simulation of 3000 individuals based on the optimal design. The approaches used either a full covariance matrix (makes no assumptions regarding covariance between parameters) or a triangular matrix (assumes no covariance between parameters), as well as the use of either a first order linearisation (FO) algorithm or the first order conditional expectation linearisation (FOCE) algorithm [193].

2.5   In Vitro-In Vivo Extrapolations/Correlations

The fate of a drug within the body will largely depend on its physical attributes - molecular weight, lipophilicity, and the level to which it is charged or not at physiological pH (pH 7.4). These attributes can be calculated from the structure of the drug itself such as the pK_a value, which describes the pH at which 50 % of the drug is unionised, or determined via a variety experiments.

One way to compare across the diverse chemical structures of drugs in the clinic in terms of their physical attributes, and then segment them accordingly uses a system such as the Biopharmaceutics Classification System (BCS). The BCS segments drugs according to permeability and solubility [196]. An extension of this, the Biopharmaceutics Drug Disposition Classification System (BDDCS) was based on metabolism and solubility, as these were more likely to be routinely measured in a drug-discovery context [197]. The BDDCS was then further modified to segment according to transporters [198]. Both the BCS and BDDCS are powerful (1000's of compounds) yet basic in their approach in order to understand and extrapolate from *in vitro* measurements up to the *in vivo* or the clinical situation.

If *in vitro* inhibition with liver transporters and enzymes, has the potential for a relevant drug-drug interaction (DDI) in the clinic, an area under the curve (AUC) ratio in the presence or absence of the inhibitor can be calculated, the 'R' value as described earlier (Eq. 2.1). This is used by regulatory agencies in their *in vitro* guidance documents [18, 19] to assess the potential for clinical DDIs and is described in more detail in Chapters 3 and 5.

To scale *in vitro* data obtained from cellular systems up to whole body requires the use of scaling factors, e.g. from human hepatocytes up to a full liver via hepatocellularity factors (from 1×10^6 cells up to /g liver [181]) and physiological weights (g of

liver/kg body weight [2, 133]). The scaled organ can then be linked to other organs of interest/importance via knowledge of the physiology of each organ (volume, blood flows, partition into tissue - physicochemical properties etc.) to obtain an approximation of the whole body. This type of representation is known as Physiologically Based Pharmacokinetic (PBPK) modelling and is an oversimplification of the underlying processes, but can give valuable information regarding the disposition of a drug in the body and the potential for DDIs. An example of a qualitative PBPK model developed to examine the interaction at the liver as the organ of interest based on uptake into hepatocytes can be seen in Fig. 2.6 and Chapter 6.

2.6   Conclusions

This chapter gives an outline on the current literature with regards to transporter mediated uptake and TrDDIs. It shows the issues that can arise when predicting clinical interactions based on *in vitro* data, and may partly be due to the large degree of overlap in transporter affinities for substrates. However, this may also be due to the redundancy built into some of the transporters in the body to protect the sanctuary organs, which are then capitalised on by tumours and microbes.

Secondly this chapter is the basis for the data analysis and experimental techniques used in the following chapters to evaluate *in vitro* drug-drug interactions across two systems of increasing complexity: the first examining a single solute carrier (hOATP1B1) over expressed in a human derived cell-line (HEK293); with the following two chapters looking at hepatocytes in rats and humans respectively. Therefore, in Chapters 3-5 the experimental techniques are similar, as we are looking at the inhibition of uptake of a substrate into cells with early timepoints important in the determination of uptake. This makes the mechanistic modelling processes the same for the determination of TrDDIs, with additional transport-metabolism interplay and drug-drug interactions in hepatocytes.
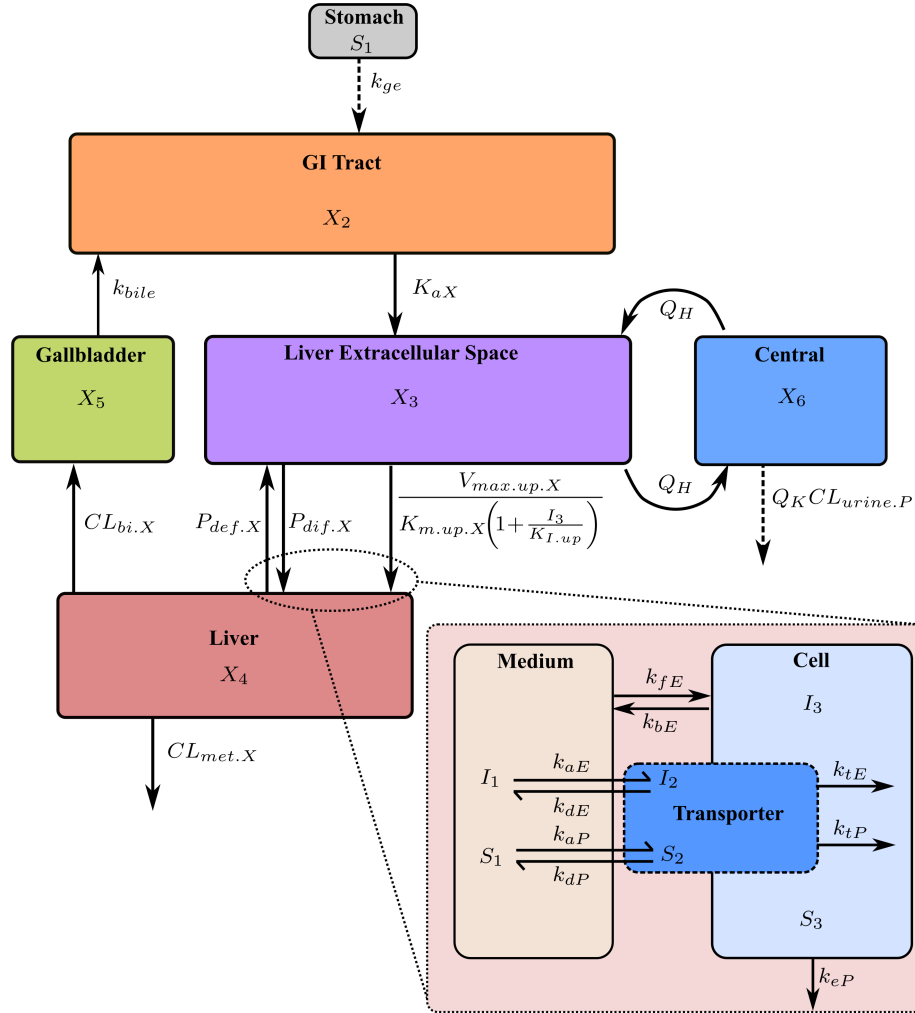
Figure 2.6: Schematic of the developed semi-mechanistic PBPK model for the concentrations in the liver compartment (X_4) assumed to be involved in the TrDDI between pitavastatin and eltrombopag, which is linked to the concentration in the central compartment (X_6) via the concentration in the liver extracellular space (X_3) through hepatic blood flow (Q_H). The dose is applied as an amount into the stomach (X_1), which is then transported into the GI Tract (X_2) with gastric emptying rate constant (k_{ge}). Drug is absorbed into X_3 with the absorption rate constant (K_{aX}), where free drug moves into the liver via saturable Michaelis-Menten kinetics $(V_{max.up.X}$ and $K_{m.up.X})$ and is inhibited by the opposing drug in X_3 (I_3) via the K_m $(K_{I.up})$. Passive movement of drug into and out of the liver with clearances $P_{dif.X}$ and $P_{def.X}$ respectively. Biliary excretion of both drugs $(CL_{bi.X})$ into X_2 through the gallbladder (X_5) with bile flow rate constant (k_{bile}) where they can be re-absorbed. Both drugs have metabolic clearance from the liver $(CL_{met.X})$, whilst pitavastatin is also cleared into the urine $(CL_{urine.P})$ with the kidney blood flow (Q_K)

38

Chapter 3

Evaluation of Uptake of 2',7'-dichlorofluorescein and its Inhibition by Gemfibrozil in HEK293-OATP1B1 Cells

3.1   Introduction

This chapter deals with the uptake of the fluorescent probe substrate 2',7'-dichloro-fluorescein (DCF) in HEK293 cells expressing the human OATP1B1 transporter protein, and the determination of the inhibition by the anti-diabetes drug gemfibrozil. The experimental work was conducted at AstraZeneca Cambridge (U.K.) as part of my PhD studentship and has previously been submitted as a short communication to *The Journal of Pharmaceutical Sciences*. Therefore this chapter will, following a brief overview, evaluate the mechanistic models used in terms of their structural and practical identifiability across different software approaches (see Chapter 2, Section 2.4 for theory and use of software) and provide an in-depth presentation of model parameter estimation and model selection.

Gemfibrozil is used to treat hyperlipidaemia either in monotherapy or in combination with a statin [199], and in type II diabetes with repaglinide [200]. A study in healthy volunteers co-dosed with repaglinide and gemfibrozil showed an 8-fold increase in plasma exposure, as well as a prolonged glucose lowering effect [200]. A similar picture was observed when cerivastatin was dosed with gemfibrozil with an increase in exposure of nearly 6-fold, along with a non-statistically significant increase in creatine kinase [201] - a biomarker for rhabdomyolysis, that if left untreated can lead to acute renal failure [202]. The use of gemfibrozil has been largely replaced with other fibrates that do not interact with repaglinide or statins [203, 204]. The inhibition of substrates by gemfibrozil, which is not a substrate for OATP1B1 itself [27] is multimodal, comprising:

- Metabolite-dependent inhibition of CYP2C8 from gemfibrozil-glucuronide [205].

- Inhibition of OATP1B1 by both gemfibrozil and gemfibrozil-glucuronide [135, 206].

Drug-drug interaction (DDI) studies with gemfibrozil and OATP1B1 are often conducted using a human cell line expressing the transporter with a selective radiolabelled probe substrate such as [³H]-estradiol-17β-glucuronide [135]. In early research, the use of radiolabelled probe substrates can be cost prohibitive, therefore a cheaper and selective substrate is required. Izumi et al. [168] found that DCF was a good substrate for OATP1B1, with V_{max} and K_m values similar to those of [³H]-estradiol-17β-glucuronide, the inhibition of DCF uptake by various inhibitors was the same as for [³H]-estradiol-17β-glucuronide.

There is increased interest in the evaluation of uptake inhibition mechanisms and whether the long-lasting inhibition of transporters can explain the discrepancy between *in vitro* and *in vivo* studies [207, 208]. Evaluation of time-dependent inhibition of selected transporters is also now recommended as part of new drug submissions to the regulatory authorities [18, 19]. Whilst the inhibition of selective substrates by gemfibrozil in HEK293-OATP1B1 has been conducted under the assumption of competitive inhibition [27, 135, 168], the mode of inhibition has not been fully evaluated and will be the aim of this chapter. This aim will be achieved through the following objectives:

- Evaluate the uptake of DCF into HEK293-OATP1B1 cells and its inhibition by gemfibrozil to evaluate whether time-dependent inhibition dominates across three inhibition scenarios (see below).

- Develop mechanistic models to describe the interaction between DCF and gemfibrozil via competitive (non-time dependent) or non-competitive (time-dependent) inhibition to gain further understanding of OATP1B1 uptake transporter interactions.

This was examined experimentally using the following scenarios (see Fig. 3.1):

1. Co-incubation of 1 μM DCF with a range of gemfibrozil incubation concentrations (1-300 μM).

2. Pre-incubation of gemfibrozil (1-300 μM) for 20 min, removal of gemfibrozil and then scenario 1.

3. Pre-incubation of gemfibrozil (1-300 μM) for 5-40 min, removal of gemfibrozil and then incubation with DCF only at 1 μM for 6 min.

3.2 Experimental Methods

3.2.1 Chemicals and Reagents

2,7-dichlorofluorescien (DCF), gemfibrozil, Hanks buffered salt solution (HBSS), high glucose Dulbeccos modified essential medium containing L-glutamine (DMEM, D6429), phosphate buffered saline, Accutase, Triton X-100, geneticin (G418),

HEPES and the BCA protein assay kit (BCA-1) were all purchased from Sigma-Aldrich (Poole, UK). Fetal bovine serum (FBS, heat inactivated) was purchased from Gibco (Thermo Fisher Scientific Inc., Loughborough,UK). Acetonitrile, was obtained from VWR International Ltd., (Lutterworth, UK) and was of analytical grade. HEK293-OATP1B1 and HEK293-MOCK cells were generated by the Department of Molecular Biology, AstraZeneca, UK and were the same cell line as used by Sharma et al. [167].

3.2.2 Cell Culture

Culture of HEK293-OATP1B1 and HEK293-MOCK cells were similar to those used by Sharma et al. [167]. Briefly, cells were cultured in DMEM containing 10 % FBS and 1 mg/ml geneticin as a selection antibiotic in 75 cm^2 or 175 cm^2 BD Biocoat^{TM} Collagen I cell culture flasks (VWR International, Lutterworth, UK) at 37 °C in a humidified 5 % CO_2 incubator and were maintained at sub-confluency by splitting twice weekly in the ratios 1:2 to 1:6 dependent on cell density. Cells were cultured in 24-well Corning® Biocoat^{TM} Poly-D-Lysine plates for 20-72 h prior to uptake studies following the addition of a fixed amount of cells (2.5×10^5 cells) [167].

3.2.3 Incubations

DCF was dissolved and serially diluted in DMSO to give stock solutions of: 40, 12, 4, 1.2, 0.4 and 0.12 μmol/ml. For the DCF only incubations, the stock solutions were added to an equal volume of DMSO and then diluted 1 in 200 in modified HBSS (supplemented with 5 mM HEPES, adjusted to pH 7.4) and maintained at 37 °C in a deep well 96-well plate until required to give final concentrations of: 100, 30, 10, 3, 1 and 0.3 nmol/ml. For the inhibition studies, gemfibrozil was dissolved in DMSO and serially diluted in DMSO to give the following stock solutions: 120, 40, 12, 4, 1.2 and 0.4 μmol/ml. For the pre-incubation arm, the gemfibrozil stock solutions were diluted 1 in 400 with modified HBSS to give final concentrations: 300, 100, 30, 10, 3 and 1 nmol/ml. For the co-incubation arm (with or without pre-incubation), the gemfibrozil stock solutions were diluted with an equal volume of 0.4 μmol/ml DCF and then diluted 1 in 200 with modified HBSS. The DMEM was aspirated, and after a pre-incubation for 20 min in modified HBSS at 37 °C, the medium was replaced with 0.3 ml HBSS containing gemfibrozil and pre-incubated for 20 min as required. The DMEM was removed and 0.3 ml of DCF (with or without gemfibrozil) was added using a multichannel pipette in duplicate (see Fig. 3.1 for experimental workflow). For DCF alone and the co-incubation with gemfibrozil scenarios (with or without pre-incubation), the medium was aspirated at pre-defined timepoints (20, 40, 60 and 80 s, then 3 and 6 min (co-incubation only)) and washed three times with ice cold HBSS and left to dry. For the pre-incubation only scenario, cells were pre-incubated for 5, 10, 20 or 40 min with gemfibrozil (1-300 nmol/ml), the medium was removed and 1 nmol/ml DCF incubated for 6 min before aspiration and treated as above. Four independent sampled wells were taken for each datapoint, with six independent sampled wells used for the pre-co-incubation scenario.
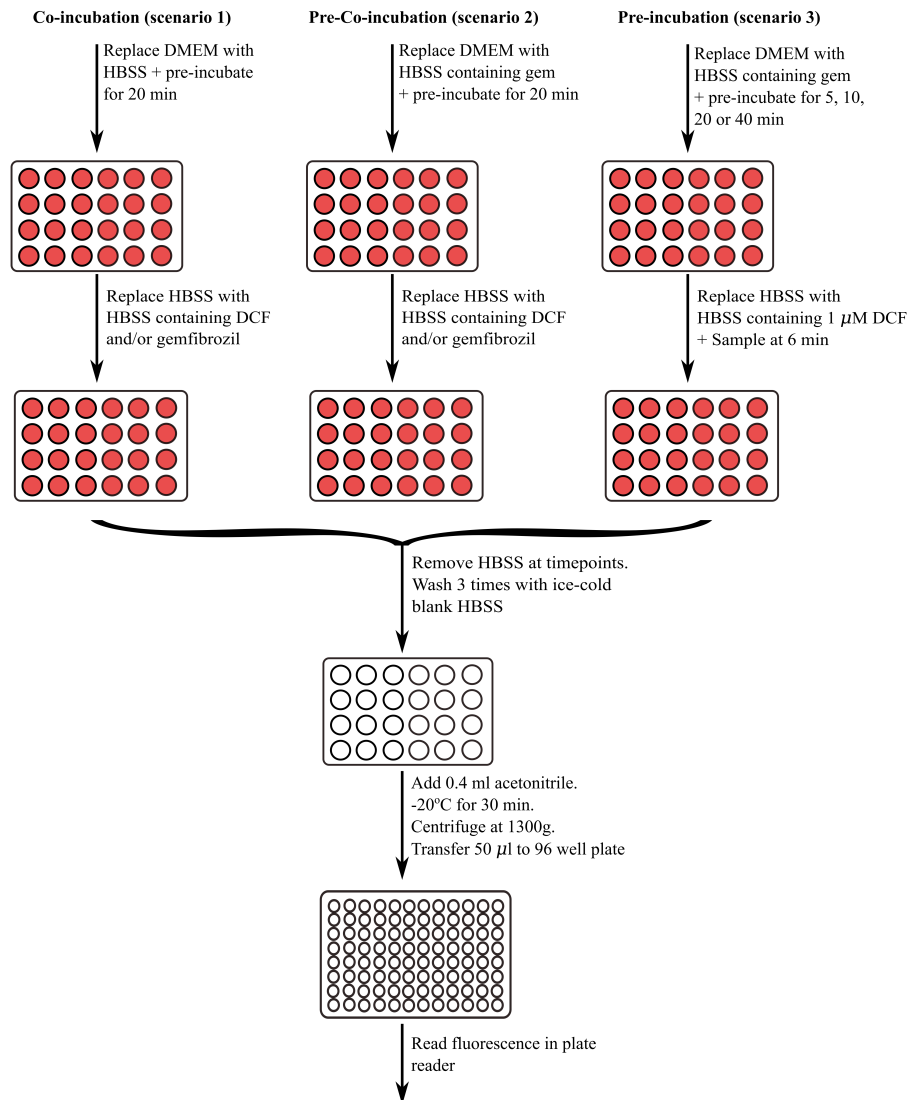
Figure 3.1: Schematic of experimental workflow in HEK293-OATP1B1 and HEK293-MOCK cells for inhibition scenario's 1, 2 and 3. In each case the cells are already plated onto the 24-well culture plates

3.2.4   HEK293-OATP1B1 Cellularity

To enable a standard volume parameter for HEK293 cells to be used in the mechanistic models, the concentration of DCF within the cell was normalised to nmol/ml/10^6 cells from pmol/ml/mg protein for both HEK293-OATP1B1 and HEK293-MOCK cells. Following treatment with Accutase$^{®}$ (5 ml per flask), HEK293 cells were taken from >3 flasks, and centrifuged at 70 g for 10 min at 5 °C in 50 ml Falcon tubes (BD VWR International, Lutterworth, UK). The cells were re-suspended in 20 ml in HBSS, counted and diluted in water to give between 3 and 0.05 $\times 10^6$ cells/ml. These were then mixed 1:1 with Triton X-100 and shaken at room temperature for 30 min. Bovine serum albumin (BSA) protein standards were prepared in 1:1 water:Triton X-100 and used as per the manufacturers instructions (BCA protein assay kit instructions, Sigma-Aldrich). Briefly, a 1 mg/ml ampoule of BSA was diluted in 1:1 water Triton X-100 to give a BSA concentration range of 25-1000 μg/ml, 0.1 ml of standard or cell lysate was added to 2 ml of bicinchoninic acid (BCA) working solution, mixed gently and incubated for 30 min at 37 °C. 0.1 ml was then placed in triplicate onto a 96-well plate suitable for spectrophotometry and read in an OPTIMA POLARstar plate reader (absorbance: 560±10 nm, BMG LABTECH Ltd., Aylesbury, UK) on three separate occasions. The cellularity measurements for HEK293-OATP1B1 and MOCK cells were then used to estimate the total amount of OATP1B1 receptors, which could then be compared to the total number of OATP1B1 transporters (T_o) obtained from the mechanistic models during parameter estimation:

$$\text{Total OATP1B1 (nmol/}10^6\text{cells)} = \frac{\left(\frac{\text{(OATP1B1 - MOCK)/1000}}{85000} \right)}{1,000,000} \tag{3.1}$$

where 85000 is the molecular weight of OATP1B1 in Daltons [101], and 1000 and 1,000,000 scale from mg/10^6 cells to nmol/10^6 cells

3.2.5   Sample Extraction and Data Analysis

0.4 ml of ice cold acetonitrile was added to each well and placed in a -20 °C freezer for $\geq$ 30 min to extract DCF from the cells. The 24-well plates were then centrifuged at 1300 g for 15 min at 5 °C and 0.05 ml of the supernatant was diluted with 0.15 ml water in a 96 well plate suitable for fluorescence measurement. A standard curve for DCF was made by serially diluting a 1000 pmol/ml DCF DMSO stock in 80:20 water:acetonitrile to give: 100, 10, 1 and 0.1 pmol/ml. The standard curve was pipetted in triplicate onto a 96 well plate suitable for fluorescence measurement and read in an OPTIMA POLARstar plate reader (excitation: 485±12 nm, emission: 520 nm, BMG LABTECH Ltd., Aylesbury, UK). The standard concentrations were determined from fitting to a straight line ($y = mx$) of the standard curve following blank well subtraction (80:20 water acetonitrile). Inclusion of an intercept in each equation lead to an increase in the % relative mean square root error (RMSRE, Eq. 3.2) of the predicted standard

concentrations from 2-3 % to 39-42 % respectively.

$$\% \ RMSRE = 100 \times \sqrt{\frac{1}{n} \sum \left(\frac{Observed_i - Predicted_i}{Observed_i} \right)^2}. \tag{3.2}$$

Sample concentrations were determined following blank subtraction and normalised from nmol/ml/ mg protein to nmol/ml/10^6 cells using:

$$\text{[Cell] (nmol/ml/mg protein)} = \frac{\left(\frac{\text{(mean DCF fluorescence - mean blank)} \times 5}{m} \right)}{\text{mg/ml protein} \times 1000} \tag{3.3}$$

and

$$\text{[Cell] (nmol/ml/}10^6 \text{ cells)} = \frac{\text{[Cell] (nmol/ml/mg protein)} \times \text{cellularity}}{V_{cell}} \tag{3.4}$$

where 5 and 1000 scale from 0.2 ml to 1 ml and from pmol/ml to nmol/ml, 'cellularity' converts from mg/ml protein to 1×10^6 cells, and V_{cell} is the cellular volume. As multiple cell volumes have been published (see Chapter 2, Table 2.3) [176, 178], data were normalised to 0.002 ml/10^6 cells [176], 0.004 ml/10^6 cells [178] or the median (0.003 ml/10^6 cells). Parameters were estimated for all the DCF data using a micro-rate constant model with two passive rate constants and transporter mediated uptake (see Table 3.1 Eqs. 3.17, 3.19 and 3.21, without inhibition, with observations from Eq. 3.28), using the inverse of each cell volume (see 3.28) and with the weighted BIC ($wBIC$, Eq. 3.39) used to distinguish which volume best described the data. An inverse V_{cell} of 333 /ml, corresponding to the median literature value of 0.003 ml/1×10^6 cells had the lowest BIC of the three inverse volumes tested, giving a $wBIC \approx 1$, whilst the volume from Boss et al. [176] and the volume from Gillen and Forbush [178] had a $wBIC \sim 0$ (see Chapter 2, Table 2.3). Therefore all data were normalised to 0.003 ml/10^6 cells (with an inverse of 333 /ml).

3.3   Mechanistic Modelling

Grandjean et al. [8] published a three compartment mechanistic model to describe the uptake of pitavastatin into hepatocytes (see Fig. 3.2) with first order passive rate constants for movement into and out of the cell (k_f and k_b respectively). A second order rate constant for association of substrate (k_a) to free transporter (T_f), and first order rate constants for dissociation from transporter (k_d) and translocation from the transporter into the cell (k_t) were also included. In this and future chapters, mechanistic models of this form for substrate with or without inhibitor, will be referred to as *micro-rate constant models* (see Fig. 3.3a and b) and Table 3.1). If the formation of substrate bound to transporter (S_2) is very rapid ($k_a >> k_d > k_t$) and the total amount of transporter (T_o) is small in comparison to the amount in the medium (S_1), then the micro-rate constant model can be reduced assuming a pseudo-steady state to obtain the Michaelis-Menten equation (see Chapter 2, Section 2.4.4 in this and future chapters, see Fig. 3.3c and d)
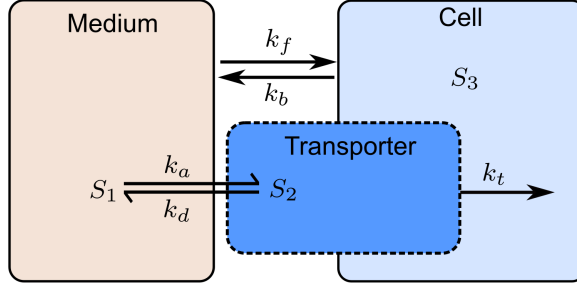
Figure 3.2: Modified schematic of the micro-rate constant model published by Grandjean et al. [8] of ODEs derived for initial parameter estimates for DCF uptake into HEK293-OATP1B1 cells (see Table 3.1, model 1 - gemfibrozil excluded). S_1, S_2 and S_3 are the amount of substrate (DCF) in the medium, bound to transporter and intracellular respectively, k_f and k_b are the passive rate constants into and out of the cell respectively, k_a is the transporter association rate constant, assuming free transporters are available, k_d and k_t are the dissociation rate constant and translocation rate constant into the cell from S_2 respectively

[15].

If the transporter component of Fig. 3.2 is written in the chemical reaction form:

$$S_1 + T_f \underset{k_d}{\overset{k_a}{\rightleftharpoons}} S_2 \overset{k_t}{\rightarrow} S_3 \tag{3.5}$$

then the law of mass action gives:

$$\frac{dS_1}{dt} = -k_a S_1 T_f + k_d S_2 \tag{3.6}$$

$$\frac{dS_2}{dt} = k_a S_1 T_f - (k_d + k_t) S_2. \tag{3.7}$$

$$\frac{dS_3}{dt} = k_t S_2 \tag{3.8}$$

As it is not normally the case that T_f is known in practice, assuming that T_o is constant, then T_f can be eliminated in Eq. 3.7 [15, 25] via the conservation law:

$$T_f = T_o - S_2 \tag{3.9}$$

and

$$\frac{dS_1}{dt} = -k_a S_1 (T_o - S_2) + k_d S_2 \tag{3.10}$$

$$\frac{dS_2}{dt} = k_a S_1 (T_o - S_2) - (k_d + k_t) S_2. \tag{3.11}$$

$$\frac{dS_3}{dt} = k_t S_2 \tag{3.12}$$

If Eq. 3.11 is extended to include inhibitor (gemfibrozil, see Fig. 3.3a and b) that either competitively binds to the transporter (I_2) or forms a complex with the transporter and the substrate (un-competitive inhibition, I_3), then similar to Eq. 3.9:

$$T_f = T_o - S_2 - I_2 - I_3 \tag{3.13}$$

45

and Eqs. 3.10-3.12 are also extended to include I_2 and I_3 (see Table 3.1 for relevant inhibitor equations):

$$\frac{dS_1}{dt} = -k_a S_1 (T_o - S_2 - I_2 - I_3) + k_d S_2 - \alpha k_a S_1 I_2 + \alpha k_d I_3 \qquad (3.14)$$

$$\frac{dS_2}{dt} = k_a S_1 (T_o - S_2 - I_2 - I_3) - (k_d + k_t) S_2 - \alpha k_{aI} S_2 I_1 + \alpha k_{dI} I_3 \qquad (3.15)$$

$$\frac{dS_3}{dt} = k_t S_2 + \alpha k_t I_3 \qquad (3.16)$$

where k_{aI} and k_{dI} are the inhibitor association and dissociation rate constants and α is the unitless constant defining the type of non-competitive inhibition.

3.3.1 Structural Identifiability Analysis

As *per* Chapters 4 and 5, prior to parameter estimation, models were evaluated for structural identifiability (see Chapter 2, Section 2.4.1) using the `Identifiability Analysis` package in Mathematica 11.3. Mechanistic models using micro-rate constants (Table 3.1, models 1 and 2) and macro-rate constants (Table 3.2, models 3 and 4), with one or two passive rate constants were evaluated assuming that DCF is an OATP1B1 substrate [209], and that gemfibrozil can bind to the transporter, but is not a substrate itself [27]. The inclusion of the α term within the non-competitive inhibition micro-rate constant mechanistic model (model 2) gives an indication of the effect of gemfibrozil binding to the transporter and subsequent binding of DCF to the complex. Here a value of $\alpha < 1$ indicates that gemfibrozil decreases the binding and translocation of DCF, whilst a value of $\alpha > 1$ indicates that gemfibrozil enhances transport of DCF [210].
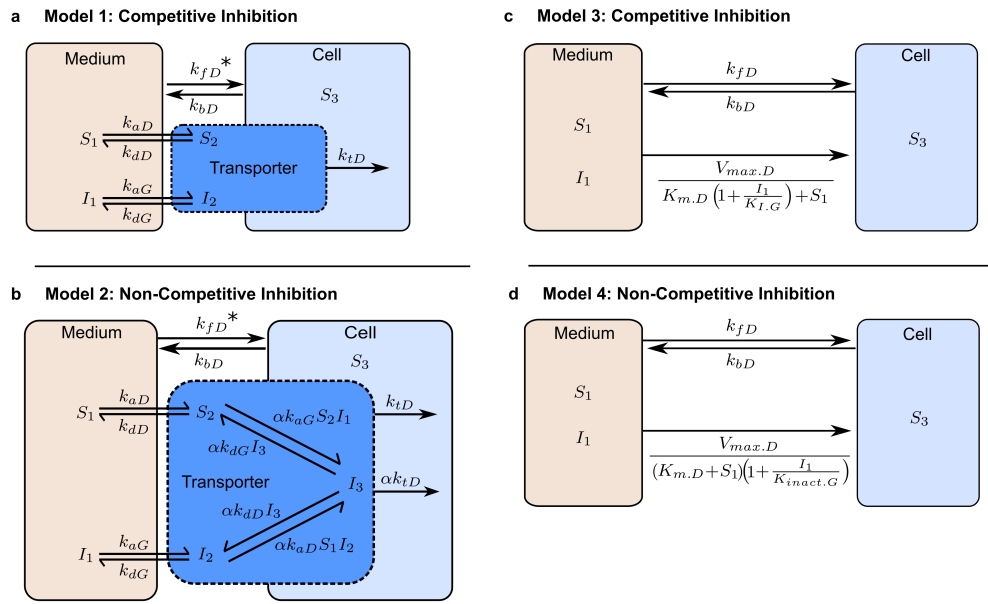
Figure 3.3: Schematic of the micro-rate constant models (a, b, Table 3.1) consisting of medium (X_1), transporter (X_2) and intracellular (X_3), and macro-rate constant models (c, d, Table 3.2) consisting of medium (X_1) and intracellular (X_2) mechanistic models. DCF following co-incubation or pre-co-incubation with gemfibrozil with competitive (**a** and **c**) and non-competitive (**b** and **d**) mode of inhibition respectively were modelled. * = for pre-co-incubation data only k_{fD} used as bidirectional passive rate constant

Table 3.1: Micro-rate constant models for competitive and non-competitive inhibition

Compartment (nmol)	Competitive Inhibition (**model 1**, Fig. 3.3a)		Non-Competitive Inhibition (**model 2**, Fig. 3.3b)	
DCF Medium (S_1)	$\frac{dS_1}{dt} = -k_{fD}S_1 - k_{aD}S_1T_f + k_{dD}S_2 + k_{bD/fD}S_3^*$	(3.17)	$\frac{dS_1}{dt} = -k_{fD}S_1 - k_{aD}S_1T_f + k_{dD}S_2 + k_{bD}S_3 - k_{aD}\alpha S_1I_2 + k_{dD}\alpha I_3$	(3.18)
DCF Transporter (S_2)	$\frac{dS_2}{dt} = k_{aD}S_1T_f - (k_{dD} + k_{tD})S_2$	(3.19)	$\frac{dS_2}{dt} = k_{aD}S_1T_f - (k_{dD} + k_{tD})S_2 - k_{aG}\alpha S_2I_1 + k_{dG}\alpha I_3$	(3.20)
DCF Intracellular (S_3)	$\frac{dS_3}{dt} = k_{fD}S_1 + k_{tD}S_2 - k_{bD/fD}S_3^*$	(3.21)	$\frac{dS_3}{dt} = k_{fD}S_1 + k_{tD}S_2 - k_{bD}S_3 + k_{tD}\alpha I_3$	(3.22)
Gemfibrozil Medium / Cell (I_1) *2	$\frac{dI_1}{dt} = -k_{aG}I_1T_f + k_{dG}I_2$	(3.23)	$\frac{dI_1}{dt} = -k_{aG}I_1T_f + k_{dG}I_2 - k_{aG}\alpha S_2I_1 + k_{dG}\alpha I_3$	(3.24)
Gemfibrozil Transporter (I_2)	$\frac{dI_2}{dt} = k_{aG}I_1T_f - k_{dG}I_2$	(3.25)	$\frac{dI_2}{dt} = k_{aG}I_1T_f - k_{dG}I_2 - k_{aD}\alpha S_1I_2 + (k_{dD} + k_{tD})\alpha I_3$	(3.26)
DCF-Transporter-gemfibrozil complex (I_3)			$\frac{dI_3}{dt} = k_{aD}\alpha S_1I_2 + k_{aG}\alpha S_2I_1 - (k_{dD} + k_{dG} + k_{tD})\alpha I_3$	(3.27)
Observations (nmol/ml)	$y_1 = \frac{1}{V_{cell}}(S_2 + S_3)$	(3.28)	$y_1 = \frac{1}{V_{cell}}(S_2 + S_3 + I_3)$	(3.29)

$X = S$ or D = DCF, or $X = I$ or G = gemfibrozil, X_1 and X_2 are the amounts in the medium and amounts bound to the transporter respectively, S_3 is amount of DCF in the cell and I_3 is the DCF-transporter-gemfibrozil complex. Unless stated, all the units for the micro-rate constants are /min/1 × 10⁶ cells, k_{fD} and k_{bD} = passive rate constant into out of the cell respectively, k_{aX}, k_{dX} and k_{tX} = transporter association (/nmol/min), dissociation and translocation into the cell respectively. T_f is the total amount of free transporters (nmol, Eq. 3.9), and α = unitless non-competitive inhibition constant. * = k_{fD} and k_{bD} for co-incubation scenario, whilst a single bidirectional passive rate constant was used for the pre-co-incubation scenario, *2 = gemfibrozil assumed to be equal in medium and intracellularly.

Table 3.2: Macro-rate constant models for competitive and non-competitive inhibition

Compartment (nmol)	Competitive Inhibition (**model 3**, Fig. 3.3)c		Non-Competitive Inhibition (**model 4**, Fig. 3.3d)	
DCF Medium (S_1)	$\dfrac{dS_1}{dt} = -k_{fD}S_1 - \dfrac{V_{max.D}S_1}{K_{m.D}\left(1+\frac{I_1}{K_{I.G}}\right)+S_1} + k_{bD}S_3$	(3.30)	$\dfrac{dS_1}{dt} = -k_{fD}S_1 - \dfrac{V_{max.D}S_1}{(K_{m.D}+S_1)\left(1+\frac{I_1}{K_{inact.G}}\right)} + k_{bD}S_3$	(3.31)
DCF Intracellular (S_3)	$\dfrac{dS_3}{dt} = k_{fD}S_1 + \dfrac{V_{max.D}S_1}{K_{m.D}(1+\frac{I_1}{K_{I.G}})+S_1} - k_{bD}S_3$	(3.32)	$\dfrac{dS_3}{dt} = k_{fD}S_1 + \dfrac{V_{max.D}S_1}{(K_{m.D}+S_1)\left(1+\frac{I_1}{K_{inact.G}}\right)} - k_{bD}S_3$	(3.33)
Gemfibrozil Medium (I_1)	$\dfrac{dI_1}{dt} = 0$	(3.34)		
Observations (nmol/ml)	$y_1 = \dfrac{1}{V_{cell}}S_3$	(3.35)	$y_1 = \dfrac{1}{V_{cell}}S_3$	(3.36)

$V_{max.D}$ and $K_{m.D}$ are the maximum uptake velocity (nmol/min) and amount at half of $V_{max.D}$ (nmol), the Michaelis-Menten constant respectively. V_{cell} is the cell volume (per 1×10^6 cells). $K_{I.G}$ is the gemfibrozil inhibition constant for competitive inhibition and K_{inact} is the non-competitive inaction constant respectively (nmol).

3.3.2 Parameter Estimation

A single passive rate constant representing movement into and out of the cell is common in the literature for macro-rate constant models, with the difference in rate only seen when the parameter is scaled via either the medium or cell volume to a passive diffusion clearance (P_{dif}) [164, 170, 173]. For the co-incubation data (scenario 1), modelling the passive movement of DCF (in the absence of gemfibrozil) through two separate rate constants as well transporter mediated uptake, decreased the BIC value by 15 compared to a single rate constant model formulation, making it the best fitting model for the given data ($wBIC = 0.999$, Eq. 3.39).

For the pre-co-incubation data (scenario 2), the use of two passive rate constants within the micro-rate constant models (models 1 and 2, Table 3.1) were not supported, with in increase in the BIC for models 1 and 2 of 35 and 37 respectively (see Table 3.4 5th and 6th ranked order), and an RSE of 500 % for the population estimate of k_{bD}. However, two passive rate constants (k_{fD} and k_{bD}) were required for the pre-co-incubation data macro-rate constant models (models 3 and 4, Table 3.2). This difference is possibly due to a lack of steady state at the final timepoint of 3 min for the pre-co-incubation scenario, compared to 6 min for the co-incubation scenario, and some loss of cells when the medium containing gembfibrozil was changed in the pre-co-incubation scenario 2.

Therefore for the co-incubation data (scenario 1), all mechanistic models used two passive rate constants for the movement of DCF into and out of the cell (k_{fD} and k_{bD} respectively, see Tables 3.1 and 3.2). For the pre-co-incubation data (scenario 2), a single passive rate constant for the movement of DCF into and out of the cell was thus used for the micro-rate constant models (models 1 and 2, designated k_{fD}, see Table 3.1), whilst the macro-rate constant models used separate rate constants for movement into and out of the cell (k_{fD} and k_{bD} respectively, models 3 and 4, Table 3.2). Incubation concentrations of DCF and gemfibrozil were converted to amounts (nmol) by multiplying by the medium volume ($V_1 = 0.3$ ml).

Initial parameter estimates were obtained for DCF only with micro-rate constants (see Fig. 3.2) using starting values of 1 in Monolix 2018R2 (Lixoft, Antony, France) for the transporter mediated parameters (k_{aD}, k_{dD}, T_o, k_{tD}) as no information was available regarding these estimates, whilst for the passive rate constants into and out of the cell (k_{fD} and k_{bD}, for the co-incubation scenario data), estimates were obtained from the HEK293-MOCK cell models (2 compartments with passive rate constants). For the macro-rate constants ($V_{max.D}$ and $K_{m.D}$) and passive rate into the cell (k_{fD}, taken from the HEK293-MOCK initial velocity), a Yamazaki plot and Lineweaver-Burke plot (Fig. 3.4a and b respectively) were used to obtain initial estimates after scaling to nmol. For both the DCF only co-incubation and pre-co-incubation data, there was very little passive uptake (see Fig. 3.4a, dotted line, 0.08 /min/1×10^6 cells), and active uptake was similar between the two datasets in the Yamazaki plot (Fig. 3.4a, solid lines), that was close to the total (Fig. 3.4a, dashed lines).

The mean calculated parameters obtained from the linear regression of the Lineweaver-
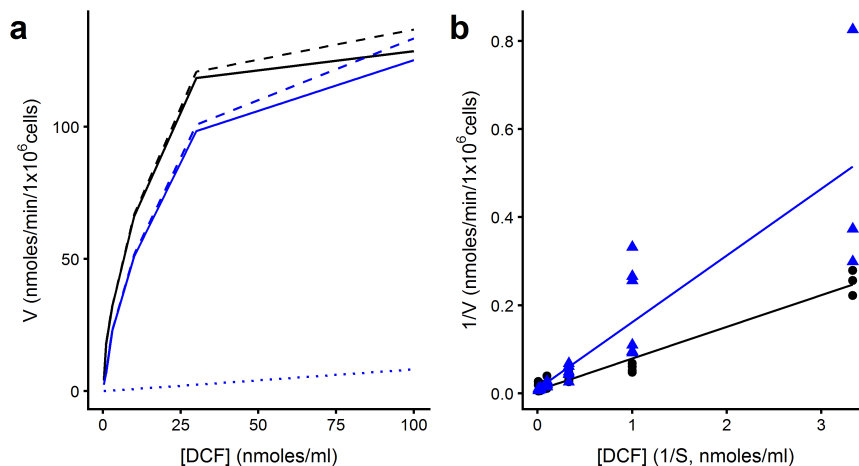
Figure 3.4: DCF concentration against initial velocity or the inverse velocity plots. Where black lines and points denote the co-incubation data for DCF only and blue lines and points denote the pre-co-incubation data for DCF only. **a** Yamazaki plot for DCF initial velocity at 0.33 min against DCF incubation concentration. Dashed line = total, dotted line = passive (obtained using the HEK293-MOCK data), solid line = saturable uptake. **b** Lineweaver-Burke plot using "Active" from **a**, where points are data and solid lines are the linear regression.

Burke plot (Fig. 3.4b, solid lines) were also similar as expected from the Yamazaki plot (V_{max} = 1/intercept = 142 (RSE = 57 %) and 102 (RSE = 176 %) pmol/min/10^6 cells, $K_m = V_{max} \times$ gradient = 10 (RSE = 57 %) and 15 (RSE = 177 %) nmol/ml, for co-incubation data and pre-co-incubation data respectively). The large errors observed in the pre-co-incubation data (see Fig. 3.4b, blue triangles) and in the Lineweaver-Burke plot estimates help to explain the difficulty in obtaining estimates for the pre-co-incubation data and will be discussed later in the chapter.

As no concentrations of gemfibrozil in the cell were measured, initial parameter estimates were obtained for DCF only, which were then used as fixed parameter estimates to help improve the robustness of the parameter estimation of the gemfibrozil rate constants (k_{aG}, k_{dG} and α). The uptake of gemfibrozil in sandwich-cultured human hepatocytes has been observed to be via passive means, and is not a substrate of hOATP1B1 [27]. Therefore, the uptake of gemfibrozil was assumed to be by passive means only and was assumed to be at steady-state in the data analysis. The simultaneous analysis of DCF in the presence of gemfibrozil for either the co-incubation or the pre-co-incubation scenarios was then undertaken with no parameters values fixed. Parameter estimates for the micro-rate and macro-rate constant models (see Table 3.1 and Table 3.2 respectively) were estimated using Monolix 2018R2 (Lixoft, Antony, France). Parameters were assumed to follow a log-normal distribution, and a proportional residual error model for the co-incubation scenario mechanistic models, and a combined constant and proportional residual error model for the pre-co-incubation mechanistic models were used.

The final chosen model was based on the weighted Bayesian information criterion (*wBIC*, Eq. 3.39) to more harshly penalise over-parameterisation within the models compared to the Akaike information criterion (AIC, Eq. 3.37) [211, 212], as well as the

sum of i individual and population prediction of the RMSRE (Eq. 3.2) given by:

$$AIC = -2.\mathcal{LL}(\theta) + 2p \tag{3.37}$$

and

$$BIC = -2.\mathcal{LL}(\theta) + log(n)p, \tag{3.38}$$

where $\mathcal{LL}$ is the log likelihood of the data, n is the total number of data points and p is the number of parameters.

$$wBIC_i = \frac{exp(-0.5\Delta_i)}{\sum_i^m exp(-0.5\Delta_i)} \tag{3.39}$$

and

$$\Delta_i = BIC_i - BIC_{min} \tag{3.40}$$

where $\frac{1}{n}$ is the inverse of the total number of datapoints multiplied by the sum of the relative square error of each datapoint i. Δ_i is the difference between the individual BIC (BIC_i) and the lowest BIC (BIC_{min}) calculated using Eq. 3.40, $exp(-0.5\Delta_i)$ is the relative likelihood and $\sum_i^m$ is the sum m of individual i relative likelihoods from the mechanistic models with the same number of datapoints used for parameter estimation (in this case a total of 4 different models) [212].

Table 3.3: Structural Identifiability analysis summary of tested models, assuming known initial conditions and observations for each model

Model	Inhibition Type	Equation numbers	Initial Conditions	No. of unknowns Parameters	No. of unknowns States	Result	No. of parameters to be identifiable (d.o.f.)
		Micro-rate constant models (Table 3.1)					
1	Competitive*	3.17, 3.19, 3.21, 3.23, 3.25, 3.28	[Y,0,0,Y,0]	7-8	5	SI	0
2	Non-competitive*	3.18, 3.20, 3.22, 3.24, 3.26, 3.29	[Y,0,0,Y,0,0]	8-9	6	SI	0
		Macro-rate constant models (Table 3.2)					
3	Competitive	3.30, 3.32, 3.34, 3.35	[Y,0,Y]	8	3*2	U	1: $K_{m.D}$ or $K_{I.G}$
4	Non-competitive	3.31, 3.33, 3.34, 3.35	[Y,0,Y]	8	3*2	U	1: $V_{max.D}$ or $K_{inact.G}$

d.o.f. = degrees of freedom, * = with k_{fD}, or k_{fD} and k_{bD}, *2 = $\frac{dx_3}{dt} = 0$, Y = positive integer, SI = structurally identifiable (local), U = unidentifiable.

Table 3.4: Goodness of fit value comparison for micro and macro parameter models for the uptake of DCF with inhibition after co-incubation with gemfibrozil (scenario 1) or pre-co-incubation with gemfibrozil (scenario 2)

Rank order*	Model Number	Model Type	Inhibition Type	BIC (wBIC)	% RMSRE (Ind + Pop = total)
			Co-incubation		
1	1	Micro rate	Competitive	1540 (1)	49 + 62 = 111
2	2	Micro rate	Non-competitive	1560 (0)	49 + 63 = 112
3	3	Macro rate	Competitive	1600 (0)	58 + 72 = 130
4	4	Macro rate	Non-competitive	1601 (0)	59 + 73 = 132
			Pre-co-incubation		
1	1*2	Micro rate	Competitive	1242 (0.93)	50 + 74 = 123
2	2*2	Micro rate	Non-competitive	1250 (0.02)	49 + 67 = 116
3	3	Macro rate	Competitive	1249 (0.03)	52 + 107 = 159
4	4	Macro rate	Non-competitive	1249 (0.03)	53 + 112 = 165
5	1	Micro rate	Competitive	1277 (0)	47 + 76 = 123
6	2	Micro rate	Non-competitive	1287 (0)	46 + 72 = 116

* = Based on wBIC (Eq. 3.39) and total % RMSRE (Eq.3.2). *2 = single bidirectional passive rate constant.

3.4   Results and Discussion

3.4.1   Structural Identifiability Analysis

The use of micro-rate constants representing competitive and non-competitive inhibition in mechanistic models for the uptake of DCF and its inhibition by gemfibrozil (Table 3.1, models 1 and 2 respectively) allowed the mechanistic models to be at least structurally locally identifiable given a known input and observations using the `Identifiability Analysis` package [16, 160]. The structural identifiability result was not affected by the use of a single passive rate constant for movement of DCF into and out of the cell (k_f) or separate passive rate constants for the movement of DCF into and out of the cell (k_f and k_d respectively, see Table 3.3).

For the macro-rate constant competitive inhibition and non-competitive inhibition models to be identifiable (see Table 3.2 models 3 and 4 respectively), $K_{m.D}$ or $K_{I.G}$ had to be known or $V_{max.D}$ or the $K_{inact.G}$ had to be known respectively for models 3 and 4 to be at least structurally locally identifiable (see Table 3.3). Alternatively if the apparent $K_{m.D.app}$ or $V_{max.D.app}$ were used (see Chapter 2, Section 2.4.4), then models 3 and 4 were at least structurally locally identifiable.

3.4.2   HEK293-OATP1B1 Cellularity

Determination of a cellularity number for HEK293-OATP1B1 cells is important for use in mechanistic models in order to normalise across data obtained from different experimental days, as well as a method for obtaining the amount of transporter at the membrane. This is under the assumption that the difference in the amount of protein between HEK293-OATP1B1 and HEK293-MOCK cells is only due to OATP1B1 protein in the membrane. A total of 33 and 31 separate measurements on three separate days were obtained for HEK293-OATP1B1 and HEK293-MOCK cells respectively. A geometric mean value of 0.685 (RSE = 4.5 %) mg/10^6 cells and 0.620 (RSE = 3.2 %) mg/10^6 cells were obtained for HEK293-OATP1B1 and HEK293-MOCK cells respectively, which were similar to human hepatocellularity values of 0.657 mg/10^6 cells [181]. The abundance of hOATP1B1 on HEK293 cell plasma membranes has been reported in the literature to be 0.18-0.36 nmols/10^6 cells [141, 213] and 0.02 nmols/10^6 cells for the AstraZeneca cell line (Sharma, P. personal communication), once converted from fmols/μg to nmols/10^6 cells, using Eq/ 3.41:

$$\text{Literature value (nmol/10}^6\text{cells)} = \frac{\text{fmol}/\mu\text{g}}{(0.685 - 0.620)/1000}. \qquad (3.41)$$

The total amount of OATP1B1 present at the plasma membrane was calculated according to Eq. 3.1, giving 0.77 (95 % confidence interval = 0.51-1.03) nmols/10^6 cells, which was within 4-fold of that found in the literature, without having to measure hOATP1B1 through peptide analysis in crude plasma membrane fractions [141, 213].
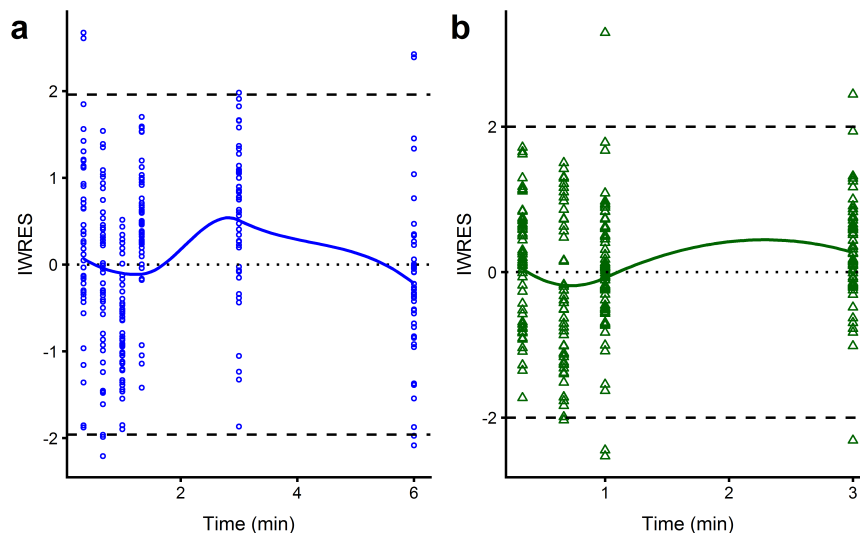
Figure 3.5: Plot of individual weighted residuals (IWRES) obtained from Monolix 2018 R2 against time for model 1. Solid line is the LOESS, dashed lines are the 95 % confidence intervals. **a** = co-incubation, blue circles = IWRES, dotted line highlights the mean IWRES of 0. **b** = pre-co-incubation, green triangles = IWRES

3.4.3 Mechanistic Modelling and Parameter Estimates

For both the co-incubation scenario 1, and the pre-co-incubation scenario 2, the best fitting model to the data based on the $wBIC$ and % RMSRE (Eqs. 3.39 and 3.2 respectively, see Table 3.4) was model 1 for competitive inhibition ($wBIC \approx 1$ and 0.93 respectively, % RMSRE = 111 % and 123 % respectively). The individual % RMSRE values were similar across all the models (49-59 %), regardless of whether micro-rate constants (model 1) or macro-rate constants (model 3) were used (see Table 3.4). The population % RMSRE values varied from 62-112 % across models with the greatest % RMSRE for the macro-rate constant models (72 and 73 % and 107 and 112 % for the co-incubation scenario 1 and pre-co-incubation scenario 2 respectively). Individual parameter estimates (mode of the conditional distribution) were therefore included in Tables 3.1 and 3.2. For the co-incubation and pre-co-incubation data, the individual weighted residuals (IWRES) locally estimated scatterplot smoothing (LOESS) line was approximately 0, with an average IWRES over the timecourse of 0.024 and 0.021 respectively, confirming that the unexplained residuals were normally distributed with a mean of 0 and symmetrical variance around zero (Fig. 3.5). The LOESS line obtained from R using the `geomsmooth` function can be misleading in this context, as the span is adjusted to fit the data (a span of 0.95 (95 % of data were used) and 1.05 were used respectively, with the latter value used to prevent a visual maximum for the pre-co-incubation IWRES data at 2 min).

For the co-incubation data (scenario 1, see Fig. 3.1), model 1 (micro-rate constant, with competitive inhibition) fitted the experimental data well for DCF alone (Fig. 3.6a, lines and shapes respectively), with saturation of uptake observed within an incubation concentration of 10-100 nmol/ml. The inhibition of 1 nmol/ml DCF by gem-

fibrozil was concentration dependent with little change up to 10 nmol/ml gemfibrozil (Fig. 3.6b, shapes), which was well described by model 1 (Fig. 3.6b, dashed lines). Non-competitive inhibition of DCF by gemfibrozil was not supported as the best fitting model, with a $wBIC \sim 0$ (see Table 3.4).

For the pre-co-incubation data (scenario 2, see Fig. 3.1), model 1 fitted the data well (Fig. 3.7a, shapes) for DCF alone across the incubation concentrations tested (Fig. 3.7a, solid lines), with saturation within 30-100 nmol/ml. Compared to the co-incubation fit, the pre-co-incubation data in the presence of increasing concentrations of gemfibrozil was more sparse (281 versus 234 datapoints used for parameter estimation respectively, with incomplete timecourses in the presence of gemfibrozil, see Fig. 3.7), with the 300 nmol/ml gemfibrozil data excluded due to insufficient fluorescence (close to background), possibly due to the added wash step prior to co-incubation of DCF with gemfibrozil. This sparseness made parameter estimation difficult, which can be seen from the ranges of BIC values between the two scenarios, where the best fitting to worst fitting model for co-incubation data (model 1 and model 4 respectively) had a Δ_i BIC of 61 (see Table 3.4), whilst for the pre-co-incubation models the best fitting to the worst fitting model (model 1 and model 2 respectively) had a Δ_i BIC of only 8. It may also be the case that the number of timepoints needed at each concentration of gemfibrozil for the pre-co-incubation scenario 2 were not sufficient to differentiate between micro-rate constant and macro-rate constant mechanistic models

Non-competitive inhibition of DCF uptake by gemfibrozil (Table 3.1 model 2, and Table 3.2 model 4) was not supported as the inhibition mechanism under either the co-incubation or pre-co-incubation scenarios 1 and 2 respectively based on the $wBIC$ (see Table 3.4). To evaluate whether there was a time dependency of inhibition to support non-competitive inhibition, gemfibrozil was pre-incubated at 1-300 nmol/ml and removed before addition of 1 nmol/ml DCF (scenario 3, see Fig. 3.1). Pre-incubation time had no effect on the uptake of 1 nmol/ml DCF, but a pre-incubation with 300 nmol/ml gemfibrozil and then 1 nmol/ml DCF was significantly different from 1 nmol/ml of DCF only ($p = 0.0017$, t-test assuming unequal variance in R using the `ggpubr` package, see Fig. 3.8). The inhibition observed at 300 nmol/ml gemfibrozil, irrespective of pre-incubation time, is likely due to the difficulty in removing all of the medium containing gemfibrozil without affecting the cell density in the well.

It is important to note, that the pre-co-incubation data were sparse in terms of full timecourses, with some of the gemfibrozil incubations only having two timepoints. This led to a large range of 268-fold difference in the parameter estimates for the transloca-tion into the cell ($k_{tD} = 1.04$ (0.05-13.4) /min/10^6 cells, model 1, Table 3.5), and a 10-fold difference in the dissociation rate constant ($k_{dD} = 0.12$ (0.06-0.81) /min/10^6 cells, model 1, Table 3.5). Therefore any conclusions drawn regarding the mode of in-hibition of DCF following pre-co-incubation with gemfibrozil when taken alone should be discounted. When the conclusions are combined with the co-incubation scenario supporting competitive inhibition, as well as a lack of difference over time in the pre-incubation scenario, it is clear that competitive inhibition alone is supported as the most
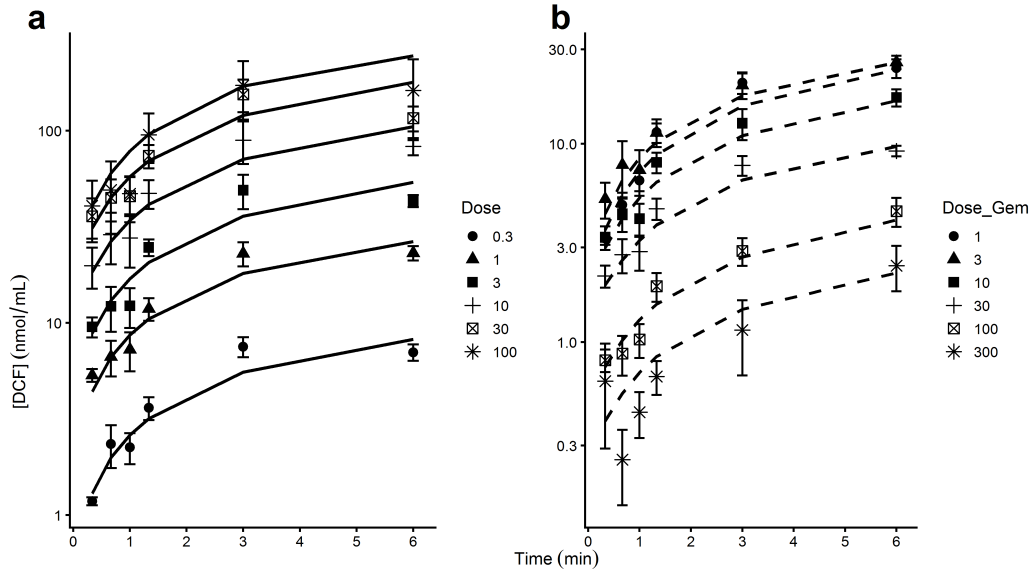
Figure 3.6: Concentration-time profile of DCF in HEK293-OATP1B1 cells. **a** following administration of DCF alone at 0.3-100 nmol/ml. **b** following co-incubation of 1 nmol/ml DCF and 1-300 nmol/ml gemfibrozil. Points are average data $\pm$ s.e.m. ($n = 4$), lines are the average of the individual fits from model 1
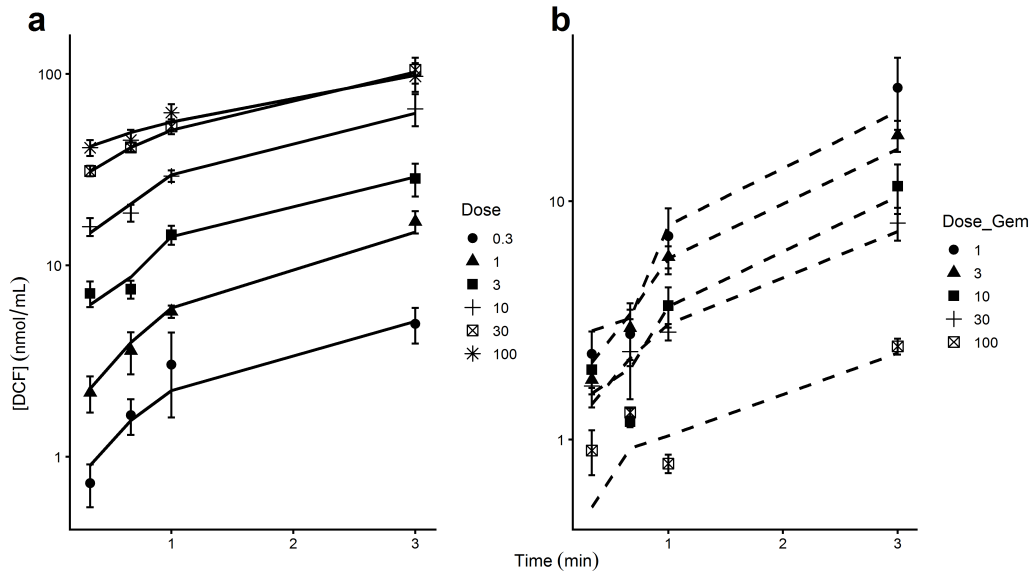
Figure 3.7: Concentration-time profile of DCF in HEK293-OATP1B1 cells. **a** following administration of DCF alone at 0.3-100 nmol/ml. **b** following pre-co-incubation of 1 nmol/ml DCF and 1-100 nmol/ml gemfibrozil. Points are data $\pm$ s.e.m. ($n = 6$), lines are the average of the individual fit from model 1 (single bidirectional passive rate constant)
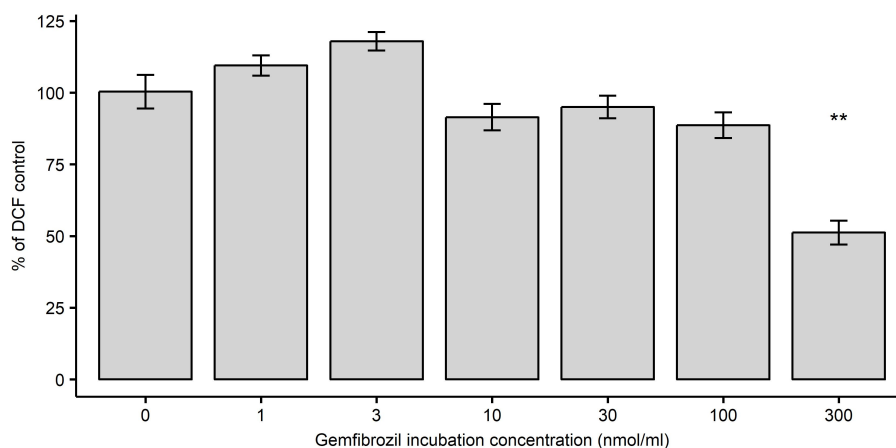
Figure 3.8: Bar chart of % of 1 nmol/ml DCF ("0") following pre-incubation of 1-300 nmol/ml gemfibrozil for 5-40 min (scenario 3). Data are the mean $\pm$ s.e.m. ($n = 16$) of all pre-incubation timepoints, as no significant difference was found between timepoints. ** $= p = 0.0017$

likely mechanism, however, if more data become available this could be re-evaluated.

3.4.3.1 Passive Rate Constants

For the micro-rate constant mechanistic models (models 1 and 2, Table 3.1), the first order passive constant for movement of DCF into the cell (k_{fD}) was similar for both inhibition experimental scenarios (model 1 as the best fitting model, Table 3.4): 0.0007 (0.0004-0.001) /min/10^6 cells and 0.0004 (0.0002-0.0008) /min/10^6 cells for the co-incubation and pre-co-incubation scenario respectively, Table 3.5). The macro-rate constant model k_{fD} (from models 3 and 4, Table 3.2) were three fold faster than the micro-rate constant model estimates for the co-incubation scenario (0.0025 (0.002-0.0033) /min/10^6 cells and 0.0024 (0.002-0.0029) /min/10^6 cells respectively, Table 3.6). For the pre-co-incubation scenario, the estimate of k_{fD} was 20-40 times faster for the macro-rate constant model (0.0066 (0.0037-0.0148) /min/10^6 cells and 0.0074 (0.0038-0.015) /min/10^6 cells respectively for model 3 and 4, Table 3.6).

Where the parameter k_{bD} was included in the mechanistic model fits (co- incubation - models 1-4, and pre-co-incubation - models 3 and 4), the parameter estimates were of the same order, ranging from 0.16 (0.1-0.22) /min/10^6 cells (co-incubation model 1, Table 3.5) to 0.5 (0.4-0.6) /min/10^6 cells (co-incubation models 3 and 4, Table 3.6). This was > 1000 times the equivalent rate out of the cell for the pre-co-incubation micro-rate constant model 1 ($k_{fD} = 0.0004$ (0.0002-0.0008) /min/10^6 cells).

The micro-rate constant estimates and macro-rate constant estimates for k_{fD} were all much less (100 and 10 fold respectively) than the HEK293-MOCK estimate (0.08 /min/10^6 cells) obtained through linear estimation (Excel Office 365, Microsoft, Washington, USA). Subtraction of HEK293-MOCK uptake from HEK293-OATP1B1 cells is common across the literature to make data analysis simpler when evaluating transporter uptake initial velocity [50, 135, 150, 209, 214, 215]. Based on the difference between the HEK293-MOCK estimate for k_{fD} and the parameter estimates described

above, may lead to false estimation of the degree of passive diffusion of a substrate. It was noted that, for estradiol-17β-glucuronide and estrone-3-sulphate, that even after MOCK subtraction, passive diffusion still had to be included in the analysis of transporter mediated uptake [214], illustrating the futility in the over-simplification of transporter mediated uptake.

3.4.3.2 Micro-Rate Constant Transporter Mediated Uptake

For the co-incubation scenario, both model 1 and model 2 had similar parameter estimates (see Table 3.5) and total % RMSRE (111 and 112 % respectively) but model 1 had the lower BIC value (1540 and 1560 respectively, Table 3.4). Association to OATP1B1 was four times faster for DCF compared to gemfibrozil ($k_{aX} = 1.89$ (1.79-1.99) /nmol/min/10^6 cells and 0.44 (0.26-0.6) /nmol/min/10^6 cells respectively, see Table 3.5), whilst dissociation from OATP1B1 was similar (5.58 (4.51-6.96) /min/10^6 cells and 3.73 (3.39-3.87) /min/10^6 cells respectively, see Table 3.5). The translocation into the cell for model 1 ($k_{tD} = 2.3$ /min/10^6 cells, Table 3.5) was similar to k_{aD}, but became the rate limiting step as the amount of DCF at the transporter increased at the point where $k_{aD} >> k_{dD}$. The total amount of OATP1B1 transporters ($T_o = 0.06$ (0.04-0.09) nmols/10^6 cells, Table 3.5) was roughly ten fold below the total estimated from the cellularity data (0.7 nmols/10^6 cells, see above), but was only three fold different to the literature values and that determined at AstraZeneca. Estimation of the T_o through mechanistic models therefore represents a more dynamic estimate than protein difference alone.

Table 3.5: Micro-rate constant individual parameter estimates for DCF following co-incubation with gemfibrozil (scenario 1) or pre-co-incubation with gemfibrozil (scenario 2). Data are the individual mode of the conditional distribution from 4 or 6 separate experiments respectively (Min-Max). All data are *per* 10^6 cells

| | Co-incubation | | Pre-co-incubation | |
	Competitive (**model 1**)	Non-competitive (**model 2**)	Competitive (**model 1**)	Non-competitive (**model 2**)
Passive				
k_{fD} (/min)*	0.0007 (0.0004-0.001)	0.0008 (0.0005-0.001)	0.0004 (0.0002-0.0008)	0.0002 (0.0001-0.0003)
k_{bD} (/min)	0.16 (0.1-0.22)	0.15 (0.1-0.17)	N/C	N/C
Transporter				
k_{aD} (/nmol/min)	1.89 (1.79-1.99)	2.95 (2.52-3.78)	0.32 (0.23-0.64)	0.36 (0.31-0.47)
k_{aG} (/nmol/min)	0.44 (0.26-0.6)	0.22 (0.14-0.39)	0.47 (0.38-0.55)	0.27 (0.22-0.36)
k_{dD} (/min)	5.58 (4.51-6.96)	4.56 (3.44-5.79)	0.12 (0.06-0.81)	0.17 (0.15-0.29)
k_{dG} (/min)	3.73 (3.39-3.87)	4.63 (2.48-5.08)	1.76 (1.47-1.96)	0.74 (0.35-1.05)
T_o (nmols)	0.06 (0.04-0.09)	0.03 (0.02-0.05)	0.11 (0.1-0.13)	0.1 (0.08-0.13)
k_{tD} (/min)	2.32 (2.21-2.39)	1.91 (1.79-2.04)	1.04 (0.05-13.4)	1.65 (0.07-10.6)
α	N/C	0.000069 (0.000061-0.000073)	N/C	0.03 (0.01-21.3)

* = single passive rate constant for pre-co-incubation data.

Table 3.6: Macro-rate constant individual parameter estimates for DCF following co-incubation with gemfibrozil (scenario 1) or pre-co-incubation with gemfibrozil (scenario 2). Data are the individual mode of the conditional distribution from 4 or 6 separate experiments respectively (Min-Max). All data are *per* 10^6 cells

| | Co-incubation | | Pre-co-incubation | |
	Competitive (**model 3**)	Non-competitive (**model 4**)	Competitive (**model 3**)	Non-competitive (**model 4**)
Passive				
k_{fD} (/min)	0.0025 (0.002-0.0033)	0.0024 (0.002-0.0029)	0.0066 (0.0037-0.0148)	0.0074 (0.0038-0.015)
k_{bD} (/min)	0.5 (0.4-0.6)	0.51 (0.42-0.58)	0.32 (0.03-5.05)	0.35 (0.03-5.06)
Transporter				
$V_{max.D}$ (pmol/min/1×10^6 cells)	217 (141-332)	232 (153-325)	127 (104-186)	116 (90.7-180)
$K_{m.D}$ (nmol/ml)*2	11.2 (10.6-11.5)	12.1 (10.2-13.4)	10.9 (6.5-13.8)	9.4 (5.7-12.2)
$K_{I.G}$ or $K_{inact.G}$ (nmol/ml)*2	31.1 (28.9-33.3)	36.7 (32.8-41.7)	18.4 (13.5-29.9)	14.1 (13.5-15.5)

* = single passive rate constant for pre-co-incubation data, *2 = scaled to nmol/ml.

Figure content (correlation/covariance matrix heatmap):

	kbD	kaD	kdD	To	ktD	kaG	kdG
kaG							0.4
ktD						0.2	0.3
To					0.5	-0.3	-0.1
kdD				-0.8	-0.5	0.3	0
kaD			-0.8	0.9	0.2	-0.4	-0.1
kbD		0.5	-0.2	0.3	-0.4	-0.7	-0.3
kfD	-0.5	0	-0.2	0.3	0.7	0.4	0.2
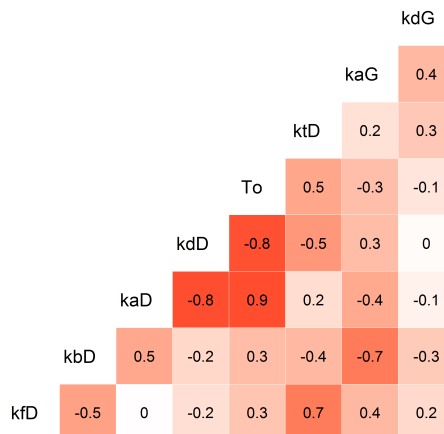
Figure 3.9: Covariance matrix of the individual random effects η for model 1 for the co-incubation scenario

The variance-covariance matrix derived from the inverse of the Fisher information matrix (obtained through linearisation in Monolix 2018R2, as the Fisher information matrix could not be obtained through the SAEM algorithm (see Chapter 2, Section 2.4.5)) [190] can be used to evaluate the practical identifiability of the model, assuming that all the unknown parameters are independent, i.e. the off-diagonal elements are zeros [184, 216].

Using the estimated individual random effects (η, taken from Monolix 2018R2) for the co-incubation data (using model 1), a covariance matrix was generated in R Studio using `GGally` [217]. There was covariance between T_o and k_{aD} and k_{bD} (Fig 3.9) which are all key parameters for the uptake of DCF into the cells, with the largest covariance of 0.9 between T_o and k_{aD}. Interestingly neither k_{aG} or k_{dG} showed this degree of covariance.

For the pre-co-incubation scenario, models 1 and 2 gave k_{aD} and k_{dD} values that were 6-10 fold and 46-26 fold less than the co-incubation values respectively (see Table 3.5). For model 1 (the best fitting model), k_{dD} varied 14-fold in the parameter estimate for scenario 2 (0.12 (0.06-0.81) /min/10^6 cells, Table 3.5). k_{tD} was similar to the value obtained for the co-incubation, model 1, but it varied 300-fold in its parameter estimate (1.04 (0.05-13.4) /min/10^6 cells, Table 3.5). k_{aG} from the pre-co-incubation scenario, model 1, was the same as the co-incubation estimate (0.47 (0.38-0.55) /nmol/min/10^6 cells and 0.44 (0.26-0.66) /nmol/min/10^6 cells respectively, Table 3.5). k_{dG} was approximately half of that obtained from the co-incubation scenario, model 1 (1.76 (1.47-1.96) /min/10^6 cells and 3.73 (3.39-3.87) /min/10^6 cells respectively, Table 3.5). The slower rates for k_{aD} and k_{dD}, coupled with a slower k_{dG} for the pre-co-incubation scenario, model 1, compared to the co-incubation scenario, model 1, would lead us to conclude that gemfibrozil is a more potent inhibitor after pre-co-incubation. Grandjean et al. [8] evaluated the uptake of pitavatatin across species in hepatocytes, for human hepatocytes where incubation concentrations were more limited compared to other species (8
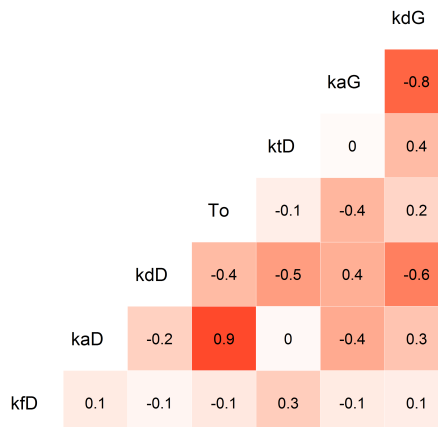
Figure 3.10: Covariance matrix of the individual random effects η for model 1 for the pre-co-incubation scenario

concentrations and 13 concentrations respectively over 4 timepoints), the errors on both k_d and k_t could not calculated [8]. This highlights the importance of obtaining sufficient data to enable accurate parameter estimations.

Using the estimated individual random effects (η, taken from Monolix 2018R2) for the pre-co-incubation data (using model 1), a covariance matrix was generated in R Studio using `GGally` [217]. Like the co-incubation parameter estimates from model 1, there was the same covariance between T_o and k_{aD} (Fig. 3.10), but not between k_{aD} and k_{dD}. Instead there was covariance between k_{aG} and k_{dG} of -0.8. Taken together more information is required to separate the covariance between k_a and k_d, or a single parameter should be used.

3.4.3.3 Macro-Rate Constant Transporter Mediated Uptake

DCF has previously been shown to be an OATP1B1 substrate with uptake 41-fold greater than in mock cells [168], with V_{max} values in the range of 128 ± 52 pmol/min/10^6 cells [168] to 172 (167-178) pmol/min/10^6 cells [150] (both converted to /10^6 cells using the cellularity value determined here) and K_m of 5.3 ± 1.5 nmol/ml [168] to 8.98 (8.14-9.83) nmol/ml [150].

The scaled $V_{max.D}$ derived from the co-incubation scenario model 1 (139 (88-215) pmol/min/10^6 cells, see Chapter 2, Section 2.4.4) was similar to the literature values above [150, 168], and similar to the values obtained from models 3 and 4 (217 (141-332) pmol/min/10^6 cells and 232 (153-325) pmol/min/10^6 cells respectively, Table 3.6). The $K_{m.D}$ estimate derived from the co-incubation scenario, model 1, (see Chapter 2, Section 2.4.4) was also similar to that in the literature [150, 168] and that obtained from models 3 and 4 (13.9 (12.5-15.7) nmol/ml, 11.2 (10.6-11.5) nmol/ml and 12.1 (10.2-13.4) nmol/ml respectively, Table 3.6).

Due to the large difference in the range of pre-co-incubation parameter estimates for k_{dD} and k_{tD}, the parameters were not scaled for macro-parameter comparison. The

$V_{max.D}$ estimates obtained from models 3 and 4 for the pre-co-incubation were similar to those for the co-incubation scenario above (127 (104-186) pmol/min/10^6 cells and 116 (91-180) pmol/min/10^6 cells respectively, Table 3.6).

The inhibition constant ($K_{I.G}$) derived from the co-incubation scenario, model 1, (28.2 (19.4-44) nmol/ml, see Chapter 2, Section 2.4.4) was the same as that for models 3 and 4 (see Table 3.6), and similar to that obtained with DCF as a substrate, and different substrates in the literature (18.1 $\pm$ 3.9 nmol/ml and 31-39 nmol/ml respectively [135, 151, 168], see Chapter 2, Table 2.2).

The $K_{I.G}$ estimates obtained from the pre-co-incubation scenario, models 3 and 4, were lower than those estimated for the co-incubation scenario, and closer to the estimate obtained with DCF as a substrate in the literature (18.4 (13.5-29.9) nmol/ml, 14.1 (13.5-15.5) nmol/ml and 18.1 $\pm$3.9 nmol/ml [168] respectively, Table 3.6).

3.5   Conclusions

This chapter attempted to evaluate the mode of inhibition of gemfibrozil on the uptake of DCF in HEK293-OATP1B1 expressing cells across different scenarios: co-incubation - used in the literature to evaluate competitive inhibition [135, 140, 215], pre-co-incubation - to evaluate competitive and time-dependent inhibition [208, 218] and pre-incubation - to evaluate lasting inhibition [218, 219]. In addition a HEK293-OATP1B1 cellularity value was obtained to aid in the mechanistic modelling of uptake through normalisation of the data to $per/10^6$ cells.

Mechanistic models consisting of rate constants (micro-rate constant models) were compared to the commonly used Michaelis-Menten reduced models (macro-rate constant models) to determine whether the increased number of parameters and states in the micro-rate constant models gave better fits to the data. The micro-rate constant model fit for the pre-co-incubation scenarios, with a large range on the transporter parameters and a reduced number of passive parameters, also highlighted the amount of data required for micro-rate constant models to obtain meaningful parameters.

Across all three scenarios (co-incubation, pre-co-incubation and pre-incubation), the competitive inhibition of DCF uptake by gemfibrozil was supported, with micro-rate constants (model 1) giving the best fits to the co-incubation and pre-co-incubation data (see Table 3.4). Non-competitive inhibition of DCF uptake by gemfibrozil in HEK293-OATP1B1 cell lines was not supported as the mode of inhibition across all three scenarios evaluated. The use of macro-rate constant mechanistic models to determine the uptake kinetics of DCF and its inhibition by gemfibrozil are not supported from both a structural identifiability perspective (unidentifiable with one degree of freedom), but also from a parameter estimation perspective, giving higher goodness of fit values when compared to the best fitting micro-rate constant models (model 3 and model 1 respectively).

Estimation of the total amount of OATP1B1 transporters from the micro-rate constant mechanistic models offers a viable alternative to measurement of hOATP1B1 from crude membranes, and was similar to the values obtained both from AstraZeneca

and the literature (3-fold difference), in addition to gaining a more in depth understanding of binding and transport and supports a mechanistic modelling approach moving forwards.

To determine whether the experimental design can be improved to decrease the covariance seen between k_a, k_d and T_o, a D-optimal design was implemented for the co-incubation data scenario with the same number of timepoints and gemfibrozil concentrations in R using `PopED` with the FO linearisation method and either a full or triangular matrix [195]. The population estimates and random variances from the combined population and individual model (ω) obtained from Monolix 2018R2. The use of the triangular matrix assuming no covariance lead to a D-optimal design with a support point at 0.33 min where duplicate samples were indicated. The use of a full covariance matrix lead to no support points and the chosen timepoints were similar to the original experimental design (0.33, 0.66, 1, 1.33, 3, 6 min). The suggested timepoints for each are given below (numbers are rounded to give realistic timepoints):

- Triangular matrix: 0.33, 0.33, 2.25, 2.75, 4.25, 6 min

- Full matrix: 0.33, 0.66, 1.33, 2, 2.75, 7 min

The following experimental chapter will take the modelling framework explored here into a more complex model of hepatocytes, where numerous transporters and enzymes are present, making good quality data across longer timecourses important.

Chapter 4

Evaluation of the Uptake and Metabolism of Atorvastatin in Fresh Rat Hepatocytes and its Inhibition by Cyclosporine A

4.1 Introduction

This chapter deals with the uptake and metabolic clearance of atorvastatin in fresh rat hepatocytes, and the inhibition of these processes by the non-selective inhibitor cyclosporine A (CsA). This chapter will determine the mode of inhibition of atorvastatin by CsA through the use of a mechanistic modelling approach. The experimental data used here, were collected during my time from UCB Pharma (Slough, UK), and their use is with the kind permission of UCB Pharma (Slough, UK). The oil-spin method described here was initially developed as part of my MSc dissertation [220], and modified with a reduction in oil temperature from 37 °C to room temperature. This work has previously been submitted to *Xenobiotica*. This chapter will, following a brief overview, evaluate the mechanistic models used in terms of their structural and practical identifiability (see Chapter 2, Section 2.4) as *per* Chapter 3 and provide an in depth presentation of model parameter estimation from experimental data.

Atorvastatin is an HMG-CoA reductase inhibitor used to treat hypercholestero-laemia, and is the third most prescribed drug in the USA [221]. Atorvastatin is taken up into hepatocytes in a concentration dependent manner with 96-98 % of the uptake as carrier mediated in rat hepatocytes [165, 172]. Uptake into hepatocytes is reported to be due to hOATP1B1 and 1B3 as determined in HEK293 cell lines, and rOatp1b2, with little or no passive uptake [135, 222, 223]. CsA is an effective immunosuppressant for use in organ transplantation, but its use is now limited due to cholestasis and nephrotoxicity [224] and has largely been replaced by immunosuppressants with less severe side effects, such as tacrolimus [225, 226]. CsA inhibits the uptake of both endogenous acids such as taurocholic acid [224] and xenobiotics such as atorvastatin [140] and pitavastatin

[208] in a competitive [140] or non-competitive manner [208], depending on whether the inhibitor is co-incubated or pre-incubated respectively (see Chapter 2, Table 2.2). CsA also inhibits CYP3A4 metabolism and P-glycoprotein [224, 225]. Statins are often dosed along with immunosuppressants in the clinic to treat the associated hypercholesterolaemia that occurs after organ transplantation, making the assessment of inhibition of statin disposition important [226, 227]. The inhibition seen *in vitro* with atorvastatin and CsA (see Chapter 2, Table 2.2) was also observed clinically in healthy volunteers with a 15-fold higher plasma exposure of atorvastatin and its metabolites compared to those on tacrolimus, with an increased risk of rhabdomyolysis in chronic patients [134].

Atorvastatin shows high intracellular binding with a determined fraction unbound in the rat hepatocytes of 0.011-0.015 [165, 228] and is metabolised by rCyp3a into two main hydroxylated metabolites, which are also found in human hepatocytes [222, 229, 230]. Disposition of CsA in rat hepatocytes has been shown to be passive with no contribution from transporters and reaches a steady state within approximately 5 min with 86 % of the initial dose associated to intracellular constituents [231]. Once within the cell there is a large degree of binding to membranes and other cellular constituents [231, 232]. Any free drug is then slowly metabolised by rCyp3a [231, 232]. The membrane binding of CsA was investigated over different incubation timescales and after 5 min most of the dose was associated with an 85 KDa protein [233], which is the same molecular weight as rOatp [234]. Shitara and Sugiyama [208] obtained parameters for the passive diffusion of CsA and then simulated timepoints with which to evaluate different inhibition sites for CsA (outside and inside) to explain the increased inhibition following pre-incubation seen in other publications [140, 235].

The aims of this chapter were:

- To describe the use a high throughput oil spin method for fresh rat hepatocytes using atorvastatin and CsA as an inhibitor.

- Develop mechanistic models to describe the interaction between atorvastatin and CsA via competitive or non-competitive inhibition of uptake and competitive inhibition of metabolism to gain further understanding of the interaction.

4.2 Experimental Methods

4.2.1 Chemicals and Reagents

Atorvastatin sodium was obtained from Sequoia Research Products Ltd (Pangbourne, UK). Cyclosporine, Percoll, high temperature silicone oil (175633), Krebs-Henseleit buffer powder (KHB,1L), sodium chloride, HEPES, collagenase (C5138) and trypan blue (0.4 %) were obtained from Sigma-Aldrich (Poole, UK). DMSO, methanol and water were obtained from Thermo Fisher Scientific Inc. (Loughborough, UK) and were of analytical grade.

4.2.2 Animals

Male Lewis rats (350-480 g) were obtained from Charles River (Margate, UK). They were housed three to a cage lined with sawdust, forage mix and shredded paper in rooms maintained at a temperature of 20 ± 2 °C with a relative humidity of 45-55 % on a 12 hour light:dark cycle with access to food and water *ad libitum*. All procedures performed were approved by the local UCB ethical review committee according to the Home Office animal procedures act (1986) by licensed individuals. Data were generated from cells isolated from three rats on different occasions.

4.2.3 Isolation of Hepatocytes

Hepatocytes were isolated using a two stage liver perfusion with collagenase as described previously [236], with the exception that collagenase was perfused at only 20-24 ml/min and not 50 ml/min to prevent undue pressure increases in the liver. Under terminal general anaesthesia with isoflurane, the liver was perfused with a calcium free-buffer (500 ml Liver Perfusion Medium, Invitrogen, Paisley, UK) at a rate of 25 ml/min in a humid 38 °C temperature controlled cabinet. The medium was then changed to modified Krebs-Henseleit Buffer (KHB, 118 mM NaCl, 5 mM KCl, 1.1 mM MgSO4, 2.5 mM CaCl2, 1.2 mM KH2PO4, 25 mM NaHCO3, 10 mM glucose supplemented with 12.5 mM HEPES (pH 7.4)) and saturated with O2/CO2, containing collagenase (0.012-0.013 % w/v). Both the Liver Perfusion Medium and modified KHB containing collagenase were kept at 38 °C in jacketed beakers and stirred and gassed continuously with 95 % O2/5 % CO2 for at least 20 min prior to use. The liver was then dissected free and transferred to ice cold modified KHB, the cells were released by the use of a cell scraper (Thermo Fisher Scientific Inc., Loughborough, UK) and filtered through 70 μm filters into 50 ml falcons (BD, Oxford, UK). The cells were centrifuged at 50 g for 5 min at 4 °C and the supernatant removed. The pellets were re-suspended in a 30:70 mixture of Percoll: modified KHB and spun at 70 g for 5 min at 7 °C. This step led to cells of high viability (> 98 %) as determined by the trypan blue (0.4 %) exclusion test with greater than 250 $\times 10^6$ cells/liver. The cells were kept on ice throughout isolation and used within 3 h of isolation.

4.2.4 Incubations

Custom-made 16-channel Teflon blocks (2 columns of 8 round-ended and bottomed troughs from Radleys, Saffron Walden, UK) were pre-incubated with 2 ml of 2 $\times 10^6$ cells/ml for 15 min, at 38.9 °C (temperature inside the Teflon blocks was 37 °C) and 109 strokes/min, placed lengthwise in an oscillating water bath (Julabo, Peterborough, UK); using this technique, cells were gently agitated to keep them in suspension, while the large interface between medium and air helped achieve adequate oxygen exchange. CsA (2 mM) was dissolved in DMSO and added during pre-incubation where required (or DMSO alone in controls), with a final concentration of 10 μM. 0.32 ml Omnistrip PCR 8-tube strips (Thermo Fisher Scientific, Loughborough, UK) were layered with

50 μl 3M NaCl and 100 μl high temperature silicone oil and placed in a 6-position PCR strip rotor in an Eppendorf 5417R centrifuge (Eppendorf, Cambridge, UK). High temperature silicone oil was chosen as its density does not change significantly between room temperature and 37 °C (1.047±0.006 g/ml and 1.043±0.004 g/ml respectively, values are mean ± SD, n=3) whilst still remaining more dense than modified KHB at 37 °C (1.024 ± 0.013 g/ml, values are mean ± SD, n=3 [220]). The difference in density at 37 °C and shape of the menisci before centrifugation (see fig. 4.1, step 2) is critical to ensure that the aqueous layers do not mix due to "flipping", and was the driving factor in miniaturising the assay [220]. Following a pre-incubation of 20 min, 10 μl of atorvastatin solution (0.05, 0.25, 0.5, 2.5, 5, 25, 50 and 150 nmol/ml final concentration) in DMSO was spiked into the Teflon blocks using an 8-way multichannel pipette. 8×100 μl samples, containing an assumed 2×10^5 cells (the minimum number of cells required to spin through the oil layer), were taken from the Teflon blocks (Fig. 4.1 step 1) at pre-defined timepoints (0.25, 0.58, 0.92, 1.25, 2.5, 5, 10, 20, 30, 40, 50 and 60 min), which were chosen based on the initial time limit of the assay, as well as the literature where the maximum of an uptake substrate is between 5-15 min [8, 33, 172]. The sample was gently pipetted down the side of the Omnistrip and immediately centrifuged for 5 s up to approximately 7000 rpm (Fig. 4.1 step 2 and 3). This was sufficient for the cells to pellet into the bottom of the 3M sodium chloride (bottom layer), and enabled the generation of a large number of samples within a short space of time (up to 384 samples in 80 min). The Omnistrips were then transferred to a 96 well matrix latch rack on ice for sample extraction (Thermo Fisher Scientific, Loughborough, UK).

4.2.5   Sample Extraction and Carryover

Within 2 h of finishing the experiment, the top medium layer and most of the middle oil layer were aspirated carefully to prevent flipping of layers leaving sufficient volume of the oil to cover the bottom layer (Fig. 4.1 step 4). The remaining bottom and middle layer were refrigerated overnight to enable easier disruption of cells. Due to the centrifugation step the menisci present before centrifugation were vastly decreased, making sample extraction more straightforward (see Fig. 4.1 steps 2 and 3). 60 μl of ice cold methanol (containing 600 nM dextromethorphan as an internal standard) was added to each tube and mixed using a multi-channel pipette on ice until the pellet was disrupted (Fig. 4.1 step 5). The matrix racks containing the Omnistrips were centrifuged at 4000 g at 5 °C for 5 min (Fig. 4.1 step 6), 50 μl of the supernatant was pipetted into a Phenomenex 2 ml deep well plate (Macclesfield, UK) and 250 μl of 40:60 methanol:water added (Fig. 4.1 steps 6 and 7). Standard curves for atorvastatin were prepared as follows: 5, 1, 0.5, 0.1, 0.05, 0.01 and 0.005 μmol/ml stocks were prepared in DMSO and then diluted by 1 in 100 in methanol giving final concentrations of 50, 10, 5, 1, 0.5, 0.1 and 0.05 nmol/ml respectively. 50 μl of this solution was then extracted as per the samples. To examine loss from the medium, 50 μl of the top layer from the latter two studies was carefully removed from the four lowest concentrations across a range of timepoints (0.25, 0.58, 0.92, 1.25, 2.5, 5, 10, 20, 30, 40, 50 and 60 min), prior
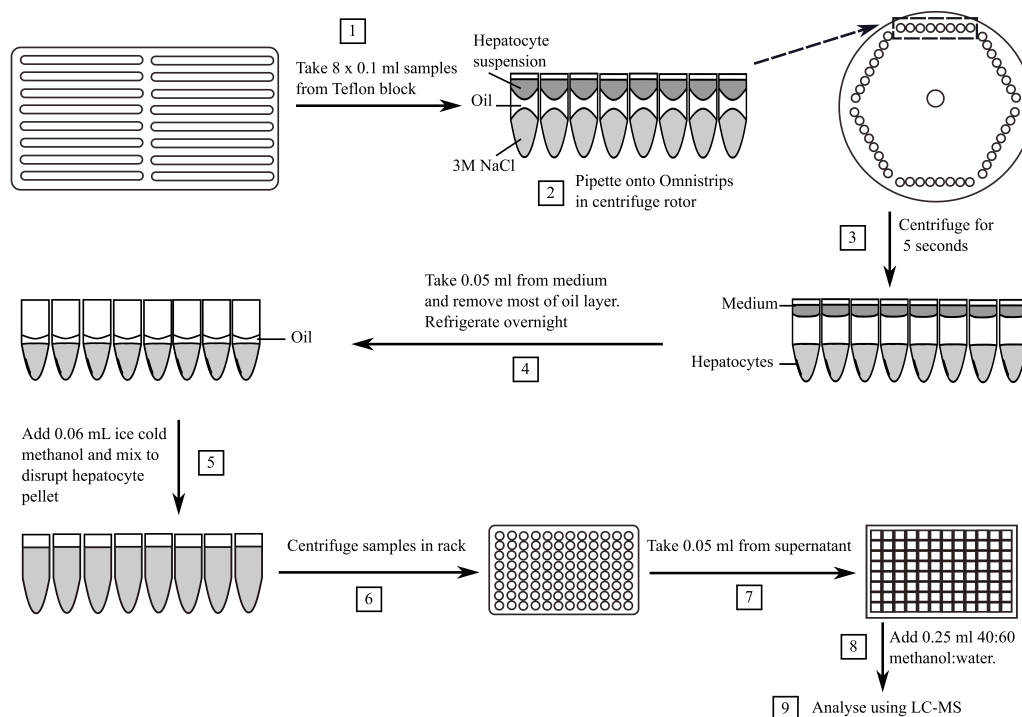
Figure 4.1: Flow chart of high throughput assay starting from incubation and separation of hepatocytes from the media via an oil spin method (steps 1-4) to extraction and analysis via LC-MS (steps 5-9). The number in the squares relates to the step number in time order as described in the Methods 4.2.4 section

to aspiration of the top and middle layer, and frozen.

To check for carry over 150 nmol/ml of atorvastatin was incubated in modified KHB in the absence of cells at 37 °C in a Teflon block. 100 μl of medium was taken and treated as per samples with hepatocytes. Carry over of atorvastatin was negligible (< 0.1 %, data not shown).

4.2.6 HPLC-Mass Spectrometry Analysis

Reconstituted samples were analysed by high-performance liquid chromatography (HPLC) high resolution mass spectrometry (HRMS) operated in positive ion mode using an Accela HPLC system and a Q-Exactive Orbitrap mass spectrometer (Thermo Scientific, Hemel Hempstead, UK). For HPLC analysis, a Luna C18 100 $\mathring{A}$ 50 x 2 mm, 5 μ column (Phenomenex, Cheshire, UK) was used with a flow rate of 0.6 ml/min at 40 °C. Mobile phase A was composed of H_2O 0.1 % formic acid, and mobile phase B was composed of acetonitrile 0.1 % formic acid. The gradient system used was as follows: initially, 20 % of B was held for 0.1 min followed by a linear gradient to 95 % of B from 0.1 to 0.8 min, 0.5 min at 95 % of B, a third linear gradient to 20 % of B at 1.3 to 1.31 min, and finally, a 0.49 min re-equilibration period at 20 % of B. Injections of 10 μl were made by a CTC Prep and Load (PAL) autosampler (CTC Analytics, Zwingen, Switzerland). For MS analysis, the capillary temperature was set at 380 °C,

the source potential was 3100 V, and the source heater was set at 350 °C. Data were acquired in centroid mode at a resolution setting of 35000 (FWHM - Full Width Half Maximum). The mass spectrometer was operated in a selected positive ion scanning mode, monitoring for the protonated masses of atorvastatin (MH559.26028) and the hydroxylated metabolites (MH575.25519) with an isolation window of 4 Da. The internal standard (dextromethorphan) was monitored at MH272.20151. The HPLC-MS data were acquired in a single run, processed and analysed using LCQuan software (version 2.7. Thermo Fisher Scientific Inc., Loughborough, UK). Atorvastatin demonstrated good linearity up to 50 nmol/ml with R2 > 0.99 and a limit of quantitation of 0.05 nmol/ml.

4.2.7 Data Analysis

The bottom layer concentration was converted to cellular concentration using a cellular volume of *per* 1×10^6 cells [170, 175]:

$$[\text{cell}] \text{ (nmol/ml)} = \frac{[\text{bottom layer}](V_b + V_{cell})}{V_{cell}} \tag{4.1}$$

where V_b is the volume of the bottom layer 3M NaCl (0.05 ml) and V_{cell} is the volume *per* 2×10^5 cells. As multiple volumes have been reported for the cellular volume (see Chapter 2, Table 2.2), initial micro-rate constant mechanistic models for atorvastatin only were evaluated with the inverse of the different volumes (0.0022-0.0065 ml *per* 1×10^6 cells [170, 174, 175]), with the weighted BIC ($wBIC$) used to distinguish which volume best described the data. An inverse volume of 906 /ml was obtained giving a volume of 0.0011 ml/2×10^5 using Eq. 4.1 obtained using an initial estimate of 0.0013 ml *per* 2×10^5 cells [170], and had a $wBIC \approx 1$ and was thus the most likely volume. The volume of 0.00078 ml/2×10^5 cells, and 0.0004 ml/2×10^5 cells calculated using Reinoso et al. [175] and Yoshikado et al. [174] respectively had $wBIC \approx 0$, and these values were therefore not used further. The volume of 906 /ml was then fixed in the rest of the parameter estimations (including macro-rate constant models). Due to the large level of extraction of atorvastatin from the media into the cell, atorvastatin could only be detected in the media in four out of twenty-four samples in the incubations at 0.05 nmol/ml, and only up to 5 min at 2.5 nmol/ml. The data from medium loss were therefore not used in any further analysis due to this sparsity (data not shown). Metabolite identification for atorvastatin was conducted qualitatively without the use of metabolite standards, therefore whilst the information is useful, it was not included in the mechanistic models.

4.3 Mechanistic Modelling

The development of a nonlinear mathematical micro-rate constant model, with the use of two rate constants to describe passive movement of substrate between the medium and cells (k_f and k_b respectively), and the movement of substrates via a transporter
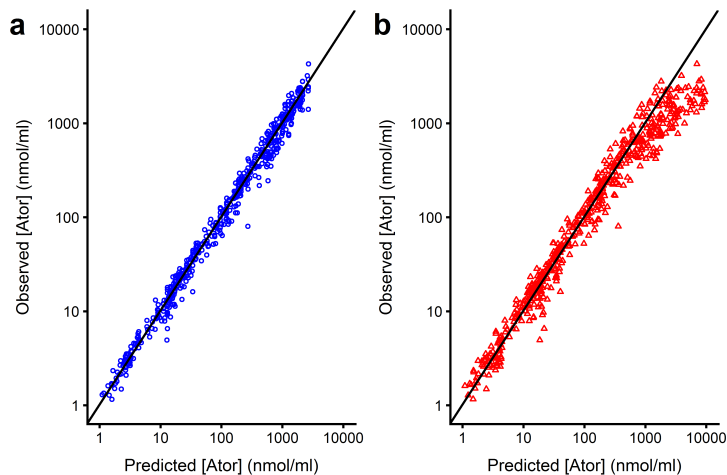
Figure 4.2: Predicted atorvastatin cellular concentration against observed individual concentration for the best fitting macro-rate constant mechanistic model, Model 3 for all data. Points are data, The black solid line represents the line of unity where observed $\equiv$ predicted

. **a** where two separate passive rate constants were used (blue circles). **b** where a single passive rate constant and fraction unbound in the cell was used (red triangles)

compartment has been published for pitavastatin [8]. Whilst Menochet et al. [173] used a single passive clearance, transporter mediated interactions via Michaelis-Menten kinetics, with the inclusion of a fraction unbound in the cell and medium and Michaelis-Menten metabolism for the phase I metabolism of repaglinide. Two separate passive rate constants (k_f and k_b) were used, as the use of a single passive rate constant with a fraction unbound in the cell led to a greater deviation of the predicted concentrations from the observed concentrations for the macro-rate constant models at higher observed concentrations compared to the use of two separate passive rates constants (see Fig. 4.2b and a respectively).

In the present study, both micro-rate constant (Table 4.1, Fig. 4.3a and b) and macro-rate constant mechanistic models (Table 4.2, fig. 4.3c and d) were evaluated for atorvastatin and its inhibition by CsA with two passive rate constants given above, and the inclusion of metabolic clearance through the Michaelis-Menten equation. As it is not normally the case that the amount of free transporters available (T_f) for the uptake of atorvastatin, assuming the total amount of transporters (T_o) are constant, then T_f can be eliminated via the conservation law derivation for transporters by adding Eqs. 4.4, 4.6, 4.8, 4.10, 4.12 and 4.13 (see previous Chapter 3 Eqs. 3.5-3.16):

$$T_f = T_o - S_2 - I_2 - I_3 \qquad (4.2)$$

where S_2 and I_2 are the amount of atorvastatin and CsA bound to transporter respectively and I_3 is the atorvastatin-transporter-CsA complex involved in non-competitive inhibition.
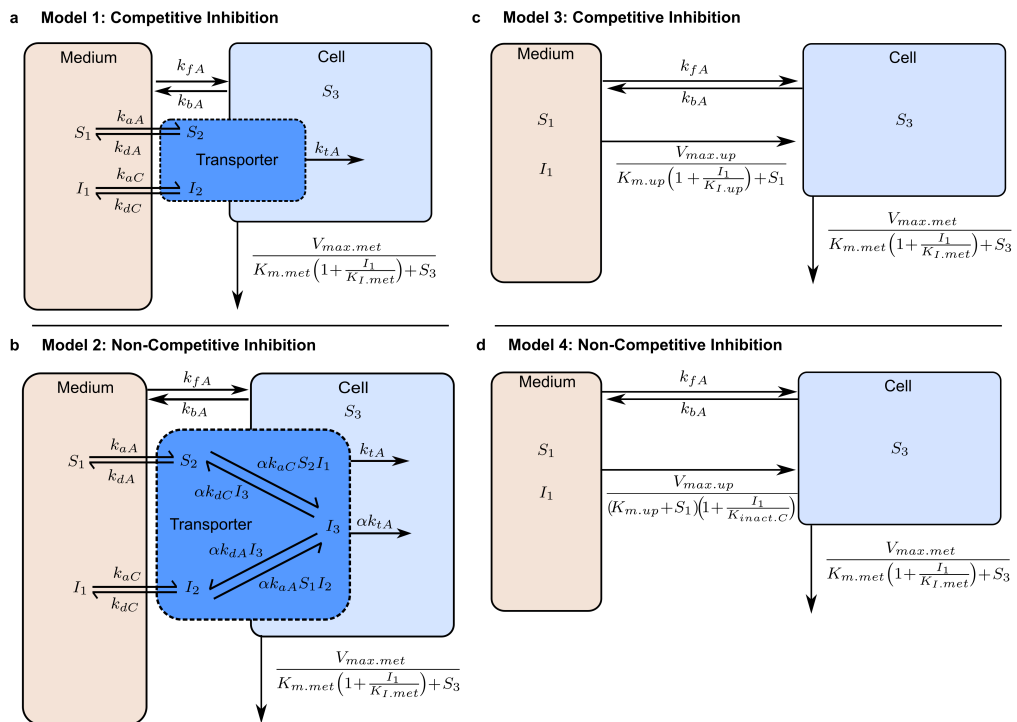
Figure 4.3: Schematic of the micro-rate constant models (Models 1 and 2, Table 4.1) consisting of medium, transporter and intracellular compartments, and macro-rate constant models (Models 3 and 4, Table 4.2) consisting of medium and intracellular compartments. Atorvastatin following pre-incubation with CsA with competitive (**a** and **c**) and non-competitive (**b** and **d**) mode of inhibition respectively were modelled

Table 4.1: Micro-rate constant models for competitive and non-competitive inhibition

Compartment (nmol)	Competitive Inhibition (Model 1, Fig. 4.3a)	Non-Competitive Inhibition (Model 2, Fig. 4.3b)
Atorvastatin Medium (S_1)	$\frac{dS_1}{dt} = -k_{fA}S_1 - k_{aA}S_1 T_f + k_{dA}S_2 + k_{bA}S_3$ (4.3)	$\frac{dS_1}{dt} = -k_{fA}S_1 - k_{aA}S_1 T_f + k_{dA}S_2 + k_{bA}S_3 - k_{aA}\alpha S_1 I_2 + k_{dA}\alpha I_3$ (4.4)
Atorvastatin Transporter (S_2)	$\frac{dS_2}{dt} = k_{aA}S_1 T_f - (k_{dA} + k_{tA})S_2$ (4.5)	$\frac{dS_2}{dt} = k_{aA}S_1 T_f - (k_{dA} + k_{tA})\,S_2 - k_{aC}\alpha S_2 I_1 + k_{dC}\alpha I_3$ (4.6)
Atorvastatin Intracellular (S_3)	$\frac{dS_3}{dt} = k_{fA}S_1 + k_{tA}S_2 - k_{bA}S_3 - \dfrac{V_{max.met}S_3}{K_{m.met}\left(1+\frac{I_1}{K_{I.met}}\right)}$ (4.7)	$\frac{dS_3}{dt} = k_{fA}S_1 + k_{tA}S_2 - k_{bA}S_3 - \dfrac{V_{max.met}S_3}{K_{m.met}\left(1+\frac{I_1}{K_{I.met}}\right)} + k_{tA}I_3\alpha$ (4.8)
Cyclosporine Medium / Cell* (I_1)	$\frac{dI_1}{dt} = -k_{aC}I_1 T_f + k_{dC}I_2$ (4.9)	$\frac{dI_1}{dt} = -k_{aC}I_1 T_f + k_{dC}I_2 - k_{aC}\alpha S_2 I_1 + k_{dC}\alpha I_3$ (4.10)
Cyclosporine Transporter (I_2)	$\frac{dI_2}{dt} = k_{aC}I_1 T_f - k_{dC}I_2$ (4.11)	$\frac{dI_2}{dt} = k_{aC}I_1 T_f - k_{dC}I_2 - k_{aA}\alpha S_1 I_2 + (k_{dA} + k_{tA})\alpha I_3$ (4.12)
Atorvastatin-Transporter -Cyclosporine Complex (I_3)		$\frac{dI_3}{dt} = k_{aC}\alpha S_2 I_1 + k_{aA}\alpha S_1 I_2 - (k_{dA} + k_{tA} + k_{dC})\alpha I_3$ (4.13)
Observations (nmol/ml)	$y_1 = \frac{1}{V_{cell}}(S_2 + S_3)$ (4.14)	$y_1 = \frac{1}{V_{cell}}(S_2 + S_3 + I_3)$ (4.15)

$X = S$ or $A = $ atorvastatin, or $X = I$ or $C = $ CsA. X_1 and X_2 are the amounts in the medium and bound to the transporter respectively, S_3 is the amount of atorvastatin in the cell and I_3 is the atorvastatin-transporter-CsA complex. Unless stated, all the units for the micro-rate constants are /min/2×10⁵ cells, k_{fX} and $k_{bX} = $ passive rate constant into out of the cell respectively, k_{aX}, k_{dX} and $k_{tX} = $ transporter association (/nmol/min), dissociation and translocation into the cell respectively, T_f is the total amount of free transporters (nmol, Eq. 4.2), $V_{max.met}$ and $K_{m.met}$ are the maximum metabolism velocity (pmol/min/2 × 10⁵ cells) and the Michaelis-Menten constant (nmol) respectively. $K_{I.met}$ is the CsA inhibition constant (nmol) and $\alpha = $ unitless non-competitive inhibition constant. V_{cell} is the cell volume *per* 2 × 10⁵ cells. * = CsA assumed to be equal in medium and intracellularly.

Table 4.2: Macro-rate constant models for competitive and non-competitive inhibition

Compartment (nmol)	Competitive Inhibition (**Model 3**, Fig. 4.3c)		Non-Competitive Inhibition (**Model 4**, Fig. 4.3d)	
Atorvastatin Medium (S_1)	$\dfrac{dS_1}{dt} = -k_{fA}S_1 - \dfrac{V_{max.up}S_1}{K_{m.up}\left(1+\dfrac{I_1}{K_{I.up}}\right)+S_1} + k_{bA}S_3$	(4.16)	$\dfrac{dS_1}{dt} = -k_{fA}S_1 - \dfrac{V_{max.up}S_1}{(K_{m.up}+S_1)\left(1+\dfrac{I_1}{K_{inact.up}}\right)} + k_{bA}S_3$	(4.17)
Atorvastatin Intracellular (S_3)	$\dfrac{dS_3}{dt} = k_{fA}S_1 + \dfrac{V_{max.up}S_1}{K_{m.up}\left(1+\dfrac{I_1}{K_{I.up}}\right)+S_1}$ $-k_{bA}S_3 - \dfrac{V_{max.met}S_3}{K_{m.met}\left(1+\dfrac{I_1}{K_{I.met}}\right)+S_3}$	(4.18)	$\dfrac{dS_3}{dt} = k_{fA}S_1 + \dfrac{V_{max.up}S_1}{(K_{m.up}+S_1)\left(1+\dfrac{I_1}{K_{inact.up}}\right)}$ $-k_{bA}S_3 - \dfrac{V_{max.met}S_3}{K_{m.met}\left(1+\dfrac{I_1}{K_{I.met}}\right)+S_3}$	(4.19)
Cyclosporine Medium (I_1)	$\dfrac{dI_1}{dt} = 0$	(4.20)		
Observations (nmoles/ml)	$y_1 = \dfrac{1}{V_{cell}}S_3$	(4.21)	$y_1 = \dfrac{1}{V_{cell}}S_3$	(4.22)

$X = S$ or $A =$ atorvastatin, or $X = I$ or $C =$ CsA, X_1 and X_3 are the amounts in the medium and the amount in the cell respectively. k_{fX} and $k_{bX} =$ passive rate constant into out of the cell respectively. $V_{max.Z}$ and $K_{m.Z}$ are the maximum velocity (pmol/min/2×10^5 cells) and the Michaelis-Menten constant (nmol), $z =$ up, uptake or met, metabolism, K_I is the CsA inhibition constant for competitive inhibition and K_{inact} is the non-competitive inaction constant (nmol). V_{cell} is the cell volume (*per* 2×10^5 cells).

4.3.1 Structural Identifiability Analysis

As *per* Chapters 3 and 5, prior to parameter estimation, models were evaluated for structural identifiability (see Chapter 2, Section 2.4.1) using the `Identifiability Analysis` package in Mathematica 11.3. Micro-rate constant models for competitive and non-competitive inhibition (see Table 4.1, Model 1, and Model 2 respectively) were evaluated assuming that atorvastatin is an uptake transporter substrate and is metabolised, and that CsA can bind to the transporter and enzyme only but is not a substrate. Macro-rate constant models for competitive and non-competitive inhibition (see Table 4.2, Model 3, and Model 4 respectively) were evaluated under the assumptions above given for the micro-rate constant models. The inclusion of the α term within the non-competitive inhibition micro-rate constant mechanistic models (Model 2) gives an indication of the effect of CsA binding to the transporter and subsequent binding of atorvastatin to the complex. Here a value of $\alpha < 1$ indicates that CsA decreases the binding and translocation of atorvastatin, whilst a value of $\alpha > 1$ indicates that CsA enhances transport of atorvastatin [210].

4.3.2 Parameter Estimation

The incubation concentrations of atorvastatin and CsA were converted to amounts (nmol) by multiplying by the sampled medium volume that holds 2×10^5 cells ($V1 = 0.1$ ml). The final chosen model was based on the weighted Bayesian information criterion ($wBIC$, Eq. 4.25) to more harshly penalise over-parameterisation (Eq. 4.24) within the models compared to the Akaike information criterion (AIC, Eq. 4.23) [211, 212]:

$$AIC = -2.\mathcal{LL}(\theta) + 2p \qquad (4.23)$$

and

$$BIC = -2.\mathcal{LL}(\theta) + log(n)p, \qquad (4.24)$$

where $\mathcal{LL}$ is the log likelihood of the data, n is the total number of data points and p is the number of parameters.

$$wBIC_i = \frac{exp(-0.5\Delta_i)}{\sum_i^m exp(-0.5\Delta_i)} \qquad (4.25)$$

and

$$\Delta_i = BIC_i - BIC_{min} \qquad (4.26)$$

Δ_i is the difference between the individual BIC (BIC_i) and the lowest BIC (BIC_{min}) calculated using Eq. 4.26, $exp(-0.5\Delta_i)$ is the relative likelihood and $\sum_i^m$ is the sum of individual i relative likelihoods from the mechanistic models with the same number of datapoints used for parameter estimation (in this case $m = 4$ different models) [212]. The final chosen model was also chosen based on the sum of i individual and population

prediction of the relative mean square root error (RMSRE) given by:

$$\% \ RMSRE = 100 \times \sqrt{\frac{1}{n} \sum \left(\frac{Observed_i - Predicted_i}{Observed_i} \right)^2}, \qquad (4.27)$$

where $\frac{1}{n}$ is the inverse of the total number of datapoints multiplied by the sum of the relative square error of each datapoint i.
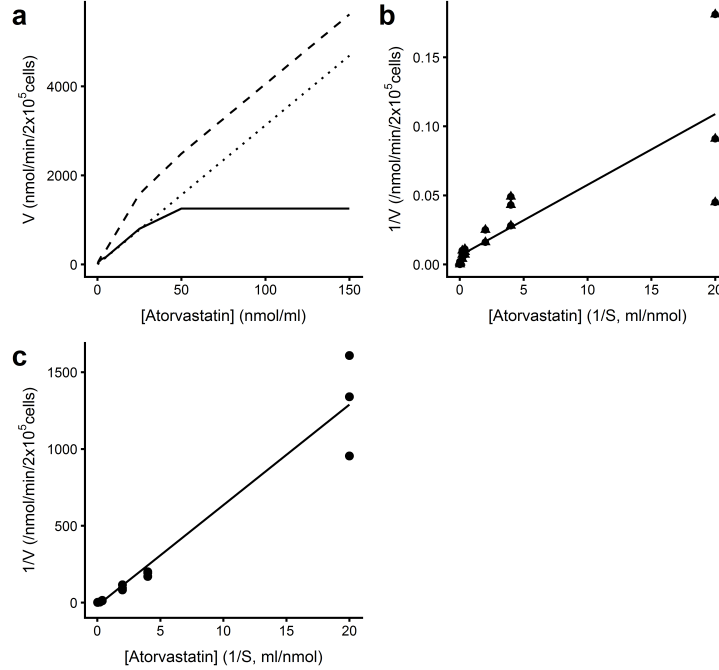
Figure 4.4: Atorvastatin concentration against velocity or the inverse of the velocity plots. **a** Yamazaki plot for atorvastatin initial velocity at 15 s against atorvastatin incubation concentration, dashed line = total, dotted line = passive, solid line = saturable uptake. **b** Lineweaver-Burke plot using "Active" from **a**. **c** Lineweaver-Burke plot for the metabolism of atorvastatin

Initial parameter estimates were obtained for atorvastatin only micro-rate constants using starting values of 1 for the transporter mediated parameters (k_{aA}, k_{dA}, T_o, k_{tA}) and the passive rate constant out of the cell (k_{bA}), as no information was available regarding these estimates within Monolix 2018R2 (Lixoft, Anthony, France). For the passive rate into the cell (k_{fA}), and any macro-rate constant parameters (i.e. Michaelis-Menten), a Yamazaki plot (for uptake, Fig. 4.4a) and Lineweaver-Burke plot (uptake and metabolism, Fig. 4.4b and c respectively) were used to obtain initial estimates after scaling to nmol (see Table 4.4). The difference in the Yamazaki plot, the Lineweaver-Burke plot and parameters (Fig. 4.4a and b respectively, see Table 4.4) for uptake parameter estimates highlight the issues with using these plots. Estimating inhibition of atorvastatin metabolism by CsA was also problematic due to the difficulty in estimating the terminal atorvastatin gradient in the presence of CsA. Therefore the $K_{I.met}$ value was estimated based on a difference in metabolic clearances, without specifically defining the mode of inhibition. The Lineweaver-Burke estimates were then scaled to nmol/min/2 × 10^5 cells and nmol for initial estimates. Parameters were ini-

Table 4.3: Goodness of fit value comparison for micro and macro parameter models for uptake of atorvastatin with inhibition by CsA

Rank order[*]	Model Number	Type	Inhibition Type	BIC ($wBIC$)	% RMSRE (ind + pop = total)
1	2	Micro rate	Non-competitive	5513.8 (0.54)	21 + 49 = 69
2	1	Micro rate	Competitive	5514.2 (0.45)	21 + 61 = 82
3	4	Macro rate	Non-competitive	5524.8 (0)	29 + 94 = 123
4	3	Macro rate	Competitive	5608.0 (0)	29 + 96 = 125

[*] = Based on total % RMSRE (Eq.4.27) and $wBIC$ (Eq. 4.25)

tially estimated for atorvastatin only with a log-normal distribution to ensure positivity with a proportional error model in Monolix 2018R2 (Lixoft, Antony France), these were then fixed to obtain CsA specific parameters before simultaneous determination of all parameters across the whole dataset (562 datapoints).

4.4 Results and Discussion

4.4.1 Structural Identifiability Analysis

The use of micro-rate constants to describe the uptake of atorvastatin in the presence of CsA, combined with competitive inhibition of the Michaelis-Menten metabolism (Models 1 and 2, Table 4.1), lead to both the competitive and non-competitive inhibition Models 1 and 2 respectively to be at least structurally locally identifiable, with no parameters required to be known (see Table 4.5). For the macro-rate constant models (Models 3 and 4, Table 4.2) with two Michaelis-Menten nonlinearities, the models were structurally unidentifiable unless two of the following parameters were known (see Table 4.5): $V_{max.up}$, $K_{m.up}$, $K_{m.met}$ and K_I or K_{inact} depending on the inhibition type.

4.4.2 Mechanistic Modelling and Parameter Estimates

The determination of uptake of substrates in rat using a high throughput assay including atorvastatin was first published in 2013, with the first individual sample taken at 30 s [166], a high throughput media loss method has also been developed including atorvastatin [237], with the first timepoint taken at 2 min. The method described here took multiple concentrations simultaneously at one timepoint using 8-way Omnistrips, with an early sample possible at 15 s. Time courses over 0.25-60 min for incubations of atorvastatin from 0.05-150 nmol/ml, in the absence or presence of CsA from all three experiments were obtained with no samples lost due to mixing of the oil and media layers. A total of 192 samples were obtained relatively simply using this method over a time period of 68 min. The analysis of data from the three experiments in a single HPLC-MS run was undertaken to decrease inter-run variability with a mean relative standard deviation across all datapoints of 25 % and 33 % for atorvastatin in the absence and presence of CsA respectively.

The best fitting model based on the % RMSRE and $wBIC$ (see Table 4.3) was Model 2 (micro-rate constant model, including non-competitive inhibition of atorvastatin uptake by CsA, and competitive inhibition of atorvastatin metabolism by CsA,
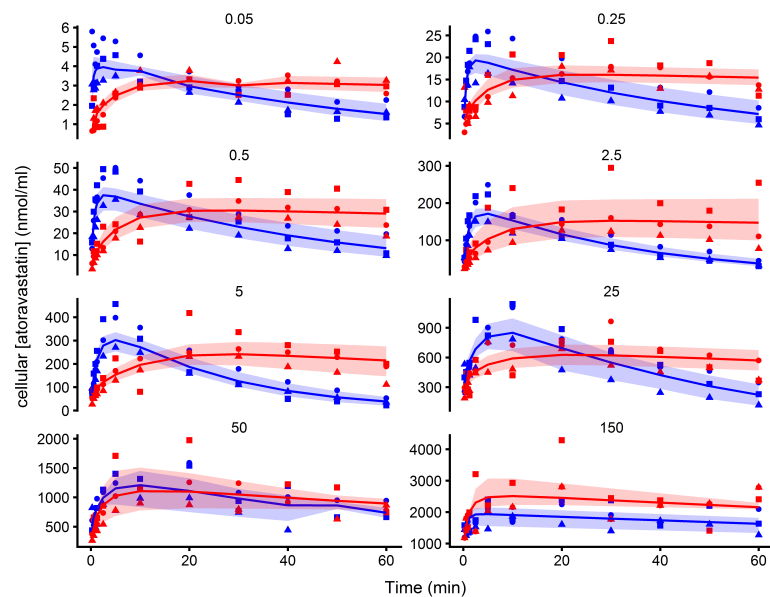
Figure 4.5: Plots of atorvastatin cellular concentration against time following the addition of atorvastatin (0.05, 0.25, 0.5, 2.5, 5, 25, 50 and 150 nmol/ml) in the absence (blue) and presence (red) of 10 nmol/ml of CsA. Each time course represents one experiment from one Teflon block trough. Shapes are data from the three separate experiments, the solid line is the average individual prediction from Model 2, bounded by the max and min individual predictions (shading)

Fig. 4.3 and Table 4.1 for ODEs). Both Models 1 and 2 were almost equal in terms of BIC, with a $wBIC$ that made Model 2 more favourable over Model 1 ($wBIC = 0.54$ and 0.45 respectively, Table 4.3). The macro-rate constant models (Models 3 and 4, Table 4.2) were unsupported as the best fitting models ($wBIC \approx 0$), again non-competitive inhibition of uptake of atorvastatin by CsA was the best fitting of the two (see Table 4.3).

Model 2 visually fitted the atorvastatin data in the absence and presence of CsA relatively well (Fig. 4.5, blue and red respectively), with a rapid increase up to a maximum at the same time as the data, which was more prolonged in the presence of CsA. As indicated by the initial estimates (see Table 4.4), CsA strongly inhibited the metabolism of atorvastatin within rat hepatocytes, as can be seen in the flat line in the individual predictions (see Fig. 4.5).

The population fits for each model had two to four times the % RMSRE compared to the individual fits (49-96 % and 21-29 % respectively, see Table 4.3), and therefore the individual parameter estimates are included and discussed here. A plot of the individual weighted residuals (IWRES) against time obtained from Monolix 2018 R2 for Model 2 look normally distributed with a mean of 0.07, close to 0 (Fig. 4.6), but are outside the 95 % confidence intervals at earlier timepoints, due to the model fits at lower atorvastatin incubation concentrations which fall outside the maximum and minimum prediction (see Fig. 4.5 blue data points and shading respectively).
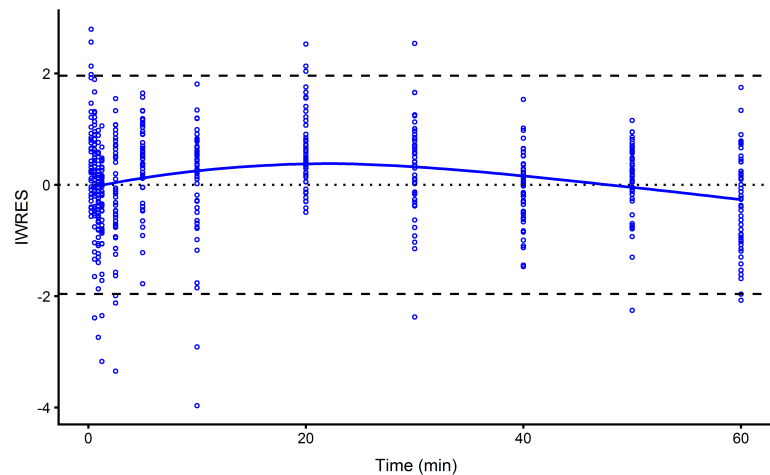
Figure 4.6: Plot of individual weighted residuals (IWRES) obtained from Monolix 2018 R2 against time for Model 2. Points are IWRES, solid line is the LOESS, dashed lines are the 95 % confidence intervals and the dotted line highlights an IWRES of 0

4.4.2.1 Passive Rate Constants

Across all four models the passive rate constant into the cell for atorvastatin (k_{fA}) varied little between 1.1-1.8 /min/10^6 cells, however, in the micro-rate constant mechanistic models the error around the k_{fA} parameter estimate was large (1.3 (0.3-28.5) and 1.1 (0.2-23.3) /min/10^6 cells for Models 1 and 2 respectively, Table 4.6). In the macro-rate constant models the error around k_{fA} was small (1.5 (0.9-2.7) and 1.8 (1-4) /min/10^6 cells for model 3 and 4 respectively, Table 4.7). The median passive rate constant out of the cell for atorvastatin ($k_{b,A}$) for Models 1 and 2 (Table 4.1) were 7-9 times faster than the rate into the cell, but again the errors were large (7.4 (0.5-44.9) and 9.3 (0.6-36.5) /min/10^6 cells respectively, Table 4.6). In the macro-rate constant models (Models 3 and 4, Table 4.2), k_{bA} was approximately double k_{fA} for Models 3 and 4, but with errors similar to the micro-rate constant models (4 (0.3-19) and 3.3 (0.4-19.6) /min/10^6 cells respectively, Table 4.7).

To compare to passive rate constants to the literature values for atorvastatin, the passive rate constants (k_{fA} and k_{bA}) are scaled from Model 2 to clearances (P_{dif} and P_{def} respectively), by multiplying by either the medium volume (500 μl) or cell volume (0.0055 μl) in which 1×10^6 cells exist. The P_{dif} for Model 2 = 0.55 (0.1-11.7) μl/min/10^6 cells) was 11-fold faster than the clearance out of the cell (P_{def}= 0.051 (0.03-0.2) μl/min/10^6 cells), possibly due to intracellular binding [165, 172, 228]. The P_{dif} of atorvastatin into hepatocytes is minor (< 1 %) compared to the uptake clearance ($CL_{.up}$ = 3375 (2722-10750) μl/min/10^6 cells, calculated according the equations in Chapter 2 for V_{max} and K_m (Eqs. 2.29 and 2.30 respectively)), therefore though the error on P_{dif} estimation was large it is of little consequence in the uptake of atorvastatin. The percentage of passive clearance to the overall uptake clearance is similar to the literature for the uptake of atorvastatin in rat hepatocyte suspensions of 1.5 % [172], but less than the estimated value in plated rat hepatocytes of a 10 % passive contribution [238].

Table 4.4: Initial macro-parameter estimates for uptake (Models 3 and 4) and metabolism (Models 1-4)

	V_{max} (RSE) (pmol/min/2×10^5 cells)	K_m (RSE) (nmol/ml)	K_{inact} or K_I (RSE)* (nmol/ml)
Uptake			
Yamazaki plot (Fig. 4.4a)	1253	5-25	
Lineweaver-Burke plot (Fig. 4.4b)	157 (80 %)	0.8 (14 %)	
Lineweaver-Burke plot (Appendix D, Fig. D.1a) (in presence of CsA)	307 (575 %)	5 (15 %)	K_{inact} 9.5 (581 %) K_I 1.8 (15 %)
Metabolism			
Lineweaver-Burke plot (Fig. 4.4d)	52 (143 %)	3.4 (5 %)	
Lineweaver-Burke plot (Appendix D, Fig. D.1b) (in presence of CsA)	1521 (3334 %)	148 (12 %)	K_I 0.06*2

* = calculated by re-arrangement of Chapter 2, Eq. 2.34 derived from Lineweaver-Burke plots in Appendix, *2=calculated by $(I/(CL * CL_{app}-1))$

Table 4.5: Structural Identifiability analysis summary of tested models, assuming known initial conditions and observations for each model

Model	Inhibition Type	Equations	Initial Conditions	No. of unknowns Parameters	States	Result	No. of parameters to be identifiable (d.o.f.)
Micro-rate constant models							
1	Competitive	4.3, 4.5, 4.7, 4.9, 4.11	[Y,0,0,Y,0]	11	5	SI	0
2	Non-competitive	4.4, 4.6, 4.8, 4.10, 4.12, 4.13	[Y,0,0,Y,0,0]	12	6	SI	0
Macro-rate constant models							
3	Competitive	4.16, 4.18, 4.20	[Y,0,Y]	8	3*	U	2: $K_{m.up}$, $K_{I.up}$, $K_{m.met}$, $K_{I.met}$
4	Non-competitive	4.17, 4.19, 4.20	[Y,0,Y]	8	3*	U	2: $V_{m.up}$, $K_{inact.up}$, $K_{m.met}$, $K_{I.met}$

d.o.f. = degrees of freedom, * = $\frac{dx_3}{dt} = 0$, Y = positive integer, SI = structurally identifiable (local), U = unidentifiable.

Table 4.6: Micro-rate constant individual parameter estimates for atorvastatin in the presence of CsA. Data are the individual mode of the conditional distribution from three separate experiments (Min-Max). All parameter estimates are scaled to *per* 10^6 cells, $V_{max.met}$ was scaled to pmol/min and K_m and K_I were scaled to nmol/ml

Parameter	Competitive	Non-competitive
Model	1	2
Passive		
k_{fA} (/min)	1.3 (0.3-28.5)	1.1 (0.2-23.3)
k_{bA} (/min)	7.4 (0.5-44.9)	9.3 (0.6-36.5)
Transporter		
k_{aA} (/nmol/min)	2.7 (1.4-12.6)	2.6 (1.2-13.3)
k_{aC} (/nmol/min)	1.2 (1-1.4)	0.36 (0.33-0.37)
k_{dA} (/min)	0.005 (0.004-0.005)	0.017 (0.015-0.021)
k_{dC} (/min)	0.54 (0.53-0.55)	0.16 (0.13-0.2)
k_{tA} (/min)	0.3 (0.3-0.3)	0.3 (0.2-0.3)
T_o (nmol)	2.3 (1.5-3.7)	2.7 (2-3.6)
α	N/C	0.013 (0.007-0.023)
Metabolism		
$V_{max.met}$ (pmol/min)	383 (283-590)	393 (285-500)
$K_{m.met}$ (nmol/ml)*	36.9 (26-46.5)	17.7 (8-30.7)
$K_{I.met}$ (nmol/ml)*	2.8 (1.7-8.2)	11 (5.5-29)

N/C = not calculated, * = calculated by dividing by V_{cell} = 0.0055 ml/10^6 cells, obtained from initial volume estimates for atorvastatin only (see above)

4.4.2.2   Micro-Rate Constant Transporter Mediated Uptake

The atorvastatin transporter association rate constant (k_{aA} = 2.6 (1.2-13.3) /nmol /min/10^6 cells, Table 4.6), was 10-fold faster than the translocation constant (k_{tA} = 0.3 (0.2-0.3) /min/10^6 cells, Table 4.6), and were the same for Models 1 and 2. The atorvastatin transporter dissocation rate constant (k_{dA} = 0.017 (0.015-0.021) /min/10^6 cells) was 150 times slower than k_{aA} and 20 times slower than k_{tA} for Model 2. It follows then, that very quickly k_{aA} approaches T_o (see Fig. 4.8, dotted blue line), and once atorvastatin is bound, it is likely to be translocated into the cell. The result is that the Michaelis-Menten assumptions (list 2.4.3) discussed in Chapter 2 hold here for atorvastatin. This also partially explains why the BIC values (see Table 4.3) obtained for atorvastatin are much closer between the micro-rate constant and macro-rate constant models (Δ_i BIC = 11 between Model 2 and 4, Table 4.3).

The CsA transporter association rate constant (k_{aC} = 0.36 (0.33-0.37) /nmol /min/10^6 cells, Table 4.6 model 2), was seven times slower than k_{aA}, whilst the dissociation rate constant (k_{dC} = 0.16 (0.13-0.2) /min/10^6 cells, Table 4.6 model 2) was ten times faster than k_{dA}. The difference in k_a and k_d between atorvastatin and CsA explains the co-incubation inhibition conclusions in the literature with the $K_{I.up}$ = 0.9(0.8−1) nmol/ml value determined here (from k_{dC}/k_{aC}), that was similar to the IC_{50} in HEK293-OATP1B1 cells of 0.48 ±0.34 nmol/ml [140] and 0.3 nmol/ml *cis*-inhibition with estradiol-17β-glucuronide [208]. The inhibition on pre-incubation therefore comes from the α term of 0.013 (0.007-0.023), which, if the $K_{I.up}$ is multiplied to obtain a $K_{inact.up}$ value of 0.012 (0.0057-0.023) nmol/ml is the same as that for pre-incubation with atorvastatin in HEKOATP1B1 cells (0.021 ±0.004 nmol/ml) [140], as well as the *trans*-inhibition of 0.026 nmol/ml calculated using estradiol-17β-glucuronide as a sub-

strate [208].

With regards to the α term in Model 2, this is best illustrated using a reaction scheme (Fig. 4.7), that is more common in the enzymology literature [210, 239]. The top row of the scheme represents normal atorvastatin transport, with CsA competitively binding to T_f on the left hand side. When either is bound (S_2 and I_2 respectively), then an opposing free molecule from the medium (I_1 and S_1 respectively) can bind leading to a complex I_3 via an α term through the current rate constants (k_a and k_d). Atorvastatin can then be translocated into the cell faster or slower, dependent on α through αk_{tA} leaving CsA bound to the transporter. It then follows, that if $\alpha < 1$ and the amount in the medium of I_1 is in excess, that over time the reaction would drive towards I_3, with transport into the cell of atorvastatin then more dependent on αk_{tA} than k_{tA} as can be seen in Fig. 4.8.

$$S_1 + T_f \underset{k_{dA}}{\overset{k_{aA}}{\rightleftharpoons}} S_2 \xrightarrow{k_{tA}} S_3 + T_f$$
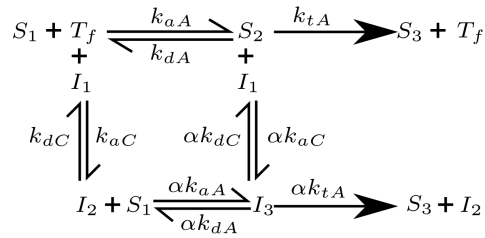
Figure 4.7: Reaction scheme for the transport of atorvastatin and its inhibition by CsA. S_1, S_2 and S_3 are the amount of atorvastatin in the medium, bound to free transporter (T_f) and intracellular respectively. I_1, I_2 and I_3 are the amount of CsA in the medium, bound to T_f and the atorvastatin-transporter-CsA complex respectively. k_a and k_d are the association and dissociation rate constants, k_tA is the translocation rate constant from tranporter into the cell for atorvastatin, α is the dimensionless term to describe the effect of CsA binding on atorvastatin transport

To illustrate how the different aspects of non-competitive inhibition affect atorvastatin and CsA, parameter estimates from Model 2 associated with the transporter (k_{aA}, k_{aC}, k_{dA}, k_{dC}, T_o and α, Table 4.6) were used to simulate the transporter response following pre-incubation with CsA using the `deSolve` package in R [1] (Fig. 4.8). In the absence of CsA (Fig. 4.8, dotted blue lines), as the incubation concentration of atorvastatin was increased, so k_{dA} has a larger effect, seen as the broadening of the peak.
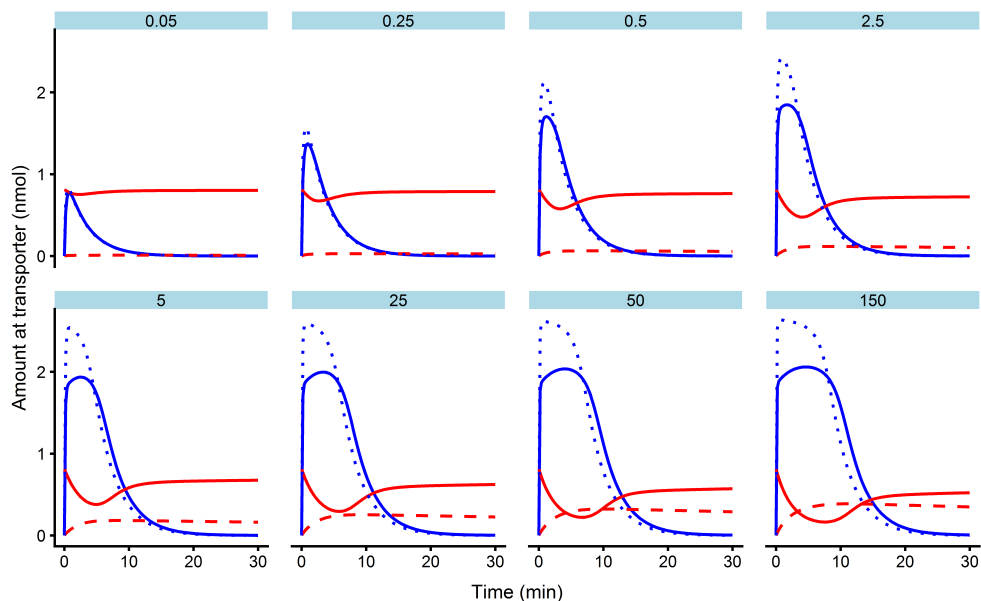
Figure 4.8: Model 2 plots of the simulated amounts of atorvastatin bound to the transporter against time in the absence (dotted blue line) and presence (solid blue line) of CsA. The solid red line is the amount of CsA bound to the transporter following pre-incubation, and the dashed red line is the atorvastatin-transporter-CsA complex

After pre-incubation with CsA, the higher affinity atorvastatin competes with CsA, leading to a decrease in atorvastatin bound (blue solid line), and also a perturbation in the amount of CsA bound (red solid line), which recovers to near the initial amount of CsA at lower atorvastatin incubation concentrations as atorvastatin is transported into the cell. The formation of the atorvastatin-transporter-CsA complex initially starts at zero and increases over time (Fig. 4.8, red dashed line). As the incubation concentration of atorvastatin increases, so the complex increases (Fig. 4.8, red dashed line).

The covariance matrix derived from the inverse of the Fisher information matrix (obtained through linearisation in Monolix 2018R2, as the Fisher information matrix could not be obtained through the SAEM algorithm (see Chapter 2, Section 2.4.5)) [190] can be used to evaluate the practical identifiability of the model, assuming that all the unknown parameters are independent, i.e. the off-diagonal elements are zeros [184, 216]. Using the estimated individual random effects (η, taken from Monolix 2018R2) for Model 2, a covariance matrix was generated in R Studio using `GGally` [217] (see Fig. 4.9).

Unlike Chapter 3, there was ≤ 0.4 covariance between k_aA, k_dA and T_o. This may be due a large increase in the amount of datapoints from 281 (DCF co-incubation scenario) to 568 and the higher concentration of timepoints up to the maximum (5 timepoints up to 3 min for the DCF co-incubation scenario and 6 timepoints up to 5 min here). A covariance of -0.8 was observed between $V_{max.met}$ and $K_{m.met}$ (Fig. 4.9 indicative of their relationship in the Michaelis-Menten equation.

	kbA	kaA	kdA	To	ktA	Vmm	Kmm	kaC	kdC	alpha	KIm
alpha											-0.1
kdC										0.2	0.4
kaC									-0.4	-0.4	0.1
Kmm								-0.1	-0.3	0.2	-0.7
Vmm							-0.8	0	0.2	0	0.5
ktA						0.2	-0.5	0	0.2	-0.2	0.3
To					0	-0.1	0.2	-0.1	0.2	0	-0.1
kdA				-0.1	0.2	0	-0.2	0.3	-0.1	-0.3	0.1
kaA			-0.1	0.4	-0.2	0.1	0.1	-0.2	0.2	0.3	0
kbA		0.1	-0.1	0.3	-0.4	0.1	0.1	0.4	-0.3	-0.1	-0.1
kfA	0.7	-0.1	0	-0.1	-0.5	-0.1	0.2	0.3	-0.4	-0.1	-0.3
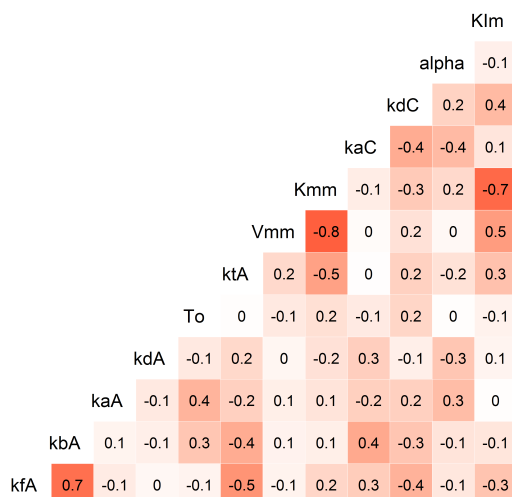
Figure 4.9: Covariance matrix of the individual random effects η for Model 2

4.4.2.3 Macro-Rate Constant Transporter Mediated Uptake

The macro-constant model for non-competitive inhibition of atorvastatin uptake (Model 4) has a $V_{max.up}$ value similar to the scaled value from Model 2 ($V_{max.up} = 850$ ($680 - 1340$) pmol/min/ 10^6 cells), Table 4.7 and $V_{max.up} = 675$ ($430 - 1116$) pmol/min/ 10^6 cells respectively). This was similar to the Yamazaki plot $V_{max.up}$ estimate $= 1253$ pmol/min/10^6 cells, Table 4.4), but not the Lineweaver-Burke plot $V_{max.up}$ estimate $= 157$ (80 %) pmol/min /10^6 cells, see Table 4.4). The scaled micro-rate and macro-rate constant parameter estimates compared favourably to that in the literature in rat hepatocytes ($V_{max.up} = 1340 \pm 320$ pmol/min /10^6 cells [172]).

The K_m estimate for Model 4 (0.09 (0.04-0.17) nmol/ml, Table 4.7) was two fold less than the scaled value from Model 2 (0.2 (0.04-0.41) nmol/ml) and was similar to that seen in plated rat hepatocytes (0.3 nmol/ml, although $V_{max.up}$ was low at 58 pmol/min/ mg protein [238]), but less than that in rat hepatocyte suspensions (4 $\pm$ 4 nmol/ml, [172]). Cellular volume estimates have a large effect on both the cellular concentration calculation prior to parameter estimation (Eq. 4.1), but also in the models themselves with normalised data. Yabe et al. [172] used the literature value of 0.0039 ml/10^6 cells [175], which gave a higher BIC for the data presented here, and is therefore a major contribution to the source of the differences. To get around this, some authors normalise the data to /mg protein [32, 237, 238] which can be accurately measured, and for rat is almost equivalent to *per* 10^6 cells [32, 181].

4.4.2.4 Metabolism

2-hydroxy atorvastatin and 4-hydroxy atorvastatin were detected within the cell extract at 15 s in the three highest dose groups (25-150 nmol/ml), whilst in the lower dose groups (0.25-5 nmol/ml), detection was variable. The peak area ratio of both metabolites was inhibited by pre-incubation by CsA, which was similar to the metabolite only

Table 4.7: Macro-rate constant individual parameter estimates for atorvastatin in the presence of CsA. Data are the individual mode of the conditional distribution from three separate experiments (Min-Max). All parameter estimates are scaled to *per* 1×10^6 cells. V_{max} was scaled to pmol/min, and K_m, K_I and $K_{inact.up}$ were scaled to nmol/ml

Parameter	Competitive	Non-Competitive
Model	3	4
Passive		
k_{fA} (/min)	1.5 (0.9-2.7)	1.8 (1-4)
k_{bA} (/min)	3 (0.3-19)	3.3 (0.4-19.6)
Transporter		
$V_{max.up}$ (pmol/min)	3220 (1460-13000)	850 (680-1340)
$K_{m.up}$ (nmol/ml)	0.74 (0.18-1.08)	0.09 (0.04-0.17)
$K_{I.up}$ or $K_{inact.up}$ (nmol/ml)	0.1 (0.07-0.22)	0.06 (0.04-1.11)
Metabolism		
$V_{max.met}$ (pmol/min)	296 (158-840)	364 (211-950)
$K_{m.met}$ (nmol/ml)	340 (251-407)	436 (296-544)
$K_{I.met}$ (nmol/ml)	1.1 (1-1.3)	0.32 (0.27-0.36)

at higher atorvastatin incubation concentrations (see Figs. 4.10 and 4.11), suggestive of competitive inhibition. The effect of CsA was greatest on 4-hydroxy atorvastatin formation compared to 2-hydroxy atorvastatin formation at lower atorvastatin doses (Figs. 4.11 and 4.10 respectively, red dotted lines). Amundsen et al. [225] also showed the inhibition by CsA on midazolam metabolism to be concentration dependent in human liver microsomes.

Neither of the macro-rate constant models (Models 3 and 4) gave realistic estimates for metabolism with a $K_{m.met}$ that was more than the highest incubation concentration for atorvastatin ($K_{m.met} = 340$ (251 − 407) and 436 (296-544) nmol/ml respectively, Table 4.7). This was also the case in the absence of CsA and suggests an instability in the data analysis and is also related to the structural unidentifiability of the macro-rate constant models with regard to the $K_{m.met}$ and $K_{I.met}$ (see Table 4.5), that was not present in the micro-rate constant models (Models 1 and 2), where the models were at least structurally locally identifiable (see Table 4.5).

$V_{max.met}$ however was similar across all four models (see Table 4.6 and 4.7). Model 2 had a $V_{max.met}$ of 393 (285-500) pmol/min/10^6 cells, with a $K_{m.met}$ of 17.7 (8-30.7) nmol/ml, giving a metabolic clearance (CL_{met}) of 22 (16-35) μl/min/10^6 cells, which was higher than the value in the literature ($CL_{met} = 4.3 \pm 0.65$ μl/min/10^6 cells (hepatocytes) - 7.6 $\pm$ 0.4 μl/min/10^6 cells (adjusted from microsomes) [165, 229]). $K_{I.met}$ was similar to $K_{m.met}$ (11 (5.5-29) and 17.7 (8-30.7) nmol/ml respectively, Table 4.6, Model 2), on the assumption that for CsA, the concentration inside the cell is approximately equal to the concentration outside the cell. From the work of Prueksaritanont et al. [231], who measured disposition of CsA in rat hepatocytes, it was reported that 86 % of the initial concentration of CsA was measured in the cell after five minutes, whilst only 16 % of the initial concentration of CsA was lost over four hours [231]. This helps to support the assumption for the CsA $K_{I.met}$ seen here.
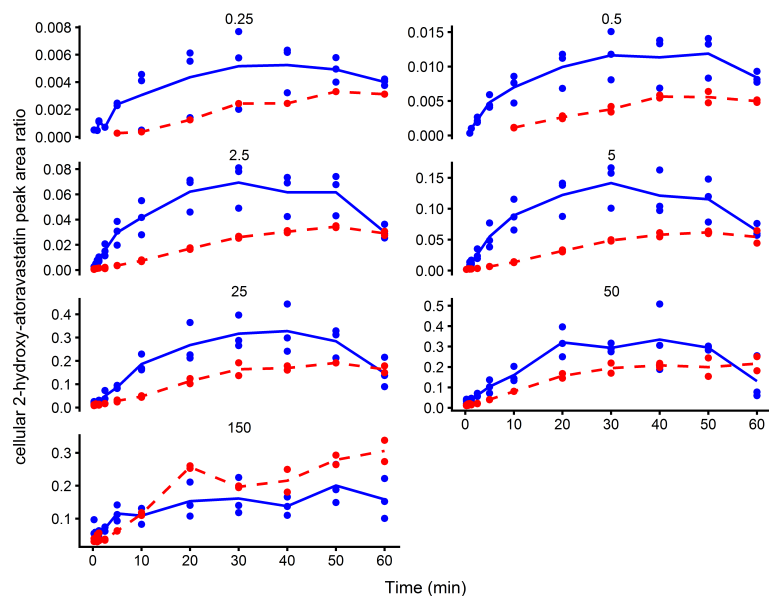
Figure 4.10: Plots of cellular 2-hydroxy atorvastatin peak area ratio against time following the addition of atorvastatin (0.25, 0.5, 2.5, 5, 25, 50 and 150 nmol/ml) in the absence (blue) and presence (red) of 10 nmol/ml CsA. Each time course represents one experiment from one Teflon block trough. Points are data ($n = 1 - 3$) and solid lines are the average peak area ratio
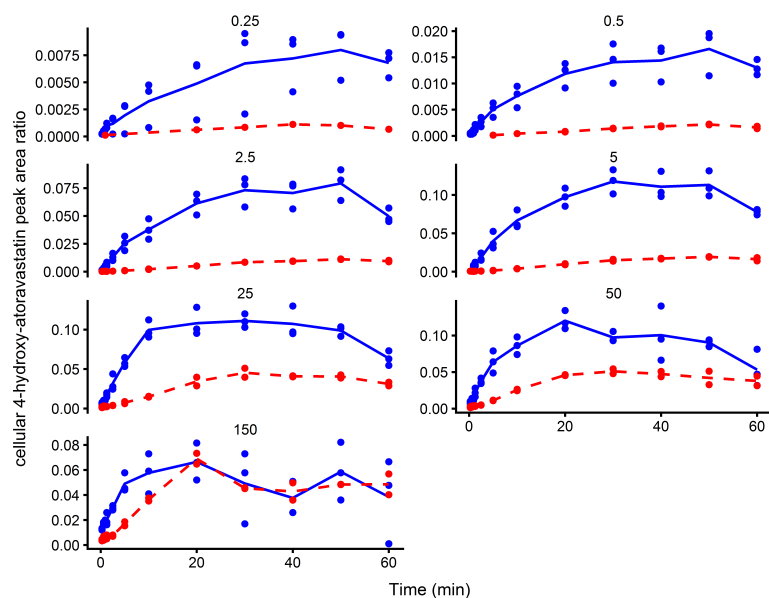
Figure 4.11: Plots of cellular 4-hydroxy atorvastatin peak area ratio against time following the addition of atorvastatin (0.25, 0.5, 2.5, 5, 25, 50 and 150 nmol/ml) in the absence (blue) and presence (red) of 10 nmol/ml CsA. Each time course represents one experiment from one Teflon block trough. Points are data ($n = 1 - 3$) and solid lines are the average peak area ratio

4.5 Conclusions

In conclusion, the data presented here show that the high throughput method developed is an improvement compared to existing methods for the assessment of atorvastatin uptake in rat hepatocytes and its inhibition by CsA given the models fits and parameter estimates. Through the use of mechanistic modelling and comparison of the % RMSRE and *wBIC*, a micro-rate constant model describing the uptake of atorvastatin and its complex inhibition by pre-incubation of CsA was developed (Model 2) and compared across models (Model 1, 3 and 4). The models all included two passive rate constants for the movement into and out of the cell for atorvastatin, as well Michaelis-Menten metabolism and subsequent competitive inhibition by CsA. Non-competitive inhibition of uptake of atorvastatin by CsA in rat hepatocytes (Model 2) through the use of micro-rate constant models, was the best fitting of the three models tested (lowest % RMSRE and BIC, Table 4.3). The use of a structurally identifiable model (Models 1 and 2) enabled the determination of uptake and metabolic processes that were similar to those in the literature. Whilst the use of macro-rate constant models (Models 3 and 4) that were structurally unidentifiable unless two parameters were known (see Table 4.5) were not able to capture the metabolic processes and as such were not the best fitting models (see Table 4.3).

Following on from Chapter 3, a D-optimal design for Model 2 was undertaken using the `PopED` function in R [195] using eight different atorvastatin concentrations and 12 different timepoints. Both the triangular matrix and full matrix gave a support point at 0.25 min (3 and 2 replicates respectively). However, given the difficulty in taking multiples of the same timepoint using this method, and the variability seen with the lower atorvastatin incubation concentrations, increasing the entire timecourse at lower concentrations may decrease the covariance. The optimal designed timepoints are as follows:

- Triangular Matrix: 0.25, 0.25, 0.25, 1.2, 8.4, 8.7, 25.5, 30, 35, 59, 67 min

- Full Matrix: 0.25, 0.25, 5.6, 9.2, 13.2, 14.3, 20.6, 39, 43, 50, 64, 65 min

Future work should be undertaken to establish the simultaneous analysis of substrate and inhibitor in a single sample so that a more holistic understanding of drug-drug interactions can be described, and is covered in Chapter 5. Quantification of metabolites both in the cell and medium should also be evaluated to improve the understanding of the complexity of metabolism and its inhibition as well as possible effects on uptake processes.

Chapter 5

Evaluation of the Uptake of Pitavastatin and Eltrombopag in Cryopreserved Human Hepatocytes

5.1   Introduction

The previous experimental chapters have described the analysis of uptake of substrates (DCF, Chapter 3 and atorvastatin, Chapter 4) and their inhibition (through gemfibrozil and cyclosporine respectively) using mechanistic models in experimental systems of increasing complexity from cell-lines to isolated hepatocytes. What was apparent in the analysis of both of the processes, was that the outcomes were limited by the lack of measurement of both substrate and inhibitor in the same sample to understand the interactions in depth. This chapter therefore will evaluate whether the simultaneous measurement of both a high affinity substrate (pitavastatin) and "inhibitor" (eltrombopag, also a substrate) can improve the fit to the more extensive data available, and determine through the use of a mechanistic modelling approach the mode of inhibition between pitavastatin and eltrombopag.

Pitavastatin, which like atorvastatin is one of the family of HMG-CoA reductase inhibitors and used to manage hypercholesterolaemia [240], was determined *in vitro* to be a substrate of OATP1B1 and OATP1B3, with a total fraction transported into cells of 0.78 by these transporters, and the remaining fraction of pitavastatin through passive movement based on the total uptake clearance. Pitavastatin is also a substrate of the efflux transporters BCRP and MRP2 [9, 132]. Pitavastatin is more sensitive to inhibition by rifampicin (OATP, BCRP and MRP2 inhibitor) than rosuvastatin; *in vitro*, both in human hepatocytes and MDCKII cells, overexpressing hOATP1B1 or hOATP1B3, as well as in healthy volunteers [9] and is thus a good candidate to use for evaluating transporter mediated drug-drug interactions (TrDDIs). In human liver microsomes pitavastatin is metabolised via lactonisation through the hUGT1A3, which can then be

further metabolised by hCYP3A4 [241]. However, this route of elimination is relatively small, compared with the major route of biliary elimination of pitavastatin (53 %) and a minor 3 % of pitavastatin in urine [240]. The generation of the lactone metabolite through UGT is also confounded as it is a breakdown product of pitavastatin, which is in equilibrium with the active acid form, and is therefore seen at similar concentrations in human plasma in healthy volunteers [9, 242].

Eltrombopag, is a thrombopoietin agonist used in the management of thrombocytopenic purpura, and the dose is individualised based on platelet count to prevent excessive clotting or lack of effect [243]. It is highly protein bound, and adsorption to plasma proteins was included in order to obtain an IC_{50} value that explained the inhibition of rosuvasatin [244]. *In vitro* studies found eltrombopag to be a substrate of hOATP1B1, hOATP2B1, hOCT1 and hBCRP, and is able to inhibit probe substrates for each transporter [244, 245]. The uptake by hOATP1B1 is disputed in the FDA new drug filing for eltrombopag [246], maybe due to the large amount of non-specific binding to plastic [245]. Clinical drug-drug interactions (DDIs) were observed between eltrombopag and rosuvastatin (as a perpetrator, [247]) and lopinavir-ritonavir (as a victim, [248]). Takeuchi et al. [244] and Elsby et al. [249] both found eltrombopag to inhibit rosuvastatin through hBCRP, and reasoned that this was the main cause of the interaction with rosuvastatin in the clinic through the use of a physiologically based pharmacokinetic model (PBPK), as well as a minor contribution from hOATP1B1 inhibition [244].

5.2 Methods

5.2.1 Chemicals

Eltrombopag and pitavastatin calcium were obtained from Toronto Research Chemicals (Toronto, Canada), caesium chloride (C3032), mineral oil (69794, density 0.872 g/l), oil red O (O0625), Dimethyl sulfoxide (DMSO, 99.5 %), formic acid (99 %) and 5,5-diethyl-1,3-diphenyl-2-iminobarbituric acid (S518891) were obtained from Sigma-Aldrich (Stockholm, Sweden). Acetonitrile, methanol, Leibovitz L15 medium (21083027) and silicone oil (15445005, density 1.08 g/l) were of analytical or cell culture grade and obtained from Thermo-Fisher Scientific Inc (Gothenburg, Sweden).

5.2.2 Use of Hepatocytes

Human hepatocytes were obtained from BioIVT (Lot Number: LYB, 10 donor LiverPool[TM] (8 Caucasians, 1 African-American and 1 Hispanic, see Appendix E, Brussels, Belgium) and thawed according to supplier recommended guidelines in Leibovitz L15 medium. Cells were counted using a haemocytometer in 0.4 % trypan blue, with a viability of 84-87 % over the three experiments and then diluted to 3×10^6 cells/ml in Leibovitz L15 medium. Hepatocytes were kept on ice prior to use and were used within 3 h of defrosting.

5.2.3 Incubations

0.4 ml of hepatocytes was diluted 1:1 with Leibovitz L15 medium either containing DMSO blank (0.1 % for pitavastatin or 0.25 % for eltrombopag alone) or eltrombopag at 90 nmol/ml and pre-incubated at 1.5×10^6 cells/ml for 15 min at 37 °C in 7 ml glass scintillation vials (PerkinElmer, Vasby, Sweden) in a shaking water bath (Grant Instruments, Cambridge, UK). Pitavastatin was dissolved and serially diluted in DMSO to give 0.12, 0.4, 1.2, 4, 12 and 40 mmol/l before being diluted 400-fold into 37 °C Leibovitz L15 medium. 30 mmol/l of eltrombopag was dissolved in DMSO, then diluted 333-fold to 90 nmol/ml in Leibovitz L15 medium. Incubations were started by the addition of 0.4 ml of pitavastatin solution at final concentrations of 0.3, 1, 3, 10, 30 and 100 nmol/ml, or by the addition of 0.4 ml of eltrombopag at a final concentration of 30 nmol/ml (final DMSO 0.35 % and 1×10^6 cells/ml hepatocyte suspension). Samples were taken at 0.25, 0.5, 1, 2, 5, 10 and 30 min following the addition of pitavastatin and the cells separated using an oil spin method, similar to Nordell et al. [250] and Grandjean et al. [8]. Briefly, 0.5 ml microtubes (12049877, Thermo-Fisher Scientific, Gothenburg, Sweden) layered with 15 μl of 4 % caesium chloride onto which 140 μl was added of 8:2 silicone oil: mineral oil, containing oil red O for visualisation purposes. Samples were taken by transferring 100 μl of hepatocyte suspension into the microtube which was then centrifuged for 15 s in a Minispin centrifuge (Eppendorf, Horsholm, Denmark), during which time the hepatocytes passed through the oil into the caesium chloride bottom layer. The tubes were then frozen on dry ice and the bottom layer cut off once frozen into a 1 ml deep well plate (260252, Thermo-Fisher Scientific, Gothenburg, Sweden). 50 μl of water suitable for UPLC (MilliQ ELGA water, Merck-Millipore, Solna, Sweden) and 150 μl of stop solution (50:50 MeOH:MeCN, containing 0.8 % formic acid and 4 nM 5,5-diethyl-1,3-diphenyl-2-iminobarbituric acid as an internal standard) were then added. Samples were mixed on a plate shaker for 1 h and then stored at 80°C overnight. Prior to analysis, samples were defrosted and mixed 30 min before centrifugation of the plates at 4000g for 20 min at 4 °C. Samples were transferred to a conical bottomed 96 well plate for analysis (249944, Thermo-Fisher Scientific, Gothenburg, Sweden) and diluted 1:1 with MilliQ ELGA water.

5.2.4 UPLC Mass Spectrometry Analysis

Samples were analysed by ultra-performance liquid chromatography (UPLC)high resolution mass spectrometry (HRMS) operated in positive ion mode using an Acquity UPLC I Class system with column and sample manager and a Xevo TQ-S mass spectrometer (Waters, Sollentuna, Sweden). For HPLC analysis, a Waters Acquity UPLC HSS T3 C18 50 x 2.1mm, 1.8 μm column (Waters, Sollentuna, Sweden) was used with a flow rate of 1ml/min at 40 °C. Mobile phase A was composed of 0.1 % formic acid in MilliQ ELGA water, and mobile phase B was composed of acetonitrile and 0.1 % formic acid. The gradient system used was as follows: initially, 0.2 % of mobile phase B was held for 1.3 min followed by a linear gradient to 95 % of mobile phase B from 1.3 to 1.8 min, and finally 0.2 % of B up to 2 min. Injections of 0.3-1 μl were made,

depending on incubation dose of pitavastatin. For MS analysis the following settings were used: capillary voltage 0.5 kV; desolvation temperature 600 °C; cone gas flow 150 l/h; nebulizer gas 7.0 bar; collision gas flow 0.15 ml/min. The mass spectrometer was operated in a selected positive ion scanning mode, monitoring for the protonated masses of pitavastatin (422.1768>290.1528) and eltrombopag (443.1298>182.9503). The internal standard was monitored at 336.2126>194.9987. The UPLC-MS data were acquired, processed and analysed using TargetLynx software (version 4.1, Waters, Sollentuna, Sweden). Eltrombopag and pitavastatin standard curves were linear up to 1000 pmol/ml with R2 > 0.96 and a limit of quantitation of 4 pmol/ml and 1 pmol/ml respectively.

5.2.5 Data Analysis

The bottom layer concentration was converted to cellular concentration using a cellular volume (V_{cell}) of 3 μl per 1×10^6 human hepatocytes [49] using:

$$[\text{cell}] \ (\text{nmol/ml}) = \left(\frac{[Bottom \ layer] \ \times \ 15.3 \ \mu l}{V_{cell}} \right) / 1000 \qquad (5.1)$$

where the cell volume (V_{cell}) *per* 1×10^5 cells was 0.3 μl and the volume of the bottom layer of caesium chloride was 15 μl, a dilution factor of 1000 was used to convert the concentration from pmol/ml to nmol/ml. As described in Chapter 2 (Table 2.3), there are various cell volumes that one could use, therefore: the median human volume of 2.7 $\mu l/10^6$ cells; 3 $\mu l/10^6$ cells (human) [49] and 3.9 $\mu l/10^6$ cells (rat) [175] were evaluated using a micro-rate constant model for pitavastatin only, which was the same as the model structure used by Grandjean et al. [8], with the addition of a metabolic elimination rate constant (k_e, see Fig. 5.1a). The volume of 3 μl [49] had the lowest Bayesian Information Criterion (BIC) value and a weighted BIC value ($wBIC = 0.79$, Eq. 5.43) and was used in the rest of this chapter, whilst the median value of 2.7 μl and 3.9 μl had $wBIC = 0.17$ and 0.039 respectively and were therefore not used further.

5.2.6 Mechanistic Modelling

A three compartment mechanistic model to describe the uptake of pitavastatin into hepatocytes through the use of micro-rate constants for passive and active processes has previously been described [8]. In the present study, this model was extended to include a first order elimination rate constant (k_e) for pitavastatin, and passive and active uptake processes for eltrombopag (see Fig. 5.1b and c). A requirement for the micro-rate constant models (see Fig. 5.1a-c) is that the amount of free transporters (T_f) available for binding of pitavastatin and eltrombopag need to be known, but it is not normally the case. As *per* previous chapters (Chapters 3 and 4), T_f can be eliminated by a steady state analysis of the states for medium, transporter and intracellularly for pitavastatin and eltrombopag (see Chapter 3, Eqs. 3.5-3.16 for derivation) to give :

$$T_f = T_o - S_2 - I_2 - I_4 \qquad (5.2)$$
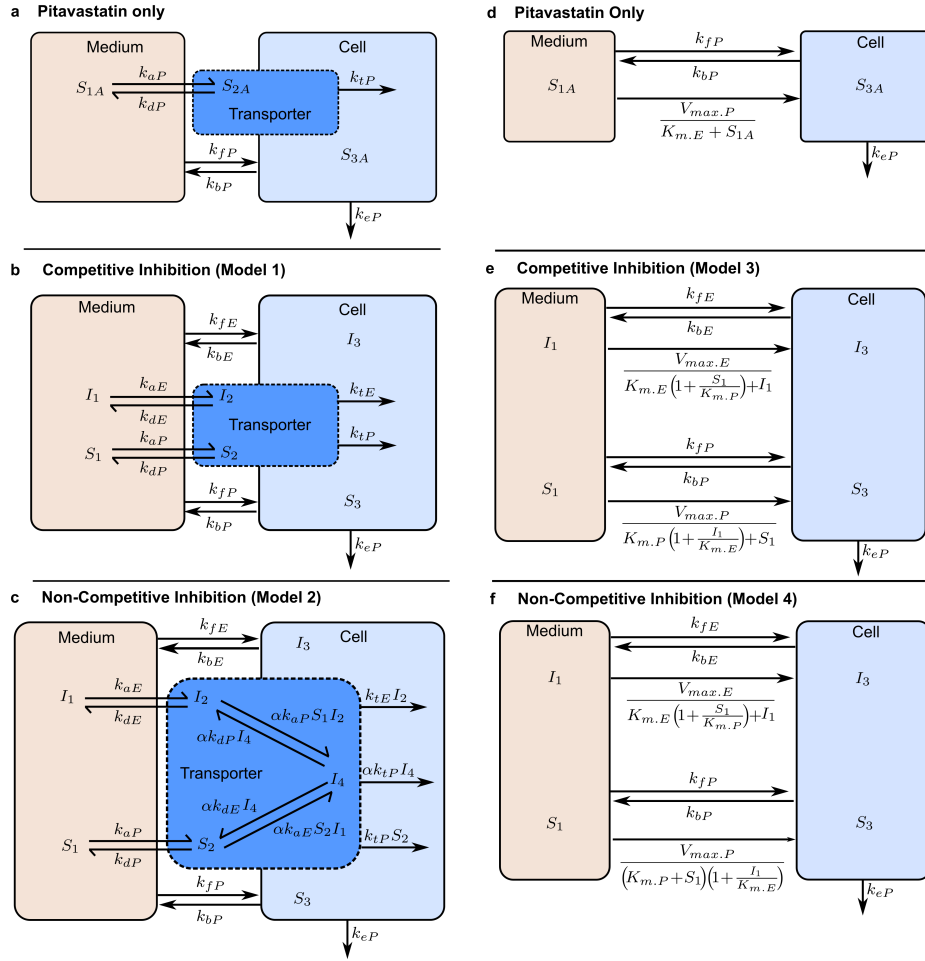
Figure 5.1: Schematic of the micro-rate constant (a-c, Table 5.1) consisting of medium, transporter and intracellular, and macro-rate constant (d-f, Table 5.2) consisting of medium and intracellular mechanistic models. **a** and **d** pitavastatin only used in parameter estimation. Pitavastatin following pre-incubation with eltrombopag with competitive (**b** and **e**) and non-competitive (**c** and f) mode of inhibition respectively.

where T_o is the total amount of transporters responsible for the uptake of pitavastatin and eltrombopag, S_2 and I_2 are the amounts bound to transporter and I_4 is the pitavastatin-transporter-eltrombopag complex.

5.2.6.1 Structural Identifiability Analysis

As *per* Chapters 3 and 4, prior to parameter estimation, models were evaluated for structural identifiability (see Chapter 2, section 2.4.1) using the `Identifiability Analysis` package in Mathematica 11.3. Micro-rate constant models (Model 1 - competitive inhibition of uptake, and Model 2 non-competitive inhibition of uptake, Table 5.1) and macro-rate constant models (Model 3 - competitive inhibition of uptake, and Model 4 - non-competitive inhibition of uptake, Table 5.2) with measurement of pitavastatin, and with or without measurement of eltrombopag were evaluated, both for competitive and non-competitive inhibition (see Tables 5.1 and 5.2 for observations), assuming that both pitavastatin and eltrombopag are substrates of uptake transporters [132, 244].

Table 5.1: Micro-rate constant models for competitive and non-competitive inhibition

Compartment	Pita Only (Fig. 5.1a)	Pita Only (Fig. 5.1a)
Pita Medium (S_{1A})	$$\frac{dS_{1A}}{dt} = -k_{fP}S_{1A} - k_{aP}S_{1A}T_f + k_{dP}S_{2A} + k_{bP}S_{3A} \quad (5.3)$$	$$\frac{dS_{1A}}{dt} = -k_{fP}S_{1A} - k_{aP}S_{1A}T_f + k_{dP}S_{2A} + k_{bP}S_{3A} \quad (5.4)$$
Pita Transporter (S_{2A})	$$\frac{dS_{2A}}{dt} = k_{aP}S_{1A}T_f - (k_{dP}+k_{tP})S_{2A} \quad (5.5)$$	$$\frac{dS_{2A}}{dt} = k_{aP}S_{1A}T_f - (k_{dP}+k_{tP})S_{2A} \quad (5.6)$$
Pita Intracellular (S_{3A})	$$\frac{dS_{3A}}{dt} = k_{fP}S_{1A} + k_{tP}S_{2A} - (k_{bP}+k_{eP})S_{3A} \quad (5.7)$$	$$\frac{dS_{3A}}{dt} = k_{fP}S_{1A} + k_{tP}S_{2A} - (k_{bP}+k_{eP})S_{3A} \quad (5.8)$$
	Competitive Inhibition (Model 1, Fig. 5.1b)	Non-Competitive Inhibition (Model 2, Fig. 5.1c)
Pita Medium (S_1)	$$\frac{dS_1}{dt} = -k_{fP}S_1 - k_{aP}S_1T_f + k_{dP}S_2 + k_{bP}S_3 \quad (5.9)$$	$$\frac{dS_1}{dt} = -k_{fP}S_1 - k_{aP}S_1T_f + k_{dP}S_2 + k_{bP}S_3 - k_{aP}\alpha S_1 I_2 + k_{dP}\alpha I_4 \quad (5.10)$$
Pita Transporter (S_2)	$$\frac{dS_2}{dt} = k_{aP}S_1T_f - (k_{dP}+k_{tP})S_2 \quad (5.11)$$	$$\frac{dS_2}{dt} = k_{aP}S_1T_f - (k_{dP}+k_{tP})S_2 - k_{aE}\alpha S_2 I_1 + k_{dE}\alpha I_4 \quad (5.12)$$
Pita Intracellular (S_3)	$$\frac{dS_3}{dt} = k_{fP}S_1 + k_{tP}S_2 - (k_{bP}+k_{eP})S_3 \quad (5.13)$$	$$\frac{dS_3}{dt} = k_{fP}S_1 + k_{tP}S_2 - (k_{bP}+k_{eP})S_3 + k_{tP}\alpha I_4 \quad (5.14)$$

Table 5.1 continued...

	Competitive Inhibition (Model 1, Fig. 5.1b)	Non-Competitive Inhibition (Model 2, Fig. 5.1c)
Etm Medium (I_1)	$$\frac{dI_1}{dt} = -\boldsymbol{k_{fE}I_1} - k_{aE}I_1T_f + k_{dE}I_2 + \boldsymbol{k_{bE}I_3} \quad (5.15)$$	$$\frac{dI_1}{dt} = -\boldsymbol{k_{fE}I_1} - k_{aE}I_1T_f + k_{dE}I_2 \\ + \boldsymbol{k_{bE}I_3} - k_{aE}\alpha S_2 I_1 + k_{dE}\alpha I_4 \quad (5.16)$$
Etm Transporter (I_2)	$$\frac{dI_2}{dt} = k_{aE}I_1T_f - (k_{dE} + \boldsymbol{k_{tE}})I_2 \quad (5.17)$$	$$\frac{dI_2}{dt} = k_{aE}I_1T_f - (k_{dE} + \boldsymbol{k_{tE}})I_2 \\ - k_{aP}\alpha S_1 I_2 + k_{dP}\alpha I_4 \quad (5.18)$$
Etm Intracellular (I_3)	$$\boldsymbol{\frac{dI_3}{dt}} = \boldsymbol{k_{fE}I_1} + \boldsymbol{k_{tE}I_2} - \boldsymbol{k_{bE}I_3} \quad (5.19)$$	$$\boldsymbol{\frac{dI_3}{dt}} = \boldsymbol{k_{fE}I_1} + \boldsymbol{k_{tE}I_2} - \boldsymbol{k_{bE}I_3} \quad (5.20)$$
Pita-Transporter -Etm complex (I_4)		$$\frac{dI_4}{dt} = k_{aP}\alpha S_1 I_2 + k_{aE}\alpha S_2 I_1 \\ - (k_{dP} + k_{dE} + k_{tP})\alpha I_4 \quad (5.21)$$
Observations (nmol/ml)	$$y_1 = \frac{1}{V_{cell}}(S_2 + S_3) \quad (5.22)$$	$$y_1 = \frac{1}{V_{cell}}(S_2 + S_3 + I_4) \quad (5.23)$$
Etm (if included)	$$y_2 = \frac{1}{V_{cell}}(I_2 + I_3) \quad (5.24)$$	$$y_2 = \frac{1}{V_{cell}}(I_2 + I_3 + I_4) \quad (5.25)$$

$X = S$ = pitavastatin (Pita), or I = eltrombopag (Etm), X_1, X_2 and X_3 are amounts in the medium, bound to the transporter and intracellular respectively, I_4 is the Pita-transporter-Etm complex. Unless stated, all the units for the micro-rate constants are /min/10^6 cells, k_{fX} and k_{bX} = passive rate constant into out of the cell, k_{aX}, k_{dX} and k_{tX} = transporter association (/nmol/min), dissociation and translocation into the cell, T_f is the total amount of free transporters (nmols, 5.2), k_{eP} = Pita metabolism rate constant and α = unitless non-competitive inhibition constant, bold = only if Etm measured

94

Table 5.2: Macro-rate constant models for competitive and non-competitive inhibition

Compartment	Pita Only (Fig. 5.1d)		Pita Only (Fig. 5.1d)	
Pita Medium (S_{1A})	$\dfrac{dS_{1A}}{dt} = -k_{fP}S_{1A} - \dfrac{V_{max.P}S_{1A}}{K_{m.P}+S_{1A}} + k_{bP}S_{3A}$	(5.26)	$\dfrac{dS_{1A}}{dt} = -k_{fP}S_{1A} - \dfrac{V_{max.P}S_{1A}}{K_{m.P}+S_{1A}} + k_{bP}S_{3A}$	(5.27)
Pita Intracellular (S_{3A})	$\dfrac{dS_{3A}}{dt} = k_{fP}S_{1A} + \dfrac{V_{max.P}S_{1A}}{K_{m.P}+S_{1A}} - (k_{bP}+k_{eP})S_{3A}$	(5.28)	$\dfrac{dS_{3A}}{dt} = k_{fP}S_{1A} + \dfrac{V_{max.P}S_{1A}}{K_{m.P}+S_{1A}} - (k_{bP}+k_{eP})S_{3A}$	(5.29)

	Competitive Inhibition (Model 3, Fig. 5.1e)		Non-Competitive Inhibition (Model 4, Fig. 5.1f)	
Pita Medium (S_1)	$\dfrac{dS_1}{dt} = -k_{fP}S_1 - \dfrac{V_{max.P}S_1}{K_{m.P}\left(1+\frac{I_1}{K_{m.E}}\right)+S_1} + k_{bP}S_3$	(5.30)	$\dfrac{dS_1}{dt} = -k_{fP}S_1 - \dfrac{V_{max.P}S_1}{(K_{m.P}+S_1)\left(1+\frac{I_1}{K_{m.E}}\right)} + k_{bP}S_3$	(5.31)
Pita Intracellular (S_3)	$\dfrac{dS_3}{dt} = k_{fP}S_1 + \dfrac{V_{max.P}S_1}{K_{m.P}(1+\frac{I_1}{K_{m.E}})+S_1} - (k_{bP}+k_{eP})S_3$	(5.32)	$\dfrac{dS_3}{dt} = k_{fP}S_1 + \dfrac{V_{max.P}S_1}{(K_{m.P}+S_1)\left(1+\frac{I_1}{K_{m.E}}\right)} - (k_{bP}+k_{eP})S_3$	(5.33)
Etm Medium (I_1)	$\boldsymbol{\dfrac{dI_1}{dt} = -k_{fE}I_1 - \dfrac{V_{max.E}I_1}{K_{m.E}(1+\frac{S_1}{K_{m.P}})+I_1} + k_{bE}I_3}$	(5.34)		
Etm Intracellular (I_3)	$\boldsymbol{\dfrac{dI_3}{dt} = k_{fE}I_1 + \dfrac{V_{max.E}I_1}{K_{m.E}(1+\frac{S_1}{K_{m.P}})+I_1} - k_{bE}I_3}$	(5.35)		
Observations (nmol/ml)	$y_1 = \dfrac{1}{V_{cell}}S_3$	(5.36)	$y_1 = \dfrac{1}{V_{cell}}S_3$	(5.37)
Etm (if included)	$y_2 = \dfrac{1}{V_{cell}}I_3$	(5.38)	$y_2 = \dfrac{1}{V_{cell}}I_3$	(5.39)

$X = S$ or P = pitavastatin (Pita), or $X = I$ or E = eltrombopag (Etm), $V_{max.X}$ and $K_{m.x}$ are the maximum uptake velocity and amount at half of the $V_{max.X}$, k_{eP} = Pita metabolism rate constant, bold = only if Etm measured

5.2.6.2 Parameter Estimation

The final chosen model was based on the weighted Bayesian information criterion ($wBIC$, Eq.5.43) to more harshly penalise over-parameterisation (Eq. 5.42) within the same set of observations compared to Akaike information criterion (AIC, Eq. 5.41) [211, 212] (with or without eltrombopag measurement), as well as the sum of the individual and population prediction of the relative mean square root error (RMSRE) given by:

$$\% \ RMSRE = 100 \times \sqrt{\frac{1}{n} \sum \left(\frac{Observed_i - Predicted_i}{Observed_i} \right)^2}, \tag{5.40}$$

$$AIC = -2.\mathcal{LL}(\theta) + 2p \tag{5.41}$$

and

$$BIC = -2.\mathcal{LL}(\theta) + log(n)p, \tag{5.42}$$

$$wBIC_i = \frac{exp(-0.5\Delta_i)}{\sum_i^m exp(-0.5\Delta_i)} \tag{5.43}$$

and

$$\Delta_i = BIC_i - BIC_{min} \tag{5.44}$$

where $\frac{1}{n}$ is the inverse of the total number of datapoints multiplied by the sum of the relative square error of each datapoint i. $\mathcal{LL}$ is the log likelihood of the data, n is the total number of data points and p is the number of parameters. Δ_i is the difference between the individual BIC (BIC_i) and the lowest BIC (BIC_{min}) calculated using Eq. 5.44, $exp(-0.5\Delta_i)$ is the relative likelihood and $\sum_i^m$ is the sum of individual i relative likelihoods from the mechanistic models with the same number of datapoints used for parameter estimation (in this case $m = 4$ different models) [212].

As eltrombopag was pre-incubated in the experimental design at 45 nmol/ml (or nmol as the incubation volume = 1 ml) and then diluted to 30 nmol by the addition of pitavastatin, a micro-rate constant model for eltrombopag only was used to obtain initial parameter estimates in Monolix suite 2018R2 (Lixoft, Antony France) (see Fig.5.3). These parameter estimates were then used in a simulation at the 45 nmol using `deSolve` in R [1] to obtain initial conditions for the simultaneous analysis of pitavastatin and eltromobopag, and fitted as free-parameters in the final model. Parameter estimation for the mechanistic models was conducted within Monolix suite 2018R2 (Lixoft, Anthony France), where to ensure positivity, a log-normal distribution was assumed for each parameter in the candidate models, together with a proportional residual error model for the observations (see Table 5.1 Eqs. 5.22-5.25 and Table 5.2 Eqs. 5.36-5.39 for micro-rate constant and macro-rate constant observations respectively).

Due to the large number of parameters to be estimated in the combined pitavastatin and eltrombopag mechanistic models, initial estimates for pitavastatin, and eltrombopag only were obtained for the micro-rate constant models (no macro-rate constant estimates could be obtained for eltrombopag alone). In all the datasets, the pitavastatin
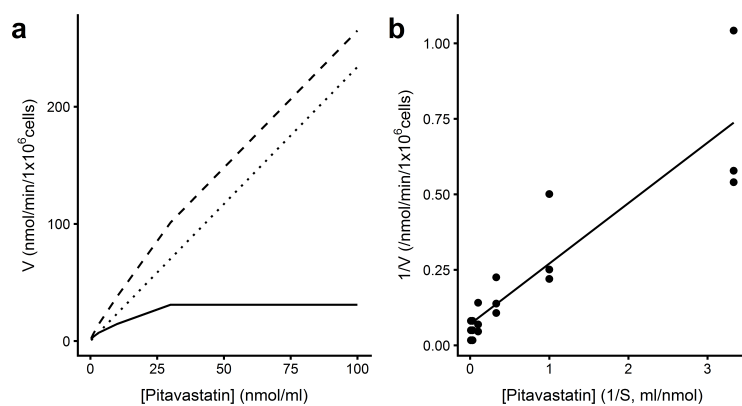
Figure 5.2: **a** Yamazaki plot of initial velocity at 15 s against pitavastatin incubation concentration, dashed line = total, dotted line = passive, solid line = saturable uptake. Approximate parameters V_{max} = 300 pmol/min/10^6 cells, K_m = 10 nmol/ml **b** Lineweaver-Burke (double reciprocal) plot using "Active" from **a**. Parameter estimates V_{max} =1/y intercept= 141 pmol/min/10^6 cells (RSE = 36 %), K_m = gradient $\times V_{max}$= 28 nmol/ml (RSE = 21 %)
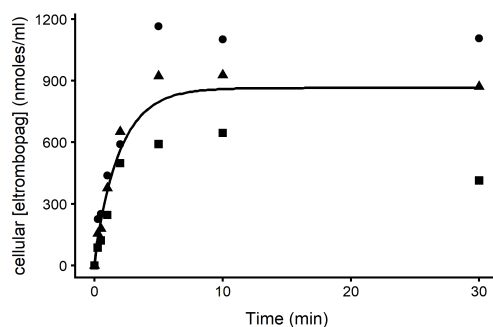
Figure 5.3: Plot of eltrombopag cellular concentration against time following a 30 nmol incubation. Shapes are the experimental data from 3 separate experiments, and the solid line is the simulation of eltrombopag (see Table 5.1 Eqs. 5.3, 5.5 and 5.7, without k_{eP})

data at an incubation concentration of 100 nmol/ml was excluded from one experiment (Triangles in Figs.5.4 and 5.6) due to the large concentrations present compared to the other experiments. The large concentrations adversely affected the total amount of transporters available for uptake to more than double the rest of dataset, and therefore the fits and parameter estimates were also affected. To enable comparisons of the micro-rate constants to those commonly used in the literature, parameters were scaled under the pseudo steady-state assumptions to $V_{max.X}$, $K_{M.X}$, $K_{I.X}$ and $K_{inact.E}$, as discussed in Chapter 2, Section 2.4.4. To obtain initial parameter estimates for the uptake of pitavastatin in the macro-rate constant models (Models 3 and 4, pitavastatin only) a Yamazaki plot and Lineweaver-Burke plot were used (Fig. 5.2a and b respectively). The V_{max} and K_m initial parameter estimates were quite different between the two methods with a 3-fold difference between the methods (V_{max} = 300 and 141 (RSE = 36 %) pmol/min/10^6 cells respectively, K_m = 10 and 28 (RSE = 21 %) nmol/ml respectively), possibly due to a larger influence in the Yamazaki plot of the higher velocities in the mean value (see Fig. 5.2b points).

Figure 5.4: Plots of hepatocyte cell concentration against time over 30 min for pitavastatin (0.3-100 nmol, blue, normalised to $t = 15$ min) with and without 15 min pre-incubation with eltrombopag (red). Points are data from three separate experiments. Solid and dashed lines are the median pitavastatin individual fits from Model 1 with measurement of eltrombopag (see Table 5.4). The shaded areas are the maximum and minimum individual fits from Monolix

5.3 Results and Discussion

5.3.1 Structural Identifiability Analysis

All candidate models (four micro-rate constant models, Table 5.1, and four macro-rate constant models, Table 5.2) were evaluated to determine whether, inclusion of the cellular measurment of eltrombopag in addition to the measurement of cellular pitavastatin aided in the structural identifiability outcomes within the `Identifiability Analysis` package [16, 160]. For the micro-rate constant models (Models 1 and 2), measurement of the cellular amount of eltrombopag did not alter the structural identifiability result, with all four models at least locally structurally identifiable, with no parameters unidentifiable as long as the initial conditions were known (see Table 5.3). For the macro-rate constant models (Models 3 and 4), measurement of eltrombopag was needed for the models to be at least locally structurally identifiable (see Table 5.3), otherwise there was one degree of freedom, with one of the following parameters to be known (for Models 3 and 4 respectively) for the model to be at least structurally locally identifiable: $K_{m.P}$ or $K_{I.E}$, and $V_{max.P}$ or $K_{inact.E}$.

5.3.2 Mechanistic Modelling and Parameter Estimates

Out of the eight mechanistic models evaluated (see Tables 5.1 and 5.2), regardless of whether eltrombopag was measured or not, the micro-rate constant model versions were always the best fitting model (Model 1), with $wBIC$ values ≈ 1 (see Table 5.4, highlighted in bold) compared to the macro-rate constant models (Model 3). In the absence
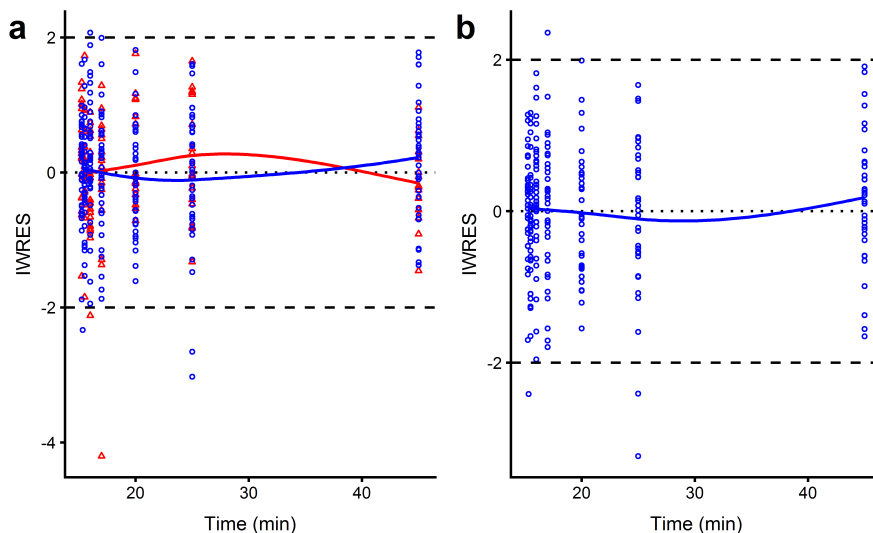
Figure 5.5: Plot of individual weighted residuals (IWRES) obtained from Monolix 2018 R2 against time for Model 1 in the presence of eltrombopag. **a** pitavastatin (blue circles) and measured eltrombopag (red triangles). **b** pitavastatin without measured eltrombopag. Solid line is the LOESS, dashed lines are the 95 % CI and the dotted line highlights an IWRES of 0

of measured eltrombopag the macro-rate constant models (Models 3 and 4) had the largest % RMSRE values for the individual predictions (RMSRE = 16 %), population predictions (RMSRE = 42 and 46 % for competitive inhibition (Model 3) and non-competitive inhibition (Model 4) respectively) and thus a total % RMSRE (58 and 62 % respectively, see Table 5.4), and were ranked as 7th and 8th of all models tested (see Table 5.4). This confirmed the structural identifiability analysis results demonstrating the utility of a formal structural identifiability analysis *a priori* (Table 5.3).

The overall best fitting mechanistic model to the data based on the total % RMSRE and *wBIC* was the micro-rate constant model, including measurement of eltrombopag for mutual competitive inhibition (Model 1, Fig. 5.1a and b, RMSRE = 41 % and *wBIC* $\approx$ 1, Table 5.4). No model accurately fitted to the population data, with residuals that were 3-4 times higher than the individual prediction residuals (see Table 5.4), therefore all parameter estimates described below use the individual mode of the conditional distribution (min-max).

The improvement of fit using micro-rate constants against macro-rate constants was also discussed by Grandjean et al. [8] who also evaluated the uptake of pitavastatin in human hepatocytes, and that work is concurrent with the comparison of models drawn here.

The best fitting micro-rate constant model (Model 1, with measurement of eltrombopag) fitted the individual data well (Fig. 5.4), with an initial increase in the pitavastatin concentration at lower doses in the cell to a maximum followed by a decrease due to loss from the cell via metabolism (0.3-10 nmol/ml incubation, Fig. 5.4, solid lines). As the dose of pitavastatin increased (30 and 100 nmol/ml incubation), the uptake was saturated, and a decrease in concentration could not be observed (Fig. 5.4),

due either to saturation of metabolism or the large concentration of pitavastatin in the cell, masking the metabolism. In the presence of eltrombopag, the transporter mediated uptake of pitavastatin was reduced (Fig. 5.4, dotted lines), which could be overcome by increasing the pitavastatin dose, until the fits overlapped the pitavastatin only data at 30 and 100 nmol incubation (Fig. 5.4).

The individual weighted residuals (IWRES) for pitavastatin in the presence of eltromboag had a mean of around zero, with visually normally distributed errors, whether eltrombopag was measured (Fig. 5.5a blue circles for pitavastatin and red triangles for eltrombopag respectively) or not (Fig. 5.5b blue circles).

The macro-rate constant best fitting model (Model 3, with measured eltrombopag see Table 5.4) fit the uptake of pitavastatin and its inhibition by eltrombopag well (Fig. 5.6). However, the elimination through metabolism was not well fitted (flat blue and dotted red line, Fig. 5.6), and was due to a 12-fold lower pitavastatin elimination rate constant for the macro-rate constant model (Model 3, with measured eltrombopag, k_{eP} = 0.018 (0.014-0.021) /min/10^6 cells, Table 5.6), compared to the micro-rate constant model (Model 1, with measured eltrombopag, k_{eP} = 0.22 (0.2-0.24) /min/10^6 cells, Table 5.5).

Table 5.3: Identifiability analysis summary of the tested models (Fig. 5.1, Models 1-4, Tables 5.1 and 5.2), assuming known initial conditions and observations for each model

Model	Observations	Inhibition Type	Equations	Initial Conditions	No. of unknowns Parameters	No. of unknowns States*	Result	No. of parameters to be identifiable (d.o.f.)
Micro-rate constant models								
1	No measurement of etm	Competitive	5.9, 5.11, 5.13, 5.15, 5.17, 5.22	[Y,0,0,Y,Y]	9	5	SI	0
1	Measurement of etm	Competitive	5.9, 5.11, 5.13, 5.15, 5.17, 5.19, 5.22, 5.24	[Y,0,0,Y,Y,Y]	12	6	SI	0
2	No measurement of etm	Non-competitive	5.10, 5.12, 5.14, 5.16, 5.18, 5.21, 5.23	[Y,0,0,Y,0]	10	6	SI	0
2	Measurement of etm	Non-competitive	5.10, 5.12, 5.14, 5.16, 5.18, 5.20, 5.21, 5.23, 5.25	[Y,0,0,Y,Y,0]	13	7	SI	0
Macro-rate constant models								
3	No measurement of etm	Competitive	5.30, 5.32, 5.36	[Y,0]	6	2	U	1: $K_{m.P}$ or $K_{I.E}$
3	Measurement of etm	Competitive	5.30, 5.32, 5.34, 5.35, 5.36, 5.38	[Y,0,Y,Y]	9	4	SI	0
4	No measurement of etm	Non-competitive	5.31, 5.33, 5.36	[Y,0]	6	2	U	1: $V_{max.P}$ or $K_{inact.E}$
4	Measurement of etm	Non-competitive	5.31, 5.33, 5.34, 5.35, 5.36, 5.38	[Y,0,Y,Y]	9	4	SI	0

d.o.f. = degrees of freedom, * = identifiability analysis conducted without inclusion of pitavastatin only Eqs.5.3-5.7 and 5.26-5.28 for micro and macro-rate constant models respectively, etm = eltrombopag, Y = positive integer, SI = structurally identifiable (local) , U = unidentifiable.

Table 5.4: Goodness of fit value comparison for the micro and macro-rate constant parameter models for the uptake of pitavastatin and its inhibition by eltrombopag (with and without measurement of eltrombopag). Bold indicates best fitting model within the measurement type according to the wBIC and % RMSRE across measurement types

Model	Rank order*	Model Type	Inhibition Type	Measured	BIC (wBIC)	% RMSRE (ind + pop = total)
1	1	**Micro rate**	**Competitive**	**Pita and etm**	**2652 (1)**	**7 + 34 = 41**
2	2	Micro rate	Non-competitive	Pita and etm	2681 (0)	7 + 31 = 38
1	3	**Micro rate**	**Competitive**	**Pita**	**1096 (1)**	**9 + 38 = 47**
3	4	Macro rate	Competitive	Pita and etm	2871 (0)	13 + 34 = 47
2	5	Micro rate	Non-competitive	Pita	1117 (0)	9 + 39 = 48
4	6	Macro rate	Non-competitive	Pita and etm	2877 (0)	13 + 36 = 49
3	7	Macro rate	Competitive	Pita	1386 (0)	16 + 42 = 58
4	8	Macro rate	Non-competitive	Pita	1378 (0)	16 + 46 = 62

* = Based on total % RMSRE (Eq.5.40) and wBIC (Eq. 5.43)

It was important that when eltrombopag measurements were included, that the model was able to adequately describe the pitavastatin and eltrombopag data as well. Model 1 (Table 5.1, with measurement of eltrombopag), with a $wBIC \approx 1$ (see Table 5.4) included eltrombopag initial conditions obtained from the eltrombopag only data at 30 nmol (see Fig. 5.3) as free parameters in the mechanistic model (final individual parameter values, Model 1 (min-max): 19.6 (18.9-20) nmol, 0.002 (0.002-0.003) nmol and 2.84 (1.37-4.37) nmol for medium (I_1), transporter (I_2) and cell (I_3) respectively). The inclusion of the initial conditions as free parameters for eltrombopag was important, due to the pre-incubation step of eltrombopag from 45 nmol to a nominal 30 nmol, which based on the dilution of eltrombopag with pitavastatin at 15 min and was not known. The total initial amount (22.4 (20.3-24.4) nmol) was similar to the nominal dose (30 nmol) after dilution from 45 nmol. Due to the variability in the data (see Fig. 5.3 data points), the plotted eltrombopag was normalised to the maximum from the geometric mean of the eltrombopag only data at 30 nmol to give a percentage value. When pitavastatin was not present (dose = 0 nmol, Fig. 5.7), there was an initial rapid increase in eltrombopag concentration followed by a decrease after 5 min. After the dilution of eltrombopag through the addition of pitavastatin doses (0.3-100 nmol), there was an initial decrease in the eltrombopag concentration, to a new lower asymptote (Fig. 5.7). In the presence of higher concentrations of pitavastatin (30-100 nmol incubation), the amount of intracellular eltrombopag decreased to a lower asymptote compared to the lower doses (0.3-10 nmol) as the eltrombopag uptake was inhibited (Fig. 5.7).

5.3.2.1 Passive Rate Constant and Binding

In the best fitting micro-rate constant model (Model 1, with measurement of eltrombopag), the passive movement of pitavastatin into the cell ($k_{fP} = 0.00055$ (0.00046-0.00061) /min/10^6 cells) was much slower ($\approx$400 fold) than the passive movement of pitavastatin out of the cell ($k_{bP} = 0.21$ $(0.18 - 0.22)$ /min/10^6 cells) (see Table 5.5). For eltrombopag, the passive movement into the cell for Model 1 ($k_{fE} = 0.05$ $(0.04 - 0.06)$ /min/10^6 cells, Table 5.5) was 10-fold slower than the passive movement out of the cell ($k_{bE} = 0.43$ $(0.35 - 0.65)$ /min/10^6 cells, Table 5.5). k_{fE} was 100 times faster than k_{fP}, whilst k_{bE} was of the same order of magnitude as k_{bP}. The passive rate constants for pitavastatin and eltrombopag for the other micro-rate constant models were the same as described above (see Table 5.5).

In the best fitting macro-rate constant model (Model 3, with measurement of eltrombopag, see Table 5.4), the passive rate constant into the cell for pitavastatin ($k_{fP} = 0.0047$ $(0.0045 - 0.0047)$ /min/10^6 cells, Table 5.6) was approximately 10 times faster than for the micro-rate constant model (Model 1, see Table 5.5). The passive rate constant out of the cell for pitavastatin ($k_{bP} = 1.04$ $(0.54 - 1.42)$ /min/10^6 cells, Table 5.6) was 5 times faster than for the micro-rate constant model (Model 1, see Table 5.5). The passive rate constant estimates for eltrombopag were around 10-fold faster in Model 3 (with measurement of eltrombopag) ($k_{fE} = 0.86$ $(0.79 - 0.91)$ /min/10^6 cells, $k_{bE} = 5.61$ $(3.98 - 10.7)$ /min/10^6 cells, Table 5.6) compared to the best fitting
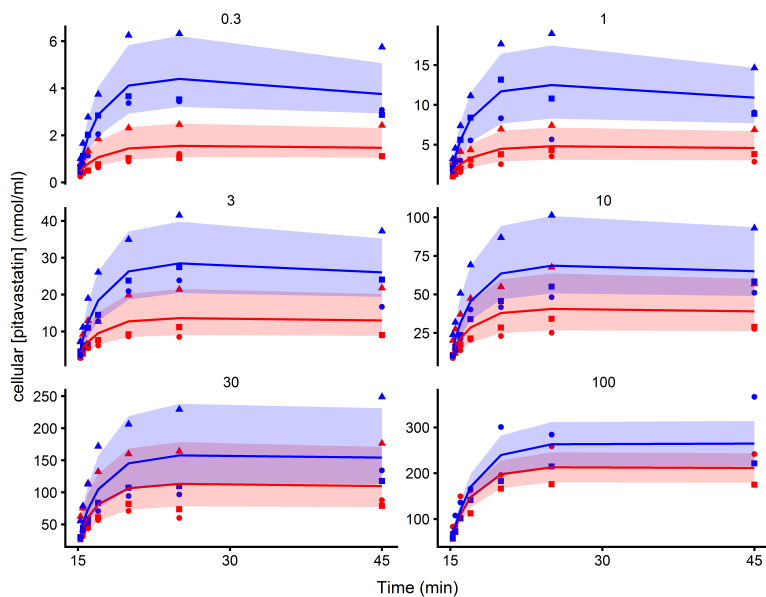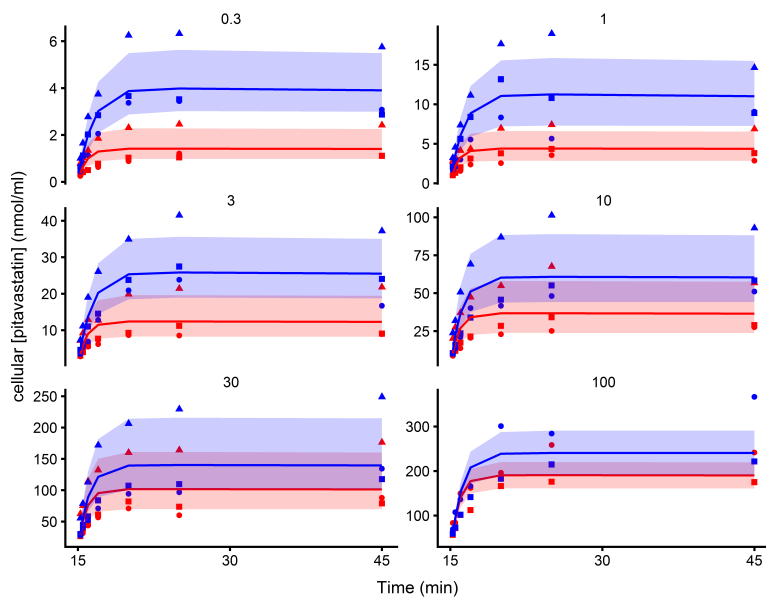
Figure 5.6: Plots of hepatocyte cell concentration against time over 30 mins for pitavastatin (0.3-100 nmol, blue, normalised to $t = 15$ min) with and without 15 min pre-incubation with eltrombopag (red). Points are data from three separate experiments, Solid and dashed lines are the median individual fits from the best fitting macro constant model (see Table 5.4, ranked 4th) in the absence and presence of eltrombopag respectively, and shaded areas are the maximum and minimum individual fits from Monolix

micro-rate constant model (see Table 5.5).

If k_{fP} is scaled up to a passive clearance (P_{dif}), that is commonly used in the literature, by multiplying by the medium volume (1000 μl), the $P_{dif.P}$ for pitavastatin is within the lower range of others in the literature (0.55 (0.46-0.61) μl/min/10^6 cells and 0.4-13 μl/min/10^6 cells [173, 174, 250, 251] respectively). The value scaled up from Grandjean et al. [8] was eight times higher (100 μl/min/10^6 cells) than the largest literature value, and was similar to that seen for more highly permeable drugs such as saquinavir ($P_{dif} = 191$ ($SE = 24$)μl/min/10^6 cells, fraction transported = 52 %, [172]) or glyburide ($P_{dif} = 100$ ($SE = 12$) μl/min/10^6 cells, fraction transported 55 % [250].

If the passive rate constant out of the cell (k_{bP}) is also scaled to a passive clearance ($P_{def.P}$), by multiplying by the cell volume of 3 μl = 0.62 (0.55-0.67) μl/min/10^6 cells, and was similar to the value obtained with micro-rate constants by Grandjean et al. [8] (0.89 (27 %) μl/min/10^6 cells). If $P_{dif.P}$ and $P_{def.P}$ are compared, the passive clearance into and out of the cell are similar when normalised to volume, and confirmed experimentally, with what is assumed in the literature regarding passive movement of drug [173, 174, 250, 251]. However, this assumption does not hold when the dominant uptake process is not transporter mediated, as was the case with eltrombopag in Model 1, with a $P_{dif.E}$ of 52 (40-64) μl/min/10^6 cells and a $P_{def.E}$ of 1.3 (1.05-1.94) μl/min/10^6 cells, and therefore caution should be used when using a single parameter to describe passive movement into and out of the cell.

When a single parameter to describe passive movement of drug, the fraction unbound in the cell ($f_{u.cell}$) is used in the literature to allow for intracellular binding on

103
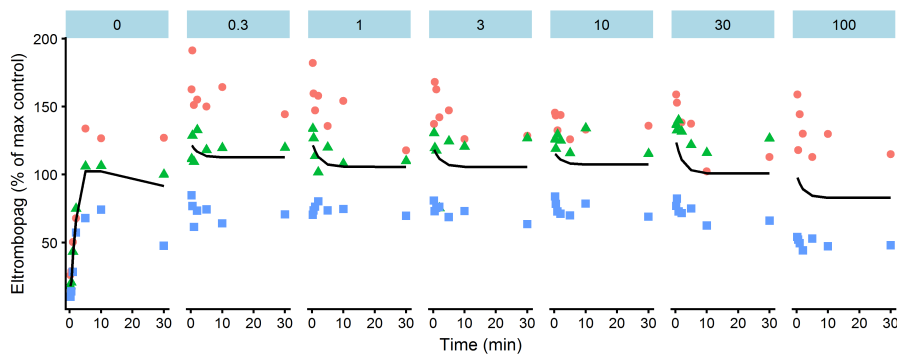
Figure 5.7: Plots of % of the maximum eltrombopag only cellular concentration against time over 30 min for eltrombopag in the presence of pitavastatin (0.3-100 nmol) added at $t = 15$ min, (normalised to $t = 0$ min). Shapes are data from three separate experiments. Solid lines are the median individual fits from the best fitting micro-rate constant model (Model 1, Table 5.4). Sub-plots are separated by dose of pitavastatin and eltrombopag only control (0)

the passive movement out of the cell [172, 173]. Estimates for $f_{u.cell}$ can be obtained using multiple techniques: heat inactivated hepatocytes [165]; linear regression obtained using the $\log D_{pH\ 7.4}$ across different compounds [172]; parameter estimation [164, 173] or as separate binding rate constants, either through separate experiments [170] or during parameter estimation as membrane binding [165, 250]. We used heat inactivated human hepatocytes across the concentrations used in the experiments, with pitavastatin (0.3, 10 and 100 nmol/ml) or 30 nmol/ml of eltrombopag, which were then incubated overnight in a Rapid Equilibrium Dialysis (RED) device. The RED device works with low volumes across a medium chamber (500 μl) and incubation chamber containing the hepatocytes (300 μl), and as such has been reported to even out the non-specific binding (NSB) between the membrane and wells, thereby improving recovery [252]. The free fraction in the incubation ($f_{u.inc}$) is calculated as:

$$f_{u.inc} = \frac{[\text{medium chamber}]\ (\text{White})}{[\text{incubation chamber}]\ (\text{Red})}. \tag{5.45}$$

The amount of non-specific binding to the labware used in the RED device experiment is important to gain information regarding the recovery of pitavastatin or eltrombopag:

$$\%\ \text{recovery} = 100 \times \frac{300 \cdot \text{Red} + 500 \cdot \text{White}}{300 \cdot (\text{incubation concentration})}. \tag{5.46}$$

For pitavastatin, the $f_{u.inc}$ values were similar at 0.3 and 10 nmol/ml (0.87 (9 % relative standard deviation (% RSD)) and 0.93 (4 %) respectively), whilst at 100 nmol/ml the data were unreliable ($f_{u.inc} > 1$). For eltrombopag the $f_{u.inc}$ following a 30 nmol incubation was 0.04 (5 %). The % recovery for both pitavastatin and eltrombopag was low at 55 % (3 %) and 10 % (5 %), and this may be due to the lack of a RED device washing step prior to use in the experiment [252]. The $f_{u.cell}$ value can be estimated

using the method of Paine et al. [165]:

$$f_{u.cell} = \frac{V_{cell}}{\frac{V_{inc}}{f_{u.inc}} - V_{medium} - k_{mem}} \tag{5.47}$$

where V_{cell} was 3.6 μl for 1.2×10^6 cells, the experimental incubation volume (V_{inc}) was 1203.6 μl, V_{medium} was 1200 μl and k_{mem} was the membrane volume fraction (1 % of the total volume = 0.0036 μl, [165]).

The low recovery for pitavastatatin and eltrombopag makes the use of $f_{u.cell}$ in data analysis unreliable. If the fraction unbound was to be included in the mechanistic models used here (see Tables 5.1 and 5.2), then the model would be structurally unidentifiable as $f_{u.cell}$ is already included in the rate constants themselves and the parameter would be inestimable as the value always approached 1 when not fixed.

5.3.2.2 Micro-Rate Constant Transporter Mediated Uptake

The transporter association rate constant (k_{aX}) and dissociation rate constant (k_{dX}) were similar between pitavastatin and eltrombopag in the best fitting micro-rate constant model (Model 1, with measurement of eltrombopag, $k_{aX} = 0.17$ (0.14-0.25) and 0.26 (0.23-0.31) /nmol/min/10^6 cells, $k_{dX} = 2.2(1.97-2.37)$ and 1.57 (1.42-2) /min/10^6 cells respectively, Table 5.5), suggesting similar binding kinetics to the transporter.

The translocation rate into the cell (k_{tX}) was six times faster for pitavastatin than for eltrombopag (Model 1, with measurement of eltrombopag, 1.65 (1.57-1.74) and 0.27 (0.24-0.32) /min/10^6 cells respectively, Table 5.5), and was what defined the difference in transporter mediated uptake between the two substrates. The transporter mediated parameters were similar across all micro-rate constant models (Models 1 and 2), with the exception of the eltrombopag translocation rate constant ($k_{tE} = 0.0004$ $(0.0003-0.0005)$ /min/10^6 cells) which was 1000 fold slower in the non-competitive inhibition model than the competitive inhibition model (see Table 5.5) probably due to k_{tE} being unaffected by α in the model structure (Eq. 5.18).

The k_{aP} value obtained for pitavastatin in human hepatocytes over 70 s in the literature was 44-fold faster (7.4 (51 %) /nmol/min/10^6 cells, [8]) than the k_{aP} value obtained here, whilst the k_{dP} and k_{tP} were of the same order of magnitude ($k_{dP} = 6.3$ /min/10^6 cells (not able to calculate error, [8]) and $k_{tP} = 4.3$ (85 %) /min/10^6 cells, [8]). The extended timepoints used here up to 30 min post addition of pitavastatin (compared to 70 s), also enabled the standard errors of the dissociation rate constant from the transporter (k_{dP}) to be determined and reduced error on k_{tP} estimated from the data.

Table 5.5: Micro-rate constant individual parameter estimates for pitavastatin in the presence of eltrombopag. Data are individual mode of the conditional distribution from three separate experiments (Min-Max). All parameter estimates are *per* million cells

Parameter Estimate	Pita and etm measured		Pita Only Measured	
	Competitive (Model 1)	Non-Competitive (Model 2)	Competitive (Model 3)	Non-Competitive (Model 4)
Passive				
k_{fP} (/min)	0.00055 (0.00046-0.00061)	0.00099 (0.0009-0.0010)	0.00078 (0.00058-0.00099)	0.00065 (0.00054-0.00068)
k_{bP} (/min)	0.21 (0.18-0.22)	0.14 (0.12-0.17)	0.24 (0.19-0.27)	0.16 (0.15-0.17)
k_{fE} (/min)	0.05 (0.04-0.06)	0.04 (0.03-0.05)	N/C	N/C
k_{bE} (/min)	0.43 (0.35-0.65)	0.42 (0.37-0.57)	N/C	N/C
Transporter				
k_{aP} (/nmol/min)	0.17 (0.14-0.25)	0.19 (0.16-0.23)	0.26 (0.25-0.26)	0.19 (0.15-0.26)
k_{aE} (/nmol/min)	0.26 (0.23-0.31)	0.13 (0.12-0.14)	0.11 (0.09-0.12)	0.06 (0.05-0.09)
k_{dP} (/min)	2.2 (1.97-2.37)	2.8 (1.66-4.35)	3.08 (2.19-3.58)	3.18 (2.26-3.86)
k_{dE} (/min)	1.57 (1.42-2)	0.24 (0.19-0.42)	1.38 (1.28-1.52)	1.13 (1.06-1.22)
T_o (nmols)	0.18 (0.11-0.37)	0.14 (0.11-0.29)	0.13 (0.08-0.28)	0.15 (0.12-0.26)
k_{tP} (/min)	1.65 (1.57-1.74)	1.61 (1.45-1.72)	1.9 (1.72-2.07)	1.86 (1.61-2.12)
k_{tE} (/min)	0.27 (0.24-0.32)	0.0004 (0.0003-0.0005)	N/C	N/C
α	N/C	0.13 (0.12-0.15)	N/C	0.07 (0.07-0.08)
Metabolism				
k_{eP} (/min)	0.22 (0.2-0.24)	0.25 (0.23-0.29)	0.19 (0.18-0.2)	0.24 (0.22-0.27)

The total amounts of transporters ($T_o = 0.18$ $(0.11 - 0.37)$ nmol/10^6 cells) determined from this data set for pitavastatin and eltrombopag are difficult to compare to measured values of uptake transporters obtained from hepatocytes or liver tissue, which vary across papers and ethnicity due to SNPs in the transporters (see Chapter 2). For pitavastatin, hOATP1B1 dominates the uptake process, with a minor contribution from hOATP1B3 [132], whilst for eltrombopag it is assumed that passive dominates, but it is also a substrate of hOATP1B1 and hOCT1 [245]. The total hepatic abundance of hOATP1B1, hOATP1B3 and hOCT1 in Caucasians obtained during a meta-analysis of literature data from liver tissue was $\sim$ 11 pmol/10^6 cells [57], which is 16-fold lower than the T_o value, assuming that only one transporter site moves one molecule into the cell. Unlike in HEK293-OATP1B1 cell-lines, where the amount of protein in hOATP1B1 containing cells and MOCK cells was measured to obtain an estimate of membrane hOATP1B1 associated protein, making the scale up of the T_o more simplistic (see Chapter 3), there are no such measurements here. The majority of the hepatocyte donors used in this study were Caucasian, with one Hispanic and one African-American, with a minimum age of 10 month old, a 4 year old female, with a maximum age of 60 years old (Appendix E). The hOATP1B1*14*14 polymorphism is present in 0.74-0.77 of African-Americans, and 0.3-0.51 of Caucasians [55] who all have increased hOATP1B1 protein expression in hepatocytes and therefore an increase in the maximum uptake velocity (V_{max}), leading to a decrease in the predicted plasma exposure of statins, due to an increased liver uptake [56]. Infants upto 1 year old have been shown to have significantly lower hepatic mRNA for hOATP1B1, hOATP1B3 and hMRP ($p = 0.05$) [253], which may also affect the total amount of transporters if the amount of protein was also decreased significantly. It is not currently known how many molecules are transported when a molecule binds to the active transporter site. Site-directed mutagenesis studies have built on the multiple affinities seen for estrone-3-sulphate, and analysed the data via Eadie-Hoffstee plots to evaluate changes in the Michaelis-Menten kinetics [254]. It is within these mutagenesis experiments, through analysis with micro-rate constants (already discussed in the article, but not instigated, [254]), that more understanding regarding how T_o determined here relates to the number of substrate moieties transported.

The covariance matrix derived from the inverse of the Fisher information matrix (obtained through linearisation in Monolix 2018R2, as the Fisher information matrix could not be obtained through the SAEM algorithm (see Chapter 2, Section 2.4.5)) [190] can be used to evaluate the practical identifiability of the model, assuming that all the unknown parameters are independent, i.e. the off-diagonal elements are zeros [184, 216]. Using the estimated individual random effects (η, taken from Monolix 2018R2) for Model 1 (with and without measurement of eltrombopag), a covariance matrix was generated in R Studio using `GGally` [217] (see Fig. 5.9 and 5.8 respectively). k_{bP} and k_{eP} had a covariance of 1 with and without measurement of eltrombopag (Fig. 5.9 and 5.8 respectively), which given that the final parameter estimates for these parameters were the same (see Table 5.5) is not unsurprising and furthers the need to

	kfP	kbP	kaP	kdP	To	ktP	keP	kaE	kdE
kdE									
kaE									-0.6
keP								0.2	-0.4
ktP							-0.6	-0.4	0.5
To						-0.2	0.2	-0.1	-0.3
kdP					-0.3	-0.5	0.4	0.6	-0.4
kaP				-0.3	0.9	-0.2	0.1	-0.1	-0.2
kbP			0.2	0.4	0.3	-0.7	1	0.2	-0.5
kfP		-0.6	-0.2	-0.5	-0.2	0.7	-0.6	-0.5	0.7
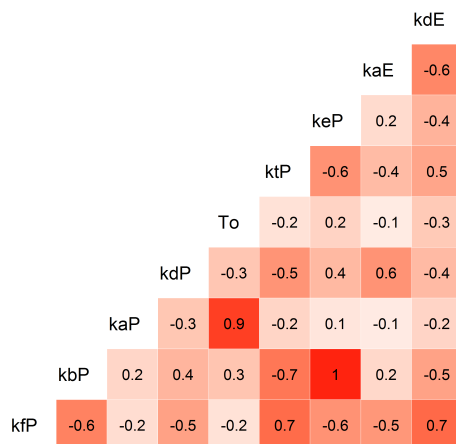
Figure 5.8: Covariance matrix of the individual random effects η for Model 1 without measurement of eltrombopag

separate the covariance between the two parameters, potentially through quantification of pitavastatin metabolites and inclusion in the mechanistic model. The covariance of 0.9 between k_{aP} and T_o was the same as that seen in Chapter 3, but not Chapter 4, where there was less limitation in terms of number of cells and possible experiments.

The large error observed with the measurement of eltrombopag (see Fig. 5.7), and the use of only a single concentration of eltrombopag, lead to a large covariance of -0.9 between k_{fE} and k_{bE} and of 0.9 between k_{dE} and k_{tE} (Fig. 5.9). More experimental data may decrease the covariance between the eltrombopag parameters, but at the cost of an extra vial of cryopreserved human hepatocytes and time on an LC-MS.

5.3.2.3 Macro-Rate Constant Transporter Mediated Uptake

For the best fitting macro-rate constant model (Model 3, with measurement of eltrombopag, Table 5.4 4th ranked model), a similar picture was seen as with the micro-rate constant models. The difference between pitavastatin and eltrombopag was in $V_{max.X}$ estimate (350 (210-1140) and 72 (70-75) pmol/min/10^6 cells respectively, Table 5.6). $K_{m.X}$ values were the same (19.6 (17.4-20.9) and 15 (13.7-16.9) nmol/ml respectively, Table 5.6). The scaled $V_{max.P}$ estimate from micro-rate constant Model 1, with measurement of eltrombopag (see Chapter 2, Section 2.4.4), was similar, but with a smaller range of parameter values ($V_{max.P}$ = 302 (177-639) pmol/min/ 10^6 cells), whilst $K_{m.P}$ was the same (22.1 (16.7-25.5) nmol/ml). The scaled $V_{max.E}$ estimate from micro-rate constant Model 1, with measurement of eltrombopag, was similar, but had a wider range of values compared to the macro-rate constant Model 3, with measurement of eltrombopag ($V_{max.E}$ = 49 (26-118) and 72 (70-75) pmol/min/10^6 cells respectively), and $K_{m.E}$ of around a half of the macro-rate constant estimate from Model 3, with measurement of eltrombopag ($K_{m.E}$ = 7.1 (7.2-9.6) and 15 (13.7-16.9) nmol/ml respectively), that was the same as the inhibition constant $K_{I.E}$ obtained from the micro-rate constant Model 1, with measurement of eltrombopag ($K_{I.E}$ = 6 (6.2-6.5) nmol/ml). $K_{I.P}$ was half of

	kbP	kaP	kdP	To	ktP	keP	kfE	kbE	kaE	kdE	ktE
kdE											0.9
kaE										-0.5	-0.5
kbE									0.2	0	-0.2
kfE								-0.9	-0.1	-0.1	0.2
keP							-0.2	0.1	0	-0.3	-0.4
ktP						-0.6	0	-0.1	-0.2	0.4	0.4
To					0	0.1	0.2	-0.2	-0.2	-0.3	-0.2
kdP				-0.3	-0.6	0.4	0	0.1	0.5	-0.5	-0.5
kaP			-0.3	0.9	-0.1	0	0.1	-0.1	-0.3	-0.2	0
kbP		0.1	0.5	0.2	-0.7	1	-0.2	0.1	0	-0.4	-0.5
kfP	-0.6	0.2	-0.6	0.1	0.8	-0.5	0.2	-0.2	-0.4	0.6	0.7
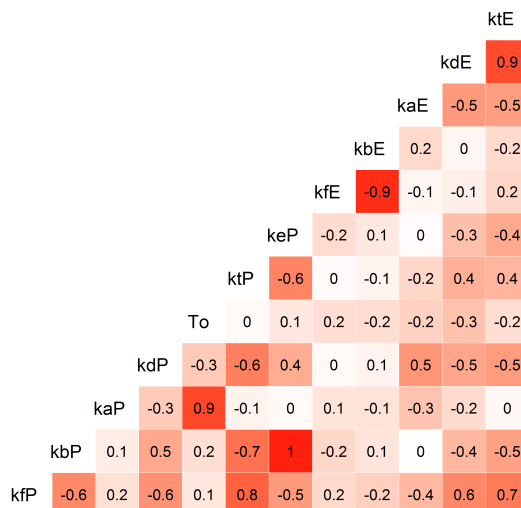
Figure 5.9: Covariance matrix of the individual random effects η for Model 1 including measurement of eltrombopag

$K_{m.P}$ (12.9 (9.5-14) nmol/ml).

Literature values for the uptake of pitavastatin in human hepatocytes show a range for $V_{max.P}$, similar to that seen here using scaled micro-rate constants with a literature $V_{max.P}$ of 65-354 pmol/min/ 10^6 cells [8, 173, 251]. However, $K_{m.P}$ was close to 10-fold lower in the literature (1.4-2 nmol/ml [8, 173, 251]. The discrepancy in $K_{m.P}$ may be driven partly by the variability in our data, with the higher concentration seen in one study (triangles in Fig. 5.4) that had the highest T_o estimates, and thus a higher V_{max} and K_m.

Whilst eltrombopag was reported to show saturable uptake in mouse hepatocytes, attributable to uptake transporters [245], it was reported only as an in inhibitor in the FDA submission document [246]. By measuring eltrombopag here, and relying on the large amount of data for pitavastatin in the presence and absence of eltrombopag, uptake kinetics for eltrombopag were obtained. By dividing V_{max} by K_m, the transporter mediated uptake clearance (CL_{up}) for pitavastatin and eltrombopag can be compared. CL_{up} was twice as fast for the more hydrophilic pitavastatin ($CL_{up.X}$ = 13 (11-26) and 7 (4-12) μl/min/10^6 cells respectively), whilst P_{dif} was 90 times faster for the more lipophilic eltrombopag. The percent of transporter mediated uptake for pitavastatin has been reported to be 90-92 % [250], which was the same here (95 % = $CL_{up}/(CL_{up}+P_{dif})$, if this is compared to eltrombopag, where the percent of transporter mediated uptake was 12 %, it is clear that whilst eltrombopag is an uptake substrate, the passive movement into the cell dominates.

Table 5.6: Macro-rate constant individual parameter estimates for pitavastatin in the presence of eltrombopag. Data are individual mode of the conditional distribution from three separate experiments (Min-Max). All parameter estimates are *per* million cells. $V_{max.up}$ was scaled to pmol/min and K_m, K_I and $K_{inact.E}$ were scaled to nmol/ml

Parameter Estimate	Pita and etm measured		Pita Only Measured	
	Competitive	Non-Competitive	Competitive	Non-Competitive
Passive				
k_{fP} (/min)	0.0047 (0.0045-0.0047)	0.0062 (0.0047-0.017)	0.0067 (0.0061-0.0069)	0.0064 (0.0057-0.0067)
k_{bP} (/min)	1.04 (0.54-1.42)	1.06 (0.53-1.52)	1.05 (0.54-1.52)	1.07 (0.55-1.53)
k_{fE} (/min)	0.86 (0.79-0.91)	0.91 (0.8-1.02)	N/C	N/C
k_{bE} (/min)	5.61 (3.98-10.7)	10.5 (7.3-19.8)	N/C	N/C
Transporter				
$V_{max.P}$ (pmol/min)	350 (210-1140)	250 (180-440)	270 (170-980)	220 (140-870)
$V_{max.E}$ (pmol/min)	72 (70-75)	17.7 (16.8-18)	N/C	N/C
$K_{m.P}$ (nmol/ml)	19.6 (17.4-20.9)	16.2 (13.2-18.1)	20.3 (14.9-23)	16.8 (14.4-19.3)
$K_{m.E}$ or $K_{inact.E}$ (nmol/ml)	15 (13.7-16.9)	36.7 (30.8-47.2)	N/C	N/C
$K_{I.E}$ or $K_{inact.E}$ (nmol/ml)	N/C	N/C	21.6 (18.5-30.7)	58 (44.2-88.9)
Metabolism				
k_{eP} (/min)	0.018 (0.014-0.021)	0.03 (0.03-0.03)	0.021 (0.02-0.022)	0.012 (0.011-0.013)

N/C = not calculated

Table 5.7: Comparison of AUC ratio values (R value) for inhibition of pitavastatin by eltrombopag (K_I = 6-6.5 nmol/ml)

Reference	Bauman et al. [255]	Nieto et al. [243]		Deng et al. [11]
Dose (mg)	50 mg volunteers	50 mg - patients	75 mg patients	75 mg - volunteers
Cmax (nmol/ml)	14	18 (steady-state)	29 (steady state)	25
EMA R value ($\geq$ 1.04)	0.57-0.53	0.75-0.69	**1.1-1.19**	**1.02-0.94**
FDA R value ($\geq$ 1.1)	1.03	1.04	**1.07**	**1.06**

5.3.2.4 Pitavastatin Elimination Rate Constants

The pitavastatin metabolism elimination rate constant obtained from the micro-rate constant models (Model 1, with measurement of eltrombopag, $k_{eP} = 0.22$ (0.2-0.24) /min/10^6 cells) was the same as the passive rate out of the cell ($k_{bP} = 0.21$ (0.18-0.22) /min/10^6 cells, Table 5.5), which shows that whilst the model is structurally locally identifiable, these two parameters can be interchanged (similar to an oral pharmacokinetic 1-compartment model where the elimination rate constant and absorption rate constant can also be changed leading to "flip-flop kinetics [184]). This was confirmed in the covariance matrix where the covariance was 1 between these two parameters (Fig. 5.9 and Fig. 5.8). As mentioned above, one way of potentially separating the covariance between k_{bP} and k_{ep} could be through quantification of pitavastatin metabolites and their inclusion in the mechanistic models. This is not trivial, as the main metabolite seen for pitavastatin in human hepatocytes is pitavastatin lactone, which is also present as an impurity in the dose, and in combination with metabolism leads to similar pitavastatin lactone and the active pitavastatin acid concentrations in human plasma [9, 241]. Menochet et al. [33] included metabolite kinetics for repaglinide and telmisartan and found a decrease in the overall relative mean standard error compared to when they were excluded from analysis and the mechanistic model. It is possible therefore that this may be beneficial here also.

It is interesting to note, that the best-fitting macro-rate constant model (Model 3, with measurement of eltrombpag) showed a clear distinction between k_{bP} and k_{eP} (1.04 (0.54-1.42) and 0.018 (0.014, 0.021) /min/10^6 cells respectively, Table 5.6), however, $k_{e.P}$ did not influence the pitavastatin data fit and gave a flat profile after 5 min that did not follow the data (Fig. 5.6). If the k_{eP} is scaled from the micro-rate constant model (Model 1, with measurement of eltrombopag) to a clearance (by multiplying by 3 μl and dividing by 0.657 mg protein/10^6 cells [181]), then the value of 1 (0.91-1.1 μl/min/mg protein) was similar to that in the literature in human liver microsomes (2.5-3.4 μl/min/mg protein [241, 256]).

5.3.2.5 Clinical Liability - Static Model

Evaluation *in vitro* of the potential for clinical DDIs is important to decrease the risk and to improve patient quality of life. A common method is the static AUC difference in the presence and absence of inhibitor (the R value, first described by Hirano et al. [132]) and is used to assess the potential for clinical DDIs in regulatory guidance documents [18, 19]:

$$\text{FDA R Value} = 1 + \frac{f_{u.plasma}I_{in.max}}{K_I}, \text{ if R} \geq 1.1, \text{ then a TrDDI is likely} \qquad (5.48)$$

$$\text{EMA R Value} = \frac{25 \cdot (f_{u.plasma}I_{in.max})}{K_I}, \text{ if R} \geq 1.04, \text{ then a TrDDI is likely} \qquad (5.49)$$

where $f_{u.plasma}$ is the fraction unbound in the plasma (set to 0.01 for eltrombopag, the minimum value proposed in the FDA draft guidance [19] due to error in measurements below 0.01), K_I is obtained from the best fitting model, and $I_{in.max}$ is calculated according to:

$$I_{in.max} \text{ (nmol/ml)} = \frac{C_{max} + \frac{F_a F_g k_a Dose}{Q_h}}{R_b} \qquad (5.50)$$

where C_{max} is the maximum plasma concentration of the inhibitor (nmol/ml), $F_a F_g$ is the fraction absorbed multiplied by the intestinal availability (pitavastatin=1 [174], eltrombopag = 0.5 [244]), k_a is the absorption rate constant (pitavastatin = 0.1 /min (minimum gastric emptying time, [132]) and eltrombopag = 0.0084 /min [244]), Q_h is human hepatic blood flow = 1450 ml/min [133]), and R_b is the blood:plasma ratio (pitavastatin = 0.425 [209], eltrombopag = 0.78 [244]) and does not appear in the EMA equation (Eq. 5.49).

As there are multiple clinical pharmacokinetic studies for eltrombopag, C_{max} and doses ranged from 14 nmol/ml [255] to 18 nmol/ml [243] at 50 mg in patients, to 25 nmol/ml and 29 nmol/ml at 75 mg in healthy volunteers [11] and patients respectively [243], the calculated R values are summarised in Table 5.7. The clinical risk of a TrDDI according to R values for the FDA guidance were below the cut-off (R value > 1.1) or close to the cut-off (R = 1.06-7 at 75mg), similar to EMA R values at 75 mg (see Table 5.7).

Clinical doses for eltrombopag start at 50 mg, or 25 mg in patients with East Asian ancestry [243], there is less potential for the inhibition of pitavastatin by eltrombopag based on the *in vitro* data presented here. Takeuchi et al. [244] evaluated the inhibition of rosuvastatin by eltrombopag using a PBPK model and found that BCRP inhibition with additional inhibition of hOATP1B1 was the likely cause of the clinical DDI. BCRP is expected to be in intracellular vesicles in human hepatocyte suspensions [257], this inhibition cannot be evaluated in the current experimental set-up, without first plating the cells for several hours. As the dose of eltrombopag is closely monitored in the clinic due to its pharmacological effect [243], the R values were also calculated with eltrombopag as the victim and pitavastatin as the perpetrator. No potential effect was seen, with values all below the cut-offs suggested by the EMA and FDA [18, 19], likely due to the low dose given of pitavastatin (2-4 mg) in the clinic [9, 258, 259] (with an estimated $I_{in.max}$ of 0.5-3 nmol/ml) compared to the estimated $K_{I.P}$ of 13 (9.5-14) nmol/ml from the micro-rate constant model (Model 1, with measurement of eltrombopag).

5.4 Conclusions

This chapter presented a comparison of micro-rate constant and macro-rate constant mechanistic models for the uptake of pitavastatin and eltrombopag and their interaction at the level of transporter mediated in cryopreserved human hepatocytes. The measurement of eltrombopag in the same sample as pitavastatin decreased the residuals

of the individual predictions. Macro-rate constant models (Models 3 and 4) were never the best at fitting to the experimental data based on the *wBIC* with the same number of datapoints and % RMSRE across experimental set-ups. A mutual competitive mode of inhibition for the uptake of pitavastatin and eltrombopag (Model1, including measurement of eltrombopag) was the overall best fitting model of the eight tested.

Future experimental work could evaluate multiple eltrombopag concentrations, as well as extra timepoints taken during the pre-incubation period, so that initial conditions for eltrombopag do not have to be estimated in the model, but would be known from the experimental data. Quantification of metabolites and their inclusion in a micro-rate constant mechanistic model may help to decrease the covariance between k_{bP} and k_{eP} and improve model fits.

With the inclusion of eltrombopag measurements, it was interesting to observe whether this would alter the D-optimal design using `PopED` [195] in R compared to the previous Chapter and improve the number of stable points. Neither the obtained triangular matrix of full matrix design gave any stable points, with the triangular matrix more akin to the design used in the experimental used here (0.25, 0.5, 1, 2, 5, 10 and 30 min). The timepoints are given as follows:

- Triangular Matrix: 0.25, 0.5, 1, 3.2, 6.2, 12.25, 38 min

- Full Matrix: 0.25, 4.25, 10.2, 11.2, 14, 17, 28 min

The scaled micro-rate constants obtained in this chapter will be used in the next chapter in a PBPK model, to evaluate whether the marginal calculated R values from a static model at 75 mg eltrombopag (see Table 5.7 R values in bold) translate in a PBPK model.

Chapter 6

Development of a Semi-Mechanistic Human Physiologically Based Pharmacokinetic Model for the Disposition of Pitavastatin and Eltrombopag

6.1 Overview

This chapter builds on the work presented in the previous chapter with regard to the TrDDI between pitavastatin and eltrombopag and, along with the work in that chapter will be submitted to *CPT: Pharmacometrics & Systems Pharmacology*. The potential for a clinical TrDDI calculated using a static interaction model [18, 19] in the previous chapter (see Chapter 5, Table 5.7), suggested that only at a dose of 75 mg of eltrombopag, was a small potential for an interaction with pitavastatin likely (R value = 1.06-1.07 at 75 mg eltrombopag and 1 mg pitavastatin). Given the large degree of inhibition observed *in vitro* in cryopreserved human hepatocytes with 30 nmol/ml of eltrombopag (see Chapter 5, Fig. 5.4), it was decided to evaluate the potential for interaction between pitavastatin and eltrombopag using a more dynamic approach through Physiologically Based Pharmacokinetic (PBPK) modelling. There are two levels of PBPK models in

the literature to evaluate TrDDIs:

1. *Semi-mechanistic PBPK models*: which focus on the organ(s) of interest only (e.g. Takeuchi et al. [244] included 4 compartments (GI tract, liver extracellular space, liver and a central compartment) to explain the TrDDI between rosuvastatin and eltrombopag - the basis for the PBPK model presented below), assuming that these can adequately explain the PK data and subsequent interactions [54, 244, 260].

2. *Full PBPK models* include all organs, not just those of focused interest with regard to TrDDIs, as such they are much larger models [38, 179, 261, 262]. For example Li et al. [179] included 19 compartments (5 for the liver, and liver extra vascular space) to evaluate the effect that ethnicity (Japanese and Caucasian) has on the pharmacokinetics of rosuvastatin and pravastatin following oral and intra-venous administration).

These are clearly very different approaches, if one was to include inhibitor in a full PBPK model, this would lead to 38+ compartments, and this is where commercial packages come to the fore, with optimised software to cater such large models (e.g. SimCYP (Certara, Princeton, USA), Gastroplus (Simulations Plus, Lancaster, USA) and PK-Sim (Bayer, Leverkusen, Germany)).

There are conflicting articles for full PBPK models with regard to the number of liver extracellular space and liver cellular compartments that can be used to fit the data, with 1, 3, 4 and 5 compartments used [54, 261–263], and this also depends on which statin was evaluated (rosuvastatin, rosuvastatin, pravastatin and cerivastatin respectively, [54, 261–263]). Yao et al. [262] evaluated 1, 3 and 5 compartments for the extravascular space and liver and found no difference in fit between the number of compartments considered, and was attributed to the robustness of the use of the "5 liver model" [262].

The aim of this chapter is to qualitatively evaluate the TrDDI between pitavastatin and eltrombopag at clinically relevant doses. As we are interested in the DDI at the level of the liver only, this will be done through a semi-mechanistic PBPK model in R using the `DeSolve` package [1, 186], based on the model of Takeuchi et al. [244].

6.2 PBPK Model

6.2.1 Identifiability Analysis

As *per* the previous chapters, prior to PBPK model development, a model for pitavastatin only (Eqs. 6.1-6.6, Table 6.1 without inhibition of uptake from eltrombopag) and then a combined model in the presence of eltromobopag (Eqs. 6.1-6.12, Table 6.1), was evaluated for structural identifiability, given the unknown parameter vector:

$$\{k_{ge}, K_{a.P}, k_{bile}, V_{max.up.P}, K_{m.up.P}, P_{dif.P}, P_{def.P}, CL_{met.P}, CL_{bi.P}, CL_{urine.P},$$
$$K_{a.E}, V_{max.up.E}, K_{m.up.E}, P_{dif.E}, P_{def.E}, CL_{met.E}, CL_{bi.E}\},$$

with known initial conditions of the doses of pitavastatin (1 mg) and eltrombopag (75 mg):
$$[1, 0, 0, 0, 0, 0, 75, 0, 0, 0, 0]$$

and observations of the blood concentration of pitavastatin ($y_1 = S_6$) and eltrombopag ($y_2 = I_6$). The structural identifiability analysis was carried out using the `Identifiability Analysis` package [16, 160] in Mathematica 11.3 (see Chapter 2, Section 2.4.1).

The PBPK models for pitavastatin only or pitavastatin with eltrombopag were at least structurally locally identifiable with no parameters unidentifiable if the following were assumed known: Volumes and blood flows, and the fraction unbound ($f_{u.pl.P}$/blood:plasma = $f_{u.blood.X}$, $f_{u.pl.E}$ and $f_{u.L.X}$).

6.2.2 PBPK Model Development

A semi-mechanistic PBPK model was fitted to rosuvastatin and eltrombopag separately to obtain parameters which were then fixed for the simulation of the TrDDI between the two drugs, assuming that hOATP1B1 was the driving force for the TrDDI [244]. The model developed here (Fig. 6.2) was based on the principle that the uptake of pitavastatin could be inhibited by eltrombopag in patients based on the data obtained from Chapter 5. Yoshikado et al. [260] used a PBPK model to adequately describe the interaction between pitavastatin or fluvastatin with CsA, based on clinical data. The PBPK model included 5 liver compartments, 3 compartments to allow for entero-hepatic recirculation as well as muscle, skin and adipose to allow distribution [260]. Both of these models simplified the uptake into clearances [244] or the ratio of active:passive uptake clearance [260] to adequately fit the data, but seemed to not describe the time to C_{max}. As the Michaelis-Menten assumptions for pitavastatin held (see previous chapter), it was decided to scale the parameters from micro-rate constants to Michaelis-Menten parameters for pitavatatin and eltrombopag (from Model 1, including eltrombopag in Chapter 5). These parameters were then scaled directly to a normal healthy 83 kg male [2] (see Table 6.2), to see if the pitavastatin data could be adequately fitted visually before the inclusion of eltrombopag due to the greater amount of *in vitro* data for
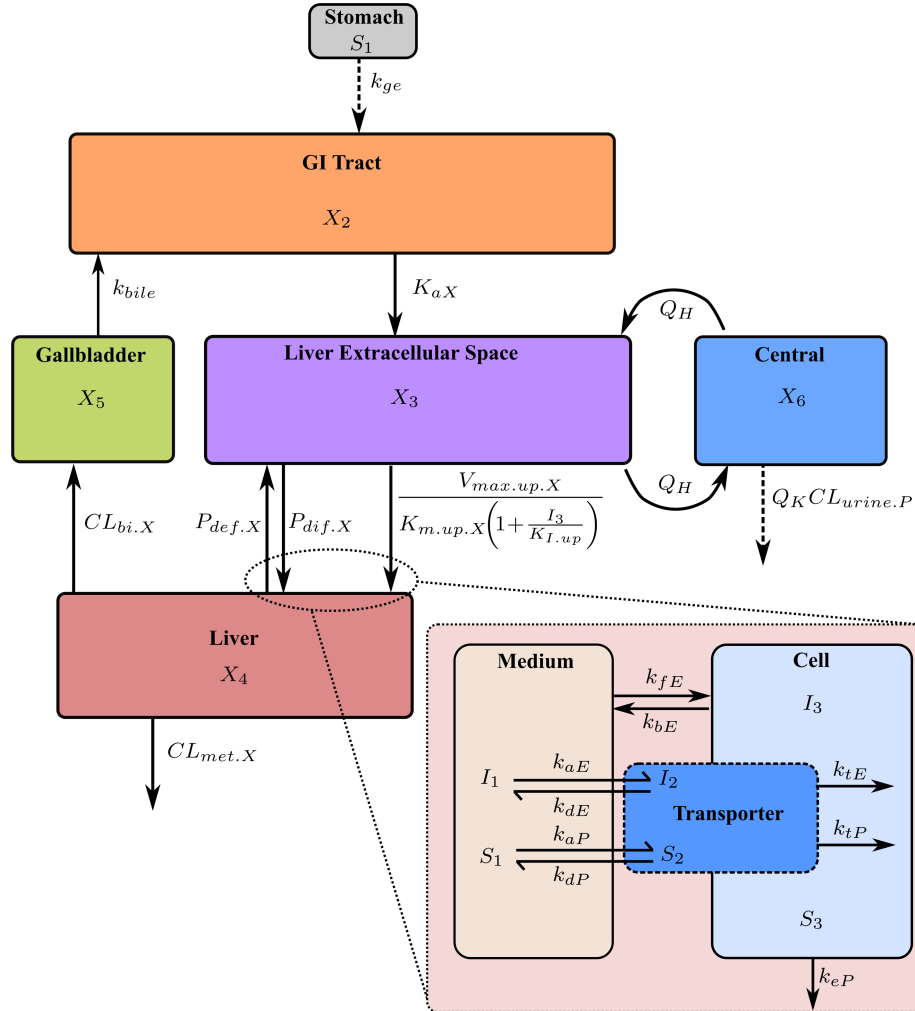
Figure 6.1: Schematic of the developed semi-mechanistic PBPK model for the concentrations in the liver compartment (X_4) assumed to be involved in the TrDDI between pitavastatin and eltrombopag, which is linked to the concentration in the central compartment (X_6) via the concentration in the liver extracellular space (X_3) through hepatic blood flow (Q_H). The dose is applied as an amount into the stomach (X_1), which is then transported into the GI Tract (X_2) with gastric emptying rate constant (k_{ge}). Drug is absorbed into X_3 with the absorption rate constant (K_{aX}), where free drug moves into the liver via saturable Michaelis-Menten kinetics $(V_{max.up.X}$ and $K_{m.up.X})$ and is inhibited by the opposing drug in X_3 (I_3) via the K_m $(K_{I.up})$. Passive movement of drug into and out of the liver with clearances $P_{dif.X}$ and $P_{def.X}$ respectively. Biliary excretion of both drugs $(CL_{bi.X})$ into X_2 through the gallbladder (X_5) with bile flow rate constant (k_{bile}) where they can be re-absorbed. Both drugs have metabolic clearance from the liver $(CL_{met.X})$, whilst pitavastatin is also cleared into the urine $(CL_{urine.P})$ with the kidney blood flow (Q_K)

117

Table 6.1: PBPK model system of ODEs instigated in R using the `deSolve` package [1] (see Fig. 6.1)

Compartment	Equation
Pitavastatin Stomach (S_1, ng)	$$\frac{dS_1}{dt} = -k_{ge}S_1 \qquad (6.1)$$
Pitavastatin GI Tract (S_2, ng)	$$\frac{dS_2}{dt} = k_{ge}S_1 - K_{a.P}S_2 + k_{bile}S_5 \qquad (6.2)$$
Pitavastatin Liver Extracellular Space (S_3, ng/ml)	$$\frac{dS_3}{dt} = \left(-f_{u.bl.P}S_3 \left(\frac{V_{max.up.P}}{K_{m.up.S}\left(1 + \frac{I_3}{K_{m.up.E}}\right) + f_{u.bl.P}S_3} + P_{dif.P} \right) \right.$$ $$\left. + Q_H f_{u.bl.P}\left(S_6 - S_3\right) + K_{a.P}S_2 + P_{def.P}f_{u.L.P}S_4 \right)/V_{ext.H} \quad (6.3)$$
Pitavastatin Liver (S_4, ng/ml)	$$\frac{dS_4}{dt} = \left(f_{u.bl.P}S_3 \left(\frac{V_{max.up.P}}{K_{m.up.S}\left(1 + \frac{I_3}{K_{m.up.E}}\right) + f_{u.bl.P}S_3} + P_{dif.P} \right) \right.$$ $$\left. - f_{u.L.P}S_4\left(CL_{met.P} + CL_{bi.P} + P_{def.P}\right) \right)/V_H \quad (6.4)$$
Pitavastatin Gallbladder (S_5, ng/ml)	$$\frac{dS_5}{dt} = CL_{bi.P}f_{u.L.P}S_4/V_{GaBl} - k_{bile}S_5 \qquad (6.5)$$
Pitavastatin Central (S_6, ng/ml)	$$\frac{dS_6}{dt} = \left(Q_H f_{u.bl.P}(S_3 - S_6) - Q_K CL_{urine.P}S_6\right)/V_{c.P} \qquad (6.6)$$
Eltrombopag Stomach (I_1, ng)	$$\frac{dI_1}{dt} = -k_{ge}I_1 \qquad (6.7)$$
Eltrombopag GI Tract (I_2, ng)	$$\frac{dI_2}{dt} = k_{ge}I_1 - K_{a.E}I_2 + k_{bile}I_5 \qquad (6.8)$$
Eltrombopag Liver Extracellular Space (I_3, ng/ml)	$$\frac{dI_3}{dt} = \left(-f_{u.pl.E}I_3 \left(\frac{V_{max.up.E}}{K_{m.up.E}\left(1 + \frac{S_3}{K_{m.up.P}}\right) + f_{u.bl.E}I_3} + P_{dif.E} \right) \right.$$ $$\left. + Q_H f_{u.bl.E}\left(I_6 - I_3\right) + K_{a.E}I_2 + P_{def.E}f_{u.L.E}I_4 \right)/V_{ext.H} \quad (6.9)$$
Eltrombopag Liver (I_4, ng/ml)	$$\frac{dI_4}{dt} = \left(f_{u.pl.E}I_3 \left(\frac{V_{max.up.E}}{K_{m.up.E}\left(1 + \frac{S_3}{K_{m.up.P}}\right) + f_{u.pl.E}I_3} + P_{dif.E} \right) \right.$$ $$\left. - f_{u.L.E}I_4\left(CL_{met.E} + CL_{bi.E} + P_{def.E}\right) \right)/V_H \quad (6.10)$$
Eltrombopag Gallbladder (I_5, ng/ml)	$$\frac{dI_5}{dt} = CL_{bi.E}f_{u.L.E}I_4/V_{GaBl} - k_{bile}I_5 \qquad (6.11)$$
Eltrombopag Central (I_6, ng/ml)	$$\frac{dI_6}{dt} = \left(Q_H f_{u.pl.E}(I_3 - I_6)\right)/V_{c.E} \qquad (6.12)$$

$X = S$ or P = pitavastatin, or $X = I$ or E = eltrombopag, X_{1-6} represent stomach, the GI Tract where absorption takes place, the liver extracellular space (volume = $V_{ext.H}$), the liver (volume = V_H), the gall bladder (volume = V_{GaBl}), central compartment (volume = $V_{c.X}$). k_{ge} = the gastric emptying rate, $K_{a.X}$ = the absorption rate, k_{bile} = the bile flow rate (all /min). $f_{u.bl.P}$, $f_{u.pl.E}$ and $f_{u.L.X}$ = the fraction unbound in the blood (pitavastatin), plasma (eltrombopag) and liver respectively. Q_H and Q_K are the liver and kidney blood flows respectively (ml/min). $CL_{met.X}$, $CL_{bi.X}$ and $CL_{urine.P}$ are the metabolic, biliary and urinary (pitavastatin only) clearance respectively (ml/min). $V_{max.up.X}$ and $K_{m.up.X}$ are the maximum uptake velocity (ng/min) and concentration at half of $V_{max.up.X}$ (ng/ml) respectively.

pitavastatin available.

Pitavastatin was applied as a 1 mg bolus into the stomach (S_1) which was then transferred into the gut, at the rate of gastric emptying (k_{ge}, taken as the inverse of a minimum gastric emptying time of 10 min [132], see Table 6.1). This was sufficient to allow enough of a time lag to prevent both drugs reaching their respective C_{max} too early (time to $C_{max} = T_{max}$), and was more simplistic than including separate intestinal segment compartments as used in a full PBPK model [261]. Pitavastatin is absorbed from the GI tract (S_2) into the liver extracellular volume (S_3) via the first order absorption rate constant $K_{a.P}$, (see Table 6.1, Eq. 6.2 and Table 6.2), assuming that all of the administered dose is absorbed (i.e. there is assumed to be no metabolism or efflux transporter activity in the gut) [260]. Movement of free pitavastatin ($f_{u.bl.P} = 0.012$ (% CV = 42), see Table 6.2) into the liver is with saturable ($V_{max.up.P}$ and $K_{m.up.P}$) and passive diffusion ($P_{dif.P}$), with diffusion allowed back into the extravascular space ($P_{def.P}$). Any liver (S_4) elimination of free pitavastatin is through metabolism ($CL_{met.P}$) or biliary excretion ($CL_{bi.P}$) into the gallbladder (S_5, volume = 36 ml (% RSE = 2.5), [264], see Table 6.2), which returns back to the GI Tract via the gallbladder emptying rate ($k_{bile} = 0.0618$ /min (% RSE = 11)) to be re-absorbed. The liver extracellular compartment ($V_{ext.H} = 556$ ml [229], once adjusted to an 83 kg male) is considered as the lumping of the hepatic portal vein, the hepatic artery and liver blood volume, which then link to the central blood volume compartment (V_{cP}) via the central vein through the hepatic blood flow (Q_H). Urinary clearance ($CL_{urine.P}$) of free pitavastatin is from the central compartment through the kidney blood flow (Q_K). The clinical study for a 1 mg oral dose of pitavastatin in healthy volunteers included measurement of pitavastatin in plasma [9], therefore, as the PBPK model was developed for pitavastatin in the blood (total blood volume = 5820 ml [2], see Table 6.2), the clinical data were converted from plasma concentration (ng/ml) to blood by dividing by the blood:plasma ratio obtained from the literature (0.425 ± 0.162, [209]).

Due to the high level of binding of eltrombopag to plasma proteins (99.8%, [243]), and the fraction of radioactivity in blood cells of 0-16 % [11], it was assumed that eltrombopag only exists in plasma (plasma volume = 3460 ml, [2]), and has a volume of distribution of 2940 ml [244]. The FDA guidance suggests the use of 1 % free drug in the plasma as a fixed value when the estimated value is below this, due to inaccuracies in estimation [19]. Given the high level of binding and low recovery (10 %) from the RED device used in the experiment in Chapter 5, the value of fraction unbound in the plasma ($f_{u.pl.E}$) of 0.002 [243], 0.01 and 0.005 were checked, with a value of 0.005 giving the best visual fit to the 75 mg clinical data for eltrombopag [11]. Eltrombopag was applied as a 75 mg bolus into the stomach (I_1), which was then transferred into the gut at the same rate as for pitavastatin through $k_g e$. The fraction of eltrombopag that was absorbable and escaped metabolism in the gut ($F_a F_g$ in the literature) was reported as 0.5 [244, 246], but assumed to be 1 here. Eltrombopag was absorbed from the GI tract into the liver extracellular space (I_3) with first order absorption rate constant ($K_{a.E} = 11$ /min). Movement of free eltrombopag into the liver is with saturable ($V_{max.up.E}$ and

$K_{m.up.E}$) and passive diffusion ($P_{dif.E}$), with diffusion back into the extravascular space through $P_{def.E}$. Any liver (I_4) elimination of free eltrombopag is via metabolic clearance ($CL_{met.E}$) or biliary excretion through the $CL_{bi.E}$ rate constant into the gallbladder (I_5, volume = 36 ml (% RSE = 2.5), [264], see Table 6.2), which returns back to the GI Tract to be re-absorbed. The liver extracellular compartment links to the central plasma volume compartment with Q_h, and no urinary elimination of eltrombopag was included as only metabolites contributed to the urinary radioactivity in humans [11]. Interactions between pitavastatin and eltrombopag only occurred at the uptake transporter level through competitive inhibition of uptake only via their respective $K_{m.up}$ values (see Fig. 6.1, $1+I/K_{I.up}$).

Table 6.2: PBPK model parameter values for an 83 kg healthy male [2]

Parameter	Calculation Method	Value	Reference
Drug Specific Parameters			
Pitavastatin			
$K_{a.P}$ (/min)	$\left(\frac{1}{MRT_{PO}-MRT_{IV}}/60\right)/k_{ge}$	$\left(\frac{1}{4.55(1.87)-2.18(2.03)}/60\right)/0.1 = 0.07(\%CV = 102)$	[10]
$f_{u.bl.P}$	$\frac{f_{u.plasma}}{Bl:Pl}$	$0.005 \pm 0.0009/0.425 \pm 0.162 = 0.0118(\%CV = 42)$	[209]
$f_{u.L.P}$	$\left(\frac{V_{cell}}{V_{inc}/f_{u.inc}}\right) - V_{med} - k_{mem}$	$3/((1203/0.87(\%RSE=9))-1200-0.03) = 0.02(\%RSE = 9)$	Exper, [165]
$V_{max.up.P}$ (ng/min)	$V_{max.up} \cdot \mathrm{MW} \cdot HPGL \cdot \mathrm{Liver\ wt}$	$0.302(0.18-0.64) \cdot 421.46 \cdot 139 \pm 25 \cdot 1695(\%CV = 16) = 3.00e^7(1.89 - 6.75e^7)$	Exper, [2, 181]
$K_{m.up.P}$ (ng/ml)	$K_{m.up} \cdot \mathrm{MW}$	$22.6(16.7 - 25.5) \cdot 421.46 = 9525(7038 - 10747)$	Exper
$P_{dif.P}$ (ml/min)	$P_{dif} \cdot HPGL \cdot \mathrm{Liver\ wt}$	$5e^{-4}(4.6e^{-4} - 6.1e^{-4}) \cdot 139 \pm 25 \cdot 1695(\%CV = 16) = 137.6(108 - 144)$	Exper, [2, 181]
$P_{def.P}$ (ml/min)	$P_{def} \cdot HPGL \cdot (\mathrm{Liver\ wt} - V_{ext.H})$	$(0.62(0.55 - 0.67) \cdot 0.003)139 \pm 25 \cdot 1139 = 295(261 - 318)$	Exper, [2, 263]
$CL_{met.P}$ (ml/min)	$CL_{met} \cdot HPGL \cdot \mathrm{Liver\ wt} \cdot f_{hep}$	$(0.22(0.2 - 0.24) \cdot 0.003)139 \pm 25 \cdot 1695(\%CV = 16) \cdot 0.6 = 155(141 - 169)$	Exper, [2, 181, 265]
$CL_{bi.P}$ (ml/min)	Total CL·f unchanged in faeces	$384 \cdot 0.43 = 165.1$	[240]
$CL_{urine.P}$ (ml/min)	Total CL·f unchanged in urine	$384 \cdot 0.03 = 11.5$	[10, 240]
$V_{c.P}$ (ml)	blood volume	$5820 (\% CV = 11)$	[2]
Eltrombopag			
$K_{a.E}$ (/min)		11	Visual to fit T_{max}
$f_{u.pl.E}$		$0.002 \to 0.005$	[243]
$f_{u.L.E}$		0.4	Visual
$V_{max.up.E}$ (ng/min)	$V_{max.up} \cdot \mathrm{MW} \cdot HPGL \cdot \mathrm{Liver\ wt}$	$0.049(0.028 - 0.116) \cdot 442 \cdot 139 \cdot 1695(\%CV = 16) = 5.42e^6(2.92e^6 - 1.21e^7)$	Exper, [2, 181]
$K_{m.up.E}$ (ng/ml)	$K_{m.up} \cdot \mathrm{MW}$	$7.0(7.4 - 7.43) \cdot 442 = 3138(3271 - 3284)$	Exper
$P_{dif.E}$ (ml/min)	$P_{dif} \cdot HPGL \cdot \mathrm{Liver\ wt}$	$0.05(0.04 - 0.06) \cdot 139 \cdot 1695(\%CV = 16) = 11780(9424 - 14136)$	Exper, [2, 181]
$P_{def.E}$ (ml/min)	$P_{def} \cdot HPGL \cdot (\mathrm{Liver\ wt} - V_{ext.H})$	$(0.62(0.55 - 0.67) \cdot 0.003)139 \pm 25 \cdot 1139 = 294(261 - 318)$	Exper, [2, 181]

Table 6.2 continued...

Parameter	Calculation Method	Value	Reference
$CL_{met.E}$ (ml/min)	$CL/F \cdot F \cdot (1 - F_{pl.E})$	$13 \cdot 0.52 \cdot (1 - 0.64) = 6.8 \to 8$	[243, 246], Visual
$CL_{bi.E}$ (ml/min)	CL/F	$= 13 \to 12$	[243, 246], Visual
$V_{c.E}$ (ml)		2940	[244]
Physiological Parameters			
$V_{ext.H}$ (ml)*		556	[263]
V_H (ml)		1570 (% CV = 16)	[2]
V_{GaBl} (ml)		36	[264]
k_{ge} (/min)	1/(gastric emptying time)	1/10 = 0.1	[132]
k_{bile} (/min)	gallbladder emptying rate	0.0618	[264]
Q_H (ml/min)		1320 (% CV = 16)	[2]
Q_K (ml/min)		1170 (% CV = 22)	[2]

"Exper" = experimental and are taken from Chapter 5, "Visual" value altered until fit more closely resembles data, * = adjusted to 83 kg male [2], $HPGL$ = hepatocytes/g liver [181].

f_{hep} = fraction of liver that is hepatocytes, % CV calculated sum (n) of individual i from combined parameters using $\%CV = \sqrt{\sum_i^n (SD/mean \times 100)^2}$.

The PBPK model was generated as a set of ODEs (Table 6.1) that were solved numerically in R [186] using the `deSolve` package [1]. To gain an estimate of error in the model a Monte-Carlo simulation of 100 subjects (healthy male, 83 kg), each parameter was factored as 100 normally distributed random numbers with a mean of the parameter estimate, and a standard deviation of 0.2 or 0.3 times the parameter estimate (for literature derived values and model derived values respectively). The code for the whole model is given in Appendix G.

6.3 Results and Discussion

Whilst the PBPK models developed here are simulations only, based on the drug characteristics and physiology, the visual fit for pitavastatin alone (Fig. 6.2a, blue line and shading) fit the data reasonably well and replicated the shape of the blood concentration versus time data well (extracted from Prueksaritanont et al. [9], with the associated errors bars). No experimentally derived parameters ($f_{u.L.P}$, $P_{dif.P}$, $P_{def.P}$, $V_{max.up}$, $K_{m.up.P}$ and $CL_{met.P}$) or other parameters were adjusted in the visual fitting process (see Table 6.2).

For eltrombopag alone (Fig. 6.3a, blue line and shading), the mean simulation (blue line) fitted the plasma concentration reasonably well and closely followed the shape of the plasma concentration versus time data (extracted from Deng et al. [11]), but the large error shading of the 95 % confidence intervals increased to large proportions during the eltrombopag elimination phase. Whilst the experimentally derived values ($P_{dif.P}$, $P_{def.P}$, $V_{max.up}$ and $K_{m.up.P}$) required no adjustment, $f_{u.L.E}$ was unreliable if calculated using the same equation as for pitavastatin (see Table 6.2 $f_{u.L.P}$), and therefore was adjusted stepwise from 1 to 0.4. The total CL/F value for eltrombopag is low (13 ml/min, [243]), this comprises both biliary ($CL_{bi.E}$) and metabolic clearances ($CL_{met.E}$), with biliary clearance expected to dominate, as 20 % of the dose was eliminated in the faeces as unchanged eltrombopag. 20 % of 13 ml/min (2.6 ml/min) was not sufficient to follow the elimination part of the plasma concentration curve and was adjusted to 12 ml/min, with the metabolism set to a third lower at 8 ml/min.

Following a 1 mg dose of pitavastatin, in the presence of 75 mg eltrombopag, and based on the inhibition of uptake only, the pitavastatin plasma concentration-time curve C_{max} more than doubled from 20 ng/ml up to 41 ng/ml to above the data from a 2 mg dose (Fig. 6.2b, open circles, taken from the FDA document), without visually altering the elimination (Fig. 6.2b, solid line). The AUC_{0-t} (calculated using the `zoo` package in R) ratio in the presence and absence of a 75 mg dose of eltrombopag (94 h.ng/ml/ 45 h.ng/ml respectively = 2.1) increased by more than the static R models would suggest (R value = 1.1-1.19 using the EMA guidelines and 1.07 using the FDA guidelines, see Chapter 5, Table 5.7). The simulated concentration of eltrombopag in the liver extra cellular compartment following a 75 mg dose (52956 ng/ml at 15 min), was much larger than the $K_{I.E}$ value calculated from the *in vitro* data obtained from the previous chapter ($K_{I.E}$ = 3138 ng/ml), making a TrDDI more likely with pitavastatin
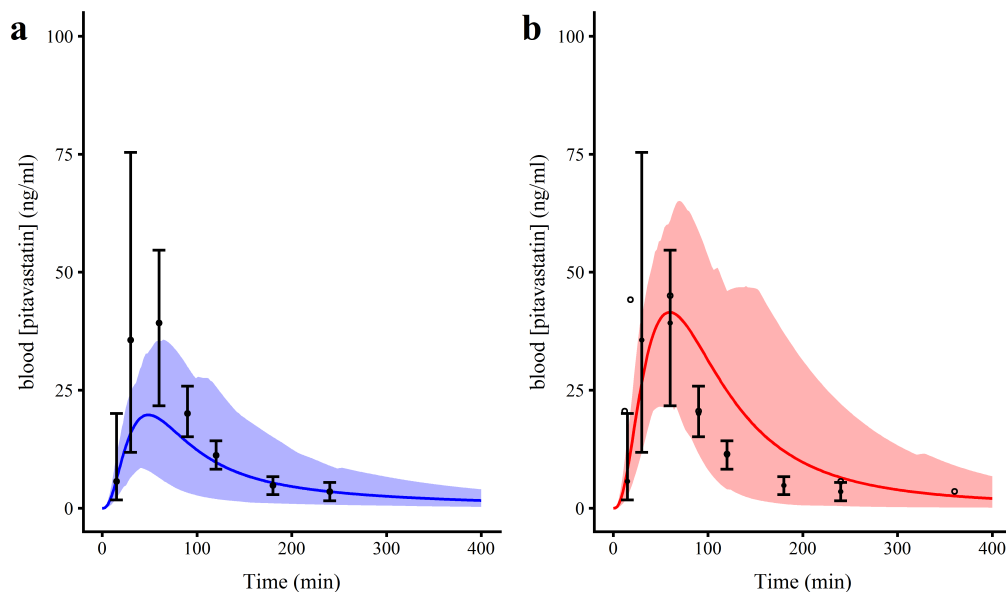
Figure 6.2: Semi-mechanistic PBPK model Monte-Carlo simulation fits (100 subjects) for pitavastatin (1 mg dose) in the absence (**a**, blue) and presence (**b**, red) of eltrombopag (75 mg). Circles and error bars are clinical data, extracted from Prueksaritanont et al. [9], solid lines are the mean, shading denotes the 95 % confidence intervals. Open circles are pitavastatin (2mg dose) extracted from the pitavastatin FDA drug submission document [10]

as the "victim" drug and eltrombopag as the "perpetrator" drug.

Following a 75 mg dose of eltrombopag, in the presence of a dose of 1 mg pitavastatin, and based on inhibition of uptake only, the eltrombopag plasma concentration-time curve did not change (Fig. 6.3b). The $P_{dif.E}$ value = 11780 (9424-14136) ml/min (Table 6.2) was much greater than the transporter mediated clearance for eltrombopag ($V_{max.up.E}/K_{m.up.E}$ = 1626 (891 − 3678) ml/min), making a TrDDI unlikely with eltrombopag as the "victim" drug. Takeuchi et al. [244] also saw no difference in the simulated eltrombopag plasma concentration following a 75 mg dose in the presence of rosuvastatin at 10 mg. Whilst the simulated rosuvastatin concentration was altered to a similar amount as shown here, only if the IC_{50} was a tenth of that estimated (i.e. 0.09 μM = 39.8 ng/ml). It was shown that pitavastatin was more sensitive to inhibition by an I.V. dose of rifampicin than rosuvastatin in a healthy volunteer study (7.6- and 3-fold increase in AUC respectively) [9], therefore it is expected that the $K_{I.E}$ value obtained here would be sufficient clinically to inhibit pitavastatin uptake into the liver, leading to a TrDDI.

6.4 Conclusions

This chapter developed a semi-mechanistic PBPK model to evaluate the effect of eltrombopag inhibition of pitavastatin uptake using the scaled data from Chapter 5. The model consisted of 5-6 compartments (GI tract including the stomach, the liver extracellular space, the liver and gallbladder and a central blood or plasma compartment).
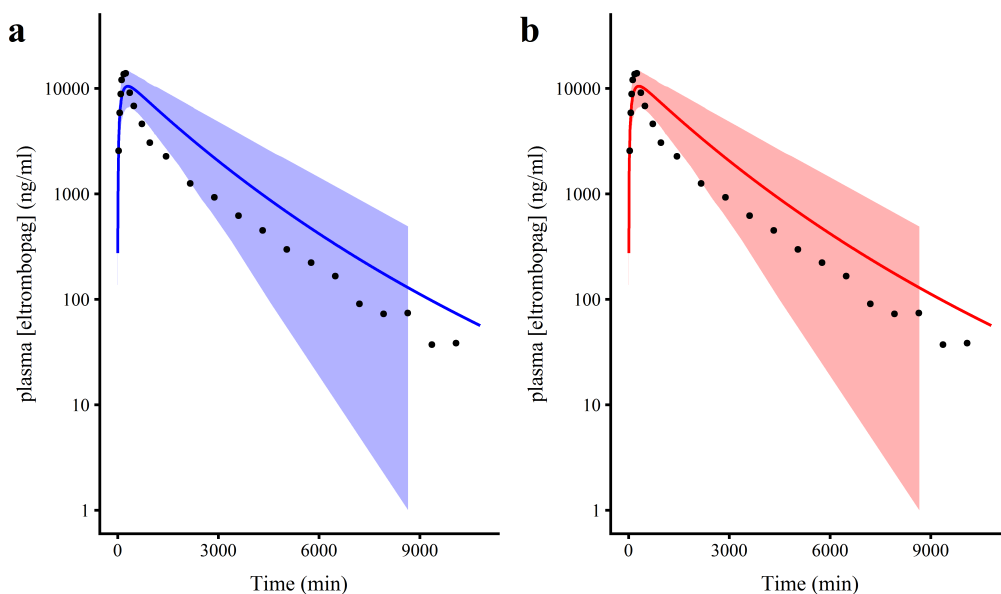
Figure 6.3: Semi-mechanistic PBPK model Monte-Carlo simulation fits (100 subjects) for eltrombopag (75 mg dose) in the absence (**a**, blue) and presence (**b**, red) of pitavastatin (1 mg). Points are clinical data, extracted from Deng et al. [11], solid lines are the mean, shading denotes the 95 % confidence intervals

Pitavastatin blood and eltrombopag plasma concentrations were then estimated using a Monte-Carlo simulation of 100 human subjects (70 kg male) following a 1mg dose of pitavastatin with a 75 mg dose of eltrombopag.

The use of a 75 mg dose of eltrombopag doubled the exposure of a 1 mg dose of pitavastatin (AUC ratio = 2.1) in the 100 virtual subjects without altering the elimination, whilst no effect was seen on the eltrombopag plasma concentration versus time profile. This makes the PBPK model a useful tool beyond the static clinical assessment 'R value' approach at least for substrates that are sensitive to inhibition through OATP1B, such as pitavastatin.

This chapter represents a preliminary analysis of *in vitro* data in a PBPK model, and is highly simplistic in its nature. The previous chapters have all shown that micro-rate constant mechanistic models offer improved data fits and are more dynamic in the mechanisms of inhibition than a macro-rate constant model. Future work is therefore potentially quite extensive, both with regard to a more robust parameter estimation approach and the development of a model that incorporates micro-rate constants, with transporter occupancy a key component.

Chapter 7

Conclusions and Further Work

There is currently a need to evaluate the interaction of drugs in the liver, and at the liver membrane for all orally absorbed drugs and food. As such the liver "sees" much higher concentrations than the rest of the body. Prior to submission of a new drug to the regulatory agencies, assessments have to be made both in terms of hepatic enzyme interactions, but also the liver plasma membrane transporters at the sinusoid and bile canaliculus [18, 19]. The interactions of drugs with liver membrane transporters are currently poorly understood at a molecular level [20]. There is strong interest in terms of the pharmacology of the transporters and how we can examine and understand these interactions through mathematical models [20–22]. There is also increased interest in the evaluation of uptake inhibition mechanisms and whether the long-lasting inhibition of transporters can explain the discrepancy between *in vitro* and *in vivo* studies [207, 208]. Evaluation of time dependent inhibition of selected transporters is also now recommended as part of new drug submissions to the regulatory authorities [18, 19]. It is these interactions and processes that this thesis evaluated in an attempt to further the knowledge base and understanding in this field.

The objective of this thesis was to improve the determination of transporter mediated drug-drug interactions (TrDDIs) in *in vitro* liver specific cellular systems through the use of structurally identifiable mechanistic models describing the dynamics of the interaction between substrates and inhibitors.

Currently the dynamics of interactions through the use of micro-rate constant models, where steady-state assumptions are not implied in data analysis are less favoured. Whilst modelling and data analysis conducted using macro-rate constant models using Michaelis-Menten type kinetics, under the assumption of rapid equilibration of substrate with the transporter (association with the transporter is almost instantaneous) are more common.

Therefore this thesis tried to answer the main aim and that above relating to steady-state assumptions with a series of objectives for a selection of substrates where active transport into the cell dominates over passive:

1. Develop mechanistic models that characterise the data, and are possible given the available observations available from *in vitro* cellular drug uptake experiments,

extending the work of Grandjean [25] to include inhibition of transport.

2. Evaluate the effectiveness of both macro-rate constant models and micro-rate constant models with the inclusion of substrate and inhibitor and determine their structural identifiability for a given model and observations available.

3. Design experiments to optimise the data collected for substrate and inhibitors for use within the mechanistic models across different cellular systems (human cell lines, rat and human hepatocytes) under different inhibition conditions.

4. Using the micro-rate constant and macro-rate constant mechanistic models, obtain robust model fits that adequately describe interaction between substrates and inhibitors, whilst gaining an insight in terms of model selectivity.

5. Evaluate whether through the use of static clinical interaction models and a more dynamic PBPK supports the potential for TrDDIs in the clinic in human hepatocytes.

7.1   Chapter Summary

Chapter 3 evaluated the uptake of a fluorescent substrate, DCF, as an alternative to the use radio labelled substrates in HEK293-OATP1B1 cells. Whilst the inhibition of selective substrates by gemfibrozil in HEK293-OATP1B1 has been conducted under the assumption of competitive inhibition [27, 135, 168], the mode of inhibition has not been fully evaluated. The mode of inhibition of DCF by gemfibrozil was therefore evaluated across three different scenarios: co-incubation with gemfibrozil, to examine for competitive inhibition; pre-incubation with gemfibrozil and then co-incubation with gembfibrozil, to evaluate time dependent effects; and finally pre-incubation with gemfibrozil, to evaluate lasting inhibition. In this chapter, the fluorescence of DCF was measured in each sample, but the analysis of the concentration of gemfibrozil was not undertaken.

For the micro-rate constant models, compartments representing the amount in the medium, the amount bound to transporter and the amount within cell were included in the mechanistic model for DCF. For gemfibrozil, only the amount in the medium and amount bound to transporter were included. As DCF was measured as a concentration, the observations in the mechanistic model were scaled from an amount to concentration by multiplication of the combined transporter and cellular amounts by the inverse of the cell volume. However, as the total number of cells was not known in the experiments, a cellularity factor was determined and the data normalised to *per* 10^6 cells, enabling the use of a cell volume/10^6 cells.

Prior to parameter estimation, the micro-rate constant models and macro-rate constant models for competitive and non-competitive inhibition underwent a formal structural identifiabilty analysis. The micro-rate constant models describing the competitive inhibition and non-competitive (time-dependent inhibition) of DCF by gemfibrozil were all at least structurally (locally) identifiable given known inputs and observations,

with no parameters unidentifiable. The macro-rate constant models were unidentifiable unless one of the parameters relating to the Michaelis-Menten uptake (K_m, K_I, V_{max} or K_{inact}) were known for competitive and non-competitive inhibition respectively.

For the co-incubation and pre-co-incubation scenarios, the micro-rate constant models were the best fitting models to the experimental data, compared to the macro-rate constant models based on the BIC values and % RMSRE for the individual predictions under the assumption of competitive inhibition (BIC = 1540 (RMSRE = 49 %) and 1600 (58 %) for the co-incubation scenatio data respectively, and 1242 (50 %) and 1249 (52 %) respectively for the pre-co-incubation scenario data). Across the scenarios, the competitive inhibition of DCF uptake by gemfibrozil into HEK293-OATP1B1 cells was the supported mechanism of inhibition, consistent with the literature.

The estimate of the total amount of transporters (T_o = 0.06 (0.04 − 0.09) nmols/10^6 cells) on the plasma membrane of HEK293-OATP1B1 cells, obtained using the micro-rate constant model for competitive inhibition of DCF by gemfibrozil was similar to that determined using the same cell line extracted from crude membranes at AstraZeneca (0.02 nmols/10^6 cells, P. Sharma, personal communication) and supports the further use of mechanistic modelling for the determination of the amount of transporters, along with more information regarding the binding and transport, in cell lines at least. This value can then be used in the future to assess inter-laboratory conditions and during PBPK model development.

Chapters 4 and 5 evaluated the uptake of a statin (atorvastatin and pitavastatin respectively) and the inhibition of uptake and metabolism (Chapter 4) by CsA and eltrombopag respectively in suspended hepatocytes (rat and human respectively). Unlike Chapter 3 which used plated HEK293-OATP1B1 cells, Chapter 4 and Chapter 5 used hepatocytes in suspensions, and therefore a centrifugal oil-spin method of separating the cells from the medium was needed, with more timepoints at the beginning of the experiment to help describe the uptake process and then prolonged timepoints to help describe elimination through metabolism. Chapter 4 used a high throughput method for hepatocyte incubations in Teflon blocks containing 16 troughs, whilst Chapter 5 used individual glass vials. The technique for both was the same - a dense bottom layer into which the cells reside after centrifugation, separated from the medium by an oil layer that is sufficiently dense that only hepatocytes can pass through, leaving the medium on top. For Chapter 4, only atorvastatin was measured in the hepatocytes, whilst in Chapter 5, in addition to the measurement of pitavastatin in the hepatocytes, eltrombopag was also measured simultaneously in the same sample.

The mechanistic models for both Chapter 4 and 5 were therefore very similar, with additional metabolism compared to Chapter 3 in the models through Michaelis-Menten parameters and a first order elimination rate constant respectively. Prior to parameter estimation, the micro-rate constant models and macro-rate constant models for competitive and non-competitive inhibition underwent a formal structural identifiabilty analysis. The inclusion of metabolism in Chapter 4 and 5 did not alter the result for the micro-rate constant models with the models for competitive and non-

competitive inhibition at least structurally (locally) identifiable, given the model inputs and observations, with no parameters unidentifiable. For the macro-rate constant models described in Chapter 4, which included two Michaelis-Menten non-linearities, the models were unidentifiable, unless 2 parameters relating to Michaelis-Menten uptake and metabolism ($K_{m.up}$, $K_{I.up}$, $K_{m.met}$, $K_{I.met}$, $V_{max.up}$ or $K_{inact.up}$) were known for competitive and non-competitive inhibition respectively. Measurement of pitavatatin and eltrombopag simultaneously in Chapter 5 led to the macro-rate constants being at least structurally (locally) identifiable, given the model inputs and observations, with no parameters unidentifiable.

In Chapter 4, a micro-rate constant model for non-competitive inhibition of atorvastatin by CsA was the best fitting model to the experimental data with a probability $wBIC = 0.54$ compared to competitive inhibition $wBIC = 0.45$. The macro-rate constant models for non-competitive and competitive inhibitions were not supported as the best fitting models with ΔBIC values of 11 and 94 compared to best fitting model respectively. Non-competitive inhibition of uptake by CsA, and competitive inhibition of metabolism with different substrates were also supported in the literature using macro-rate constant models [140, 208, 225].

In Chapter 5, simultaneous measurement of pitavastatin and eltrombopag in a micro-rate constant model for competitive inhibition of pitavatatin by eltrombopag was the best fitting model to the experimental data, with a decrease in the individual RMSRE compared to when pitavatatin only was measured (RMSRE = 7 % and 9 % respectively). Macro-rate constant models were never the best fitting model to the experimental data, partially due to the inability to adequately follow the elimination of pitavastatin from the cell through metabolism.

The use of a static clinical interaction models by calculation of the 'R value' [18, 19] for the effect of a 75 mg dose eltrombopag on a 1 mg dose of pitavastatin suggested little potential for a clinical TrDDI based on the calculated maximum liver inlet concentration (R value = 1.06-1.07), despite the large degree of inhibition seen in the *in vitro* data. This is partly due to the high level of plasma protein binding of eltrombopag, leading to an underestimation of the clinical interaction potential. Therefore in Chapter 6, a semi-mechanistic PBPK model was developed which included compartments the gastro-intestinal tract (GI tract), the blood flow linked to the liver extracellular space (the liver inlet), where the interaction is expected to take place between pitavastatin and eltrombopag, and the liver and central blood volume for elimination of drug. The estimated potential for a clinical interaction for the PBPK model, based on the calculated area under the pitavastatin blood curve ratio, in the presence and absence of eltrombopag, the AUC ratio = 2.1 was double that estimated using a static model, and therefore caution should be exercised if a clinical interaction study was to be conducted between pitavastatin and eltrombopag.

7.2 Future Work

Across the experimental chapters (Chapters 3-5), the future experimental work follows similar processes:

- Measurement of inhibitor at multiple concentrations simultaneously with substrate in the same sample will aid in the structural identifiability of macro-rate constant models, and help in the estimation of parameters in micro-rate constants.

- The experimental determination of the degree of binding interaction of substrates and inhibitors can help in the robust fitting of parameters (k_a and k_d) and further the knowledge of transporter pharmacology.

- Accurate measurement of the total amount of plasma membrane transporters in different cellular systems (cell lines and hepatocytes) in comparison with that obtained from micro-rate constant mechanistic models in the same cellular system used (e.g. like in Chapter 4). This can be used to confirm whether the T_o parameter value obtained is comparable to the measurement in crude membrane fractions.

- Quantification of metabolites should be considered to improve the understanding of the complexity of metabolism and its inhibition as well as possible effects on uptake processes. The use of LC-MSMS analysis should make this relatively straightforward.

- An initial D-optimal design analysis was carried out for each of the experimental chapters based on the best fitting mechanistic model, with the same number of timepoints and concentrations.

  – Chapter 3: The full matrix was similar to that obtained experimentally for the co-incubation data, with a greater spread of timepoints after 1.33 min. This suggests that the pre-co-incubation design could be improved using the co-incubation D-optimal design.

  – Chapter 4: Neither the full or triangular matrix removed the stable point at 0.25 min. As the model fits do not fit as well at low incubation concentrations of atorvastatin, future work should increase replicates at the lower concentrations before further D-optimal design experiments are undertaken.

  – Chapter 5: The triangular matrix was similar to that obtained experimentally, but with a shift at later timepoints by 1-2 min and a final timepoint at 38 min. This may assist in the more accurate determination of the elimination rate constant to separate it from the passive rate constant for the movement of pitavastatin out of the cell.

- The use of an increased number of substrates and inhibitors will help to build a relationship with regard to transporter kinetics at the molecular level through micro-rate constant models.

The development of a more robust parameter estimation approach for the semi-mechanistic PBPK model described in Chapter 6 to gain accurate parameter estimates, rather than a visual fit requires extensive work if the incorporation of micro-rate constants are to be included. Measurement of the amount of transporters in the same experimental system to allow scaling from *in vitro* up to *in vivo* in animals and humans, as well as the use of micro-rate constant mechanistic models will enable more accurate predictions of DDIs to be determined *a priori*, rather than *a posteriori* as they are now.

7.3 Final Conclusions

This thesis and the chapters herein have shown that across experimental systems, micro-rate constant models offer a significant improvement in structural identifiability with each micro-rate constant model at least structurally locally identifiable. The structural (local) identifiability of a model and the parameters therein was shown in each case to give an improved model fit to the experimental data, compared to their macro-rate constant model counterparts, which needed up to two parameters to be already known prior to fitting to experimental data. However, the use of micro-rate constant models also require sufficient data to cover the timecourse of uptake and metabolism, and as such may not be wholly suitable very early in research when a transport inhibitor "yes/no" may suffice. Indeed in Chapters 3-5 (with the exception of the pre-co-incubation scenario from Chapter 3), both the micro-rate constant and macro-rate constant mechanistic models were in agreement with the mode of inhibition. This provides evidence that the micro-rate constant mechanistic models are not over parameterised, but as well as a mode of inhibition confirmation, provide much more information regarding the binding kinetics and transport of substrate and inhibitors that could otherwise be missed using macro-rate constant models. Once more transporter data become available for more selected substrates and inhibitors where a more in depth analysis is required, then the use of micro-rate constant mechanistic models for robust parameter estimation should become the go-to approach for TrDDI assessment. What is apparent across each of the experimental chapters, is the combined use of simple tools to evaluate whether a mechanistic model is at least structurally identifiable, along with robust parameter estimation from well designed experiments are essential if the parameters are to be taken into other models. For example the combined measurement of pitavastatin and eltrombopag in human hepatocytes assisted in the semi-mechanistic PBPK model development to include Michaelis-Menten uptake into the liver.

7.4 Personal Reflection

The development of the work presented in this thesis has been both a very enjoyable and tough experience. Having freedom to be able to learn new concepts and implement them in mechanistic modelling, such as gaining an understanding of identifiability analysis and tracking the results of this into the parameter estimates derived from the models clearly

defines how closely they are linked. If more experimental scientists made this connection before conducting their research and experimental design, this would be of great benefit in the prediction of TrDDIs.

Undertaking a PhD really improves the resourcefulness and mental resilience of any researcher who undertakes one, as you really have to keep going when the results and models do not go the way you expected initially. As the quote said at the beginning of this PhD *"See first, think later, then test"*, should be a state of being during the PhD and beyond.

Appendix A

Structural Identifiability of a Three Compartment Model for Substrate and Inhibitor

restart

Loading LinearAlgebra
Loading Groebner
with(*LinearAlgebra*) :
with(*Groebner*) :

Many thanks to Dr Neil Evans for the following code:

Forsman Code (modified)

```
lieDer :=proc(h, f)
  local N, V:
  N := Dimension(f) :
  V := map((a, b)→diff(b, a), [seq(x[t], t = 1 ..N)], h) :
  DotProduct(f, Vector(V), conjugate = false)
  end:

listLieDer := proc(h, f, N)
  local Lfs, i, tmp :
  Lfs := [h] :  tmp := h :
  for i to N do
    tmp := lieDer(tmp, f) :
    Lfs := [op(Lfs), tmp];
  od;
  end:
obsIdeal := proc(h, f, N)
  local L, Lfs, tmp :
  Lfs := listLieDer(h, f, N) :
  L := [seq(y[t] − Lfs[t + 1], t = 0 ..N)];
  end:

iorel := proc(f, h)
  local n, L :
  n := Dimension(f) :
  L := obsIdeal(h, f, n) :
  UnivariatePolynomial(y[n], map(numer@expand, L), [seq(x[t], t = 1 ..n),
   y[n]]);
  end:
```

ONF Approach Code

```
SIAio := proc(f, h, np, x0)
  local out, n, A, B, pqSub, eqn, tmp, ics, soln :
  out := iorel(f, h);
  n := Dimension(f) :
  A := coeff(out, y[n]) :
  B := eval(out, y[n] = 0) :
  pqSub := [seq(p[i] = q[i], i = 1 ..np)] :
  eqn := A·eval(B, pqSub) − eval(A, pqSub)·B :
  tmp := collect(eqn, [seq(y[i − 1], i = 1 ..n)], 'distributed') :
  eqn := {coeffs(tmp, [seq(y[i − 1], i = 1 ..n)])} :
```

```
  ics ≔ eval(listLieDer(h, f, n − 1), [seq(x[i] = x0[i], i = 1 .. n)]) :
  tmp ≔ ics − eval(ics, pqSub) :
  eqn ≔ eqn union {op(tmp)} :
  tmp ≔ convert(eqn, list) :
  soln ≔ solve(tmp, [seq(q[i], i = 1 .. np)]) :
  out, simplify(ics), soln;
end:
```

$startTime := time( ) :$
$F := Vector([-p[1] \cdot x[1] - p[2] \cdot x[1] \cdot (p[3] - (d[1] - x[1] - x[2]) - (d[2] - x[3])) + p[4] \cdot (d[1]$
$\quad -x[1] - x[2]) + p[5] \cdot x[2], p[1] \cdot x[1] + p[6] \cdot (d[1] - x[1] - x[2]) - p[5] \cdot x[2], -p[7] \cdot x[3]$
$\quad \cdot (p[3] - (d[1] - x[1] - x[2]) - (d[2] - x[3])) + p[8] \cdot (d[2] - x[3])]) :$

$H := 333 \cdot x[2] :$
$SIAio(F, H, 8, [d[1], 0, d[2]]);$
$timeTaken := time( ) - startTime;$

$-36926037\, d_1^3 p_1^2 p_2 p_4 p_6 p_7 - 36926037\, d_1^3 p_1^2 p_2 p_6^2 p_7 + 36926037\, d_1^3 p_1 p_2^2 p_6^2 p_8 - 36926037$

$\qquad d_1^2 d_2 p_1^2 p_2 p_4 p_6 p_7 - 36926037\, d_1^2 d_2 p_1^2 p_2 p_6^2 p_7 + 36926037\, d_1^2 d_2 p_1 p_2 p_4 p_6^2 p_7 + 36926037$

$\qquad d_1^2 d_2 p_1 p_2 p_6^3 p_7 + 36926037\, d_1^2 p_1^2 p_2 p_3 p_4 p_6 p_7 + 36926037\, d_1^2 p_1^2 p_2 p_3 p_6^2 p_7 + 110889\, d_1^2$

$\qquad p_1^2 p_2 p_4 p_5 p_7 y_0 + 332667\, d_1^2 p_1^2 p_2 p_4 p_6 p_7 y_0 + 110889\, d_1^2 p_1^2 p_2 p_5 p_6 p_7 y_0 + 332667\, d_1^2 p_1^2 p_2$

$\qquad p_6^2 p_7 y_0 - 36926037\, d_1^2 p_1 p_2^2 p_3 p_6^2 p_8 - 221778\, d_1^2 p_1 p_2^2 p_5 p_6 p_8 y_0 - 332667\, d_1^2 p_1 p_2^2 p_6^2 p_8 y_0$

$\qquad - 36926037\, d_1^2 p_1 p_2 p_3 p_4 p_6^2 p_7 - 36926037\, d_1^2 p_1 p_2 p_3 p_6^3 p_7 + 221778\, d_1^2 p_1 p_2 p_4 p_5 p_6 p_7 y_0$

$\qquad + 221778\, d_1^2 p_1 p_2 p_5 p_6^2 p_7 y_0 + 36926037\, d_1^2 p_2^2 p_3 p_6^3 p_8 - 110889\, d_1^2 p_2^2 p_5 p_6^2 p_8 y_0$

$\qquad + 110889\, d_1 d_2 p_1^2 p_2 p_4 p_5 p_7 y_0 + 221778\, d_1 d_2 p_1^2 p_2 p_4 p_6 p_7 y_0 + 110889\, d_1 d_2$

$\qquad p_1^2 p_2 p_5 p_6 p_7 y_0 + 221778\, d_1 d_2 p_1^2 p_2 p_6^2 p_7 y_0 - 221778\, d_1 d_2 p_1 p_2 p_4 p_6^2 p_7 y_0$

$\qquad - 221778\, d_1 d_2 p_1 p_2 p_6^3 p_7 y_0 - 110889\, d_1 d_2 p_2 p_4 p_5 p_6^2 p_7 y_0 - 110889\, d_1 d_2 p_2 p_5 p_6^3 p_7 y_0$

$\qquad - 110889\, d_1 p_1^2 p_2 p_3 p_4 p_5 p_7 y_0 - 221778\, d_1 p_1^2 p_2 p_3 p_4 p_6 p_7 y_0 - 110889\, d_1$

$\qquad p_1^2 p_2 p_3 p_5 p_6 p_7 y_0 - 221778\, d_1 p_1^2 p_2 p_3 p_6^2 p_7 y_0 - 666\, d_1 p_1^2 p_2 p_4 p_5 p_7 y_0^2 - 999\, d_1$

$\qquad p_1^2 p_2 p_4 p_6 p_7 y_0^2 - 666\, d_1 p_1^2 p_2 p_5 p_6 p_7 y_0^2 - 999\, d_1 p_1^2 p_2 p_6^2 p_7 y_0^2 + 221778\, d_1 p_1$

$\qquad p_2^2 p_3 p_5 p_6 p_8 y_0 + 221778\, d_1 p_1 p_2^2 p_3 p_6^2 p_8 y_0 + 333\, d_1 p_1 p_2^2 p_5^2 p_8 y_0^2 + 1332\, d_1 p_1 p_2^2 p_5 p_6 p_8$

$\qquad y_0^2 + 999\, d_1 p_1 p_2^2 p_6^2 p_8 y_0^2 + 221778\, d_1 p_1 p_2 p_3 p_4 p_6^2 p_7 y_0 + 221778\, d_1 p_1 p_2 p_3 p_6^3 p_7 y_0$

$\qquad - 666\, d_1 p_1 p_2 p_4 p_5^2 p_7 y_0^2 - 1332\, d_1 p_1 p_2 p_4 p_5 p_6 p_7 y_0^2 - 666\, d_1 p_1 p_2 p_5^2 p_6 p_7 y_0^2$

$\qquad - 1332\, d_1 p_1 p_2 p_5 p_6^2 p_7 y_0^2 - 221778\, d_1 p_2^2 p_3 p_5 p_6^2 p_8 y_0 - 221778\, d_1 p_2^2 p_3 p_6^3 p_8 y_0 + 666\, d_1$

$\qquad p_2^2 p_5^2 p_6 p_8 y_0^2 + 666\, d_1 p_2^2 p_5 p_6^2 p_8 y_0^2 + 110889\, d_1 p_2 p_3 p_4 p_5 p_6^2 p_7 y_0 + 110889\, d_1 p_2 p_3 p_5$

$\qquad p_6^3 p_7 y_0 - 333\, d_1 p_2 p_4 p_5^2 p_6 p_7 y_0^2 - 333\, d_1 p_2 p_5^2 p_6^2 p_7 y_0^2 - 333\, d_2 p_1^2 p_2 p_4 p_5 p_7 y_0^2 - 333\, d_2$

$\qquad p_1^2 p_2 p_4 p_6 p_7 y_0^2 - 333\, d_2 p_1^2 p_2 p_5 p_6 p_7 y_0^2 - 333\, d_2 p_1^2 p_2 p_6^2 p_7 y_0^2 - 333\, d_2 p_1 p_2 p_4 p_5^2 p_7 y_0^2$

$$+ 333\, d_2 p_1 p_2 p_4 p_6^2 p_7 y_0^2 - 333\, d_2 p_1 p_2 p_5^2 p_6 p_7 y_0^2 + 333\, d_2 p_1 p_2 p_5^3 p_7 y_0^2 + 333\, d_2 p_2 p_4$$
$$p_5^2 p_6 p_7 y_0^2 + 333\, d_2 p_2 p_4 p_5 p_6^2 p_7 y_0^2 + 333\, d_2 p_2 p_5^2 p_6^2 p_7 y_0^2 + 333\, d_2 p_2 p_5 p_6^3 p_7 y_0^2 + 333$$
$$p_1^2 p_2 p_3 p_4 p_5 p_7 y_0^2 + 333\, p_1^2 p_2 p_3 p_4 p_6 p_7 y_0^2 + 333\, p_1^2 p_2 p_3 p_5 p_6 p_7 y_0^2 + 333\, p_1^2 p_2 p_3 p_6^2 p_7 y_0^2$$
$$+ p_1^2 p_2 p_4 p_5 p_7 y_0^3 + p_1^2 p_2 p_4 p_6 p_7 y_0^3 + p_1^2 p_2 p_5 p_6 p_7 y_0^3 + p_1^2 p_2 p_6^2 p_7 y_0^3 - 333\, p_1 p_2^2 p_3 p_5^2 p_8$$
$$y_0^2 - 666\, p_1 p_2^2 p_3 p_5 p_6 p_8 y_0^2 - 333\, p_1 p_2^2 p_3 p_6^2 p_8 y_0^2 - p_1 p_2^2 p_5^2 p_8 y_0^3 - 2\, p_1 p_2^2 p_5 p_6 p_8 y_0^3 - p_1$$
$$p_2^2 p_6^2 p_8 y_0^3 + 333\, p_1 p_2 p_3 p_4 p_5^2 p_7 y_0^2 - 333\, p_1 p_2 p_3 p_4 p_6^2 p_7 y_0^2 + 333\, p_1 p_2 p_3 p_5^2 p_6 p_7 y_0^2$$
$$- 333\, p_1 p_2 p_3 p_6^3 p_7 y_0^2 + 2\, p_1 p_2 p_4 p_5^2 p_7 y_0^3 + 2\, p_1 p_2 p_4 p_5 p_6 p_7 y_0^3 + 2\, p_1 p_2 p_5^2 p_6 p_7 y_0^3$$
$$+ 2\, p_1 p_2 p_5 p_6^2 p_7 y_0^3 + 333\, p_2^2 p_3 p_5^2 p_6 p_8 y_0^2 + 666\, p_2^2 p_3 p_5 p_6^2 p_8 y_0^2 + 333\, p_2^2 p_3 p_6^3 p_8 y_0^2 - p_2^2$$
$$p_5^3 p_8 y_0^3 - 2\, p_2^2 p_5^2 p_6 p_8 y_0^3 - p_2^2 p_5 p_6^2 p_8 y_0^3 - 333\, p_2 p_3 p_4 p_5^2 p_6 p_7 y_0^2 - 333\, p_2 p_3 p_4 p_5 p_6^2 p_7 y_0^2$$
$$- 333\, p_2 p_3 p_5^2 p_6^2 p_7 y_0^2 - 333\, p_2 p_3 p_5 p_6^3 p_7 y_0^2 + p_2 p_4 p_5^3 p_7 y_0^3 + p_2 p_4 p_5^2 p_6 p_7 y_0^3 + p_2$$
$$p_5^3 p_6 p_7 y_0^3 + p_2 p_5^2 p_6^2 p_7 y_0^3 + 36926037\, d_1^2 p_1^3 p_4^2 p_7 + 73852074\, d_1^2 p_1^3 p_4 p_6 p_7 + 36926037\, d_1^2$$
$$p_1^3 p_6^2 p_7 - 36926037\, d_1^2 p_1^2 p_2 p_4 p_6 p_8 + 110889\, d_1^2 p_1^2 p_2 p_4 p_7 y_1 - 36926037\, d_1^2 p_1^2 p_2 p_6^2 p_8$$
$$+ 221778\, d_1^2 p_1^2 p_2 p_6 p_7 y_1 - 36926037\, d_1^2 p_1^2 p_4^2 p_6 p_7 - 73852074\, d_1^2 p_1^2 p_4 p_6^2 p_7 - 36926037$$
$$d_1^2 p_1^2 p_6^3 p_7 - 110889\, d_1^2 p_1 p_2^2 p_6^2 y_1 - 221778\, d_1^2 p_1 p_2^2 p_6 p_8 y_1 + 36926037\, d_1^2 p_1 p_2 p_4 p_6^2 p_8$$
$$+ 221778\, d_1^2 p_1 p_2 p_4 p_6 p_7 y_1 + 110889\, d_1^2 p_1 p_2 p_5 p_6 p_7 y_1 + 36926037\, d_1^2 p_1 p_2 p_6^3 p_8$$
$$+ 221778\, d_1^2 p_1 p_2 p_6^2 p_7 y_1 - 110889\, d_1^2 p_2^2 p_5 p_6^2 y_1 - 110889\, d_1^2 p_2^2 p_6^2 p_8 y_1 + 110889\, d_1 d_2$$
$$p_1^2 p_2 p_4 p_7 y_1 + 221778\, d_1 d_2 p_1^2 p_2 p_6 p_7 y_1 + 110889\, d_1 d_2 p_1 p_2 p_5 p_6 p_7 y_1$$
$$- 110889\, d_1 d_2 p_1 p_2 p_6^2 p_7 y_1 - 110889\, d_1 d_2 p_2 p_4 p_6^2 p_7 y_1 - 110889\, d_1 d_2 p_2 p_5 p_6^2 p_7 y_1$$
$$- 110889\, d_1 d_2 p_2 p_6^3 p_7 y_1 - 221778\, d_1 p_1^3 p_4^2 p_7 y_0 - 443556\, d_1 p_1^3 p_4 p_6 p_7 y_0 - 221778\, d_1 p_1^3$$
$$p_6^2 p_7 y_0 - 110889\, d_1 p_1^2 p_2 p_3 p_4 p_7 y_1 - 221778\, d_1 p_1^2 p_2 p_3 p_6 p_7 y_1 + 110889\, d_1$$
$$p_1^2 p_2 p_4 p_5 p_8 y_0 + 221778\, d_1 p_1^2 p_2 p_4 p_6 p_8 y_0 - 666\, d_1 p_1^2 p_2 p_4 p_7 y_0 y_1 + 110889\, d_1$$
$$p_1^2 p_2 p_5 p_6 p_8 y_0 - 333\, d_1 p_1^2 p_2 p_5 p_7 y_0 y_1 + 221778\, d_1 p_1^2 p_2 p_6^2 p_8 y_0 - 1332\, d_1$$
$$p_1^2 p_2 p_6 p_7 y_0 y_1 - 221778\, d_1 p_1^2 p_4^2 p_5 p_7 y_0 + 221778\, d_1 p_1^2 p_4^2 p_6 p_7 y_0 - 443556\, d_1$$
$$p_1^2 p_4 p_5 p_6 p_7 y_0 + 443556\, d_1 p_1^2 p_4 p_6^2 p_7 y_0 - 221778\, d_1 p_1^2 p_5 p_6^2 p_7 y_0 + 221778\, d_1 p_1^2 p_6^3 p_7 y_0$$
$$+ 221778\, d_1 p_1 p_2^2 p_3 p_6 p_8 y_1 + 666\, d_1 p_1 p_2^2 p_5 p_6 y_0 y_1 + 666\, d_1 p_1 p_2^2 p_5 p_8 y_0 y_1 + 666\, d_1 p_1$$
$$p_2^2 p_6^2 y_0 y_1 + 1332\, d_1 p_1 p_2^2 p_6 p_8 y_0 y_1 - 110889\, d_1 p_1 p_2 p_3 p_5 p_6 p_7 y_1 + 110889\, d_1 p_1 p_2 p_3$$
$$p_6^2 p_7 y_1 - 1332\, d_1 p_1 p_2 p_4 p_5 p_7 y_0 y_1 - 221778\, d_1 p_1 p_2 p_4 p_6^2 p_8 y_0$$
$$- 1332\, d_1 p_1 p_2 p_4 p_6 p_7 y_0 y_1 - 333\, d_1 p_1 p_2 p_5^2 p_7 y_0 y_1 - 2331\, d_1 p_1 p_2 p_5 p_6 p_7 y_0 y_1$$
$$- 221778\, d_1 p_1 p_2 p_6^3 p_8 y_0 - 1332\, d_1 p_1 p_2 p_6^2 p_7 y_0 y_1 + 221778\, d_1 p_1 p_4^2 p_5 p_6 p_7 y_0$$

$$+ 443556\, d_1 p_1 p_4 p_5 p_6^2 p_7 y_0 + 221778\, d_1 p_1 p_5 p_6^3 p_7 y_0 - 221778\, d_1 p_2^2 p_3 p_6^2 p_8 y_1 + 666\, d_1$$

$$p_2^2 p_5^2 p_6 y_0 y_1 + 666\, d_1 p_2^2 p_5 p_6^2 y_0 y_1 + 1332\, d_1 p_2^2 p_5 p_6 p_8 y_0 y_1 + 666\, d_1 p_2^2 p_6^2 p_8 y_0 y_1$$

$$+ 110889\, d_1 p_2 p_3 p_4 p_6^2 p_7 y_1 + 110889\, d_1 p_2 p_3 p_5 p_6^2 p_7 y_1 + 110889\, d_1 p_2 p_3 p_6^3 p_7 y_1$$

$$- 110889\, d_1 p_2 p_4 p_5 p_6^2 p_8 y_0 - 666\, d_1 p_2 p_4 p_5 p_6 p_7 y_0 y_1 - 333\, d_1 p_2 p_5^2 p_6 p_7 y_0 y_1$$

$$- 110889\, d_1 p_2 p_5 p_6^3 p_8 y_0 - 666\, d_1 p_2 p_5 p_6^2 p_7 y_0 y_1 - 333\, d_2 p_1^2 p_2 p_4 p_7 y_0 y_1 - 333\, d_2$$

$$p_1^2 p_2 p_5 p_7 y_0 y_1 - 666\, d_2 p_1^2 p_2 p_6 p_7 y_0 y_1 - 666\, d_2 p_1 p_2 p_4 p_5 p_7 y_0 y_1 - 333\, d_2 p_1 p_2$$

$$p_5^2 p_7 y_0 y_1 - 666\, d_2 p_1 p_2 p_5 p_6 p_7 y_0 y_1 + 333\, d_2 p_1 p_2 p_6^2 p_7 y_0 y_1 + 666\, d_2 p_2 p_4 p_5 p_6 p_7 y_0 y_1$$

$$+ 333\, d_2 p_2 p_4 p_6^2 p_7 y_0 y_1 + 333\, d_2 p_2 p_5^2 p_6 p_7 y_0 y_1 + 999\, d_2 p_2 p_5 p_6^2 p_7 y_0 y_1 + 333\, d_2 p_2$$

$$p_6^3 p_7 y_0 y_1 + 333\, p_1^3 p_4^2 p_7 y_0^2 + 666\, p_1^3 p_4 p_6 p_7 y_0^2 + 333\, p_1^3 p_6^2 p_7 y_0^2 + 333\, p_1^2 p_2 p_3 p_4 p_7 y_0 y_1$$

$$+ 333\, p_1^2 p_2 p_3 p_5 p_7 y_0 y_1 + 666\, p_1^2 p_2 p_3 p_6 p_7 y_0 y_1 - 333\, p_1^2 p_2 p_4 p_5 p_8 y_0^2 - 333$$

$$p_1^2 p_2 p_4 p_6 p_8 y_0^2 + p_1^2 p_2 p_4 p_7 y_0^2 y_1 - 333\, p_1^2 p_2 p_5 p_6 p_8 y_0^2 + p_1^2 p_2 p_5 p_7 y_0^2 y_1 - 333\, p_1^2 p_2 p_6^2 p_8$$

$$y_0^2 + 2\, p_1^2 p_2 p_6 p_7 y_0^2 y_1 + 666\, p_1^2 p_4^2 p_5 p_7 y_0^2 - 333\, p_1^2 p_4^2 p_6 p_7 y_0^2 + 1332\, p_1^2 p_4 p_5 p_6 p_7 y_0^2$$

$$- 666\, p_1^2 p_4 p_6^2 p_7 y_0^2 + 666\, p_1^2 p_5 p_6^2 p_7 y_0^2 - 333\, p_1^2 p_6^3 p_7 y_0^2 - 666\, p_1 p_2^2 p_3 p_5 p_8 y_0 y_1 - 666\, p_1$$

$$p_2^2 p_3 p_6 p_8 y_0 y_1 - p_1 p_2^2 p_5^2 y_0^2 y_1 - 2\, p_1 p_2^2 p_5 p_6 y_0^2 y_1 - 2\, p_1 p_2^2 p_5 p_8 y_0^2 y_1 - p_1 p_2^2 p_6^2 y_0^2 y_1$$

$$- 2\, p_1 p_2^2 p_6 p_8 y_0^2 y_1 + 666\, p_1 p_2 p_3 p_4 p_5 p_7 y_0 y_1 + 333\, p_1 p_2 p_3 p_5^2 p_7 y_0 y_1$$

$$+ 666\, p_1 p_2 p_3 p_5 p_6 p_7 y_0 y_1 - 333\, p_1 p_2 p_3 p_6^2 p_7 y_0 y_1 - 333\, p_1 p_2 p_4 p_5^2 p_8 y_0^2$$

$$+ 4\, p_1 p_2 p_4 p_5 p_7 y_0^2 y_1 + 333\, p_1 p_2 p_4 p_6^2 p_8 y_0^2 + 2\, p_1 p_2 p_4 p_6 p_7 y_0^2 y_1 - 333\, p_1 p_2 p_5^2 p_6 p_8 y_0^2$$

$$+ 2\, p_1 p_2 p_5^2 p_7 y_0^2 y_1 + 6\, p_1 p_2 p_5 p_6 p_7 y_0^2 y_1 + 333\, p_1 p_2 p_6^3 p_8 y_0^2 + 2\, p_1 p_2 p_6^2 p_7 y_0^2 y_1 + 333\, p_1$$

$$p_4^2 p_5^2 p_7 y_0^2 - 666\, p_1 p_4^2 p_5 p_6 p_7 y_0^2 + 666\, p_1 p_4 p_5^2 p_6 p_7 y_0^2 - 1332\, p_1 p_4 p_5 p_6^2 p_7 y_0^2 + 333\, p_1 p_5^2$$

$$p_6^2 p_7 y_0^2 - 666\, p_1 p_5 p_6^3 p_7 y_0^2 + 666\, p_2^2 p_3 p_5 p_6 p_8 y_0 y_1 + 666\, p_2^2 p_3 p_6^2 p_8 y_0 y_1 - p_2^2 p_5^3 y_0^2 y_1 - 2$$

$$p_2^2 p_5^2 p_6 y_0^2 y_1 - 3\, p_2^2 p_5^2 p_8 y_0^2 y_1 - p_2^2 p_5 p_6^2 y_0^2 y_1 - 4\, p_2^2 p_5 p_6 p_8 y_0^2 y_1 - p_2^2 p_6^2 p_8 y_0^2 y_1$$

$$- 666\, p_2 p_3 p_4 p_5 p_6 p_7 y_0 y_1 - 333\, p_2 p_3 p_4 p_6^2 p_7 y_0 y_1 - 333\, p_2 p_3 p_5^2 p_6 p_7 y_0 y_1$$

$$- 999\, p_2 p_3 p_5 p_6^2 p_7 y_0 y_1 - 333\, p_2 p_3 p_6^3 p_7 y_0 y_1 + 333\, p_2 p_4 p_5^2 p_6 p_8 y_0^2 + 3\, p_2 p_4 p_5^2 p_7 y_0^2 y_1$$

$$+ 333\, p_2 p_4 p_5 p_6^2 p_8 y_0^2 + 2\, p_2 p_4 p_5 p_6 p_7 y_0^2 y_1 + p_2 p_5^3 p_7 y_0^2 y_1 + 333\, p_2 p_5^2 p_6^2 p_8 y_0^2 + 4\, p_2$$

$$p_5^2 p_6 p_7 y_0^2 y_1 + 333\, p_2 p_5 p_6^3 p_8 y_0^2 + 2\, p_2 p_5 p_6^2 p_7 y_0^2 y_1 - 333\, p_4^2 p_5^2 p_6 p_7 y_0^2 - 666\, p_4 p_5^2 p_6^2 p_7 y_0^2$$

$$- 333\, p_5^2 p_6^3 p_7 y_0^2 + 110889\, d_1^2 p_1 p_2 p_6 p_7 y_2 - 110889\, d_1^2 p_2^2 p_6^2 y_2$$

$$+ 110889\, d_1 d_2 p_1 p_2 p_6 p_7 y_2 - 110889\, d_1 d_2 p_2 p_6^2 p_7 y_2 - 221778\, d_1 p_1^3 p_4 p_7 y_1 - 221778\, d_1$$

$$p_1^3 p_6 p_7 y_1 - 110889\, d_1 p_1^2 p_2 p_4 p_5 y_1 + 110889\, d_1 p_1^2 p_2 p_4 p_8 y_1 - 110889\, d_1 p_1^2 p_2 p_5 p_6 y_1$$

$$+ 221778\, d_1 p_1^2 p_2 p_6 p_8 y_1 - 333\, d_1 p_1^2 p_2 p_7 y_1^2 - 221778\, d_1 p_1^2 p_4^2 p_7 y_1 - 221778\, d_1$$

$$p_1^2 p_4 p_5 p_7 y_1 - 221778\, d_1 p_1^2 p_4 p_6 p_7 y_1 - 221778\, d_1 p_1^2 p_5 p_6 p_7 y_1 + 666\, d_1 p_1 p_2^2 p_6 y_1^2$$

$$+ 333\, d_1 p_1 p_2^2 p_8 y_1^2 - 110889\, d_1 p_1 p_2 p_3 p_6 p_7 y_2 + 221778\, d_1 p_1 p_2 p_4 p_5 p_6 y_1$$

$$- 666\, d_1 p_1 p_2 p_4 p_7 y_1^2 + 221778\, d_1 p_1 p_2 p_5 p_6^2 y_1 + 110889\, d_1 p_1 p_2 p_5 p_6 p_8 y_1$$

$$- 333\, d_1 p_1 p_2 p_5 p_7 y_0 y_2 - 333\, d_1 p_1 p_2 p_5 p_7 y_1^2 - 110889\, d_1 p_1 p_2 p_6^2 p_8 y_1$$

$$- 666\, d_1 p_1 p_2 p_6 p_7 y_0 y_2 - 999\, d_1 p_1 p_2 p_6 p_7 y_1^2 + 221778\, d_1 p_1 p_4^2 p_6 p_7 y_1$$

$$+ 221778\, d_1 p_1 p_4 p_5 p_6 p_7 y_1 + 443556\, d_1 p_1 p_4 p_6^2 p_7 y_1 + 221778\, d_1 p_1 p_5 p_6^2 p_7 y_1$$

$$+ 221778\, d_1 p_1 p_6^3 p_7 y_1 + 666\, d_1 p_2^2 p_5 p_6 y_0 y_2 + 666\, d_1 p_2^2 p_5 p_6 y_1^2 + 666\, d_1 p_2^2 p_6^2 y_0 y_2$$

$$+ 666\, d_1 p_2^2 p_6 p_8 y_1^2 + 110889\, d_1 p_2 p_3 p_6^2 p_7 y_2 - 110889\, d_1 p_2 p_4 p_5 p_6^2 y_1 - 110889\, d_1 p_2 p_4$$

$$p_6^2 p_8 y_1 - 333\, d_1 p_2 p_4 p_6 p_7 y_1^2 - 110889\, d_1 p_2 p_5 p_6^3 y_1 - 110889\, d_1 p_2 p_5 p_6^2 p_8 y_1$$

$$- 333\, d_1 p_2 p_5 p_6 p_7 y_0 y_2 - 333\, d_1 p_2 p_5 p_6 p_7 y_1^2 - 110889\, d_1 p_2 p_6^3 p_8 y_1 - 333\, d_1 p_2 p_6^2 p_7 y_1^2$$

$$- 333\, d_2 p_1^2 p_2 p_7 y_1^2 - 333\, d_2 p_1 p_2 p_4 p_7 y_1^2 - 333\, d_2 p_1 p_2 p_5 p_7 y_0 y_2 - 333\, d_2 p_1 p_2 p_5 p_7 y_1^2$$

$$- 333\, d_2 p_1 p_2 p_6 p_7 y_0 y_2 + 333\, d_2 p_2 p_4 p_6 p_7 y_1^2 + 333\, d_2 p_2 p_5 p_6 p_7 y_0 y_2$$

$$+ 333\, d_2 p_2 p_5 p_6 p_7 y_1^2 + 333\, d_2 p_2 p_6^2 p_7 y_0 y_2 + 333\, d_2 p_2 p_6^2 p_7 y_1^2 + 666\, p_1^3 p_4 p_7 y_0 y_1 + 666$$

$$p_1^3 p_6 p_7 y_0 y_1 + 333\, p_1^2 p_2 p_3 p_7 y_1^2 - 333\, p_1^2 p_2 p_4 p_8 y_0 y_1 - 333\, p_1^2 p_2 p_5 p_8 y_0 y_1 - 666$$

$$p_1^2 p_2 p_6 p_8 y_0 y_1 + p_1^2 p_2 p_7 y_0 y_1^2 + 666\, p_1^2 p_4^2 p_7 y_0 y_1 + 1332\, p_1^2 p_4 p_5 p_7 y_0 y_1 + 666$$

$$p_1^2 p_4 p_6 p_7 y_0 y_1 + 1332\, p_1^2 p_5 p_6 p_7 y_0 y_1 - 333\, p_1 p_2^2 p_3 p_8 y_1^2 - 2\, p_1 p_2^2 p_5 y_0 y_1^2 - 2\, p_1 p_2^2 p_6 y_0$$

$$y_1^2 - p_1 p_2^2 p_8 y_0 y_1^2 + 333\, p_1 p_2 p_3 p_4 p_7 y_1^2 + 333\, p_1 p_2 p_3 p_5 p_7 y_0 y_2 + 333\, p_1 p_2 p_3 p_5 p_7 y_1^2$$

$$+ 333\, p_1 p_2 p_3 p_6 p_7 y_0 y_2 - 666\, p_1 p_2 p_4 p_5 p_8 y_0 y_1 + 2\, p_1 p_2 p_4 p_7 y_0 y_1^2 - 333\, p_1 p_2 p_5^2 p_8 y_0 y_1$$

$$- 666\, p_1 p_2 p_5 p_6 p_8 y_0 y_1 + p_1 p_2 p_5 p_7 y_0^2 y_2 + 3\, p_1 p_2 p_5 p_7 y_0 y_1^2 + 333\, p_1 p_2 p_6^2 p_8 y_0 y_1$$

$$+ p_1 p_2 p_6 p_7 y_0^2 y_2 + 3\, p_1 p_2 p_6 p_7 y_0 y_1^2 + 666\, p_1 p_4^2 p_5 p_7 y_0 y_1 - 666\, p_1 p_4^2 p_6 p_7 y_0 y_1$$

$$+ 666\, p_1 p_4 p_5^2 p_7 y_0 y_1 - 1332\, p_1 p_4 p_6^2 p_7 y_0 y_1 + 666\, p_1 p_5^2 p_6 p_7 y_0 y_1 - 666\, p_1 p_5 p_6^2 p_7 y_0 y_1$$

$$- 666\, p_1 p_6^3 p_7 y_0 y_1 + 333\, p_2^2 p_3 p_6 p_8 y_1^2 - p_2^2 p_5^2 y_0^2 y_2 - 2\, p_2^2 p_5^2 y_0 y_1^2 - 2\, p_2^2 p_5 p_6 y_0^2 y_2 - 2$$

$$p_2^2 p_5 p_6 y_0 y_1^2 - 3\, p_2^2 p_5 p_8 y_0 y_1^2 - p_2^2 p_6^2 y_0^2 y_2 - 2\, p_2^2 p_6 p_8 y_0 y_1^2 - 333\, p_2 p_3 p_4 p_6 p_7 y_1^2$$

$$- 333\, p_2 p_3 p_5 p_6 p_7 y_0 y_2 - 333\, p_2 p_3 p_5 p_6 p_7 y_1^2 - 333\, p_2 p_3 p_6^2 p_7 y_0 y_2 - 333\, p_2 p_3 p_6^2 p_7 y_1^2$$

$$+ 666\, p_2 p_4 p_5 p_6 p_8 y_0 y_1 + 3\, p_2 p_4 p_5 p_7 y_0 y_1^2 + 333\, p_2 p_4 p_6^2 p_8 y_0 y_1 + p_2 p_4 p_6 p_7 y_0 y_1^2$$

$$+ 333\, p_2 p_5^2 p_6 p_8 y_0 y_1 + p_2 p_5^2 p_7 y_0^2 y_2 + 2\, p_2 p_5^2 p_7 y_0 y_1^2 + 999\, p_2 p_5 p_6^2 p_8 y_0 y_1 + p_2 p_5 p_6 p_7$$

$$y_0^2 y_2 + 4\, p_2 p_5 p_6 p_7 y_0 y_1^2 + 333\, p_2 p_6^3 p_8 y_0 y_1 + p_2 p_6^2 p_7 y_0 y_1^2 - 666\, p_4^2 p_5 p_6 p_7 y_0 y_1 - 666\, p_4$$

$$p_5^2 p_6 p_7 y_0 y_1 - 1332\, p_4 p_5 p_6^2 p_7 y_0 y_1 - 666\, p_5^2 p_6^2 p_7 y_0 y_1 - 666\, p_5 p_6^3 p_7 y_0 y_1 - 110889\, d_1$$

$$p_1^2 p_2 p_4 y_2 - 221778\, d_1 p_1^2 p_4 p_7 y_2 - 221778\, d_1 p_1^2 p_6 p_7 y_2 + 221778\, d_1 p_1 p_2 p_4 p_6 y_2$$

$$+ 110889\, d_1 p_1 p_2 p_5 p_6 y_2 + 110889\, d_1 p_1 p_2 p_6^2 y_2 + 110889\, d_1 p_1 p_2 p_6 p_8 y_2$$

$$- 333\, d_1 p_1 p_2 p_7 y_1 y_2 + 221778\, d_1 p_1 p_4 p_6 p_7 y_2 + 221778\, d_1 p_1 p_6^2 p_7 y_2 + 666\, d_1 p_2^2 p_6 y_1 y_2$$

$$- 110889\, d_1 p_2 p_4 p_6^2 y_2 - 110889\, d_1 p_2 p_5 p_6^2 y_2 - 110889\, d_1 p_2 p_6^3 y_2 - 110889\, d_1 p_2 p_6^2 p_8 y_2$$

$$- 333\, d_1 p_2 p_6 p_7 y_1 y_2 - 333\, d_2 p_1 p_2 p_7 y_1 y_2 + 333\, d_2 p_2 p_6 p_7 y_1 y_2 + 333\, p_1^3 p_7 y_1^2 + 333$$

$$p_1^2 p_2 p_4 y_0 y_2 - 333\, p_1^2 p_2 p_4 y_1^2 - 333\, p_1^2 p_2 p_5 y_0 y_2 + 333\, p_1^2 p_2 p_5 y_1^2 - 333\, p_1^2 p_2 p_8 y_1^2 + 666$$

$$p_1^2 p_4 p_7 y_0 y_2 + 666\, p_1^2 p_4 p_7 y_1^2 + 666\, p_1^2 p_5 p_7 y_1^2 + 666\, p_1^2 p_6 p_7 y_0 y_2 + 333\, p_1^2 p_6 p_7 y_1^2 - p_1 p_2^2$$

$$y_1^3 + 333\, p_1 p_2 p_3 p_7 y_1 y_2 - 666\, p_1 p_2 p_4 p_6 y_0 y_2 + 666\, p_1 p_2 p_4 p_6 y_1^2 - 333\, p_1 p_2 p_4 p_8 y_1^2$$

$$- 333\, p_1 p_2 p_5^2 y_0 y_2 + 333\, p_1 p_2 p_5^2 y_1^2 - 333\, p_1 p_2 p_5 p_8 y_0 y_2 - 333\, p_1 p_2 p_5 p_8 y_1^2 - 333\, p_1 p_2$$

$$p_6^2 y_0 y_2 + 333\, p_1 p_2 p_6^2 y_1^2 - 333\, p_1 p_2 p_6 p_8 y_0 y_2 + p_1 p_2 p_7 y_0 y_1 y_2 + p_1 p_2 p_7 y_1^3 + 333\, p_1$$

$$p_4^2 p_7 y_1^2 + 666\, p_1 p_4 p_5 p_7 y_0 y_2 + 666\, p_1 p_4 p_5 p_7 y_1^2 - 666\, p_1 p_4 p_6 p_7 y_0 y_2 + 333\, p_1 p_5^2 p_7 y_1^2$$

$$+ 666\, p_1 p_5 p_6 p_7 y_0 y_2 - 666\, p_1 p_6^2 p_7 y_0 y_2 - 333\, p_1 p_6^2 p_7 y_1^2 - 2\, p_2^2 p_5 y_0 y_1 y_2 - p_2^2 p_5 y_1^3 - 2$$

$$p_2^2 p_6 y_0 y_1 y_2 - p_2^2 p_8 y_1^3 - 333\, p_2 p_3 p_6 p_7 y_1 y_2 + 333\, p_2 p_4 p_6^2 y_0 y_2 - 333\, p_2 p_4 p_6^2 y_1^2$$

$$+ 333\, p_2 p_4 p_6 p_8 y_1^2 + p_2 p_4 p_7 y_1^3 + 333\, p_2 p_5^2 p_6 y_0 y_2 - 333\, p_2 p_5^2 p_6 y_1^2 + 333\, p_2 p_5 p_6^2 y_0 y_2$$

$$- 333\, p_2 p_5 p_6^2 y_1^2 + 333\, p_2 p_5 p_6 p_8 y_0 y_2 + 333\, p_2 p_5 p_6 p_8 y_1^2 + 2\, p_2 p_5 p_7 y_0 y_1 y_2 + p_2 p_5 p_7 y_1^3$$

$$+ 333\, p_2 p_6^3 y_0 y_2 - 333\, p_2 p_6^3 y_1^2 + 333\, p_2 p_6^2 p_8 y_0 y_2 + 333\, p_2 p_6^2 p_8 y_1^2 + p_2 p_6 p_7 y_0 y_1 y_2$$

$$+ p_2 p_6 p_7 y_1^3 - 333\, p_4^2 p_6 p_7 y_1^2 - 666\, p_4 p_5 p_6 p_7 y_0 y_2 - 666\, p_4 p_5 p_6 p_7 y_1^2 - 666\, p_4 p_6^2 p_7 y_1^2$$

$$- 333\, p_5^2 p_6 p_7 y_1^2 - 666\, p_5 p_6^2 p_7 y_0 y_2 - 666\, p_5 p_6^2 p_7 y_1^2 - 333\, p_6^3 p_7 y_1^2 + 110889\, d_1 p_1 p_2 p_6 y_3$$

$$- 110889\, d_1 p_2 p_6^2 y_3 + 666\, p_1^2 p_7 y_1 y_2 - 333\, p_1 p_2 p_5 y_0 y_3 + 333\, p_1 p_2 p_5 y_1 y_2$$

$$- 333\, p_1 p_2 p_6 y_0 y_3 + 333\, p_1 p_2 p_6 y_1 y_2 - 333\, p_1 p_2 p_8 y_1 y_2 + 666\, p_1 p_4 p_7 y_1 y_2$$

$$+ 666\, p_1 p_5 p_7 y_1 y_2 - p_2^2 y_1^2 y_2 + 333\, p_2 p_5 p_6 y_0 y_3 - 333\, p_2 p_5 p_6 y_1 y_2 + 333\, p_2 p_6^2 y_0 y_3$$

$$- 333\, p_2 p_6^2 y_1 y_2 + 333\, p_2 p_6 p_8 y_1 y_2 + p_2 p_7 y_1^2 y_2 - 666\, p_4 p_6 p_7 y_1 y_2 - 666\, p_5 p_6 p_7 y_1 y_2$$

$$- 666\, p_6^2 p_7 y_1 y_2 - 333\, p_1 p_2 y_1 y_3 + 333\, p_1 p_2 y_2^2 + 333\, p_1 p_7 y_2^2 + 333\, p_2 p_6 y_1 y_3$$

$$- 333\, p_2 p_6 y_2^2 - 333\, p_6 p_7 y_2^2,\ \left[0,\ 333\, p_1 d_1,\ -333\, d_1 \left(p_1^2 + \left(p_2 p_3 + p_5 \right) p_1 - p_2 p_3 p_6 \right) \right],$$

$$\left[\left[q_1 = p_1,\ q_2 = 0,\ q_3 = q_3,\ q_4 = q_4,\ q_5 = -\frac{-p_1 p_2 p_3 + p_2 p_3 p_6 - p_1 p_5}{p_1},\ q_6 = q_6,\ q_7 = 0,\ q_8 \right.\right.$$

$$\left. = q_8 \right],\ \left[q_1 = p_1,\ q_2 = 0,\ q_3 = q_3,\ q_4 = q_4,\ q_5 = -\frac{-p_1 p_2 p_3 + p_2 p_3 p_6 - p_1 p_5}{p_1},\ q_6 = p_1,\ q_7 = q_7,\ q_8 \right.$$

$$\left. = q_8 \right],\ \left[q_1 = p_1,\ q_2 = q_2,\ q_7 = q_2,\ q_3 = q_3,\ q_4 = q_4,\ q_5 = -\frac{-p_1 p_2 p_3 + p_2 p_3 p_6 - p_1 p_5}{p_1},\ q_6 = p_1, \right.$$

$$\left.\left. q_8 = q_4 + p_1 \right],\ \left[q_1 = p_1,\ q_2 = p_2,\ q_3 = p_3,\ q_4 = p_4,\ q_5 = p_5,\ q_6 = p_6,\ q_7 = p_7,\ q_8 = p_8 \right]\right]$$

Appendix B

Structural Identifiability Example with the `Identifiability Analysis` Package - Micro-rate Constant Model

Needs["IdentifiabilityAnalysis"]

deq = {

$x_1'[t] == -\theta_1 * x_1[t] - \theta_2 * x_1[t] * (\theta_3 - x_2[t] - x_5[t]) + \theta_4 * x_2[t] + \theta_5 * x_3[t],$

$x_2'[t] == \theta_2 * x_1[t] * (\theta_3 - x_2[t] - x_5[t]) - (\theta_4 + \theta_6) * x_2[t],$

$x_3'[t] == \theta_1 * x_1[t] + \theta_6 * x_2[t] - (\theta_5 + \theta_7) * x_3[t],$

$x_4'[t] == -\theta_8 * x_4[t] - \theta_9 * x_4[t] * (\theta_3 - x_2[t] - x_5[t]) + \theta_{10} * x_5[t] + \theta_{11} * x_6[t],$

$x_5'[t] == \theta_9 * x_4[t] * (\theta_3 - x_2[t] - x_5[t]) - \theta_{10} * x_5[t],$

$x_6'[t] == \theta_8 * x_4[t] - \theta_{11} * x_6[t]$

};

Dose = 3;

Doseb = 30;

modelStates = $\{x_1, x_2, x_3, x_4, x_5, x_6\}$;

ic = $\{x_1[0]==$Dose$, x_2[0]==0, x_3[0]==0, x_4[0]==$Doseb$, x_5[0]==0, x_6[0] == 0\}$;

modelParameters = Table $[\theta_i, \{i, 12\}]$;

observationVector = $\{\theta_{12} * (x_5[t] + x_6[t])$

};

iad = IdentifiabilityAnalysis[{{deq, ic}, observationVector}, modelStates, modelParameters, t, u]

IdentifiabilityAnalysisData[True, $<>$]

iad["DegreesOfFreedom"]

iad["NonIdentifiableParameters"]

Appendix C

Structural Identifiability Example with the `Identifiability Analysis` Package - Macro-rate Constant Model

Needs["IdentifiabilityAnalysis"]

deq = {

$x_1'[t] == -\theta_1 * x_1[t] - (\theta_2 * x_1[t]) / (\theta_3 * (1 + 30 / \theta_4) + x_1[t]) + \theta_5 * x_2[t],$

$x_2'[t] == \theta_1 * x_1[t] + (\theta_2 * x_1[t]) / (\theta_3 * (1 + 30 / \theta_4) + x_1[t]) - (\theta_5 + \theta_6) * x_2[t]$

};

Dose = 5;

modelStates = $\{x_1, x_2\}$;

ic = $\{x_1[0] == \text{Dose}, x_2[0] == 0\}$;

modelParameters = Table$[\theta_i, \{i, 6\}]$;

observationVector = $\{333 * x_2[t]$

};

iad = IdentifiabilityAnalysis[{{deq, ic}, observationVector}, modelStates, modelParameters, t, u]

IdentifiabilityAnalysisData[False, $<>$]

iad["DegreesOfFreedom"]

1

iad["NonIdentifiableParameters"]

$\{\theta_3, \theta_4\}$

Appendix D

Lineweaver-Burke Plots Obtained From Initial Velocity Determinations of Atorvastatin in the Presence of Cyclosporine A From Chapter 4
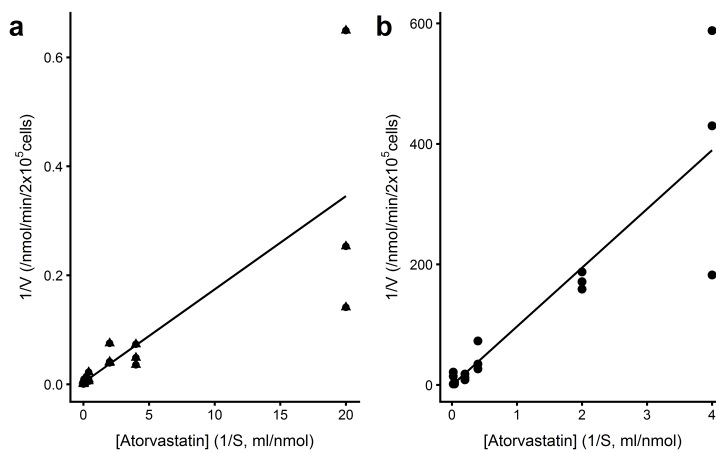
Figure D.1: Atorvastatin concentration against velocity or the inverse of the velocity plots. **a** Lineweaver-Burke plot using "Active" in presence of CsA. **b** Lineweaver-Burke plot for the metabolism of atorvastatin in the presence of CsA

Appendix E

Cryopreserved Human Hepatocyte Donor Sheet Used in Chapter 5

Age/ Gender:	Race:	Cause of death:	Height:	Weight:	Social history:	Medical history:	EBV	RPR	CMV	Hepatitis B	Hepatitis C	HIV
38M	C	MVA; 2nd to Trauma	73"	264lb	ETOH: significant ETOH in past – none last 12 mos; tobacco: 20pack/year; Drugs: snorted cocaine and heroin in last 12 months	Disc removal w/rod place, bone graft lower spine, pos. for opiates upon admittance Meds: vanco, zosyn	Not reported	Neg	Not reported	Neg	Neg	Neg
35M	C	Anoxia	71"	82 Kg	Unknown ETOH use; Tobacco: Smoker but amount/duration unknown; Drugs: Polysubstance abuse	TBI (traumatic brain injury from MVA with partial cralniectomy5 months ago, seizures, spinal fusion sx. Meds: Depakote	IgG+	Neg	Neg	Neg	Neg	Neg
60F	C	Head Trauma, 2nd to fall	62"	116Kg	ETOH: occasional; Tobacco: 1 ppd x 30 years; no drug use.	Gastric bypass 8 yrs ago; Hx of T2D diagnosed few mos ago, possible HTN	Pos	Neg	Neg	Neg	Neg	Neg
4F	C	Anoxia; 2nd to cardio-vascular	3'2"	14 Kg	No ETOH, Tobacco or drug use	G-tube 4 yrs, Nissan Funilization and Trach placement 4 yrs ago	Neg	Neg	Neg	Neg	Neg	Neg
34M	AA	Head Trauma due to Blunt injury	5'7"	150lb	ETOH: Daily 1 pt bourbon or whiskey since age 15; Tobacco: 1-2 ppd x 23yrs; Drugs: THC since age 23	Influenza A H3 and Corroavirus positive. No other history.	Not reported	Neg	Neg	Neg	Neg	Neg
48F	C	Cardiac Arrest; 2nd to Seizure Activity	60"	159lb	No ETOH, Tobacco or drug use	Lobectomy d/t hx of seizures from epilepsy dx at 9 months. Meds: Lamictal	Not reported	Neg	IgG +	Neg	Neg	Neg
55F	C	ICH	63"	72 Kg	ETOH: 1-3 beers/day, tobacco: 1-2 ppd x 30yrs; no drug use	HTN, COPD, emphysema, blood clots in legs due to birth control pills, carpal tunnel surgery, rapid heart beat.	Neg	Neg	Pos	Neg	Neg	Neg
53M	C	Anoxic injury; 2nd to MVA	68"	73 Kg	ETOH: social; Tobacco: yes; no drug use	Cardiac arrest, HB Vaccine	Not reported	Neg	Neg	Neg	Neg	Neg

[signature]

Caution: This product was prepared from fresh human tissue. Treat all products containing human-derived materials as potentially infectious, as no known test methods can offer assurance that products derived from human tissues will not transmit infectious agents.

These products are for research use only. Do not use in animals or humans. These products have not been approved for any diagnostic or clinical procedures.

1450 South Rolling Road Baltimore, MD 21227   Phone: 410.394.7600   Fax 410.455.1245   www.bioreclamationivt.com

---

LiverPool™* 10-DONOR MIXED GENDER POOLED CRYOPRESERVED HUMAN HEPATOCYTES, PEG-FREE
PRODUCT NUMBER: S01205

Lot Number: LYB **

Storage Conditions: below -150°C (vapour phase of liquid nitrogen freezer)

Test Results:

Specification	Result	
≥80% post-thaw viability by trypan blue exclusion	86	%
≥ 5 million viable cells	8.28	million viable cells

Lot Characterization Results:

Assay	Result	
ECOD: total rate of formation of 7-HC and metabolites	105	pmol/min/million cells
UGT/ST:		
rate of formation of 7-hydroxycoumarin glucuronide	392	pmol/min/million cells
rate of formation of 7-hydroxycoumarin sulfate	36.1	pmol/min/million cells
CYP1A2: rate of formation of acetaminophen	32.9	pmol/min/million cells
CYP2A6: total rate of formation of 7-HC and metabolites	92.3	pmol/min/million cells
CYP2B6: rate of formation of hydroxybupropion	42.6	pmol/min/million cells
CYP2C8: rate of formation of desethylamodiaquine	225	pmol/min/million cells
CYP2C9: rate of formation of 4'-methylhydroxytolbutamide	42.0	pmol/min/million cells
CYP2C19: rate of formation of 4'-hydroxymephenytoin	23.7	pmol/min/million cells
CYP2D6: rate of formation of dextrorphan	28.5	pmol/min/million cells
CYP2E1: rate of formation of 6-hydroxychlorzoxazone	39.1	pmol/min/million cells
CYP3A4:		
rate of formation of 6β-hydroxytestosterone	127	pmol/min/million cells
rate of formation of 1-hydroxymidazolam	81.8	pmol/min/million cells

*The process for producing the LiverPool™ pooled human hepatocyte products is covered by one or more U.S. or foreign patents and patent applications, including U.S. Patent No. 7,604,929.

**Updated with remaining characterization data.

Donor Demographics, as reported to BioreclamationIVT:

Age/ Gender:	Race:	Cause of death:	Height:	Weight:	Social history:	Medical history:	EBV	RPR	CMV	Hepatitis B	Hepatitis C	HIV
47M	C	Head Trauma, Fall	6'1"	64.4Kg	ETOH: 2.5-3 drinks daily x 20 yrs ; tobacco: 1 PPD x 20 yrs; drug: marijuana several x week for 20 yrs.	Asthma	IgG+	Neg	Neg	Neg	Neg	Neg
10moF	H	Anoxia; 2nd to Drowning	2'2"	19 lb	No ETOH, Tobacco or Drug use	Jaundice at birth. No other medical history	Neg	Neg	Neg	Neg	Neg	Neg

Caution: This product was prepared from fresh human tissue. Treat all products containing human-derived materials as potentially infectious, as no known test methods can offer assurance that products derived from human tissues will not transmit infectious agents.

These products are for research use only. Do not use in animals or humans. These products have not been approved for any diagnostic or clinical procedures.

1450 South Rolling Road Baltimore, MD 21227   Phone: 410.394.7600   Fax 410.455.1245   www.bioreclamationivt.com

Appendix F

Model files for Best Fitting Models from Chapters 3, 4 and 5

The data files for Chapter 3 for use in Monolix 2018R2 can be found below, and as a copy in the online thesis version.

DCFGem_Combo.txt :

DCFGem_PC_Combo.txt:

DCF_Gem_Pre.txt:

The code for the model files for Chapter 3 for use in Monolix 2018R2 for the best fitting model (micro-rate constant with competitive inhibition for the co-incubation and pre-co-incubation data) are included below, and all the files are included in the online thesis version:

```
DESCRIPTION:   model to describe DCF uptake into HEK293-OATP1B1 cells
; and inhibition by gemfibrozil

[LONGITUDINAL]
input = {k13,k31,k12,k21,To,k23,k45,k54}
; input = {k3,k12,k21,To,k23,k45,k54}   ; for Pre-Co-incubation data

PK:
depot(type=1,target=x1)
depot(type=2,target=x4)


EQUATION:
; k13 and k31 = kfD and kbD
; k12, k21 and k23 = kaD, kdD and kt
; k45 and k54 = kaG and kdG
; x1-3: DCF S1, S2 and S3
; x4-5: gemfibrozil I1 and I2
ddt_x1 = -k12*x1*(To-x5-x2) - k13*x1 + k21*x2 + k31*x3
;ddt_x1 = -k12*x1*(To-x5-x2) - k3*x1 + k21*x2 + k3*x3  ; For Pre-Co-incubation data
ddt_x2 = k12*x1*(To-x5-x2) - (k21 + k23)*x2
ddt_x3 = k13*x1 + k23*x2 - k31*x3
; ddt_x3 = k3*x1 + k23*x2 - k3*x3        ; For Pre-Co-incubation data
ddt_x4 = - k45*x4*(To-x5-x2) + k54*x5
ddt_x5 = k45*x4*(To-x5-x2) - k54*x5

cell = (x2+x3)*333

OUTPUT:
output = {cell}
```

R code for the statistical analysis of the pre-incubation data (DV = % of control):

```
library(ggplot2)
library(plyr)
library(grid)
library(extrafont)
library(cowplot)
library(ggpubr)
```

```
DCF_Pre <- read.table("DCF_Gem_Pre.txt",head=TRUE)
#Data: ID,   DOSE, TIME, DV

DCF_Pre$TIME <- as.factor(DCF_Pre$TIME)
DCF_Pre$DOSE <- as.factor(DCF_Pre$DOSE)

# unequal variation = default, unpaired = default
compare_means(data=DCF_Pre,DV~DOSE,
                                    method="t.test",
                                    ref.group = "0")
compare_means(data=DCF_Pre,DV~TIME,
                                    method="t.test",
                                    ref.group = "0")

theme_set(theme_cowplot(font_size=8,font_family = "Arial"))

fig1 <- ggbarplot(data=DCF_Pre,x="DOSE",
y="DV",
add="mean_se",
position=position_dodge(0.8),
fill = "lightgrey",
width=0.8)+
stat_compare_means(method="t.test",
label="p.signif",
label.y=90,
hide.ns="TRUE",
ref="0")+
theme(axis.text=element_text(size=8),
axis.title=element_text(size=8)
)+
xlab("Gemfibrozil_incubation_concentration_(nmol/ml)")+
ylab("%_of_DCF_control")
fig1

fig2 <- ggdraw(fig1)+
theme(rect=element_rect(fill="white"))

ggsave("DCF_Pre.jpg",fig2,width=6,height=3,units="in",dpi=600)
```

The data files for Chapter 4 for use in Monolix 2018R2 can be found below, and as a copy in the online thesis version.

AtorCsA_Combined.txt :
The code for the model files for Chapter 4 for use in Monolix 2018R2 for the best fitting model (micro-rate constant with non-competitive inhibition) is included below, and all the files are included in the online thesis version:

```
DESCRIPTION:   model to describe atorvastatin uptake into hepatocytes
; and its inhibition by CsA

[LONGITUDINAL]
input = {k13,k31,k12,k21,To,k23,Vm,Km,Ki,k45,k54,alpha}

PK:
depot(type=2,target=x1)
depot(type=1,target=x4)

EQUATION:
; k13 and k31 = kfA and kbA
; k12, k21 and k23 = kaA, kdA and ktA
; Vm, Km and Ki = Vmax.met, Km.met and KI.met
; k45, k54, alpha = kaC, kdC
; x1-3: atorvastatin S1, S2 and S3
; x4-6: CsA I1, I2 and I4
ddt_x1 = -k12*x1*(To-x5-x2-x6) - k13*x1 + k21*x2 + k31*x3 - k12*alpha*x1*x5 + k21*alpha*x6
ddt_x2 = k12*x1*(To-x5-x2-x6) - (k21 + k23)*x2 - k45*alpha*x2*x4 + k54*alpha*x6
ddt_x3 = k13*x1 + k23*x2 - k31*x3 - (Vm*x3)/(Km*(1+x4/Ki)) + k23*alpha*x6
ddt_x4 = -k45*x4*(To-x5-x2-x6) + k54*x5 - k45*alpha*x2*x4 + k54*alpha*x6
ddt_x5 = k45*x4*(To-x4-x2-x6) - k54*x5 - k12*alpha*x1*x5 + (k21+k23)*alpha*x6
ddt_x6 = k12*alpha*x1*x5 + k45*alpha*x2*x4 - (k21+k54+k23)*alpha*x6

cell = 906*(x2 + x3 + x6)

OUTPUT:
output = {cell}
```

The data files for Chapter 5 for use in Monolix 2018R2 can be found below, and as a copy in the online thesis version.

Pita_Etm_Combo_all.txt (with measurement of eltrombopag) :

P_E_Init_NoEtm.txt (without measurement of eltrombopag) :
The code for the model files for Chapter 5 for use in Monolix 2018R2 for the best fitting model (micro-rate constant with competitive inhibition, with measurement of eltrombopag) is included below, and all the files are included in the online thesis version:

DESCRIPTION: **model** to describe pitavastatin uptake into hepatocytes and inhibition **by** eltrombopag

[LONGITUDINAL]
input = {k13,k31,k12,k21,To,k23,k30,k46,k64,k45,k54,k56,x40,x50,x60}

PK:
depot(type=2,target=x1A)
depot(type=3,target=x1)
;depot(type=1,target=x4)

EQUATION:
;initial conditions:
t0 = 15
x4_0 = x40
x5_0 = x50
x6_0 = x60
; k13 and k31 = kfP and kbP
; k12, k21 and k23 = kaP, kdP and ktP
; k30 = pitavastatin met
; k46 and k64 = kfE and kbE
; k45, k54, alpha = kaC, kdC
; x1A–x3A = pitavastatin S1A, S2A and S3A
; x1–3: pitavastatin S1, S2 and S3
; x4–6: eltrombopag I1, I2 and I3

ddt_x1A = −k12*x1A*(To−x2A) − k13*x1A + k21*x2A + k31*x3A
ddt_x2A = k12*x1A*(To−x2A) − (k21 + k23)*x2A
ddt_x3A = k13*x1A + k23*x2A − (k31+k30)*x3A
ddt_x1 = −k12*x1*(To−x5−x2) − k13*x1 + k21*x2 + k31*x3
ddt_x2 = k12*x1*(To−x5−x2) − (k21 + k23)*x2
ddt_x3 = k13*x1 + k23*x2 − (k31+k30)*x3
ddt_x4 = −k46*x4 − k45*x4*(To−x5−x2) + k54*x5 + k64*x6
ddt_x5 = k45*x4*(To−x5−x2) − (k54+k56)*x5
ddt_x6 = k46*x4 + k56*x5 − k64*x6

pita1 = (x2A+x3A)*333
pita2 = (x2+x3)*333
etm = (x5+x6)*333

OUTPUT:
output = {pita1,pita2,etm}
table = {x4,x5,x6,x2}

Appendix G

Semi-Mechanistic Human Physiologically Based Pharmacokinetic Model for Pitavastatin and Eltrombopag Code

Copy of the R code developed in RStudio 1.1.456 with R 3.5.1 [186] using the `deSolve` package [1] for the semi-quantitative PBPK model:

```
####################################################################
# This PBPK model was written by Simon J. Carter 2019 with        #
# suggestions from Carlos S. Traynor regarding the Monte-Carlo    #
# simulations                                                     #
# Biomedical and Biological Systems Laboratory                    #
# University of Warwick                                           #
# Coventry, UK. CV4 7AL                                           #
####################################################################

library(deSolve)
library(ggplot2)
library(grid)
library(gridExtra)
library(extrafont)
library(cowplot)
library(zoo)
# first time use of extrafont:
#font_import()
#loadfonts()

# Model Based on: Takeuchi et al (2014). DMD 45:726-734, with added biliary excretion into the gut and delay co
# Clinical data: Prueksaritanont et al. (2014). Br.J.Clin.Pharmacol 78(3): 587-598 (1mg)
#                FDA Clinical Pharmacology submission (2014). fig.3: 8mg instant release dose
Prueksaritanont <- read.csv('Prueksaritanont_2014_Pita.csv',head=TRUE)
Prueksaritanont$Time <- Prueksaritanont$Time*60
Prueksaritanont$DV<- Prueksaritanont$DV/0.425
Prueksaritanont$Pos_err<- Prueksaritanont$Pos_err/0.425
Prueksaritanont$Neg_err<- Prueksaritanont$Neg_err/0.425
FDA_Pita_2 <- read.csv('FDA_Pita_09_2mg_PO.csv',head=T)
FDA_Pita_2$Time <- FDA_Pita_2$Time*60
FDA_Pita_2$DV <- FDA_Pita_2$DV/0.425
FDA_2009 <- read.table('FDA_Etm.txt',head=TRUE) # conc in ng/mL 50mg dose
Deng <- read.csv('Deng_75_2011.csv',head=T)
Deng$Time <- Deng$Time*60
Deng$DV <- Deng$DV/0.718
# assuming that 100% of the dose is available to be absorbed (Fa=1)

# CfPP = fu.plasma/BL:PL
theme_set(theme_cowplot(font_size=8,font_family = "Times_New_Roman"))
####################################################################
```

```
# Vz for pita. FDA = 226*0.51=133.2L. Gives very low plasma values. Total Body Water = 42L
# HPGL:139, Sohlenius-Sternbeck (2006). ToxInVit 20: 1582-1583.
# wt of liver: 1695 (% CV = 16): Price (2003). Crit. Rev. Toxicol: 33:5. 469-503
#

# Number of virtual subjects:
n = 100


################## Pitavastatin Specific parameters ################
ktransP_v = rnorm(n, 0.1, sd = 0.2*0.1)                  #/min, min gastric emptying time =10'. Hirano (2006)
kaP_v = rnorm(n, 0.07, sd = 0.3*0.07)                    # FDA doc, ka=1/(MRT_PO - MRT_IV)=1/(4.55(1.87)-2.18(2.03))=
CL_BiPi_v = rnorm(n, 165, sd = 0.2*165)                  # Biliary CL, Total CL = 384mL/min (AUSPAR 2013)*0.43(fractio
CL_MePi_v = rnorm(n, 155,sd = 0.3*99)                    # ml/min. 0.22 (0.2-0.24)*0.003*139*1695 = 155 (141-169)
CLur_v = rnorm(n, 11.5, sd = 0.2*11.5)                   # ml/min.Urine. FDA (p.48) = 3% of total = renal clearance
fTP_v = rnorm(n, 0.02, sd = 0.3*0.02)                    # fu, tissue from RED expt #2
VmP_v = rnorm(n, 29988021 , sd = 0.3*29988021 )          # ng/min/liver. 0.302(0.18-0.64)*421.46*139*1695 = 29988021 (
Cfpp_v = rnorm(n, 0.012, sd = 0.4*0.012)                 # fu.pl/BL:PL=0.005 (0.0009) (Aus TGA, 2013)/0.425 (0.162) (I.
KmP_v = rnorm(n,  9525, sd = 0.3*9525)                   # ng/ml.  22.6*421.46 = 9525 (7038-10747)
PdPi_v = rnorm(n, 137.6, sd = 0.3*137.6)                 # P. diff into heps. ml/min. 5e-4*139*1695 = 137.6 (108-144)
PdePi_v = rnorm(n, 295, sd = 0.3*295)                    # P. diff out of heps. ml/min. 0.21*0.003*139*(1695-(556*1.03)=


################## Eltrombopag Specific parameters ####################
kaE_v = rnorm(n, 11, sd = 0.2*11)                        # /min, FDA (2009), Ka2 = 0.189/h = 0.003
CL_BiE_v = rnorm(n, 13, sd = 0.2*13)                     # Biliary CL, Total CL/F = 13*0.52*0.2(Unchanged dos
CL_MeE_v = rnorm(n, 6.8,sd = 0.2*6.8)                    # ml/min. total CL=13*0.52*0.36 = 6.76 (FDA, 2009, 64% of
#CLur_v = rnorm(n , 11.5, sd = 0.2*11.5)                 # ml/min.Urine. = 0% of total = renal clearance
fTE_v = rnorm(n, 0.4, sd = 0.2*0.4)                      # fu, tissue from RED expt #2 = 0.001!
VmE_v = rnorm(n, 5102733, sd = 0.3*5102733)              # ng/min/liver. 0.049(0.028-0.116)*442*139*1695 = 5102733 (291.
CfpE_v = rnorm(n, 0.005, sd = 0.1*0.005)                 # fu.pl. = 0.002 (Nieto et al (2011). Haematologica 96:e33)
KmE_v = rnorm(n,  3138, sd = 0.3*3138)                   # ng/ml.  7.1 (7.4-7.43)*442 = 3138 (3271-3284)
PdE_v = rnorm(n, 11780, sd = 0.3*11780)                  # P. diff into heps. ml/min. 0.05(0.04-0.06)*139*1695 = 11780 (
PdeE_v = rnorm(n, 294, sd = 0.3*294)                     # P. diff out of heps. ml/min. 0.62(0.55-0.67)*0.003*139*(1695-
VcE_v = rnorm(n, 2940, sd = 0.2*2940)                    # ml. Takeuchi et al (2014)


################## Physiological Parameters ##########################
VcP_v = rnorm(n, 5820, sd = 0.1*5820)                    # Total blood volume (ml). Price et al (2003)
Vext_H_v = rnorm(n, 556, sd = 0.2*556)                   # ml. Watanabe et al (2009). JPET 328:652-662
VH_v = rnorm(n, 1570, sd = 0.2*1570)                     # vol of liver (ml). Price et al (2003)
VGaBl_v = rnorm(n, 36, sd = 0.2*36)                      # Gallbladder volume (mL), Guiastrennec et al (2016)
Qh_v = rnorm(n, 1320, sd = 0.2*1320)                     # Hepatic blood flow (ml/min)
BiTrans_v = rnorm(n, 0.0618, sd = 0.2*0.062)             # /min. Gallbladder emptying rate. Guiastrennec et al (2016).
Qk_v = rnorm(n, 1170,sd = 0.2*1170)                      # Kidneys blood flow (ml/min), Price et al (2003)


##################Functions#########################################
#############Pitavastatin Only#################################
PitaODE <- function(t, In_Cond, parameters)
{with(as.list(c(In_Cond, parameters)),{
# pita lag compartment
dy1dt <- -ktransP*y1
# Pita gut compartment (y2)
dy2dt <-  - kaP*y2 + BiTrans*y5 + ktransP*y1
# Pita liver extracellular space (y3)
dy3dt <- (kaP*y2
- Cfpp*y3*((VmP/(KmP+y3*Cfpp))+PdPi)
+ Qh*Cfpp*(y6-y3)
+ PdePi*y4*fTP
)/Vext_H
# Pita liver (y4)
dy4dt <- (Cfpp*y3*((VmP/(KmP+y3*Cfpp)) + PdPi )
- (CL_MePi + CL_BiPi + PdePi)*y4*fTP
)/VH
# Pita GaBl (y5)
dy5dt <- (CL_BiPi*y4*fTP)/VGaBl - BiTrans*y5
# Pita blood (y6)
dy6dt <- (Qh*Cfpp*(y3-y6) -Qk*CLur*y6*Cfpp)/VcP

list(c(dy1dt,dy2dt,dy3dt,dy4dt,dy5dt,dy6dt)) })  }
# pitavastatin only times:
times <- c(seq(0,400,1)) # min

# Initial Conditions for pitavastatin only
In_Cond <- c(y1=1000000,y2=0,y3=0,y4=0,y5=0,y6=0)
out <- list()

# Loop for Monte-Carlo simulations of n subsjects
for(i in seq_along(1:n)){
parameters_Norm <- c(
ktransP = ktransP_v[i]    ,
kaP = kaP_v[i]            ,
CL_BiPi = CL_BiPi_v[i]    ,
CL_MePi = CL_MePi_v[i]    ,
```

```r
    CLur = CLur_v[i]             ,
    fTP = fTP_v[i]               ,
    VmP = VmP_v[i]               ,
    Cfpp = Cfpp_v[i]             ,
    KmP = KmP_v[i]               ,
    PdPi = PdPi_v[i]             ,
    PdePi = PdePi_v[i]           ,
    VcP = VcP_v[i]               ,
    Vext_H = Vext_H_v[i]         ,
    VH = VH_v[i]                 ,
    VGaBl = VGaBl_v[i]           ,
    Qh = Qh_v[i]                 ,
    BiTrans = BiTrans_v[i]       ,
    Qk = Qk_v[i]
    )
    out[[i]]<- ode(y = In_Cond, times = times, func = PitaODE, parms = parameters_Norm)

    }

    newout <- lapply(out, function(x) x[, 7])
    newout <- do.call(rbind, newout)

    meany6 <- apply(newout, 2, mean, na.rm = TRUE)
    qy6 <- apply(newout, 2, quantile, probs = c(.05, .95) )

    fig1<-ggplot(data.frame( m = meany6, q05 = qy6[1, ], q95 = qy6[2, ], time = times))+
    geom_line(aes(x=time,y=meany6), colour="Blue") +
    geom_ribbon(aes(x = time, ymin = q05, ymax= q95),fill="Blue",alpha=0.3)+
    labs(x="Time_(min)",y="blood_[pitavastatin]_(ng/ml)")

    fig2 <- fig1 + geom_point(data=Prueksaritanont,aes(x=Time,y=DV),size=0.6)+
    geom_errorbar(data=Prueksaritanont,aes(x=Time,ymin=Neg_err,ymax=Pos_err))+
    ylim(0,100)

    ############Eltrombopag Only###################################
    EtmODE <- function(t, In_Cond, parameters)
    {with(as.list(c(In_Cond, parameters)),{
    # Etm stomach
    dy7dt <- -ktransP*y7
    # Etm gut compartment (y8)
    dy8dt <- - kaE*y8 + BiTrans*y11 + ktransP*y7
    # Etm liver extracellular space (y9)
    dy9dt <- (kaE*y8
    - CfpE*y9*((VmE/(KmE+y9*CfpE)) + PdE)
    + Qh*CfpE*(y12-y9)
    + PdeE*y10*fTE
    )/Vext_H
    # etm liver (y10)
    dy10dt <- (CfpE*y9*((VmE/(KmE+y9*CfpE)) + PdE)
    - (CL_MeE + CL_BiE + PdeE)*y10*fTE
    )/VH
    # etm GaBl (y11)
    dy11dt <- (CL_BiE*y10*fTE)/VGaBl - BiTrans*y11
    # etm blood (y11)
    dy12dt <- (Qh*CfpE*(y9-y12))/VcE

    list(c(dy7dt,dy8dt,dy9dt,dy10dt,dy11dt,dy12dt)) })   }

    #Eltrombopag times
    times <- c(seq(0,10800,5)) # min

    # Initial conditions for eltrombopag only:
    In_CondE <- c(y7=75000000,y8=0,y9=0,y10=0,y11=0,y12=0)

    out <- list()

    for(i in seq_along(1:n)){
    parameters_NormE <- c(
    ktransP = ktransP_v[i]       ,
    kaE = kaE_v[i]               ,
    CL_BiE = CL_BiE_v[i]         ,
    CL_MeE = CL_MeE_v[i]         ,
    fTE = fTE_v[i]               ,
    VmE = VmE_v[i]               ,
    CfpE = CfpE_v[i]             ,
    KmE = KmE_v[i]               ,
    PdE = PdE_v[i]               ,
    PdeE = PdeE_v[i]             ,
    VcE = VcE_v[i]               ,
    Vext_H = Vext_H_v[i]         ,
    VH = VH_v[i]                 ,
    VGaBl = VGaBl_v[i]           ,
```

```
Qh = Qh_v[i]                    ,
BiTrans = BiTrans_v[i]
)
out[[i]]<- ode(y = In_CondE, times = times, func = EtmODE, parms = parameters_NormE)
}

newout <- lapply(out, function(x) x[, 7])
newout <- do.call(rbind, newout)

meany12 <- apply(newout, 2, mean, na.rm = TRUE)
qy12 <- apply(newout, 2, quantile, probs = c(0.05, 0.95) )

figA<-ggplot(data.frame( m = meany12, q05 = qy12[1, ], q95 = qy12[2, ], time = times))+
geom_line(aes(x=time,y=meany12), colour="Blue") +
geom_ribbon(aes(x = time, ymin = q05, ymax= q95),fill="Blue",alpha=0.3)+
labs(x="Time_(min)",y="plasma_[eltrombopag]_(ng/ml)")

figB <- figA + geom_point(data=Deng,aes(x=Time,y=DV),size=0.6)+
scale_y_log10(limits=c(1,30000))+
xlim(5,10800)
figB
#############Pitavastatin and Eltrombopag#######################
PitaEtmODE <- function(t, In_Cond, parameters)
{with(as.list(c(In_Cond, parameters)),{
# pita lag compartment
dy1dt <- -ktransP*y1
# Pita gut compartment (y2)
dy2dt <-  - kaP*y2 + BiTrans*y5 + ktransP*y1
# Pita liver extracellular space (y3)
dy3dt <- (kaP*y2
- Cfpp*y3*((VmP/(KmP*(1+y9/KmE)+y3*Cfpp))+PdPi)
+ Qh*Cfpp*(y6-y3)
+ PdePi*y4*fTP
)/Vext_H
# Pita liver (y4)
dy4dt <- (Cfpp*y3*((VmP/(KmP*(1+y9/KmE) + y3*Cfpp)) + PdPi)
- (CL_MePi + CL_BiPi + PdePi)*y4*fTP
)/VH
# Pita GaBl (y5)
dy5dt <- (CL_BiPi*y4*fTP)/VGaBl - BiTrans*y5
# Pita blood (y6)
dy6dt <- (Qh*Cfpp*(y3-y6) -Qk*CLur*y6*Cfpp)/VcP
#Etm stomach
dy7dt <- -ktransP*y7
# Etm gut compartment (y8)
dy8dt <- - kaE*y8 + BiTrans*y11 + ktransP*y7
# Etm liver extracellular space (y9)
dy9dt <- (kaE*y8
- CfpE*y9*VmE/(KmE*(1+y3/KmP)+y9*CfpE) - CfpE*y9*PdE
+ Qh*CfpE*(y12-y9)
+ PdeE*y10*fTE
)/Vext_H
# etm liver (y10)
dy10dt <- (CfpE*y9*VmE/(KmE*(1+y3/KmP)+y9*CfpE) + CfpE*y9*PdE
- (CL_MeE + CL_BiE + PdeE)*y10*fTE
)/VH
# etm GaBl (y11)
dy11dt <- (CL_BiE*y10*fTE)/VGaBl - BiTrans*y11
# etm blood (y11)
dy12dt <- (Qh*CfpE*(y9-y12))/VcE

list(c(dy1dt,dy2dt,dy3dt,dy4dt,dy5dt,dy6dt,dy7dt,dy8dt,dy9dt,dy10dt,dy11dt,dy12dt)) })  }


# Use relevant time depending on plot required:
times <- c(seq(0,400,2))   # min
times <- c(seq(0,10800,5))

out <- list()
# Initial conditions for pitavastatin and eltrombopag together
In_CondPE <- c(y1=1000000,y2=0,y3=0,y4=0,y5=0,y6=0,y7=75000000,y8=0,y9=0,y10=0,y11=0,y12=0)

for(i in seq_along(1:n)){
parameters_NormPE <- c(
ktransP = ktransP_v[i]    ,
kaP = kaP_v[i]            ,
CL_BiPi = CL_BiPi_v[i]    ,
CL_MePi = CL_MePi_v[i]    ,
CLur = CLur_v[i]          ,
fTP = fTP_v[i]            ,
VmP = VmP_v[i]            ,
Cfpp = Cfpp_v[i]          ,
```

```
  KmP = KmP_v[i]                ,
  PdPi = PdPi_v[i]              ,
  PdePi = PdePi_v[i]            ,
  kaE = kaE_v[i]                ,
  CL_BiE = CL_BiE_v[i]          ,
  CL_MeE =CL_MeE_v[i]           ,
  fTE = fTE_v[i]                ,
  VmE = VmE_v[i]                ,
  CfpE = CfpE_v[i]              ,
  KmE = KmE_v[i]                ,
  PdE = PdE_v[i]                ,
  PdeE = PdeE_v[i]              ,
  VcP = VcP_v[i]                ,
  Vext_H = Vext_H_v[i]          ,
  VH = VH_v[i]                  ,
  VGaBl = VGaBl_v[i]            ,
  Qh = Qh_v[i]                  ,
  BiTrans = BiTrans_v[i]        ,
  Qk = Qk_v[i]                  ,
  VcE = VcE_v[i]
  )

  out[[i]]<- ode(y = In_CondPE, times = times, func = PitaEtmODE, parms = parameters_NormPE)
}


# Pita blood
newout <- lapply(out, function(x) x[, 7])
newout <- do.call(rbind, newout)
# Pita extravascular space
newout2 <- lapply(out, function(x) x[, 4])
newout2 <- do.call(rbind, newout2)
# Etm plasma
newout3 <- lapply(out, function(x) x[, 13])
newout3 <- do.call(rbind, newout3)
# Etm extravascular space
newout4 <- lapply(out, function(x) x[, 10])
newout4 <- do.call(rbind, newout4)


meany3i <- apply(newout2, 2, mean, na.rm=TRUE)
qy3i <- apply(newout2, 2, quantile, probs = c(.05, .95) )

meany6i <- apply(newout, 2, mean, na.rm = TRUE)
qy6i <- apply(newout, 2, quantile, probs = c(.05, .95) )

meany8i <- apply(newout4,2 ,mean,na.rm=TRUE)
q8i <- apply(newout4, 2, quantile, probs = c(.05, .95) )

meany12i <- apply(newout3,2 ,mean,na.rm=TRUE)
q12i <- apply(newout3, 2, quantile, probs = c(.05, .95) )

# Pita Grid plot
fig3<-ggplot(data.frame(m = meany6i, q05 = qy6i[1, ], q95 = qy6i[2, ], time = times))+
geom_line(aes(x=time,y=meany6i), colour="Red") +
geom_ribbon(aes(x = time, ymin = q05, ymax= q95),fill="Red",alpha=0.3)+
labs(x="Time_(min)",y="blood_[pitavastatin]_(ng/ml)")

fig4 <- fig3 + geom_point(data=Prueksaritanont,aes(x=Time,y=DV),size=0.6,shape=16)+
geom_errorbar(data=Prueksaritanont,aes(x=Time,ymin=Neg_err,ymax=Pos_err))+
geom_point(data=FDA_Pita_2,aes(x=Time,y=DV),size=0.6,shape=1)+
ylim(0,100)

fig5 <- plot_grid(fig2,fig4,align="h",labels=c("a","b"))

ggsave("Pita_Etm_1mg_75mg.png",fig5,width=135,height=80,units="mm",dpi=900)


#############
# Etm Grid plot
figC<-ggplot(data.frame( m = meany12i, q05 = q12i[1, ], q95 = q12i[2, ], time = times))+
geom_line(aes(x=time,y=meany12i), colour="Red") +
geom_ribbon(aes(x = time, ymin = q05, ymax= q95),fill="Red",alpha=0.3)+
labs(x="Time_(min)",y="plasma_[eltrombopag]_(ng/ml)")

figD <- figC + geom_point(data=Deng,aes(x=Time,y=DV),size=0.6)+
scale_y_log10(limits=c(1,30000))+
xlim(5,10800)

figE <- plot_grid(figB,figD,align="h",labels=c("a","b"))

ggsave("Etm_Pita_75mg_1mg.png",figE,width=135,height=80,units="mm",dpi=900)
```

```r
# Pitavastatin calculations
times <- c(seq(0,400,1))
#AUC Calc: Pita (h.ng/ml)
AUC_PE <- sum(diff(times)*rollmean(meany6i,2))/60 # Pita AUC in presence of etm
AUC_P <- sum(diff(times)*rollmean(meany6,2))/60   # Pita AUC in absence of etm
Cmax_PE <- max(meany6i)                           # Pita Cmax in presence of etm
Tmax_PE <- which.max(meany6i)                     # Tmax (-1) in presence of etm (hr)
Tmax_PE <- (Tmax_PE -1)/60
Cmax_P <- max(meany6)                             # Pita Cmax in absence of etm
Tmax_P <- which.max(meany6)                       # Tmax (-1) in absence of etm
Tmax_P <- (Tmax_P -1)/60


# Eltrombopag calculations
times <- c(seq(0,10800,5))
AUC_EP <- sum(diff(times)*rollmean(meany12i,2))/60000 # Etm AUC in presence of pita, hr.ng.ml
AUC_E <- sum(diff(times)*rollmean(meany12,2))/60000   # Etm AUC in absence of pita, hr.ng.ml
Cmax_EP <- max(meany12i)/1000                         # Etm Cmax in presence of pita
Tmax_EP <- which.max(meany12i)                        # Tmax (-1) in presence of pita (hr)
Tmax_EP <- (Tmax_EP*5-5)/60
Cmax_E <- max(meany12)/1000                           # etm Cmax in absence of pita
Tmax_E <- which.max(meany12)                          # Tmax (-1) in absence of pita
Tmax_E <- (Tmax_E*5-5)/60
Cmax_EPliver <- max(meany8i)
Tmax_EPliver <- which.max(meany8i)                    # Tmax in extravascular space (min)
Tmax_EPliver <- (Tmax_EPliver*5-5)
res <- as.data.frame(rbind(Cmax_P,Tmax_P,AUC_P,
Cmax_PE,Tmax_PE,AUC_PE,
Cmax_E,Tmax_E,AUC_E,
Cmax_EP,Tmax_EP,
Cmax_EPliver,Tmax_EPliver,
AUC_EP))
write.csv(res,'Pita_Etm_PK.csv')
```

Bibliography

[1] K. Soetaert, T. Petzoldt, and R. Woodrow-Setzer. Solving differential equations in r. *The R Journal*, 2(2):5–15, 2010.

[2] P. S. Price, R. B. Conolly, C. F. Chaisson, E. A. Gross, J. S. Young, E. T. Mathis, and D. R. Tedder. Modeling interindividual variation in physiological factors used in pbpk models of humans. *Crit Rev Toxicol*, 33(5):469–503, 2003.

[3] Y. Huang, M. J. Lemieux, J. Song, M. Auer, and D. N. Wang. Structure and mechanism of the glycerol-3-phosphate transporter from escherichia coli. *Science*, 301(5633):616–20, 2003.

[4] J. W. McCormick, P. D. Vogel, and J. G. Wise. Multiple drug transport pathways through human p-glycoprotein. *Biochemistry*, 54(28):4374–90, 2015.

[5] H. E. Meyer zu Schwabedissen, C. Verstuyft, H. K. Kroemer, L. Becquemont, and R. B. Kim. Human multidrug and toxin extrusion 1 (mate1/slc47a1) transporter: functional characterization, interaction with oct2 (slc22a2), and single nucleotide polymorphisms. *Am J Physiol Renal Physiol*, 298(4):F997–f1005, 2010.

[6] F. J. Sharom. Complex interplay between the p-glycoprotein multidrug efflux pump and the membrane: Its role in modulating protein function. *Front Oncol*, 4:41, 2014.

[7] G. Chang. Multidrug resistance abc transporters. *FEBS Lett*, 555(1):102–5, 2003.

[8] T. R. Grandjean, M. J. Chappell, A. M. Lench, J. W. Yates, and C. J. O'Donnell. Experimental and mathematical analysis of in vitro pitavastatin hepatic uptake across species. *Xenobiotica*, 44(11):961–74, 2014.

[9] T. Prueksaritanont, X. Chu, R. Evers, S. O. Klopfer, L. Caro, P. A. Kothare, C. Dempsey, S. Rasmussen, R. Houle, G. Chan, X. Cai, R. Valesky, I. P. Fraser, and S. A. Stoch. Pitavastatin is a more sensitive and selective organic anion-transporting polypeptide 1b clinical probe than rosuvastatin. *Br J Clin Pharmacol*, 78(3):587–98, 2014.

[10] U.S. Department of Health CDER), Human Services Food, Drug Administration Center for Drug Evaluation, and Research. Clinical pharmacology and biopharmaceutics review, application number: 22-363, 2009. URL `https://www.accessdata.fda.gov/drugsatfda_docs/nda/2009/022363s000_ClinPharmR_P1.pdf`. Date Accessed: January 2019.

[11] Y. Deng, A. Madatian, M. B. Wire, C. Bowen, J. W. Park, D. Williams, B. Peng, E. Schubert, F. Gorycki, M. Levy, and P. D. Gorycki. Metabolism and disposition of eltrombopag, an oral, nonpeptide thrombopoietin receptor agonist, in healthy human subjects. *Drug Metab Dispos*, 39(9):1734–46, 2011.

[12] Office for National Statistics (ONS). Statistical bulletin: National life tables, uk: 2014 to 2016. trends for the uk and constituent countries in the average number of years people will live beyond their current age measured by "period life expectancy", analysed by age and sex., 2017. URL `https://www.ons.gov.uk/peoplepopulationandcommunity/birthsdeathsandmarriages/lifeexpectancies/bulletins/nationallifetablesunitedkingdom/2014to2016`. Date Accessed: October 2017.

[13] Global Burden of Disease Study 2016 Collaboration. Global, regional, and national incidence, prevalence, and years lived with disability for 328 diseases and injuries for 195 countries, 1990-2016: a systematic analysis for the global burden of disease study 2016. *Lancet*, 390(10100):1211–1259, 2017.

[14] P.L. Bonate. *Pharmacokinetic-Pharmacodynamic Modeling and Simulation*. Springer US, 3 edition, 2011.

[15] J. A. Jacquez. Nonlinear compartmental systems. In *Compartmental Analysis in Biology and Medicine*, page 92. BioMedware, Ann Arbor, USA, 3 edition, 1996.

[16] M. Anguelova, J. Karlsson, and M. Jirstrand. Minimal output sets for identifiability. *Math Biosci*, 239(1):139–53, 2012.

[17] D. J. Bearup, N. D. Evans, and M. J. Chappell. The input-output relationship approach to structural identifiability analysis. *Comput Methods Programs Biomed*, 109(2):171–81, 2013.

[18] European Medicines Agency (EMA). Cpmp/ewp/560/95/rev. 1 corr. 2: Guidelines on the investigation of drug interactions, 2013. URL `http://www.ema.europa.eu/docs/en_GB/document_library/Scientific_guideline/2012/07/WC500129606.pdf`. Date Accessed: November 2018.

[19] U.S. Department of Health (CDER), Human Services Food, Drug Administration Center for Drug Evaluation, and Research. Guidance for industry, drug interaction studiesstudy design, data analysis, implications for dosing, and labeling recommendations, 2017. URL `https://www.fda.gov/downloads/Drugs/GuidanceComplianceRegulatoryInformation/Guidances/UCM292362.pdf`. Date Accessed: November 2018.

[20] A. Schlessinger, M. A. Welch, H. van Vlijmen, K. Korzekwa, P. W. Swaan, and P. Matsson. Molecular modeling of drug-transporter interactions-an international transporter consortium perspective. *Clin Pharmacol Ther*, 104(5):818–835, 2018.

[21] K. M. Giacomini, A. Galetin, and S. M. Huang. The international transporter consortium: Summarizing advances in the role of transporters in drug development. *Clin Pharmacol Ther*, 104(5):766–771, 2018.

[22] D. B. Kell and S. G. Oliver. How drugs get into cells: tested and testable predictions to help discriminate between transporter-mediated uptake and lipoidal bilayer diffusion. *Front Pharmacol*, 5:231, 2014.

[23] I. H. Segel. Rapid equilibrium partial and mixed-type inhibition. In *Enzyme Kinetics: Behaviour and Analysis of Rapid Equilibrium and Steady-State Enzyme Systems*, page 161. John Wiley and Sons Inc, U.S.A., 1993.

[24] T. R. Grandjean, M. J. Chappell, J. W. Yates, and N. D. Evans. Structural identifiability analyses of candidate models for in vitro pitavastatin hepatic uptake. *Comput Methods Programs Biomed*, 114(3):e60–9, 2014.

[25] T. R. Grandjean. *Mathematical modelling of transporter kinetics*. Phd thesis, University of Warwick, 2013.

[26] Y. Shitara and Y. Sugiyama. Pharmacokinetic and pharmacodynamic alterations of 3-hydroxy-3-methylglutaryl coenzyme a (hmg-coa) reductase inhibitors: drug-drug interactions and interindividual differences in transporter and metabolic enzyme functions. *Pharmacol Ther*, 112(1):71–105, 2006.

[27] E. Kimoto, R. Li, R. J. Scialis, Y. Lai, and M. V. Varma. Hepatic disposition of gemfibrozil and its major metabolite gemfibrozil 1-o-beta-glucuronide. *Mol Pharm*, 12(11):3943–52, 2015.

[28] Y. Shitara. Clinical importance of oatp1b1 and oatp1b3 in drug-drug interactions. *Drug Metab Pharmacokinet*, 26(3):220–7, 2011.

[29] E. Perland and R. Fredriksson. Classification systems of secondary active transporters. *Trends Pharmacol Sci*, 38(3):305–315, 2017.

[30] M. A. Hediger, B. Clemencon, R. E. Burrier, and E. A. Bruford. The abcs of membrane transporters in health and disease (slc series): introduction. *Mol Aspects Med*, 34(2-3):95–107, 2013.

[31] S. O'Hagan and D. B. Kell. The apparent permeabilities of caco-2 cells to marketed drugs: magnitude, and independence from both biophysical properties and endogenite similarities. *PeerJ*, 3:e1405, 2015.

[32] D. Hallifax and J. B. Houston. Uptake and intracellular binding of lipophilic amine drugs by isolated rat hepatocytes and implications for prediction of in vivo metabolic clearance. *Drug Metab Dispos*, 34(11):1829–36, 2006.

[33] K. Menochet, K. E. Kenworthy, J. B. Houston, and A. Galetin. Simultaneous assessment of uptake and metabolism in rat hepatocytes: a comprehensive mechanistic model. *J Pharmacol Exp Ther*, 341(1):2–15, 2012.

[34] HUGO Gene Nomenclature Committee at the European Bioinformatics Institute. Hgnc guidelines, 2018. URL https://www.genenames.org/about/guidelines/. Date Accessed: January 2019.

[35] B. Hagenbuch and B. Stieger. The slco (former slc21) superfamily of transporters. *Mol Aspects Med*, 34(2-3):396–412, 2013.

[36] M. Rask-Andersen, S. Masuram, R. Fredriksson, and H. B. Schioth. Solute carriers as drug targets: current use, clinical trials and prospective. *Mol Aspects Med*, 34(2-3):702–10, 2013.

[37] M. D. Nyquist, B. Prasad, and E. A. Mostaghel. Harnessing solute carrier transporters for precision oncology. *Molecules*, 22(4), 2017.

[38] M. Roth, A. Obaidat, and B. Hagenbuch. Oatps, oats and octs: the organic anion and cation transporters of the slco and slc22a gene superfamilies. *Br J Pharmacol*, 165(5):1260–87, 2012.

[39] H. Koepsell, K. Lips, and C. Volk. Polyspecific organic cation transporters: structure, function, physiological roles, and biopharmaceutical implications. *Pharm Res*, 24(7):1227–51, 2007.

[40] L. Wang, B. Prasad, L. Salphati, X. Chu, A. Gupta, C. E. Hop, R. Evers, and J. D. Unadkat. Interspecies variability in expression of hepatobiliary transporters across human, dog, monkey, and rat as determined by quantitative proteomics. *Drug Metab Dispos*, 43(3):367–74, 2015.

[41] F. Meier-Abt, Y. Mokrab, and K. Mizuguchi. Organic anion transporting polypeptides of the oatp/slco superfamily: identification of new members in nonmammalian species, comparative modeling and a potential transport mode. *J Membr Biol*, 208(3):213–27, 2005.

[42] HUGO Gene Nomenclature Committee at the European Bioinformatics Institute. Solute carriers (slc), 2018. URL https://www.genenames.org/cgi-bin/genefamilies/set/752. Date Accessed: November 2018.

[43] M. Murray and F. Zhou. Trafficking and other regulatory mechanisms for organic anion transporting polypeptides and organic anion transporters that modulate cellular drug and xenobiotic influx and that are dysregulated in disease. *British Journal of Pharmacology*, 174(13):1908–1924, 2017.

[44] B. Stieger and B. Hagenbuch. Organic anion-transporting polypeptides. *Curr Top Membr*, 73:205–32, 2014.

[45] Consortium International Transporter, K. M. Giacomini, S. M. Huang, D. J. Tweedie, L. Z. Benet, K. L. Brouwer, X. Chu, A. Dahlin, R. Evers, V. Fischer, K. M. Hillgren, K. A. Hoffmaster, T. Ishikawa, D. Keppler, R. B. Kim, C. A. Lee, M. Niemi, J. W. Polli, Y. Sugiyama, P. W. Swaan, J. A. Ware, S. H. Wright, S. W. Yee, M. J. Zamek-Gliszczynski, and L. Zhang. Membrane transporters in drug development. *Nat Rev Drug Discov*, 9(3):215–36, 2010.

[46] H. Glaeser, D. G. Bailey, G. K. Dresser, J. C. Gregor, U. I. Schwarz, J. S. McGrath, E. Jolicoeur, W. Lee, B. F. Leake, R. G. Tirona, and R. B. Kim. Intestinal drug transporter expression and the impact of grapefruit juice in humans. *Clin Pharmacol Ther*, 81(3):362–70, 2007.

[47] M. Drozdzik, C. Groer, J. Penski, J. Lapczuk, M. Ostrowski, Y. Lai, B. Prasad, J. D. Unadkat, W. Siegmund, and S. Oswald. Protein abundance of clinically relevant multidrug transporters along the entire length of the human intestine. *Mol Pharm*, 11(10):3547–55, 2014.

[48] K. Nakamura, M. Hirayama-Kurogi, S. Ito, T. Kuno, T. Yoneyama, W. Obuchi, T. Terasaki, and S. Ohtsuki. Large-scale multiplex absolute protein quantification of drug-metabolizing enzymes and transporters in human intestine, liver, and kidney microsomes by swath-ms: Comparison with mrm/srm and hr-mrm/prm. *Proteomics*, 16(15-16):2106–17, 2016.

[49] J. R. Wisniewski, A. Vildhede, A. Noren, and P. Artursson. In-depth quantitative analysis and comparison of the human hepatocyte and hepatoma cell line hepg2 proteomes. *J Proteomics*, 136:234–47, 2016.

[50] T. Suga, H. Yamaguchi, T. Sato, M. Maekawa, J. Goto, and N. Mano. Preference of conjugated bile acids over unconjugated bile acids as substrates for oatp1b1 and oatp1b3. *PLoS One*, 12(1):e0169719, 2017.

[51] H. Liu and J. Sahi. Role of hepatic drug transporters in drug development. *J Clin Pharmacol*, 56 Suppl 7:S11–22, 2016.

[52] A. Kalliokoski, M. Neuvonen, P. J. Neuvonen, and M. Niemi. The effect of slco1b1 polymorphism on repaglinide pharmacokinetics persists over a wide dose range. *Br J Clin Pharmacol*, 66(6):818–25, 2008.

[53] K. Morimoto, T. Oishi, S. Ueda, M. Ueda, M. Hosokawa, and K. Chiba. A novel variant allele of oatp-c (slco1b1) found in a japanese patient with pravastatin-induced myopathy. *Drug Metab Pharmacokinet*, 19(6):453–5, 2004.

[54] S. Bosgra, E. van de Steeg, M. L. Vlaming, K. C. Verhoeckx, M. T. Huisman, M. Verwei, and H. M. Wortelboer. Predicting carrier-mediated hepatic disposition of rosuvastatin in man by scaling from individual transfected cell-lines in vitro using absolute transporter protein quantification and pbpk modeling. *Eur J Pharm Sci*, 65:156–66, 2014.

[55] S. P. Romaine, K. M. Bailey, A. S. Hall, and A. J. Balmforth. The influence of slco1b1 (oatp1b1) gene polymorphisms on response to statin therapy. *Pharmacogenomics J*, 10(1):1–11, 2010.

[56] B. Prasad, R. Evers, A. Gupta, C. E. Hop, L. Salphati, S. Shukla, S. V. Ambudkar, and J. D. Unadkat. Interindividual variability in hepatic organic anion-transporting polypeptides and p-glycoprotein (abcb1) protein expression: quantification by liquid chromatography tandem mass spectroscopy and influence of genotype, age, and sex. *Drug Metab Dispos*, 42(1): 78–88, 2014.

[57] H. J. Burt, A. E. Riedmaier, M. D. Harwood, H. K. Crewe, K. L. Gill, and S. Neuhoff. Abundance of hepatic transporters in caucasians: A meta-analysis. *Drug Metab Dispos*, 44(10):1550–61, 2016.

[58] E. van de Steeg, V. Stranecky, H. Hartmannova, L. Noskova, M. Hrebicek, E. Wagenaar, A. van Esch, D. R. de Waart, R. P. Oude Elferink, K. E. Kenworthy, E. Sticova, M. al Edreesi, A. S. Knisely, S. Kmoch, M. Jirsa, and A. H. Schinkel. Complete oatp1b1 and oatp1b3 deficiency causes human rotor syndrome by interrupting conjugated bilirubin reuptake into the liver. *J Clin Invest*, 122(2):519–28, 2012.

[59] B. Gao, S. R. Vavricka, P. J. Meier, and B. Stieger. Differential cellular expression of organic anion transporting peptides oatp1a2 and oatp2b1 in the human retina and brain: implications for carrier-mediated transport of neuropeptides and neurosteriods in the cns. *Pflugers Arch*, 467(7):1481–1493, 2015.

[60] J. Badee, B. Achour, A. Rostami-Hodjegan, and A. Galetin. Meta-analysis of expression of hepatic organic anion-transporting polypeptide (oatp) transporters in cellular systems relative to human liver tissue. *Drug Metab Dispos*, 43 (4):424–32, 2015.

[61] E. A. Mostaghel, E. Cho, A. Zhang, M. Alyamani, A. Kaipainen, S. Green, B. T. Marck, N. Sharifi, J. L. Wright, R. Gulati, L. D. True, M. Loda, A. M. Matsumoto, D. Tamae, T. N. Penning, S. P. Balk, P. W. Kantoff, P. S. Nelson, M. E. Taplin, and R. B. Montgomery. Association of tissue abiraterone levels and slco genotype with intraprostatic steroids and pathologic response in men with high-risk localized prostate cancer. *Clin Cancer Res*, 23(16):4592–4601, 2017.

[62] X. Wang, L. C. Harshman, W. Xie, M. Nakabayashi, F. Qu, M. M. Pomerantz, G. S. Lee, and P. W. Kantoff. Association of slco2b1 genotypes with time to progression and overall survival in patients receiving androgen-deprivation therapy for prostate cancer. *J Clin Oncol*, 34(4):352–9, 2016.

[63] L. R. Schwarz, R. Burr, M. Schwenk, E. Pfaff, and H. Greim. Uptake of taurocholic acid into isolated rat-liver cells. *Eur J Biochem*, 55(3):617–23, 1975.

[64] S. A. Weinman. Electrogenicity of na(+)-coupled bile acid transporters. *Yale J Biol Med*, 70(4):331–40, 1997.

[65] P. A. Dawson, T. Lan, and A. Rao. Bile acid transporters. *J Lipid Res*, 50(12):2340–57, 2009.

[66] R. Liu, C. Chen, X. Xia, Q. Liao, Q. Wang, P. J. Newcombe, S. Xu, M. Chen, Y. Ding, X. Li, Z. Liao, F. Li, M. Du, H. Huang, R. Dong, W. Deng, Y. Wang, B. Zeng, Q. Pan, D. Jiang, H. Zeng, P. Sham, Y. Cao, P. H. Maxwell, Z. L. Gao, L. Peng, and Y. Wang. Homozygous p.ser267phe in slc10a1 is associated with a new type of hypercholanemia and implications for personalized medicine. *Sci Rep*, 7(1):9214, 2017.

[67] E. R. Verrier, C. C. Colpitts, C. Bach, L. Heydmann, L. Zona, F. Xiao, C. Thumann, E. Crouchet, R. Gaudin, C. Sureau, F. L. Cosset, J. A. McKeating, P. Pessaux, Y. Hoshida, C. Schuster, M. B. Zeisel, and T. F. Baumert. Solute carrier ntcp regulates innate antiviral immune responses targeting hepatitis c virus infection of hepatocytes. *Cell Rep*, 17(5):1357–1368, 2016.

[68] H. Koepsell. Role of organic cation transporters in drug-drug interaction. *Expert Opin Drug Metab Toxicol*, 11(10):1619–33, 2015.

[69] A. Mahrooz, A. Alizadeh, M. B. Hashemi-Soteh, M. Ghaffari-Cherati, and S. R. Hosseyni-Talei. Polymorphic variants rs3088442 and rs2292334 in the organic cation transporter 3 (oct3) gene and susceptibility against type 2 diabetes: Role of their interaction. *Arch Med Res*, 48(2):162–168, 2017.

157

[70] C. Jacobs, B. Pearce, M. Du Plessis, N. Hoosain, and M. Benjeddou. Genetic polymorphisms and haplotypes of the organic cation transporter 1 gene (slc22a1) in the xhosa population of south africa. *Genet Mol Biol*, 37(2):350–9, 2014.

[71] A. T. Nies, K. Damme, S. Kruck, E. Schaeffeler, and M. Schwab. Structure and function of multidrug and toxin extrusion proteins (mates) and their relevance to drug therapy and personalized medicine. *Arch Toxicol*, 90(7):1555–84, 2016.

[72] B. Prasad, K. Johnson, S. Billington, C. Lee, G. W. Chung, C. D. Brown, E. J. Kelly, J. Himmelfarb, and J. D. Unadkat. Abundance of drug transporters in the human kidney cortex as quantified by quantitative targeted proteomics. *Drug Metab Dispos*, 44(12):1920–1924, 2016.

[73] S. L. Stocker, K. M. Morrissey, S. W. Yee, R. A. Castro, L. Xu, A. Dahlin, A. H. Ramirez, D. M. Roden, R. A. Wilke, C. A. McCarty, R. L. Davis, C. M. Brett, and K. M. Giacomini. The effect of novel promoter variants in mate1 and mate2 on the pharmacokinetics and pharmacodynamics of metformin. *Clin Pharmacol Ther*, 93(2):186–94, 2013.

[74] K. Kato, H. Mori, T. Kito, M. Yokochi, S. Ito, K. Inoue, A. Yonezawa, T. Katsura, Y. Kumagai, H. Yuasa, Y. Moriyama, K. Inui, H. Kusuhara, and Y. Sugiyama. Investigation of endogenous compounds for assessing the drug interactions in the urinary excretion involving multidrug and toxin extrusion proteins. *Pharm Res*, 31(1):136–47, 2014.

[75] F. Staud, L. Cerveny, D. Ahmadimoghaddam, and M. Ceckova. Multidrug and toxin extrusion proteins (mate/slc47); role in pharmacokinetics. *Int J Biochem Cell Biol*, 45(9):2007–11, 2013.

[76] Z. L. Johnson and J. Chen. Atp binding enables substrate release from multidrug resistance protein 1. *Cell*, 172(1-2): 81–89.e10, 2018.

[77] S. B. Levy. Active efflux mechanisms for antimicrobial resistance. *Antimicrob Agents Chemother*, 36(4):695–703, 1992.

[78] K. Ueda, D. P. Clark, C. J. Chen, I. B. Roninson, M. M. Gottesman, and I. Pastan. The human multidrug resistance (mdr1) gene. cdna cloning and transcription initiation. *J Biol Chem*, 262(2):505–8, 1987.

[79] HUGO Gene Nomenclature Committee at the European Bioinformatics Institute. Atp binding cassette transporters (abc), 2018. URL https://www.genenames.org/cgi-bin/genefamilies/set/417. Date Accessed: November 2018.

[80] L. M. Hodges, S. M. Markova, L. W. Chinn, J. M. Gow, D. L. Kroetz, T. E. Klein, and R. B. Altman. Very important pharmacogene summary: Abcb1 (mdr1, p-glycoprotein). *Pharmacogenet Genomics*, 21(3):152–61, 2011.

[81] S. Wolking, E. Schaeffeler, H. Lerche, M. Schwab, and A. T. Nies. Impact of genetic polymorphisms of abcb1 (mdr1, p-glycoprotein) on drug disposition and potential clinical implications: Update of the literature. *Clin Pharmacokinet*, 54(7): 709–35, 2015.

[82] J. Gregers, H. Green, I. J. Christensen, K. Dalhoff, H. Schroeder, N. Carlsen, S. Rosthoej, B. Lausen, K. Schmiegelow, and C. Peterson. Polymorphisms in the abcb1 gene and effect on outcome and toxicity in childhood acute lymphoblastic leukemia. *Pharmacogenomics J*, 15(4):372–9, 2015.

[83] X. Zhong, M. Y. Liu, X. H. Sun, and M. J. Wei. Association between abcb1 polymorphisms and haplotypes and alzheimer's disease: a meta-analysis. *Sci Rep*, 6:32708, 2016.

[84] Y. Zhou, M. M. Gottesman, and I. Pastan. Domain exchangeability between the multidrug transporter (mdr1) and phosphatidylcholine flippase (mdr2). *Mol Pharmacol*, 56(5):997–1004, 1999.

[85] R. Mittra, M. Pavy, N. Subramanian, A. M. George, M. L. O'Mara, I. D. Kerr, and R. Callaghan. Location of contact residues in pharmacologically distinct drug binding sites on p-glycoprotein. *Biochem Pharmacol*, 123:19–28, 2017.

[86] A. Seelig and E. Landwojtowicz. Structure-activity relationship of p-glycoprotein substrates and modifiers. *Eur J Pharm Sci*, 12(1):31–40, 2000.

[87] W. Y. Kim and L. Z. Benet. P-glycoprotein (p-gp/mdr1)-mediated efflux of sex-steroid hormones and modulation of p-gp expression in vitro. *Pharm Res*, 21(7):1284–93, 2004.

[88] S. P. Cole. Multidrug resistance protein 1 (mrp1, abcc1), a "multitasking" atp-binding cassette (abc) transporter. *J Biol Chem*, 289(45):30880–8, 2014.

[89] HUGO Gene Nomenclature Committee at the European Bioinformatics Institute. Atp binding cassette (abc) c subfamily, 2018. URL https://www.genenames.org/cgi-bin/genefamilies/set/807. Date Accessed: November 2018.

[90] E. Bakos and L. Homolya. Portrait of multifaceted transporter, the multidrug resistance-associated protein 1 (mrp1/abcc1). *Pflugers Arch*, 453(5):621–41, 2007.

[91] M. Slomka, M. Sobalska-Kwapis, M. Korycka-Machala, G. Bartosz, J. Dziadek, and D. Strapagiel. Genetic variation of the abc transporter gene abcc1 (multidrug resistance protein 1-mrp1) in the polish population. *BMC Genet*, 16:114, 2015.

[92] D. W. Loe, K. C. Almquist, S. P. Cole, and R. G. Deeley. Atp-dependent 17 beta-estradiol 17-(beta-d-glucuronide) transport by multidrug resistance protein (mrp). inhibition by cholestatic steroids. *J Biol Chem*, 271(16):9683–9, 1996.

[93] A. Goma, R. Mir, F. Martinez-Soler, A. Tortosa, A. Vidal, E. Condom, R. Perez-Tomas, and P. Gimenez-Bonafe. Multidrug resistance protein 1 localization in lipid raft domains and prostasomes in prostate cancer cell lines. *Onco Targets Ther*, 7: 2215–25, 2014.

[94] M. Bagnoli, G. L. Beretta, L. Gatti, S. Pilotti, P. Alberti, E. Tarantino, M. Barbareschi, S. Canevari, D. Mezzanzanica, and P. Perego. Clinicopathological impact of abcc1/mrp1 and abcc4/mrp4 in epithelial ovarian carcinoma. *BioMed Research International*, 2013:7, 2013.

[95] A. T. Nies and D. Keppler. The apical conjugate efflux pump abcc2 (mrp2). *Pflugers Arch*, 453(5):643–59, 2007.

[96] J. Konig, A. T. Nies, Y. Cui, I. Leier, and D. Keppler. Conjugate export pumps of the multidrug resistance protein (mrp) family: localization, substrate specificity, and mrp2-mediated drug resistance. *Biochim Biophys Acta*, 1461(2):377–94, 1999.

[97] D. Keppler. The roles of mrp2, mrp3, oatp1b1, and oatp1b3 in conjugated hyperbilirubinemia. *Drug Metab Dispos*, 42(4): 561–5, 2014.

[98] X. Wen, M. S. Joy, and L. M. Aleksunes. In vitro transport activity and trafficking of mrp2/abcc2 polymorphic variants. *Pharm Res*, 34(8):1637–1647, 2017.

[99] G. S. Miszczuk, I. R. Barosso, M. C. Larocca, J. Marrone, R. A. Marinelli, A. C. Boaglio, E. J. Sanchez Pozzi, M. G. Roma, and F. A. Crocenzi. Mechanisms of canalicular transporter endocytosis in the cholestatic rat liver. *Biochim Biophys Acta Mol Basis Dis*, 1864(4 Pt A):1072–1085, 2018.

[100] T. Takechi, T. Hirota, T. Sakai, N. Maeda, D. Kobayashi, and I. Ieiri. Interindividual differences in the expression of atp-binding cassette and solute carrier family transporters in human skin: Dna methylation regulates transcriptional activity of the human abcc3 gene. *Drug Metab Dispos*, 46(5):628–635, 2018.

[101] E. van de Steeg, E. Wagenaar, C. M. van der Kruijssen, J. E. Burggraaff, D. R. de Waart, R. P. Elferink, K. E. Kenworthy, and A. H. Schinkel. Organic anion transporting polypeptide 1a/1b-knockout mice provide insights into hepatic handling of bilirubin, bile acids, and drugs. *J Clin Invest*, 120(8):2942–52, 2010.

[102] S. A. Balaji, N. Udupa, M. R. Chamallamudi, V. Gupta, and A. Rangarajan. Role of the drug transporter abcc3 in breast cancer chemoresistance. *PLoS One*, 11(5):e0155013, 2016.

[103] P. Borst, C. de Wolf, and K. van de Wetering. Multidrug resistance-associated proteins 3, 4, and 5. *Pflugers Arch*, 453(5): 661–73, 2007.

[104] F. G. Russel, J. B. Koenderink, and R. Masereeuw. Multidrug resistance protein 4 (mrp4/abcc4): a versatile efflux transporter for drugs and signalling molecules. *Trends Pharmacol Sci*, 29(4):200–7, 2008.

[105] S. B. Cheepala, A. Pitre, Y. Fukuda, K. Takenaka, Y. Zhang, Y. Wang, S. Frase, T. Pestina, T. K. Gartner, C. Jackson, and J. D. Schuetz. The abcc4 membrane transporter modulates platelet aggregation. *Blood*, 126(20):2307–19, 2015.

[106] B. Decouture, E. Dreano, T. Belleville-Rolland, O. Kuci, B. Dizier, A. Bazaa, B. Coqueran, A. M. Lompre, C. V. Denis, J. S. Hulot, C. Bachelot-Loza, and P. Gaussem. Impaired platelet activation and camp homeostasis in mrp4-deficient mice. *Blood*, 126(15):1823–30, 2015.

[107] X. Zhao, Y. Guo, W. Yue, L. Zhang, M. Gu, and Y. Wang. Abcc4 is required for cell proliferation and tumorigenesis in non-small cell lung cancer. *Onco Targets Ther*, 7:343–51, 2014.

[108] S. Likanonsakul, B. Suntisuklappon, R. Nitiyanontakij, W. Prasithsirikul, E. E. Nakayama, T. Shioda, and C. Sangsajja. A single-nucleotide polymorphism in abcc4 is associated with tenofovir-related beta2-microglobulinuria in thai patients with hiv-1 infection. *PLoS One*, 11(1):e0147724, 2016.

[109] N. Memon, K. M. Bircsak, F. Archer, C. J. Gibson, P. Ohman-Strickland, B. I. Weinberger, M. M. Parast, A. M. Vetrano, and L. M. Aleksunes. Regional expression of the bcrp/abcg2 transporter in term human placentas. *Reprod Toxicol*, 43:72–77, 2014.

[110] S. Dauchy, F. Dutheil, R. J. Weaver, F. Chassoux, C. Daumas-Duport, P. O. Couraud, J. M. Scherrmann, I. De Waziers, and X. Decleves. Abc transporters, cytochromes p450 and their main transcription factors: expression at the human blood-brain barrier. *J Neurochem*, 107(6):1518–28, 2008.

[111] Q. Mao and J. D. Unadkat. Role of the breast cancer resistance protein (bcrp/abcg2) in drug transport–an update. *AAPS J*, 17(1):65–82, 2015.

[112] B. Zambo, Z. Bartos, O. Mozner, E. Szabo, G. Varady, G. Poor, M. Palinkas, H. Andrikovics, T. Hegedus, L. Homolya, and B. Sarkadi. Clinically relevant mutations in the abcg2 transporter uncovered by genetic analysis linked to erythrocyte membrane protein expression. *Sci Rep*, 8(1):7487, 2018.

[113] R. Warta, D. Theile, C. Mogler, E. Herpel, N. Grabe, B. Lahrmann, P. K. Plinkert, C. Herold-Mende, J. Weiss, and G. Dyckhoff. Association of drug transporter expression with mortality and progression-free survival in stage iv head and neck squamous cell carcinoma. *PLoS One*, 9(9):e108908, 2014.

[114] J. Hu, J. Li, X. Yue, J. Wang, J. Liu, L. Sun, and D. Kong. Expression of the cancer stem cell markers abcg2 and oct-4 in right-sided colon cancer predicts recurrence and poor outcomes. *Oncotarget*, 8(17):28463–28470, 2017.

[115] A. Reustle, P. Fisel, O. Renner, F. Buttner, S. Winter, S. Rausch, S. Kruck, A. T. Nies, J. Hennenlotter, M. Scharpf, F. Fend, A. Stenzl, J. Bedke, M. Schwab, and E. Schaeffeler. Characterization of the breast cancer resistance protein (bcrp/abcg2) in clear cell renal cell carcinoma. *Int J Cancer*, 2018.

[116] B. Stieger, Y. Meier, and P. J. Meier. The bile salt export pump. *Pflugers Arch*, 453(5):611–20, 2007.

[117] B. Prusinskas, S. Kathemann, D. Pilic, B. Hegen, P. Kuster, V. Keitel, D. Haussinger, R. Buscher, H. A. Baba, P. F. Hoyer, and E. Lainka. Cholestasis after pediatric liver transplantation-recurrence of a progressive familial intrahepatic cholestasis phenotype as a rare differential diagnosis: A case report. *Transplant Proc*, 49(7):1628–1633, 2017.

[118] Y. Chen, X. Song, L. Valanejad, A. Vasilenko, V. More, X. Qiu, W. Chen, Y. Lai, A. Slitt, M. Stoner, B. Yan, and R. Deng. Bile salt export pump is dysregulated with altered farnesoid x receptor isoform expression in patients with hepatocellular carcinoma. *Hepatology*, 57(4):1530–41, 2013.

[119] M. A. Welch, K. Kock, T. J. Urban, K. L. Brouwer, and P. W. Swaan. Toward predicting drug-induced liver injury: parallel computational approaches to identify multidrug resistance protein 4 and bile salt export pump inhibitors. *Drug Metab Dispos*, 43(5):725–34, 2015.

[120] R. Chan and L. Z. Benet. Evaluation of the relevance of dili predictive hypotheses in early drug development: Review of in vitro methodologies vs bddcs classification. *Toxicol Res (Camb)*, 7(3):358–370, 2018.

[121] G.G. Gibson and P. Skett. In *Introduction to Drug Metabolism*. Nelson Thornes Publishers, 3 edition, 2001.

[122] HUGO Gene Nomenclature Committee at the European Bioinformatics Institute. Cytochrome p450 (cyp), 2018. URL www.genenames.org/cgi-bin/genefamilies/set/862. Date Accessed: November 2018.

[123] U. M. Zanger, M. Turpeinen, K. Klein, and M. Schwab. Functional pharmacogenetics/genomics of human cytochromes p450 involved in drug biotransformation. *Anal Bioanal Chem*, 392(6):1093–108, 2008.

[124] A. Vildhede, J. R. Wisniewski, A. Noren, M. Karlgren, and P. Artursson. Comparative proteomic analysis of human liver tissue and isolated hepatocytes with a focus on proteins determining drug exposure. *J Proteome Res*, 14(8):3305–14, 2015.

[125] S. A. Peters, C. R. Jones, A. L. Ungell, and O. J. Hatley. Predicting drug extraction in the human gut wall: Assessing contributions from drug metabolizing enzymes and transporter proteins using preclinical models. *Clin Pharmacokinet*, 55 (6):673–96, 2016.

[126] Y. Zhou, M. Ingelman-Sundberg, and V. M. Lauschke. Worldwide distribution of cytochrome p450 alleles: A meta-analysis of population-scale sequencing projects. *Clin Pharmacol Ther*, 102(4):688–700, 2017.

[127] R. Fujiwara, E. Yoda, and R. H. Tukey. Species differences in drug glucuronidation: Humanized udp-glucuronosyltransferase 1 mice and their application for predicting drug glucuronidation and drug-induced toxicity in humans. *Drug Metab Pharmacokinet*, 33(1):9–16, 2018.

[128] T. R. Van Vleet, H. Liu, A. Lee, and E. A. G. Blomme. Acyl glucuronide metabolites: Implications for drug safety assessment. *Toxicol Lett*, 272:1–7, 2017.

[129] M. W. H. Coughtrie. Function and organization of the human cytosolic sulfotransferase (sult) family. *Chem Biol Interact*, 259(Pt A):2–7, 2016.

[130] S. Nowell and C. N. Falany. Pharmacogenetics of human cytosolic sulfotransferases. *Oncogene*, 25(11):1673–8, 2006.

[131] N. Allocati, M. Masulli, C. Di Ilio, and L. Federici. Glutathione transferases: substrates, inihibitors and pro-drugs in cancer and neurodegenerative diseases. *Oncogenesis*, 7(1):8, 2018.

[132] M. Hirano, K. Maeda, Y. Shitara, and Y. Sugiyama. Drug-drug interaction between pitavastatin and various drugs via oatp1b1. *Drug Metab Dispos*, 34(7):1229–36, 2006.

[133] B. Davies and T. Morris. Physiological parameters in laboratory animals and humans. *Pharm Res*, 10(7):1093–5, 1993.

[134] W. P. Lemahieu, M. Hermann, A. Asberg, K. Verbeke, H. Holdaas, Y. Vanrenterghem, and B. D. Maes. Combined therapy with atorvastatin and calcineurin inhibitors: no interactions with tacrolimus. *Am J Transplant*, 5(9):2236–43, 2005.

[135] P. Sharma, C. J. Butters, V. Smith, R. Elsby, and D. Surry. Prediction of the in vivo oatp1b1-mediated drug-drug interaction potential of an investigational drug against a range of statins. *Eur J Pharm Sci*, 47(1):244–55, 2012.

[136] Q. Pei, J. Y. Liu, J. Y. Yin, G. P. Yang, S. K. Liu, Y. Zheng, P. Xie, C. X. Guo, M. Luo, H. H. Zhou, X. Li, and Z. Q. Liu. Repaglinide-irbesartan drug interaction: effects of slco1b1 polymorphism on repaglinide pharmacokinetics and pharmacodynamics in chinese population. *Eur J Clin Pharmacol*, 74(8):1021–1028, 2018.

[137] H. Chapy, S. Klieber, P. Brun, S. Gerbal-Chaloin, X. Boulenc, and O. Nicolas. Pbpk modeling of irbesartan: incorporation of hepatic uptake. *Biopharm Drug Dispos*, 36(8):491–506, 2015.

[138] M. J. Zamek-Gliszczynski, X. Chu, J. A. Cook, J. M. Custodio, A. Galetin, K. M. Giacomini, C. A. Lee, M. F. Paine, A. S. Ray, J. A. Ware, M. B. Wittwer, and L. Zhang. Itc commentary on metformin clinical drug-drug interaction study design that enables an efficacy- and safety-based dose adjustment decision. *Clin Pharmacol Ther*, 104(5):781–784, 2018.

[139] A. J. Nieuweboer, S. Hu, C. Gui, B. Hagenbuch, I. M. Ghobadi Moghaddam-Helmantel, A. A. Gibson, P. de Bruijn, R. H. Mathijssen, and A. Sparreboom. Influence of drug formulation on oatp1b-mediated transport of paclitaxel. *Cancer Res*, 74 (11):3137–45, 2014.

[140] R. Amundsen, H. Christensen, B. Zabihyan, and A. Asberg. Cyclosporine a, but not tacrolimus, shows relevant inhibition of organic anion-transporting protein 1b1-mediated transport of atorvastatin. *Drug Metab Dispos*, 38(9):1499–504, 2010.

[141] M. Karlgren, A. Vildhede, U. Norinder, J. R. Wisniewski, E. Kimoto, Y. Lai, U. Haglund, and P. Artursson. Classification of inhibitors of hepatic organic anion transporting polypeptides (oatps): influence of protein expression on drug-drug interactions. *Journal of medicinal chemistry*, 55(10):4740–4763, 2012.

[142] A. Vildhede, M. Karlgren, E. K. Svedberg, J. R. Wisniewski, Y. Lai, A. Noren, and P. Artursson. Hepatic uptake of atorvastatin: influence of variability in transporter expression on uptake clearance and drug-drug interactions. *Drug Metab Dispos*, 42(7):1210–8, 2014.

[143] L. C. Ellis, G. M. Hawksworth, and R. J. Weaver. Atp-dependent transport of statins by human and rat mrp2/mrp2. *Toxicol Appl Pharmacol*, 269(2):187–94, 2013.

[144] X. Wu, L. R. Whitfield, and B. H. Stewart. Atorvastatin transport in the caco-2 cell model: contributions of p-glycoprotein and the proton-monocarboxylic acid co-transporter. *Pharm Res*, 17(2):209–15, 2000.

[145] M. Gertz, C. M. Cartwright, M. J. Hobbs, K. E. Kenworthy, M. Rowland, J. B. Houston, and A. Galetin. Cyclosporine inhibition of hepatic and intestinal cyp3a4, uptake and efflux transporters: application of pbpk modeling in the assessment of drug-drug interaction potential. *Pharm Res*, 30(3):761–80, 2013.

[146] S. J. Kim, K. Toshimoto, Y. Yao, T. Yoshikado, and Y. Sugiyama. Quantitative analysis of complex drug-drug interactions between repaglinide and cyclosporin a/gemfibrozil using physiologically based pharmacokinetic models with in vitro transporter/enzyme inhibition data. *J Pharm Sci*, 106(9):2715–2726, 2017.

[147] T. Dujic, A. Causevic, T. Bego, M. Malenica, Z. Velija-Asimi, E. R. Pearson, and S. Semiz. Organic cation transporter 1 variants and gastrointestinal side effects of metformin in patients with type 2 diabetes. *Diabet Med*, 33(4):511–4, 2016.

[148] J. W. Higgins, A. B. Ke, and M. J. Zamek-Gliszczynski. Clinical cyp3a inhibitor alternatives to ketoconazole, clarithromycin and itraconazole, are not transported into the liver by hepatic organic anion transporting polypeptides and organic cation transporter 1. *Drug Metab Dispos*, 42(11):1780–4, 2014.

[149] W. Yamashiro, K. Maeda, M. Hirouchi, Y. Adachi, Z. Hu, and Y. Sugiyama. Involvement of transporters in the hepatic uptake and biliary excretion of valsartan, a selective antagonist of the angiotensin ii at1-receptor, in humans. *Drug Metab Dispos*, 34(7):1247–54, 2006.

[150] H. Koide, M. Tsujimoto, A. Takeuchi, M. Tanaka, Y. Ikegami, M. Tagami, S. Abe, M. Hashimoto, T. Minegaki, and K. Nishiguchi. Substrate-dependent effects of molecular-targeted anticancer agents on activity of organic anion transporting polypeptide 1b1. *Xenobiotica*, 48(10):1059–1071, 2018.

[151] S. J. Yang, B. J. Kim, L. Mo, and H. K. Han. Alteration of the intravenous and oral pharmacokinetics of valsartan via the concurrent use of gemfibrozil in rats. *Biopharm Drug Dispos*, 37(5):245–51, 2016.

[152] H. H. Lee, B. F. Leake, W. Teft, R. G. Tirona, R. B. Kim, and R. H. Ho. Contribution of hepatic organic anion-transporting polypeptides to docetaxel uptake and clearance. *Mol Cancer Ther*, 14(4):994–1003, 2015.

[153] S. Hu, R. H. Mathijssen, P. de Bruijn, S. D. Baker, and A. Sparreboom. Inhibition of oatp1b1 by tyrosine kinase inhibitors: in vitro-in vivo correlations. *Br J Cancer*, 110(4):894–8, 2014.

[154] A. Yamada, K. Maeda, K. Kiyotani, T. Mushiroda, Y. Nakamura, and Y. Sugiyama. Kinetic interpretation of the importance of oatp1b3 and mrp2 in docetaxel-induced hematopoietic toxicity. *CPT Pharmacometrics Syst Pharmacol*, 3:e126, 2014.

[155] M. T. Huisman, A. A. Chhatta, O. van Tellingen, J. H. Beijnen, and A. H. Schinkel. Mrp2 (abcc2) transports taxanes and confers paclitaxel resistance and both processes are stimulated by probenecid. *Int J Cancer*, 116(5):824–9, 2005.

[156] S. Vajda, K. R. Godfrey, and H. Rabitz. Similarity transformation approach to identifiability analysis of nonlinear compartmental models. *Math Biosci*, 93(2):217–48, 1989.

[157] N. D. Evans, M.J. Chapman, M. J. Chappell, and K.R. Godfrey. Identifiability of uncontrolled nonlinear rational systems. *Automatica*, 38(10):1799–1805, 2002.

[158] N. D. Evans, H. A. J. Moyse, D. Lowe, R. Higgins, D. Mitchell, D. Zehnder, and M. J. Chappel. Structural identifiability of surface binding reactions involving heterogeneous analyte: Application to surface plasmon resonance experiments. *Automatica*, 49:48–57, 2013.

[159] N. Meshkat, C. E. Kuo, and 3rd DiStefano, J. On finding and using identifiable parameter combinations in nonlinear dynamic systems biology models and combos: a novel web implementation. *PLoS One*, 9(10):e110261, 2014.

[160] J. Karlsson, M. Anguelova, and M. Jirstrand. An efficient method for structural identifiability analysis of large dynamic systems. In *16th IFAC Symposium on System Identification*, volume 45, pages 941–946, Belgium, 2012. Elsevier.

[161] A. F. Villaverde, A. Barreiro, and A. Papachristodoulou. Structural identifiability of dynamic systems biology models. *PLoS Comput Biol*, 12(10):e1005153, 2016.

[162] M. Schwenk, R. Burr, and E. Pfaff. Influence of viability on bromosulfophthalein uptake by isolated hepatocytes. *Naunyn Schmiedebergs Arch Pharmacol*, 295(1):99–102, 1976.

[163] M. Yamazaki, H. Suzuki, M. Hanano, T. Tokui, T. Komai, and Y. Sugiyama. Na(+)-independent multispecific anion transporter mediates active transport of pravastatin into rat liver. *Am J Physiol*, 264(1 Pt 1):G36–44, 1993.

[164] A. Poirier, T. Lav, R. Portmann, M-E. Brun, F. Senner, M. Kansy, H-P. Grimm, and C. Funk. Design, data analysis, and simulation of in vitro drug transport kinetic experiments using a mechanistic in vitro model. *Drug Metabolism and Disposition*, 36(12):2434–2444, 2008.

[165] S. W. Paine, A. J. Parker, P. Gardiner, P. J. Webborn, and R. J. Riley. Prediction of the pharmacokinetics of atorvastatin, cerivastatin, and indomethacin using kinetic models applied to isolated rat hepatocytes. *Drug Metab Dispos*, 36(7):1365–74, 2008.

[166] L. Li, A. Nouraldeen, and A. G. Wilson. Evaluation of transporter-mediated hepatic uptake in a non-radioactive high-throughput assay: a study of kinetics, species difference and plasma protein effect. *Xenobiotica*, 43(3):253–62, 2013.

[167] P. Sharma, V. E. Holmes, R. Elsby, C. Lambert, and D. Surry. Validation of cell-based oatp1b1 assays to assess drug transport and the potential for drug-drug interaction to support regulatory submissions. *Xenobiotica*, 40(1):24–37, 2010.

[168] S. Izumi, Y. Nozaki, T. Komori, O. Takenaka, K. Maeda, H. Kusuhara, and Y. Sugiyama. Investigation of fluorescein derivatives as substrates of organic anion transporting polypeptide (oatp) 1b1 to develop sensitive fluorescence-based oatp1b1 inhibition assays. *Mol Pharm*, 13(2):438–48, 2016.

[169] M. Ishigami, T. Tokui, T. Komai, K. Tsukahara, M. Yamazaki, and Y. Sugiyama. Evaluation of the uptake of pravastatin by perfused rat liver and primary cultured rat hepatocytes. *Pharm Res*, 12(11):1741–5, 1995.

[170] M. Baker and T. Parton. Kinetic determinants of hepatic clearance: plasma protein binding and hepatic uptake. *Xenobiotica*, 37(10-11):1110–34, 2007.

[171] M. G. Soars, K. Grime, J. L. Sproston, P. J. Webborn, and R. J. Riley. Use of hepatocytes to assess the contribution of hepatic uptake to clearance in vivo. *Drug Metab Dispos*, 35(6):859–65, 2007.

[172] Y. Yabe, A. Galetin, and J. B. Houston. Kinetic characterization of rat hepatic uptake of 16 actively transported drugs. *Drug Metab Dispos*, 39(10):1808–14, 2011.

[173] K. Menochet, K. E. Kenworthy, J. B. Houston, and A. Galetin. Use of mechanistic modeling to assess interindividual variability and interspecies differences in active uptake in human and rat hepatocytes. *Drug Metab Dispos*, 40(9):1744–56, 2012.

[174] T. Yoshikado, K. Toshimoto, T. Nakada, K. Ikejiri, H. Kusuhara, K. Maeda, and Y. Sugiyama. Comparison of methods for estimating unbound intracellular-to-medium concentration ratios in rat and human hepatocytes using statins. *Drug Metab Dispos*, 45(7):779–789, 2017.

[175] R. F. Reinoso, B. A. Telfer, B. S. Brennan, and M. Rowland. Uptake of teicoplanin by isolated rat hepatocytes: comparison with in vivo hepatic distribution. *Drug Metab Dispos*, 29(4 Pt 1):453–9, 2001.

[176] D. Boss, J. Kuhn, P. Jourdain, C. Depeursinge, P. J. Magistretti, and P. Marquet. Measurement of absolute cell volume, osmotic membrane water permeability, and refractive index of transmembrane water and solute flux by digital holographic microscopy. *J Biomed Opt*, 18(3):036007, 2013.

[177] C. J. Epstein. Cell size, nuclear content, and the development of polyploidy in the mammalian liver. *Proc Natl Acad Sci U S A*, 57(2):327–34, 1967.

[178] C. M. Gillen and 3rd Forbush, B. Functional interaction of the k-cl cotransporter (kcc1) with the na-k-cl cotransporter in hek-293 cells. *Am J Physiol*, 276(2 Pt 1):C328–36, 1999.

[179] R. Li, H. A. Barton, and T. S. Maurer. Toward prospective prediction of pharmacokinetics in oatp1b1 genetic variant populations. *CPT Pharmacometrics Syst Pharmacol*, 3:e151, 2014.

[180] A. Mateus, P. Matsson, and P. Artursson. Rapid measurement of intracellular unbound drug concentrations. *Mol Pharm*, 10(6):2467–78, 2013.

[181] A. K. Sohlenius-Sternbeck. Determination of the hepatocellularity number for human, dog, rabbit, rat and mouse livers from protein concentration measurements. *Toxicol In Vitro*, 20(8):1582–6, 2006.

[182] E. Kuhn and M. Lavielle. Maximum likelihood estimation in nonlinear mixed effects models. *Comput. Stat. Data Anal.*, 49 (4):1020–1038, 2005.

[183] D. L. Janzen, M. Jirstrand, M. J. Chappell, and N. D. Evans. Three novel approaches to structural identifiability analysis in mixed-effects models. *Comput Methods Programs Biomed*, 2016.

[184] M. Lavielle and L. Aarons. What do we mean by identifiability in mixed effects models? *J Pharmacokinet Pharmacodyn*, 43 (1):111–22, 2016.

[185] D. L. I. Janzen, M. Jirstrand, M. J. Chappell, and N. D. Evans. Extending existing structural identifiability analysis methods to mixed-effects models. *Math Biosci*, 295:1–10, 2018.

[186] R Core Team. R: A language and environment for statistical computing, 2017.

[187] Gabriela Stegmann, Ross Jacobucci, Jeffrey R. Harring, and Kevin J. Grimm. Nonlinear mixed-effects modeling programs in r. *Structural Equation Modeling: A Multidisciplinary Journal*, 25(1):160–165, 2018.

[188] A. Raue, B. Steiert, M. Schelker, C. Kreutz, T. Maiwald, H. Hass, J. Vanlier, C. Tonsing, L. Adlung, R. Engesser, W. Mader, T. Heinemann, J. Hasenauer, M. Schilling, T. Hofer, E. Klipp, F. Theis, U. Klingmuller, B. Schoberl, and J. Timmer. Data2dynamics: a modeling environment tailored to parameter estimation in dynamical systems. *Bioinformatics*, 31(21): 3558–60, 2015.

[189] J. A. Jacquez. Parameter estimation and optimal sampling times. In *Compartmental Analysis in Biology and Medicine*, pages 355–392. BioMedware, Ann Arbor, USA, 3 edition, 1996.

[190] M. Lavielle. In *Mixed Effects Models for the Population Approach: Models, Tasks, Methods and Tools*. Taylor and Francis, 2014.

[191] K. Ogungbenro and L. Aarons. Design of population pharmacokinetic experiments using prior information. *Xenobiotica*, 37 (10-11):1311–30, 2007.

[192] E. Germovsek, I. Lutsar, K. Kipper, M. O. Karlsson, T. Planche, C. Chazallon, L. Meyer, U. M. T. Trafojer, T. Metsvaht, I. Fournier, M. Sharland, P. Heath, and J. F. Standing. Plasma and csf pharmacokinetics of meropenem in neonates and young infants: results from the neomero studies. *J Antimicrob Chemother*, 73(7):1908–1916, 2018.

[193] E. A. Stromberg, J. Nyberg, and A. C. Hooker. The effect of fisher information matrix approximation methods in population optimal design calculations. *J Pharmacokinet Pharmacodyn*, 43(6):609–619, 2016.

[194] C. Dumont, G. Lestini, H. Le Nagard, F. Mentre, E. Comets, and T. T. Nguyen. Pfim 4.0, an extended r program for design evaluation and optimization in nonlinear mixed-effect models. *Comput Methods Programs Biomed*, 156:217–229, 2018.

[195] J. Nyberg, S. Ueckert, E. A. Stromberg, S. Hennig, M. O. Karlsson, and A. C. Hooker. Poped: an extended, parallelized, nonlinear mixed effects models optimal design tool. *Comput Methods Programs Biomed*, 108(2):789–805, 2012.

[196] G. L. Amidon, H. Lennernas, V. P. Shah, and J. R. Crison. A theoretical basis for a biopharmaceutic drug classification: the correlation of in vitro drug product dissolution and in vivo bioavailability. *Pharm Res*, 12(3):413–20, 1995.

[197] C. Y. Wu and L. Z. Benet. Predicting drug disposition via application of bcs: transport/absorption/ elimination interplay and development of a biopharmaceutics drug disposition classification system. *Pharm Res*, 22(1):11–23, 2005.

[198] C. M. Hosey, R. Chan, and L. Z. Benet. Bddcs predictions, self-correcting aspects of bddcs assignments, bddcs assignment corrections, and classification for more than 175 additional drugs. *AAPS J*, 18(1):251–60, 2016.

[199] J. D. Spence, C. E. Munoz, L. Hendricks, L. Latchinian, and H. E. Khouri. Pharmacokinetics of the combination of fluvastatin and gemfibrozil. *Am J Cardiol*, 76(2):80A–83A, 1995.

[200] M. Niemi, J. T. Backman, M. Neuvonen, and P. J. Neuvonen. Effects of gemfibrozil, itraconazole, and their combination on the pharmacokinetics and pharmacodynamics of repaglinide: potentially hazardous interaction between gemfibrozil and repaglinide. *Diabetologia*, 46(3):347–51, 2003.

[201] J. T. Backman, C. Kyrklund, M. Neuvonen, and P. J. Neuvonen. Gemfibrozil greatly increases plasma concentrations of cerivastatin. *Clin Pharmacol Ther*, 72(6):685–91, 2002.

[202] R. Vanholder, M. S. Sever, E. Erek, and N. Lameire. Rhabdomyolysis. *J Am Soc Nephrol*, 11(8):1553–61, 2000.

[203] L. I. Kajosaari, J. T. Backman, M. Neuvonen, J. Laitila, and P. J. Neuvonen. Lack of effect of bezafibrate and fenofibrate on the pharmacokinetics and pharmacodynamics of repaglinide. *Br J Clin Pharmacol*, 58(4):390–6, 2004.

[204] A. Tornio, P. J. Neuvonen, M. Niemi, and J. T. Backman. Role of gemfibrozil as an inhibitor of cyp2c8 and membrane transporters. *Expert Opin Drug Metab Toxicol*, 13(1):83–95, 2017.

[205] B. W. Ogilvie, D. Zhang, W. Li, A. D. Rodrigues, A. E. Gipson, J. Holsapple, P. Toren, and A. Parkinson. Glucuronidation converts gemfibrozil to a potent, metabolism-dependent inhibitor of cyp2c8: implications for drug-drug interactions. *Drug Metab Dispos*, 34(1):191–7, 2006.

[206] M. V. Varma, J. Lin, Y. A. Bi, E. Kimoto, and A. D. Rodrigues. Quantitative rationalization of gemfibrozil drug interactions: Consideration of transporters-enzyme interplay and the role of circulating metabolite gemfibrozil 1-o-beta-glucuronide. *Drug Metab Dispos*, 43(7):1108–18, 2015.

[207] S. Pahwa, K. Alam, A. Crowe, T. Farasyn, S. Neuhoff, O. Hatley, K. Ding, and W. Yue. Pretreatment with rifampicin and tyrosine kinase inhibitor dasatinib potentiates the inhibitory effects toward oatp1b1- and oatp1b3-mediated transport. *J Pharm Sci*, 106(8):2123–2135, 2017.

[208] Y. Shitara and Y. Sugiyama. Preincubation-dependent and long-lasting inhibition of organic anion transporting polypeptide (oatp) and its impact on drug-drug interactions. *Pharmacol Ther*, 177:67–80, 2017.

[209] S. Izumi, Y. Nozaki, T. Komori, O. Takenaka, K. Maeda, H. Kusuhara, and Y. Sugiyama. Comparison of the predictability of human hepatic clearance for organic anion transporting polypeptide substrate drugs between different in vitro-in vivo extrapolation approaches. *J Pharm Sci*, 106(9):2678–2687, 2017.

[210] R. A. Copeland. Reversible modes of inhibitor interactions with enzymes. In *Evaluation of Enzyme Inhibitors in Drug Discovery: A Guide for Medicinal Chemists and Pharmacologists*, pages 57–119. John Wiley and Sons, New Jersey, United States of America, 2 edition, 2013.

[211] K. Aho, D. Derryberry, and T. Peterson. Model selection for ecologists: the worldviews of aic and bic. *Ecology*, 95(3):631–6, 2014.

[212] D. R. Burnham, K. P. ; Anderson. Information and likelihood theory. In *Model Selection and Multimodel Inference: A practical Information-Theoretic Approach*, pages 60–80. Springer, second edition, 2002.

[213] A. Kunze, J. Huwyler, G. Camenisch, and B. Poller. Prediction of organic anion-transporting polypeptide 1b1- and 1b3-mediated hepatic uptake of statins based on transporter protein expression and activity data. *Drug Metab Dispos*, 42(9): 1514–21, 2014.

[214] M. Iwai, H. Suzuki, I. Ieiri, K. Otsubo, and Y. Sugiyama. Functional analysis of single nucleotide polymorphisms of hepatic organic anion transporter oatp1b1 (oatp-c). *Pharmacogenetics*, 14(11):749–57, 2004.

[215] Y. Oh, Y. S. Jeong, M. S. Kim, J. S. Min, G. Ryoo, J. E. Park, Y. Jun, Y. K. Song, S. E. Chun, S. Han, S. K. Bae, S. J. Chung, and W. Lee. Inhibition of organic anion transporting polypeptide 1b1 and 1b3 by betulinic acid: Effects of preincubation and albumin in the media. *J Pharm Sci*, 107(6):1713–1723, 2018.

[216] J. W. Yates. Structural identifiability of physiologically based pharmacokinetic models. *J Pharmacokinet Pharmacodyn*, 33 (4):421–39, 2006.

[217] B. Schloerke, J. Crowley, D. Cook, H. Hofmann, H. Wickham, F. Briatte, M. Marbach, E. Thoen, A. Elberg, and J. Larmarange. Ggally: Extension to 'ggplot2', 2018.

[218] Y. Shitara, T. Itoh, H. Sato, A. P. Li, and Y. Sugiyama. Inhibition of transporter-mediated hepatic uptake as a mechanism for drug-drug interaction between cerivastatin and cyclosporin a. *J Pharmacol Exp Ther*, 304(2):610–6, 2003.

[219] S. Izumi, Y. Nozaki, K. Maeda, T. Komori, O. Takenaka, H. Kusuhara, and Y. Sugiyama. Investigation of the impact of substrate selection on in vitro organic anion transporting polypeptide 1b1 inhibition profiles for the prediction of drug-drug interactions. *Drug Metab Dispos*, 43(2):235–47, 2015.

[220] S. J. Carter. The development of a high throughput method to determine the uptake of drugs into rat hepatocytes with application to pravastatin. Msc, King's College London, 2009.

[221] A.V. Fuentes, M. D. Pineda, and K. C. N. Venkata. Comprehension of top 200 prescribed drugs in the us as a resource for pharmacy teaching, training and practice. *Pharmacy (Basel, Switzerland)*, 6(2):43, 2018.

[222] E. P. Neve, P. Artursson, M. Ingelman-Sundberg, and M. Karlgren. An integrated in vitro model for simultaneous assessment of drug uptake, metabolism, and efflux. *Mol Pharm*, 10(8):3152–63, 2013.

[223] C. S. Yim, Y. S. Jeong, S. Y. Lee, W. Pyeon, H. M. Ryu, J. H. Lee, K. R. Lee, H. J. Maeng, and S. J. Chung. Specific inhibition of the distribution of lobeglitazone to the liver by atorvastatin in rats: Evidence for a rat organic anion transporting polypeptide 1b2-mediated interaction in hepatic transport. *Drug Metab Dispos*, 45(3):246–259, 2017.

[224] G. Fricker and A. Fahr. Mechanisms of hepatic transport of cyclosporin a: an explanation for its cholestatic action? *Yale J Biol Med*, 70(4):379–90, 1997.

[225] R. Amundsen, A. Asberg, I. K. Ohm, and H. Christensen. Cyclosporine a- and tacrolimus-mediated inhibition of cyp3a4 and cyp3a5 in vitro. *Drug Metab Dispos*, 40(4):655–61, 2012.

[226] B. Skalicka, M. Kubanek, I. Malek, Y. Vymetalova, L. Hoskova, M. Podzimkova, and J. Kautzner. Conversion to tacrolimus and atorvastatin in cyclosporine-treated heart transplant recipients with dyslipidemia refractory to fluvastatin. *J Heart Lung Transplant*, 28(6):598–604, 2009.

[227] R. Imamura, N. Ichimaru, T. Moriyama, Y. Shi, Y. Namba, N. Nonomura, K. Matsumiya, K. Toki, S. Takahara, and A. Okuyama. Long term efficacy of simvastatin in renal transplant recipients treated with cyclosporine or tacrolimus. *Clin Transplant*, 19(5):616–21, 2005.

[228] P. Kulkarni, K. Korzekwa, and S. Nagar. Intracellular unbound atorvastatin concentrations in the presence of metabolism and transport. *J Pharmacol Exp Ther*, 359(1):26–36, 2016.

[229] T. Watanabe, H. Kusuhara, K. Maeda, H. Kanamaru, Y. Saito, Z. Hu, and Y. Sugiyama. Investigation of the rate-determining process in the hepatic elimination of hmg-coa reductase inhibitors in rats and humans. *Drug Metab Dispos*, 38(2):215–22, 2010.

[230] Y. Y. Lau, H. Okochi, Y. Huang, and L. Z. Benet. Multiple transporters affect the disposition of atorvastatin and its two active hydroxy metabolites: application of in vitro and ex situ systems. *J Pharmacol Exp Ther*, 316(2):762–71, 2006.

[231] T. Prueksaritanont, M. Koike, B. A. Hoener, and L. Z. Benet. Transport and metabolism of cyclosporine in isolated rat hepatocytes. the effects of lipids. *Biochem Pharmacol*, 43(9):1997–2006, 1992.

[232] K. Umehara and G. Camenisch. Novel in vitro-in vivo extrapolation (ivive) method to predict hepatic organ clearance in rat. *Pharm Res*, 29(2):603–17, 2012.

[233] K. Ziegler and M. Frimmer. Identification of cyclosporin binding sites in rat liver plasma membranes, isolated hepatocytes, and hepatoma cells by photoaffinity labeling using [3h]cyclosporin-diaziridine. *Biochim Biophys Acta*, 855(1):147–56, 1986.

[234] B. Hagenbuch and C. Gui. Xenobiotic transporters of the human organic anion transporting polypeptides (oatp) family. *Xenobiotica*, 38(7-8):778–801, 2008.

[235] Y. Shitara, K. Takeuchi, Y. Nagamatsu, S. Wada, Y. Sugiyama, and T. Horie. Long-lasting inhibitory effects of cyclosporin a, but not tacrolimus, on oatp1b1- and oatp1b3-mediated uptake. *Drug Metab Pharmacokinet*, 27(4):368–78, 2012.

[236] P. O. Seglen. Preparation of isolated rat liver cells. *Methods Cell Biol*, 13:29–83, 1976.

[237] J. Harrison, T. De Bruyn, A. S. Darwich, and J. B. Houston. Simultaneous assessment in vitro of transporter and metabolic processes in hepatic drug clearance: Use of a media loss approach. *Drug Metab Dispos*, 46(4):405–414, 2018.

[238] M. Liao, Q. Zhu, A. Zhu, C. Gemski, B. Ma, E. Guan, A. P. Li, G. Xiao, and C. Q. Xia. Comparison of uptake transporter functions in hepatocytes in different species to determine the optimal model for evaluating drug transporter activities in humans. *Xenobiotica*, pages 1–11, 2018.

[239] I. H. Segel. Kinetics of unireactant enzymes. In *Enzyme Kinetics: Behaviour and Analysis of Rapid Equilibrium and Steady-State Enzyme Systems*, pages 19–42. John Wiley and Sons Inc, U.S.A., 1993.

[240] (TGA) Therapeutic Goods Administration. Australian public assessment report for pitavastatin, 2013. URL https://www.tga.gov.au/auspar/auspar-pitavastatin. Date Accessed: October 2018.

[241] H. Fujino, I. Yamada, S. Shimada, M. Yoneda, and J. Kojima. Metabolic fate of pitavastatin, a new inhibitor of hmg-coa reductase: human udp-glucuronosyltransferase enzymes involved in lactonization. *Xenobiotica*, 33(1):27–41, 2003.

[242] Antony R. G., Pannala R. R., Nimmakayala S., and Jadi S. Degradation pathway for pitavastatin calcium by validated stability indicating uplc method. *American Journal of Analytical Chemistry*, Vol.01No.02:8, 2010.

[243] M. Nieto, G. Calvo, I. Hudson, P. Feldschreiber, D. Brown, C. C. Lee, G. Lay, A. Valeri, E. Abadie, A. Thomas, and F. Pignatti. The european medicines agency review of eltrombopag (revolade) for the treatment of adult chronic immune (idiopathic) thrombocytopenic purpura: summary of the scientific assessment of the committee for medicinal products for human use. *Haematologica*, 96(9):e33–e40, 2011.

[244] K. Takeuchi, T. Sugiura, K. Matsubara, R. Sato, T. Shimizu, Y. Masuo, M. Horikawa, N. Nakamichi, N. Ishiwata, and Y. Kato. Interaction of novel platelet-increasing agent eltrombopag with rosuvastatin via breast cancer resistance protein in humans. *Drug Metab Dispos*, 42(4):726–34, 2014.

[245] K. Takeuchi, T. Sugiura, S. Umeda, K. Matsubara, M. Horikawa, N. Nakamichi, D. L. Silver, N. Ishiwata, and Y. Kato. Pharmacokinetics and hepatic uptake of eltrombopag, a novel platelet-increasing agent. *Drug Metab Dispos*, 39(6):1088–96, 2011.

[246] U.S. Department of Health CDER), Human Services Food, Drug Administration Center for Drug Evaluation, and Research. Clinical pharmacology and biopharmaceutics review, application number: Nda 22-291, 2013. URL `https://www.accessdata.fda.gov/drugsatfda_docs/nda/2008/022291s000_ClinPharmR_P1.pdf`. Date Accessed: October 2018.

[247] A. J. Allred, C. J. Bowen, J. W. Park, B. Peng, D. D. Williams, M. B. Wire, and E. Lee. Eltrombopag increases plasma rosuvastatin exposure in healthy volunteers. *Br J Clin Pharmacol*, 72(2):321–9, 2011.

[248] M. B. Wire, H. B. McLean, C. Pendry, D. Theodore, J. W. Park, and B. Peng. Assessment of the pharmacokinetic interaction between eltrombopag and lopinavir-ritonavir in healthy adult subjects. *Antimicrob Agents Chemother*, 56(6):2846–51, 2012.

[249] R. Elsby, P. Martin, D. Surry, P. Sharma, and K. Fenner. Solitary inhibition of the breast cancer resistance protein efflux transporter results in a clinically significant drug-drug interaction with rosuvastatin by causing up to a 2-fold increase in statin exposure. *Drug Metab Dispos*, 44(3):398–408, 2016.

[250] P. Nordell, S. Winiwarter, and C. Hilgendorf. Resolving the distribution-metabolism interplay of eight oatp substrates in the standard clearance assay with suspended human cryopreserved hepatocytes. *Mol Pharm*, 10(12):4443–51, 2013.

[251] H. Fujino, D. Nakai, R. Nakagomi, M. Saito, T. Tokui, and J. Kojima. Metabolic stability and uptake by human hepatocytes of pitavastatin, a new inhibitor of hmg-coa reductase. *Arzneimittelforschung*, 54(7):382–8, 2004.

[252] N. J. Waters, R. Jones, G. Williams, and B. Sohal. Validation of a rapid equilibrium dialysis approach for the measurement of plasma protein binding. *J Pharm Sci*, 97(10):4586–95, 2008.

[253] M.G. Mooij, U.I. Schwarz, B.A. de Koning, J.S. Leeder, R. Gaedigk, J.N. Samsom, E. Spaans, J.B. van Goudoever, D. Tibboel, R.B. Kim, and S.N. de Wildt. Ontogeny of human hepatic and intestinal transporter gene expression during childhood: Age matters. *Drug Metab Dispos*, 42(8):1268–74, 2014.

[254] S. Ohnishi, A. Hays, and B. Hagenbuch. Cysteine scanning mutagenesis of transmembrane domain 10 in organic anion transporting polypeptide 1b1. *Biochemistry*, 53(14):2261–70, 2014.

[255] J. W. Bauman, C. T. Vincent, B. Peng, M. B. Wire, D. D. Williams, and J. W. Park. Effect of hepatic or renal impairment on eltrombopag pharmacokinetics. *J Clin Pharmacol*, 51(5):739–50, 2011.

[256] I. Yamada, H. Fujino, S. Shimada, and J. Kojima. Metabolic fate of pitavastatin, a new inhibitor of hmg-coa reductase: similarities and difference in the metabolism of pitavastatin in monkeys and humans. *Xenobiotica*, 33(7):789–803, 2003.

[257] D. A. Bow, J. L. Perry, D. S. Miller, J. B. Pritchard, and K. L. Brouwer. Localization of p-gp (abcb1) and mrp2 (abcc2) in freshly isolated rat hepatocytes. *Drug Metab Dispos*, 36(1):198–202, 2008.

[258] Z. Luo, Y. Zhang, J. Gu, P. Feng, and Y. Wang. Pharmacokinetic properties of single- and multiple-dose pitavastatin calcium tablets in healthy chinese volunteers. *Curr Ther Res Clin Exp*, 77:52–7, 2015.

[259] X. Qi, L. Ding, A. Wen, N. Zhou, X. Du, and S. Shakya. Simple lc-ms/ms methods for simultaneous determination of pitavastatin and its lactone metabolite in human plasma and urine involving a procedure for inhibiting the conversion of pitavastatin lactone to pitavastatin in plasma and its application to a pharmacokinetic study. *J Pharm Biomed Anal*, 72:8–15, 2013.

[260] T. Yoshikado, K. Yoshida, N. Kotani, T. Nakada, R. Asaumi, K. Toshimoto, K. Maeda, H. Kusuhara, and Y. Sugiyama. Quantitative analyses of hepatic oatp-mediated interactions between statins and inhibitors using pbpk modeling with a parameter optimization method. *Clin Pharmacol Ther*, 100(5):513–523, 2016.

[261] M. Jamei, F. Bajot, S. Neuhoff, Z. Barter, J. Yang, A. Rostami-Hodjegan, and K. Rowland-Yeo. A mechanistic framework for in vitro-in vivo extrapolation of liver membrane transporters: prediction of drug-drug interaction between rosuvastatin and cyclosporine. *Clin Pharmacokinet*, 53(1):73–87, 2014.

[262] Y. Yao, K. Toshimoto, S.J. Kim, T. Yoshikado, and Y Sugiyama. Quantitative analysis of complex drug-drug interactions between cerivastatin and metabolism/transport inhibitors using physiologically based pharmacokinetic modeling. *Drug Metab Dispos*, 46(7):924–933, 2018.

[263] T. Watanabe, H. Kusuhara, K. Maeda, Y. Shitara, and Y. Sugiyama. Physiologically based pharmacokinetic modeling to predict transporter-mediated clearance and distribution of pravastatin in humans. *J Pharmacol Exp Ther*, 328(2):652–62, 2009.

[264] B. Guiastrennec, D.P. Sonne, M. Hansen, J.I. Bagger, A. Lund, J.F. Rehfeld, O. Alskr, M.O. Karlsson, T. Vilsbll, F.K. Knop, and M. Bergstrand. Mechanism-based modeling of gastric emptying rate and gallbladder emptying in response to caloric intake. *CPT Pharmacometrics Syst Pharmacol*, 5(12):692–700, 2016.

[265] M. S. Roberts, B. M. Magnusson, F. J. Burczynski, and M. Weiss. Enterohepatic circulation: physiological, pharmacokinetic and clinical implications. *Clin Pharmacokinet*, 41(10):751–90, 2002.